

Graphene and Polymer Nanoparticle Electrocatalysis

A thesis submitted for the degree of

Doctor of Philosophy

in Physical and Theoretical Chemistry

Lifu Chen

St. Cross College

Trinity Term 2019

Graphene and Polymer Nanoparticle Electrocatalysis

Lifu Chen
St. Cross College, University of Oxford
A thesis submitted for the degree of D.Phil. in Physical and Theoretical Chemistry
Trinity Term, 2019

Abstract

This thesis reports experimental work with two main aims: the first is the detection and characterisation of single graphene and polymer nanoparticles with an emphasis on their electrocatalysis; the second is to develop a more comprehensive understanding of nanoscale interfacial reactions kinetically and mechanistically.

Understanding adsorption processes underpins applications in advanced catalysts and ultra-sensitive sensors. The adsorption of catechol on graphene nanoplatelets (GNPs) is first investigated and quantified electrochemically and spectroscopically. Two electrochemical techniques are applied, notably cyclic voltammetry of ensembles and nano-impacts of single particles to study catechol adsorbed on GNPs. Generic methodologies are developed for the study of surface adsorption on GNPs and a molecular phase transition is seen. This is further applied to first investigate the adsorption of phenyl hydroquinone, where a more complicated flat-edge-end adsorption manner is seen with two phase transitions, and second the role of adsorption in electrocatalysis, where a lower overpotential of dopamine oxidation at a *single* GNP as compared to glassy carbon is observed. This approach is then further protocolised and proposed as an accurate surface area characterisation technique for both graphene and graphene oxide materials with high surface areas and complex internal structures.

In a second set of studies, the electrocatalytic behaviour of Nafion nanoparticles, a cation exchange polymer widely applied in fuel cells, is investigated. The catalytic oxygen reduction by *ensembles* and *single* Nafion particles doped with methyl viologen is investigated. The results reveal the relative kinetics of the ensembles and single particles and a generic novel approach to catalysis is proposed applying *homogeneous* electron mediators *heterogeneously* by immobilising the former in particles used to modify electrode interfaces. ‘Fake’ catalytic features of *undoped* Nafion particles are then fully explored, revealing the complexity in the voltammetry of electrodes modified by ensembles of nanoparticles.

The ion transport and charge transfer *within* Nafion films and particles are then characterised and compared. The contrasting behaviour shows the transport in the particles is significantly faster than in films of similar thickness. This leads to the investigation and development of a novel type of reference electrode based on immobilisation of both components of redox couples within Nafion films. The proposed Nafion film reference electrodes demonstrate superior stability with respect to life-time and multiple cycling.

Acknowledgements

First of all, I would like to thank and express my deep gratitude to my supervisor, Professor Richard Compton, for his extraordinary support and guidance throughout my D.Phil. study. It has been a real privilege to be a part of such amazing research group. Thank you for taking a chance regardless that my undergraduate background was in Chemical Engineering and all I knew about electrochemistry was Faraday's first law. You took me into your group and the electrochemistry. I am very grateful for the open-door policy and the constructive advice (as well as the jokes) in every meeting. Thank you for believing in me and offering me so many opportunities and challenges. You are my supervisor, my mentor and a role model. Aside from science, I have learned to be a better person, to work hard and enjoy the beer, to be strict and have some humour. I will carry all of these with me through my career and future.

I also want to thank Dr. Eden. E. L. Tanner, Dr. Christopher Batchelor-McAuley and Dr. Xiuting Li for their help advice and on-hand teaching. Thank you for always being there when I was in trouble, or in the most of cases, totally lost. Thank for your generous help and incredible patience. You really took me under your wings and taught me how to do research. Special thanks must go to Dr. Enno Kätelhön and Dr. Chuhong Lin for their simulation work on my experimental results. It is always fantastic to see the experiment matches the simulation and we 'beat' the science.

To Daisy, Ryan and Yuanzhe, it is such a privilege to work with you. You are smart and hardworking and it has been a great pleasure for me to witness you becoming great independent scientists. I learned a lot during this process and I hope I was helpful to you. To Korbua, thank you for all the-good-time chats and memory that will always make me smile. To my Ruochen, thank you so much for being my lunch buddy and taking me to St. John's for lunch every day. To Jake, Alex, Yuki, Dia, Xiaosheng, Haonan, Bertold, Xin, Raphael, Sabine, Giorgia, Wallans, Grace and many more, the Compton group members of past and present have always made me feel welcome and added fun to lab life.

Lastly, I would like to thank my family, for their love, care and never-ending support. I was not strong enough to be here but you made it happen. To You, knowing you is the best thing happened in my life. Our relationship shares the same starting date with my D.Phil. Now I am going be Dr. Chen and I hope you will be Mrs. Chen in the very near future.

Contents

Abstract……i

Acknowledgements……ii

Contents……iii

Glossary……x

Chapter 1 Introduction to Electrochemistry

1.1 Electrochemical Equilibrium……2

1.2 Electrode Kinetics……6

1.3 Mass Transport……10

1.3.1 Diffusion……10

1.3.2 Convection……13

1.3.3 Migration……14

1.4 Faradaic and non-Faradaic processes……15

1.5 Electrochemical Cells……17

1.6 Macroelectrodes and Microelectrodes……19

1.7 Electrochemical Techniques ……21

1.7.1 Cyclic Voltammetry……21

1.7.1.1 Voltammetry at Macroelectrodes……22

1.7.1.2 Surface bound and thin layer voltammetry……27

1.7.1.3 Voltammetry at Microelectrodes……29

1.7.2 Chronoamperometry……31

1.8 Single Nanoparticle Electrochemistry……32

1.8.1 Nanomaterials……32

1.8.2 Nano-impacts……34

Bibliography……36

Chapter 2 Introduction to UV-visible Spectroscopy

2.1 Properties of UV and visible Radiation……40

2.2 Absorption of Electromagnetic Radiation……41

2.3 Instrumentation……43

Bibliography……44

Chapter 3 Experimental

3.1 Chemicals and Reagents……45

3.1.1 Graphene Nanoplatelets……46

3.1.2 Preparation of GNP Suspensions……47

3.1.3 Synthesis of Nafion Particles……47

3.2 Electrochemical Instrumentation……48

3.2.1 Carbon Macro- and Micro- electrode Preparations……48

3.2.1 Carbon Fibre Micro Electrode Fabrication……49

3.3 Non-electrochemical Instrumentation……49

Bibliography……49

Chapter 4 Catechol Adsorption on Graphene Nanoplatelets: Isotherm, Flat to Vertical Phase Transition and Desorption Kinetics

4.1 Introduction……51

4.2 Experimental……53

4.2.1 Buffer Solution……53

4.2.2 Preparation of GNP Suspensions……53

4.2.3 Cyclic Voltammetry at EPPG Electrodes……54

4.2.4 Nano-impact Experiments……54

4.2.5 UV-vis Experiments……55

4.3 Results and Discussion……55

4.3.1 Cyclic Voltammetry of Catechol Modified GNPs……55

4.3.2 UV-vis Studies of Catechol Adsorption on GNPs……57

4.3.3 Nano-impacts of Catechol-GNPs and Unmodified-GNPs……61

4.4 Conclusions……68

Bibliography……68

Chapter 5 Adsorption on Graphene: Flat to Edge to End Transitions of Phenyl Hydroquinone

5.1 Introduction……72

5.2 Experimental……73

5.2.1 Buffer Solution……73

5.2.2 UV-vis Spectroscopy……73

5.2.3 Preparation of PHQ-GNP Stock Suspensions……74

5.2.4 Electrochemical Measurements……74

5.3 Results and Discussion……75

5.3.1 Adsorption Isotherm of Phenyl Hydroquinone on Graphene……75

5.3.2 Cyclic Voltammetry of Phenyl Hydroquinone……80

5.3.3 Nano-impacts of Individual PHQ-GNPs……81

5.4 Conclusions……85

Bibliography……85

Chapter 6 Impact Electrochemistry Reveals that Graphene Nanoplatelets Catalyse the Oxidation of Dopamine *via* Adsorption

6.1 Introduction……88

6.2 Experimental……89

6.2.1 Buffer Solution……89

6.2.2 UV-vis Spectroscopy and Adsorption Measurements……89

6.2.3 Preparation of GNP Suspensions for Nano-impact Experiments……90

6.2.4 Electrochemical Measurements……90

6.3 Results and Discussion……91

6.3.1 Adsorption of Dopamine on GNPs……91

6.3.2 Oxidation of Dopamine on Micro and Macro Carbon Electrodes……94

6.3.3 Oxidation of Dopamine on Single GNPs……99

6.4 Conclusions……107

Bibliography……108

Chapter 7 Surface Area Measurements of Graphene and Graphene Oxide *via* Dopamine Adsorption

7.1 Introduction……111

7.2 Experimental……113

7.2.1 Materials and Reagents……113

7.2.2 Characterisation of Graphene and Graphene Oxide Samples……114

7.2.3 BET Measurements……114

7.2.4 Dopamine Adsorption Measurements……115

7.2.5 Methylene Blue Adsorption Measurements……116

7.3 Results and Discussion……116

7.3.1 Characterisation of Graphene and Graphene Oxide Samples……116

7.3.2 Adsorption of Dopamine and Methylene Blue on Graphene and GO……119

7.3.3 Comparison of BET, Dopamine and MB Absorption Techniques……126

7.4 Conclusions……128

Bibliography……129

Chapter 8 Single Entity Electrocatalysis: Oxygen Reduction Mediated *via* Methyl Viologen Doped Nafion Nanoparticles

8.1 Introduction……132

8.2 Experimental……133

8.2.1 Synthesis of MV-Nafion Particles……133

8.2.2 Cyclic Voltammetry of Ensembles of MV-Nafion Particles……133

8.2.3 Impact Electrochemistry of Single MV-Nafion Particles……134

8.3 Theory and Simulation……135

8.3.1 Theoretical Model……135

8.3.1.1 Simulation of the Cyclic Voltammetry of Nafion Particle Modified Electrode……..137

8.3.1.2 Simulation of the Potential-Dependent Current Signals of Single Nafion Particles ……..141

8.3.2 Theoretical Results……142

8.3.2.1 Macroelectrodes Modified by MV^{2+} doped Nafion Particle Ensembles……142

8.3.2.1 Single MV^{2+} doped Nafion Particles……144

8.4 Results and Discussion……145

8.4.1 Experimental Results……146

8.4.1.1 Macroelectrodes Modified by MV^{2+} doped Nafion Particle Ensembles……146

8.4.1.2 Single MV^{2+} doped Nafion Particles……153

8.4.2 Simulation of Experimental Results……158

8.4.2.1 Kinetic Study of MV^{2+} Doped Nafion Particle Ensembles……158

8.2.2.2 Kinetic Study of Single MV^{2+} Doped Nafion Particles……160

8.5 Conclusions……162

Bibliography……163

Chapter 9 Unscrambling Illusory Inhibition and Catalysis in Nanoparticle Electrochemistry

9.1 Introduction……166

9.2 Experimental……168

9.2.1 Materials and Reagent……168

9.2.2 Electrochemical Measurements……168

9.3 Theoretical Model……169

9.4 Results and Discussion……172

9.4.1 Simulation Results……172

9.4.2 Experimental Results……177

9.4.2.1 Validation of the Theoretical Results……177

9.4.2.2 A More Complex System: Oxygen Reduction……184

9.4.2.3 Electrostatic Interactions……187

9.4.2.3.1 Hexaammineruthenium (III) Reduction……188

9.4.2.3.3 Ferrocenemethanol Oxidation……190

9.4.2.3.3 Ferrocyanide Oxidation……191

9.5 Conclusions……193

Bibliography……193

Chapter 10 Electrochemical Characterisation and Comparison of Transport in Nafion Films and Particles

10.1 Introduction……197

10.2 Experimental……198

10.2.1 Preparation and Electrochemical Characterisation of MV-Nafion Films on Electrodes……198

10.2.2 Preparation and Electrochemical Characterisation of single MV-Nafion Particles……199

10.2.3 Preparation and Electrochemical Characterisation of Layers of MV-Nafion Particles on Electrodes…199

10.3 Theory and Simulation……200

10.3.1 Nafion thin-film simulation……200

10.3.2 Single Nafion Particle Simulation……202

10.3.3 Dimensional and Dimensionless Simulation……204

10.4 Results……207

10.4.1 Ion Transport in Nafion Thin-film Coated Electrodes……207

10.4.2 Ion Transport in Single Nafion Particles……212

10.4.3 Ion transport in Nafion particle modified electrodes……214

10.5 Discussion and Perspectives……217

10.6 Conclusions ……218

Bibliography……218

Chapter 11 Reference Electrodes for Electrochemical Sensors Based on Redox Couples Immobilized within Nafion Films

11.1 Introduction……221

11.2 Experimental……223

11.2.1 Chemical Reagents……223

11.2.2 Electrochemical Measurements……224
11.2.3 Fabrication of the Nafion Film Reference Electrodes……224
11.2.4 Fabrication of the Doped Nafion Particle Reference Electrodes……229
11.2.4 Characterisation and Stability Study of Nafion Film Reference Electrodes……229
11.3 Results and Discussion……230
11.3.1 Electrode Performance Optimisation……230
11.3.2 Effect of Doping Ratio……231
11.3.3 Effect of Film Thickness……233
11.3.4 Effect of Film Morphology……248
11.3.5 Stability of the Fc/Fc^+ Nafion Film Reference Electrodes ……242
11.3.6 Reproducibility of the Fc/Fc^+ Nafion Films……247
11.4 Conclusions……248
Bibliography……248
Chapter 12 Overall Conclusions……250
Appendix A……253
Appendix B……254
Appendix C……260
Appendix D……262
Appendix E……269

Glossary

Roman Symbols

Symbol	Meaning	Units
a_j	activity of species *j*	mol m^{-3}
$a_{j,0}$	activity of species *j* at electrode surface	mol m^{-3}
A	electrode area	m^2
c_j	concentration of species *j*	mol m^{-3}
c_j^*	bulk concentration of species *j*	mol m^{-3}
$c_{j,0}$	concentration of species *j* at electrode surface	mol m^{-3}
D_j	diffusion coefficient of species *j*	m^2 s^{-1}
E	potential applied at the working electrode	V
E^0	standard electrode potential	V
E_f^0	formal potential	V
E_{mid}	mid-point potential	V
$E_{1/2}$	half-wave potential	V
E_p	peak potential	V
ΔE_p	peak-to-peak separation	V
F	Faraday constant ≈ 96485	C mol^{-1}
f	frequency	s^{-1}
G	Gibbs energy	J mol^{-1}
$\Delta G_0^{\ddagger}$	standard Gibbs energy of activation	J mol^{-1}
I	current	A
I_p	peak current	A
I_{ss}	steady-state current	A
j_j	flux of species *j*	mol m^{-2} s^{-1}

k^0	standard electrochemical rate constant	m s^{-1}
k_{ox}	oxidation rate constant	m s^{-1}
k_{red}	reduction rate constant	m s^{-1}
K	adsorption constant	m^3 mol^{-1}
l	path length	m
m	mass	g
m_T	mass transport coefficient	m s^{-1}
M	molar mass	g mol^{-1}
n	number of electrons transferred	dimensionless
N_i	number of species j	dimensionless
N_A	Avogadro constant ≈ 6.022×10^{23}	mol^{-1}
Q	charge	C
R	Universal Gas Constant ≈ 8.314	J K^{-1} mol^{-1}
r_e	electrode radius	m
T	absolute temperature	K
t	time	s
v	potential scan rate	V s^{-1}
z_j	ionic charge of species j	dimensionless

Greek Symbols

Symbol	Meaning	Unit
α	reductive transfer coefficient	dimensionless
β	oxidative transfer coefficient	dimensionless
δ	diffusion layer thickness	m
ε	extinction coefficient	m^2 mol^{-1}
η	overpotential ($E - E_f^0$)	V
γ	activity coefficient	dimensionless
λ	wavelength	m
$\bar{\mu}$	electrochemical potential	J mol^{-1}

μ	chemical potential	J mol^{-1}
τ	dimensionless time	dimensionless
ϕ	electrical potential	V
ϕ_m	electric potential of the metallic electrode	V
ϕ_s	electric potential of the solution	V
ρ	density	g m^{-3}
θ	fractional surface coverage	dimensionless
Γ	surface coverage	mol m^{-2}

Abbreviations

Abbreviation	**Meaning**
BET	Brunauer-Emmett-Teller
BPPG	Basal Plane Pyrolytic Graphite
CE	counter electrode
CV	cyclic voltammetry
DA	dopamine
DF	dilution factor
EDL	electrical double layer
EPPG	Edge Plane Pyrolytic Graphite
GC	glassy carbon
GNP	graphene nanoplatelet
HOMO	highest occupied molecular orbital
IHP	Inner Helmholtz Plane
MV	methyl viologen
OHP	Outer Helmholtz Plane
PHQ	phenyl hydroquinone
PVFc	poly(vinylferrocene)
PZC	potential of zero charge
RDS	rate-determining step
RE	reference electrode

SCE	saturated calomel electrode
SECM	scanning electrochemical microscopy
SEM	scanning electron microscope
SHE	standard hydrogen electrode
SPM	scanning probe microscopy
TEM	transmission electron microscopy
UV-vis	ultraviolet-visible spectroscopy
WE	working electrode
XPS	X-ray photoelectron spectroscopy

Chapter 1

Introduction to Electrochemistry

Electrochemistry is the branch of chemistry concerned with the interrelation between electricity and chemical change. Rather than studying the *direct* electron transfer between molecules and/or atoms, electrochemical reactions describe overall reactions where the individual redox components are *separate* but connected via an external electric circuit and an intervening electrolyte. The electrochemical reactions are either a chemical reaction caused by the passage of an electric current, as in electrolysis, or production of an electric current by a spontaneous chemical reaction as in a battery.

This introductory Chapter provides an overview of the fundamentals of electrochemistry and the principles underlying the electrochemical techniques employed in this thesis.

1.1 Electrochemical Equilibrium

Electrochemistry involves the study of chemical reactions and electron transfer across the interface of an electronic conductor (an electrode) and an ionic conductor (an electrolyte). Particularly considering a metallic electrode immersed in a solution containing a redox species *A* and *B*, the metal can act as both *source* or *sink* of electrons, bringing the reduction or oxidation of a species at the electrode-solution interface:

$$A_{(aq)} + e^-_{(metal)} \rightleftharpoons B_{(aq)} \tag{1.1}$$

In the electronic structure of a metal, the electrons energy levels in the conduction bands form an effective continuum and are filled up to an energy maximum known as the *Fermi level*, as schematically shown in Figure 1.1. In contrast, the energy levels associated with solution-phase species, *A* and *B*, are discrete. Considering, from a thermodynamic aspect, the situation where the Fermi level of the metal (electrode) is relatively higher than the lowest unoccupied molecular orbital (LUMO) of *A* in the solution phase, it is energetically favourable for electrons to transfer from the Fermi level to the vacant orbital in *A* to generate *B*. As this electron transfer proceeds, the Fermi level of the electrode becomes progressively lower while the energy levels of the solution phase species rise since the charge developed on the two phases, the electrode and the solution, change the energy levels in both. Ultimately when the energy levels match, the *reverse* reaction can occur, where the electrons transfer from B to the metallic phase. When the rates of the forward and backward reactions are matched, a dynamic equilibrium is established and no further net charge is possible after this point.[1,2] As a result of this equilibrium process, there is a charge separation introduced at the electrode/solution interface and gives rise to an *electrode potential*.

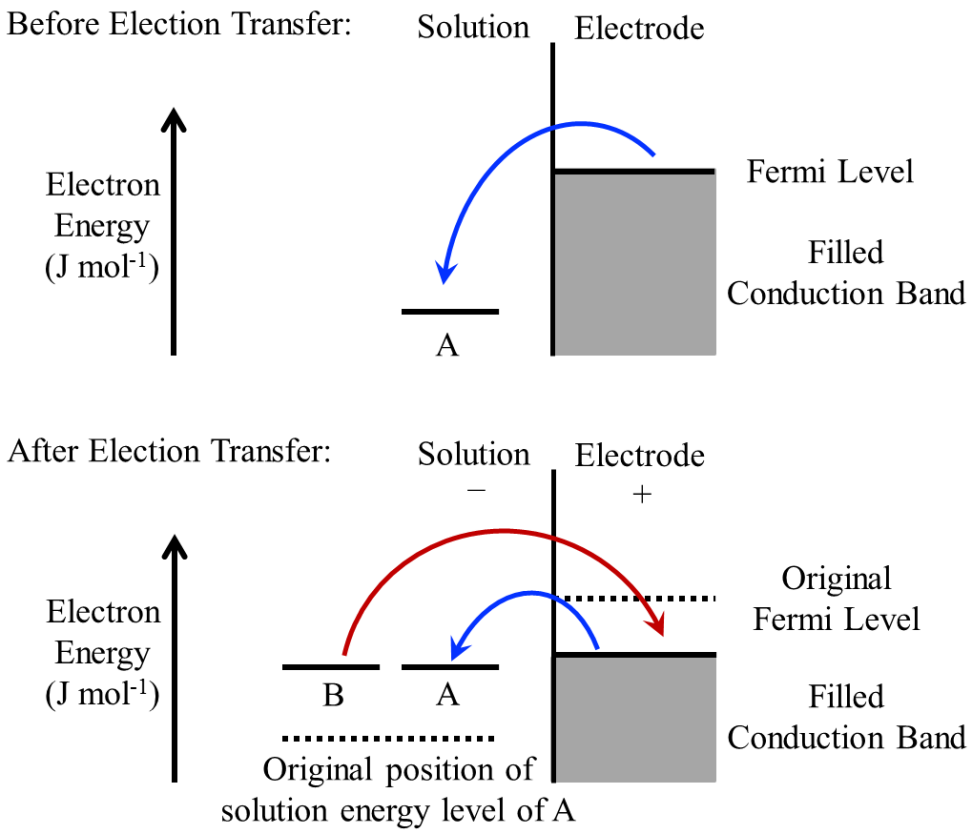


Figure 1.1. Illustration of energy levels of the solution-phase species and the metallic electrode during the attainment of electrochemical equilibrium between *A* and *B*.

For an electrochemical equilibrium as discussed above, the position of the equilibrium is balanced by both the chemical and electrical energies of all the involved entities. The electrochemical potential, $\bar{\mu}_j$, of a species *j* is defined as:

$$\bar{\mu}_j = \mu_j + Z_j F \phi \tag{1.2}$$

where μ_j and Z_j denote the chemical potential and the charge of species *j*, respectively. *F* is the Faraday constant (96485 C mol^{-1}) corresponding to the charge on one mole of electrons. ϕ is the potential of the electrode (ϕ_M) or solution phase (ϕ_S) of species *j*.

For the equilibrium of Eqn.(1.1), the electrochemical potential is:

$$\bar{\mu}_A + \bar{\mu}_{e^-} = \bar{\mu}_B \tag{1.3}$$

hence,

$$\left(\mu_A + Z_A F\phi_S\right) + \left(\mu_{e^-} - F\phi_M\right) = \left(\mu_B + \left(Z_A - 1\right)F\phi_S\right) \tag{1.4}$$

$$F\left(\phi_S - \phi_M\right) = \mu_B - \mu_A - \mu_{e^-} \tag{1.5}$$

The chemical potential (μ_j) is defined as:

$$\mu_j = \mu_j^0 + RT\, ln\, a_{j,0} \tag{1.6}$$

where μ_j^0 is the standard chemical potential of species *j*, *R* is the universal gas constant (8.314 J $K^{-1}mol^{-1}$), T is the absolute temperature (K), and $a_{j,0}$ is the activity of species *j* in solution.

Expanding and substituting Eqn.(1.6) into Eqn.(1.5) gives,

$$\phi_M - \phi_S = \frac{\Delta\mu^0}{F} + \frac{RT}{F} ln\left(\frac{a_{A,0}}{a_{B,0}}\right) \tag{1.7}$$

where

$$\Delta\mu^0 = \mu_A^0 + \mu_{e^-} - \mu_B^0 \tag{1.8}$$

which is a constant at a given temperature and pressure.

Equation (1.7) is the *Nernst equation* associated with a single electrode/solution interface, which *conceptually* relates the quantity $\phi_M - \phi_S$ to the activities of the reaction species. In reality it is *experimentally* impossible to measure such an absolute value at a single electrode/solution interface. Therefore a second electrode/solution interface is necessarily introduced to make the measurement feasible. If the content of solution at the second electrode/solution interface is maintained constant, the measured potential difference between two electrodes, *E*, represents the potential of the electrode of the interest. Such second electrode is called a 'reference electrode'.[3]

$$E = \left(\phi_M - \phi_S\right)_{test} - \left(\phi_M - \phi_S\right)_{reference} \tag{1.9}$$

For the *two-electrode* system, the Nernst equation is expressed as:

$$E = E^0 + \frac{RT}{F} ln\left(\frac{a_{A,0}}{a_{B,0}}\right) \tag{1.10}$$

where E^0 is the standard electrode potential against the standard hydrogen electrode (SHE, 1atm, 298K, 1 unit activity) as reference electrode.

In particular, the absolute *concentrations* of the chemical species rather than *activities* are often known, easily controlled and measured. The activity for species *j* can be expressed with respect to their corresponding concentration[4]

$$a_j = \gamma_j c_j \tag{1.11}$$

where γ_i is the activity coefficient of species *j* (unitless), and is the factor accounting for the non-ideality of solution due to the ion-ion and ion-solvent interactions in the electrolyte. c_j is the concentration of the species *j*.

To avoid any inconvenience in dealing with activities in practice, the formal potential (E_f^0) is defined as:

$$E_f^0 = E^0 + \frac{RT}{F} ln\left(\frac{\gamma_A}{\gamma_B}\right) \tag{1.12}$$

Thus the Nernst equation can be expressed as:

$$E = E_f^0 + \frac{RT}{F} ln\left(\frac{c_{A,0}}{c_{B,0}}\right) \tag{1.13}$$

The above *Nernst Equation* describes the electrode potential for an electrochemical reaction at dynamic equilibrium. The establishment of the latter requires fast electrode kinetics. Therefore, in the following section, the electrode kinetics will be considered and elaborated.

1.2 Electrode kinetics

As discussed above, the Nernst equation only applies under electrochemical equilibrium conditions which in turn requires fast electrode kinetics. Thermodynamics describe the equilibrium state while kinetics *quantitatively* describe the rates of chemical change. In experimental practice, instead of allowing the equilibrium to establish, a potential is usually applied to the electrode to disturb this equilibrium so as to characterise the redox reactions of interest. The unequal rate of reduction and oxidation brings a non-zero net flux of electrons between the redox species and the electrode. Understanding the rates of electron transfer, therefore, are essential for investigation of the electrode process.

Consider the one–electron transfer reaction as discussed above in Eqn.(1.1):

$$A_{(aq)} + e^-_{(metal)} \underset{k_{ox}}{\overset{k_{red}}{\rightleftharpoons}} B_{(aq)} \tag{1.14}$$

The net electrical *current* (*I*) passing through the electrode can be quantified as:

$$I = FAj \tag{1.15}$$

where A is the geometric area of the electrode, and j (mol m^2 s^{-1}) is the heterogeneous reaction flux at the interface:

$$j = k_{red}c_{A,0} - k_{ox}c_{B,0} \tag{1.16}$$

where k_{red} and k_{ox} are the heterogeneous rate constants for the reduction and oxidation, respectively. $c_{j,0}$ is the concentration of species j at the electrode surface, which is usually differ from that in bulk solution.[5]

In accordance with *the Transition State Theory*,[6,7] the electrochemical rate constants k_{red} and k_{ox} can be related to the Gibbs energies of activation assuming an Arrhenius behaviour:[3]

$$k_{red} = A_{red}\, exp\left(-\frac{\Delta G^{\ddagger}_{red}}{RT}\right) \tag{1.17}$$

$$k_{ox} = A_{ox}\, exp\left(-\frac{\Delta G^{\ddagger}_{ox}}{RT}\right) \tag{1.18}$$

where $\Delta G^{\ddagger}_{red}$ and $\Delta G^{\ddagger}_{ox}$ are the Gibbs energies of activation of the reduction and oxidation, respectively, also known as the "energy barriers" to the reaction. A_{red} and A_{ox} are the pre-exponential factors, depending of the reaction frequency of the electroactive species with the electrode surface. A typical reaction profile including the positions of the reactants, products and transition state ($\ddagger$) is demonstrated in Figure 1.2.

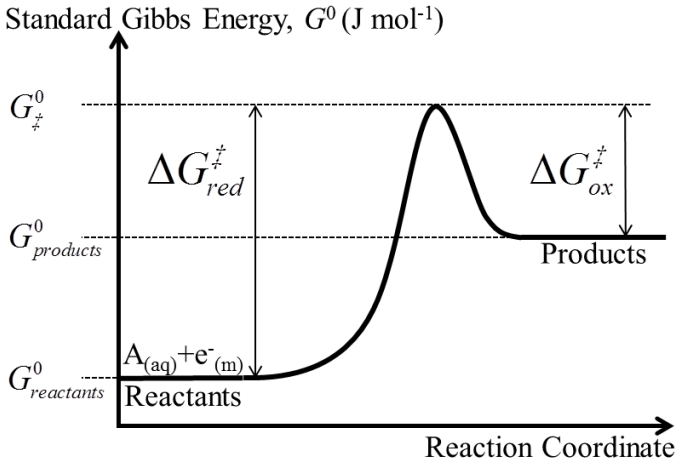


Figure 1.2. A reaction profile for a general one-electron transfer process: $A + e^- \leftrightharpoons B$. $\ddagger$ donates the transition state.

At a fixed temperature and pressure, the Gibbs energies of activation of the reduction and oxidation are expressed as:

$$\Delta G^{\ddagger}_{red} = \Delta G^{\ddagger}_{0} + \alpha F\left(E - E^{0}_{f}\right) \tag{1.19}$$

$$\Delta G^{\ddagger}_{ox} = \Delta G^{\ddagger}_{0} - \beta F\left(E - E^{0}_{f}\right) \tag{1.20}$$

where $\Delta G^{\ddagger}_{0}$ is the standard Gibbs energy. E and E^{0}_{f} are applied potential and formal potential respectively. α and β are the *cathodic* and *anodic* transfer coefficients, respectively, whose values range from zero to one with a sum of unity for a one-electron transfer process.

The magnitude of transfer coefficients reflects the position of the transition state (‡).[8,9] If α is close to zero, the transition state resembles $A + e^-$, while if α is near unity, it resembles *B*. In most cases, the value of α is found to be near 0.5 (i.e. $\alpha \sim \beta \sim 0.5$), suggesting the transition state sits intermediate between the reactants and products.[10,11]

Substituting Eqn.(1.19) and (1.20) into Eqn.(1.17) and (1.18), respectively, gives

$$k_{red} = A_{red}\, exp\left(-\frac{\Delta G_0^{\ddagger}}{RT}\right) exp\left(-\frac{\alpha F\left(E - E_f^0\right)}{RT}\right) \tag{1.21}$$

$$k_{ox} = A_{ox}\, exp\left(-\frac{\Delta G_0^{\ddagger}}{RT}\right) exp\left(\frac{\beta F\left(E - E_f^0\right)}{RT}\right) \tag{1.22}$$

The standard electrochemical rate constant (k^0) is defined as:[12,13]

$$k^0 = A_{red}\, exp\left(-\frac{\Delta G_0^{\ddagger}}{RT}\right) = A_{ox}\, exp\left(-\frac{\Delta G_0^{\ddagger}}{RT}\right) \tag{1.23}$$

hence,

$$k_{red} = k^0\, exp\left(-\frac{\alpha F\left(E - E_f^0\right)}{RT}\right) \tag{1.24}$$

$$k_{ox} = k^0\, exp\left(\frac{\beta F\left(E - E_f^0\right)}{RT}\right) \tag{1.25}$$

where $E - E^0_f$ is defined as the overpotential (η) of the redox reaction, and reflects the potential difference between the potential applied to the electrode and the formal potential of the redox couple.

Substituting Eqn.(1.24) and (1.25), the rate law shown in Eqn.(1.16) gives the following important *flux-potential* relation:

$$j = k^0 c_{A,0}\, exp\left(-\frac{\alpha F\left(E - E_f^0\right)}{RT}\right) - k^0 c_{B,0}\, exp\left(\frac{\beta F\left(E - E_f^0\right)}{RT}\right) \tag{1.26}$$

This is the *Butler-Volmer equation*,[12-14] from which the *Tafel Law* can be derived as follows.

When the above reduction process, as in Eqn.(1.14), is relatively much faster than the reverse oxidation process the latter becomes negligible, and the flux can be expressed as:

$$j = k^0 c_{A,0}\, exp\left(-\frac{\alpha F\left(E - E_f^0\right)}{RT} \right) \tag{1.27}$$

Similarly, for an oxidation process ($B_{(aq)} - e^-_{(metal)} \rightleftharpoons A_{(aq)}$):

$$j = -k^0 c_{B,0}\, exp\left(\frac{\beta F\left(E - E_f^0\right)}{RT} \right) \tag{1.28}$$

Provided that $c_{A,0}$ and $c_{B,0}$ do not change significantly from their bulk values over the range of potential studied:

$$ln\left|I_{red}\right| = -\frac{\alpha FE}{RT} + constant \tag{1.29}$$

$$ln\left|I_{ox}\right| = \frac{\beta FE}{RT} + constant \tag{1.30}$$

where I_{red} and I_{ox} are the reduction and oxidation current, respectively. A plot of $ln|I|$ against E is referred to a *Tafel plot* as shown in Figure 1.3 The transfer coefficient can be determined from the gradient of the Tafel plots.

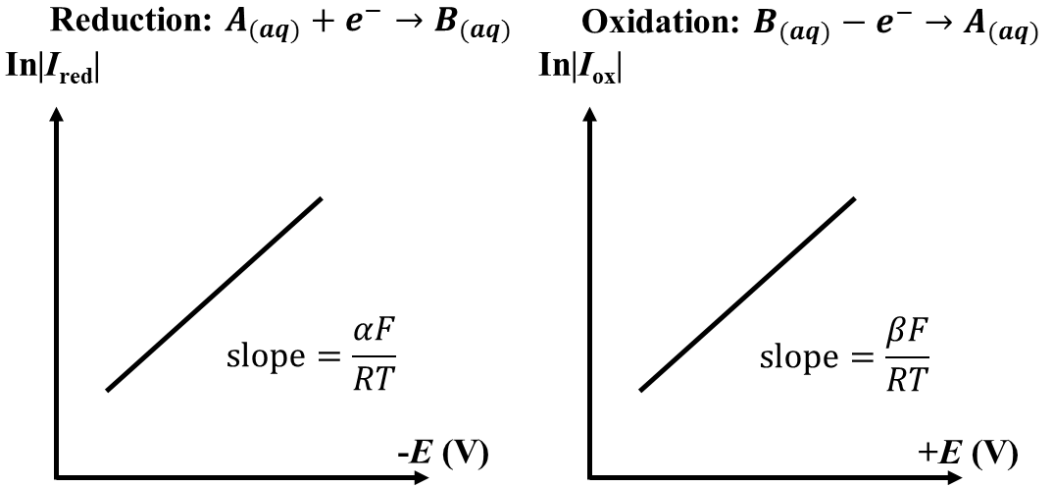


Figure 1.3. Tafel plots.

1.3 Mass transport

The previous section discussed electrode kinetics at the electrode-solution interface, where the reactant is consumed resulting in a lower concentration in the vicinity of the electrode. This encourages the movement of the reactants from bulk solution to the electrode surface, which is known as mass transport. Three main processes contribute to the mass transport of electroactive species to an electrode, notably diffusion, convection and migration.[15] The *Nernst-Plank equation* quantifies the total mass transport, within one-dimensional Cartesian coordinates:[3]

$$j_j(x) = -D_j \frac{\partial c_j(x)}{\partial x} + c_j v(x) - \frac{z_j F}{RT} D_j c_j \frac{\partial \phi(x)}{\partial x} \tag{1.31}$$

where $j_j(x)$ is the total flux (mol m^2 s^{-1}) of a species j at distance x from the electrode surface, $c_j(x)$ is the concentration, z_j is the ionic charge, $\emptyset(x)$ is the electric potential, and $v(x)$ is the local fluid velocity. The terms on the right-hand side refer to the diffusional flux, convectional flux and migratory flux respectively.

In practice, for an electrochemical measurement, the effects of migration and convection are usually eliminated to provide a simple diffusion only system, as will be discussed in detail in below.

1.3.1 Diffusion

Diffusion is a spontaneous movement of a species down its concentration gradient so as to maximize entropy. When a suitable potential is applied at an electrode, the reactant is consumed and depletion occurs in the vicinity of the electrode surface, inducing a concentration gradient from the bulk to the reaction interface. This electrochemically induced depletion zone of the reactant near the electrode surface is the *diffusion layer*, as

represented in Figure 1.4. Fick's laws of diffusion describe this variation in concentration in both space and time.[16,17]

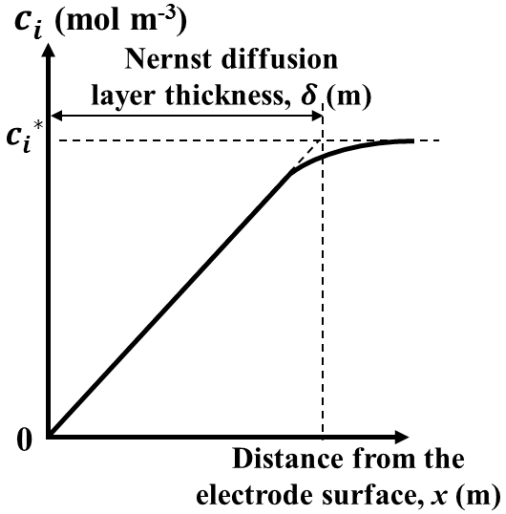


Figure 1.4. The one-dimensional Nernst diffusion layer.

Fick's First Law, derived experimentally, describes how the flux J through a unit area in a unit time (mol m^{-2} s^{-1}) relates to the concentration gradient in one dimension:

$$J = -D\frac{\partial c}{\partial x} \tag{1.32}$$

where the flux J is the number of moles passing through a unit area in a unit time, $\partial c/\partial x$ is the local concentration gradient. The negative sign in Eqn(1.32) accounts for the movement of the species from a higher concentration area to a lower one.

Fick's second law describes the change in concentration with time (t) at a certain point, x:

$$\frac{\partial c}{\partial t} = D\frac{\partial^2 c}{\partial x^2} \tag{1.33}$$

Fick's laws can be understood from a one-definitional microscopic model, as illustrated in Figure 1.5. Consider linear diffusion in the direction perpendicular to a cross-sectional plane A, which separates a box evenly into two compartments with an infinitesimally small thickness (δx) of solution containing particles (molecules, ions). The concentration of the left and right sides are c_1 and c_2, respectively. The particles move randomly in solution and cross the plane A, and have equal probabilities of moving to the right and to the left. In a

defined time period δt, the number of particles transporting from left to right through the plane is $c_1 A\delta x/2$ and from right to left is $c_2 A\delta x/2$.

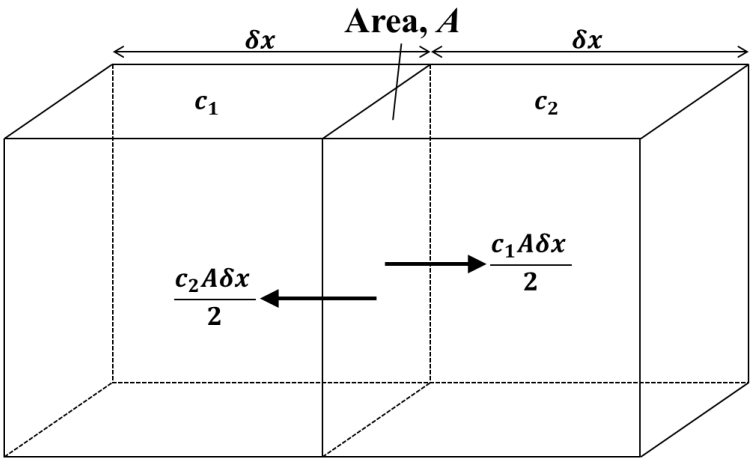


Figure 1.5. A microscopic model of *Fick's First Law* of diffusion in one dimension.

Overall, the net rate of particles transferred through a plane A is thus expressed as:

$$Rate = \frac{(c_1 - c_2) A\delta x}{2\delta t} \tag{1.34}$$

Accordingly, the diffusional flux (J) is expressed as:

$$J = \frac{(c_1 - c_2)\delta x}{2\delta t} \tag{1.35}$$

As the local concentration gradient is:

$$\frac{c_1 - c_2}{\delta x} \sim \frac{\partial c}{\partial x} \tag{1.36}$$

Substitution of Eqn. (1.36) into (1.35) gives:

$$J = -\frac{(\delta x)^2}{2\delta t}\frac{\partial c}{\partial x} \tag{1.37}$$

Note that the negative sign in reflects the flux flows from high to low concentrations.

This is equivalent to *Fick's First Law* (Eqn.(1.32)) when

$$D = \frac{(\delta x)^2}{2\delta t} \tag{1.38}$$

Therefore, importantly, the diffusion coefficient allows a measurement of the mean-square of distance ($\langle x^2 \rangle$) travelled by a particle in a certain time *t*, as described by the Einstein-Smoluchowski equation:[18,19]

$$\sqrt{\langle x^2 \rangle} = \sqrt{2Dt} \tag{1.39}$$

This gives a measure of the diffusion layer thickness, *d*.[20,21]

If considering three-dimensional diffusion, the root mean square distance becomes

$$\sqrt{\langle x^2 \rangle + \langle y^2 \rangle + \langle z^2 \rangle} = \sqrt{6Dt} \tag{1.40}$$

1.3.2 Convection

Convection refers to the movement of species due to a mechanical force. There are two general forms of convection: natural and forced convection. *Natural* convection is an intrinsic property of electrochemical reaction, resulting from density and/or thermal gradients in solution.[22] The former is induced by the chemical changes at the working and/or counter electrodes when the reaction takes place while the latter is usually caused by imperfection in thermostatting or strongly exothermic or endothermic reactions. This form of convection is undesirable and complicates the system of interest. To minimise the effect of density gradients, the experimental time for measurement should be controlled to within a relatively short time.[23] Meanwhile, the electrochemical system needs to be carefully thermostated, as is the case in this thesis. *Forced* convection arises from the mechanical agitation of the solution gas bubbling, stirring or pumping. In most cases, it is deliberately induced to dominate the mass transport the system, allowing well-defined quantitative analysis. For example, forced convention is commonly applied in hydrodynamic studies using a rotating disc electrode or a channel flow cell.[2,3,24] The flux, $J_{c,j}$, due to convection is given by:

$$J_{c,j}(x) = c_j v(x) \tag{1.41}$$

where $v(x)$ is the solution velocity (m s^{-1}) and $c_j(x)$ is the concentration.

1.3.3 Migration

Migration describes the movement of charged species in solution due to the effect of an electrical field resulting from the potential drop at the electrode/solution interface.[2,3,25] For any species j, the migratory flux, $J_{m,j}$, is expressed as:

$$j_{m,j}(x) = -\frac{z_j F}{RT} D_j c_j \frac{\partial \phi(x)}{\partial x} \tag{1.42}$$

Z_j is the charge of the ion j and $\partial \emptyset(x)/\partial x$ is the potential gradient or electric field (V m^{-1}).

At the vicinity to the electrode, the total flux J_j of electroactive substance arises from a mixed transport of diffusion and migration. The diffusional flux, $J_{d,j}$, and the migratory flux, $J_{m,j}$, can be in the same or opposite directions depending on the direction of the electric field and the charge on the electroactive species.[26] Figure 1.6 provides a schematic illustration of three different scenarios where a positive, negative and neutral charged electroactive species undergoes a reduction process. The migratory flux is always in the same direction as the diffusional flux for cationic species reduced at cathodes or anionic species oxidized at anodes, while it opposes the diffusional flux when anions are reduced at cathodes or cations oxidized at anodes.

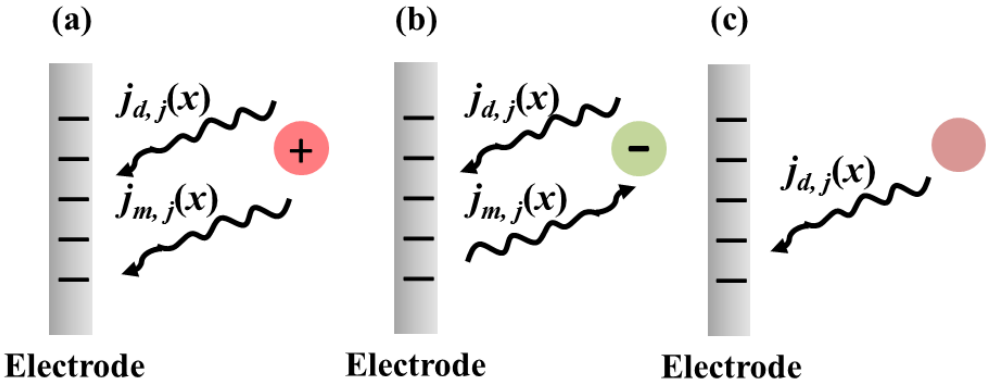


Figure 1.6. Reduction processes with different contributions of migratory flux: (a) positively charged species, (b) negatively charged species, (c) uncharged species.

Migration can severely affect the current in electrochemical systems. To eliminate this effect, a sufficiently large amount of supporting electrolyte consisting of non-electroactive ions, typically with support ratios over 30 for steady-state[27] and 100 for transient measurements,[28-33] is added into the system. In this way, most of the current in bulk solution is carried by the supporting electrolyte due to their much higher concentration. Moreover, the ohmic drop between the working and reference electrodes (as described in Section 1.5) can be minimised due to a much enhanced conductivity of the solution, offering a more accurate control of the potential at the working electrode. Another benefit is that the presence of excess electrolyte maintains a uniform ionic strength throughout the solution, even during the electrolysis, thus fixing the formal potentials of the redox couples. Furthermore, the supporting electrolyte compresses the electrical double layer (see Section 1.4) to within a distance of 10-20 Å from the electrode over which the electron quantum tunnelling can take place at sufficiently fast rates.[5] Migration of electroactive species is thus negligible at high supporting electrolyte concentrations.

1.4 Faradaic and non-Faradaic processes

There are two types of processes that can occur at a working electrode surface giving rise to a current, notably Faradaic and non-Faradaic processes. The *Faradaic* reaction of electroactive species is governed by Faraday's law of electrolysis, where the electron(s) are transferred across the electrode/solution interface resulting in the redox process:[34]

$$m = \frac{QM}{nF} \tag{1.43}$$

where m is the mass (g) of the electroactive species, Q is the total electric charge (C) passed, M is the molar mass (g mol^{-1}) of the species, n is the number of electrons transferred per ion, and F is the Faraday constant (96485 C mol^{-1}).

A non-Faradaic process is defined as a charging process where the electrons do not cross the electrode/solution interface when the suitable potential is applied. Contributions towards this non-Faradaic process arise from the buildup of charges at the interface attributed to changes in the applied potential or solution composition.

Changes in the applied potential at the electrode induce charge buildup on the electrode surface, resulting in the redistribution of electrolyte and/or the reorientation of dipole solvent molecules. This drives electrostatic interactions causing a charging current, which is known as a capacitative current. The entire array of the charged species and the oriented dipoles adjacent to the electrode surface is known as the *electrical double layer* (EDL).[3] As depicted in Figure 1.7, the electrical double layer is composed of several parts. The inner layer, also called compact or Stern Layer, is located closest to the electrode surface, where the solvent molecules and desolvated ions, are directly in contact with the electrode surface attributed to the the electrostatic forces. The distance, x_1, from the electrical centres of these specifically adsorbed molecules to the electrode surface is referred to as the *Inner Helmholtz Plane* (IHP). The *Outer Helmholtz Plane* (OHP) is the closest distance, x_2, to which solvated ions can approach the interface *via* long-range electrostatic forces only rather than via specific adsorption. Between the OHP and bulk solution is the diffuse layer where solvated ions move thermally by virtue of Brownian motion but the electrostatic attraction is sufficient that there is an excess of anions over cations for a positively charged electrode (see Figure 1.7). These layers consisting of the electrical double layer maintain electrical neutrality at the electrode/solution interfacial region. The decay of the electrostatic potential across these layers in Figure 1.7 schematically shows that potential deceases rapidly and linearly with the distance from the electrode surface within the compact *Helmholtz* layer. This potential drop is the driving force for electrochemical

reaction to occur. In contrast to the compact layer, the potential decays gradually in the diffuse layer to that of the electro-neutral bulk solution.

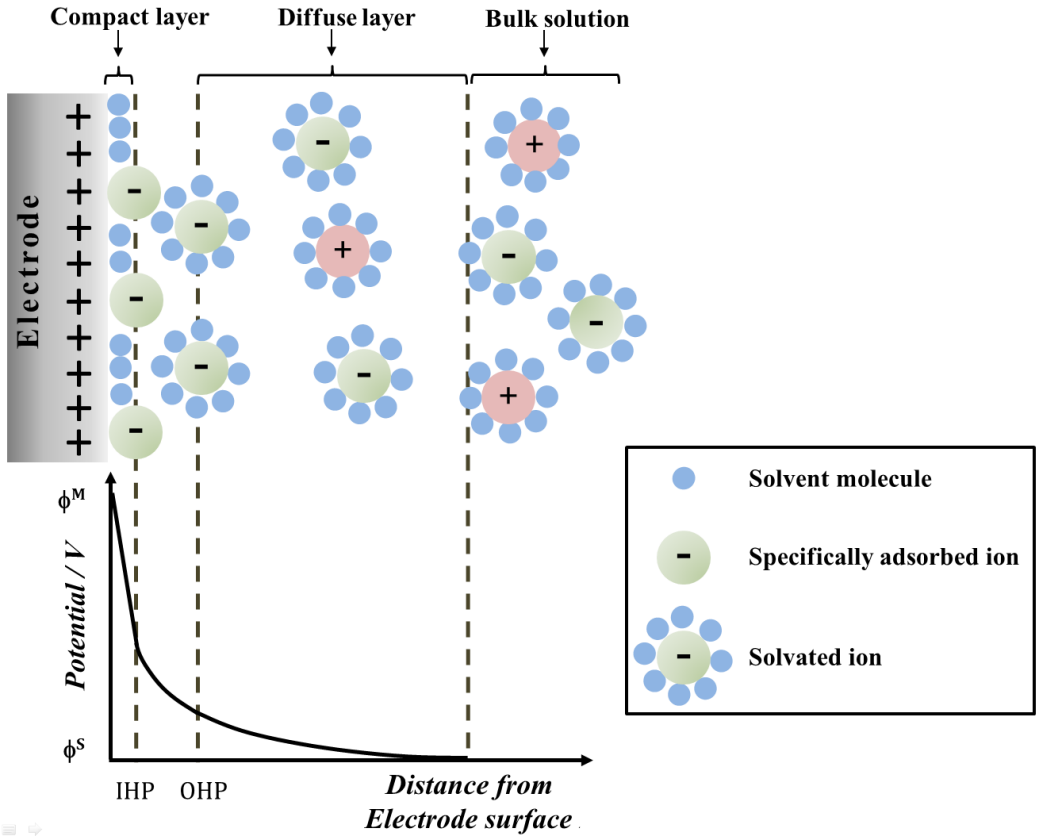


Figure 1.7. Model of the electrical double layer (top) and the potential drop $\emptyset_m - \emptyset_s$ across the double layer (bottom), where anions are specifically adsorbed at a positive electrode. The green, red and blue spheres represent the anions, cations and solvent molecules, respectively, in the solution phase.

1.5 Electrochemical Cells

A three-electrode system is widely employed in most electrochemical experiments, as schematically shown in Figure 1.8. The working electrode (WE) provides the electrochemical interface, where the reaction of interest occurs. The reference electrode (RE) facilitates the measurement and control of the working electrode/solution interface throughout the experiment, as discussed in Section 1.1. The counter electrode, connected with the working electrode, allows the passage of the current to complete the circuit.

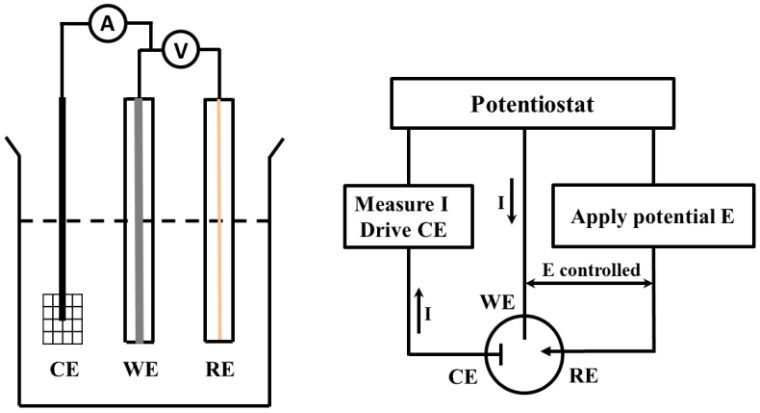


Figure 1.8. Schematic diagram of a three-electrode cell (WE: working electrode; RE reference electrode; CE: counter electrode).

A potentiostat is used to control all three electrodes, as illustrated in Figure 1.8. A fixed potential, *E*, between the working electrode (WE) and the reference electrode (RE) is first imposed with only minimal (negligible) current passing through the latter. As the reference electrode serves to provide a constant value of $(\phi_M - \phi_S)_{\mathrm{RE}}$, any variation in the potential between the WE and the RE will bring a direct change in $(\phi_M - \phi_S)_{\mathrm{WE}}$ if $(\phi_M - \phi_S)_{\mathrm{RE}}$ is constant. The potential changes on the working electrode usually drive the redox reaction of interest where a current is generated and measured. The potentiostat then drives the counter electrode (CE) to whatever potential is required to pass the same current as flowing through the working electrode. Otherwise, if only two electrodes are present in solution, appreciable current must pass through the reference electrode to complete the electric circuit. This would lead to the chemical changes within the reference electrode hence altering the potential of the reference electrode to an unknown value according to the Nernst equation. Moreover, it can cause an unknown potential drop (*IR*), also named as "ohmic drop", between the working and reference electrodes due to the electrical resistance, *R*, in the bulk solution, such that,

$$E = \left(\phi_M - \phi_S\right)_{WE} - \left(\phi_M - \phi_S\right)_{RE} + IR \tag{1.44}$$

hence if *IR* is unknown, the 'driving force' $(\phi_M - \phi_S)_{\mathrm{WE}}$ is also uncertain.

To avoid this, the third electrode, the counter electrode, is required to pass the same amount of current as the working electrode. Note that the counter electrode should be inert in the electrolyte solution studied to avoid any interference with the reaction of interest and highly conductive to guarantee an easy passage of the current. A graphite rod or a platinum wire/mesh is commonly used.

The two-electrode (working and reference) system is possibly applicable when a microelectrode is employed as the working electrode since only very low current (~ 10^{-9} A) passes through it.[35,36] Thus, the electrolytic change in the reference electrode is negligible and the *IR* term in Eqn.(1.44) greatly is minimized and can be neglected.

1.6 Macroelectrodes and Microelectrodes

Working electrodes can be divided into two categories, namely macroelectrodes and microelectrodes, according to their characteristic dimensions. The former usually have sizes on a scale of millimetres or more, while a microelectrode is micron-sized. This discrepancy in size brings distinct diffusion patterns of the species toward the electrode, as illustrated in Figure 1.9, resulting in contrasting voltammatric behaviours, as will be discussed in next section.

For macrodisc electrodes, the electrode geometry is often approximated as a plane with infinite dimensions. *Linear diffusion* therefore prevails during electrolysis, where the diffusion is one-dimensional and linear in the direction perpendicular to the electrode surface. The electrode shows 'uniform accessibility'. The thickness of the diffusion layer ($\delta \sim \sqrt{2Dt}$) is much smaller than the electrode radius, as discussed in section 1.3.1. In practice, diffusion at the edge of the electrode can be non-linear. This effect however is insignificant and negligible, contributing less than 2% of the current for an electrode of diameter larger than 2 mm.[37]

In contrast, microdisc electrodes have much smaller sizes than the thickness of the diffusion layer formed during electrolysis ($r_e << \delta$) and in the case of a disc bringing the development of a hemispherical diffusion layer where the electroactive species diffuse towards the electrode from all directions. This *convergent diffusion* is much more efficient than the linear one at macroelectrodes, thus leads to high rates of mass transport. The small dimension of microelectrode provides several additional advantages including a decreased ohmic drop (Section 1.1), reduced capacitative currents (Section 1.4), and enhanced Faradaic current density. Owing to the high mass transport rates, the measurement of faster electron transfer process becomes achievable at microelectrodes.

Microwire/microcylinder electrodes have intermediate character – the length of the cylinder is macro in scale while the radius is micron size dimensioned. These are used in part of this thesis. The fabrication procedure of a carbon fiber wire microelectrode with a length of around 1 mm and a diameter of 7 μm is described in Chapter 3. The high mass transport rate and large surface area favour the measurement and characterization of large solid particles such as graphene nanoplatelets used in Chapters 4-7. The mass transport towards the wire/cylindrical microelectrode includes linear diffusion at the side and convergent diffusion on the end, as illustrated in Figure 1.9.[38]

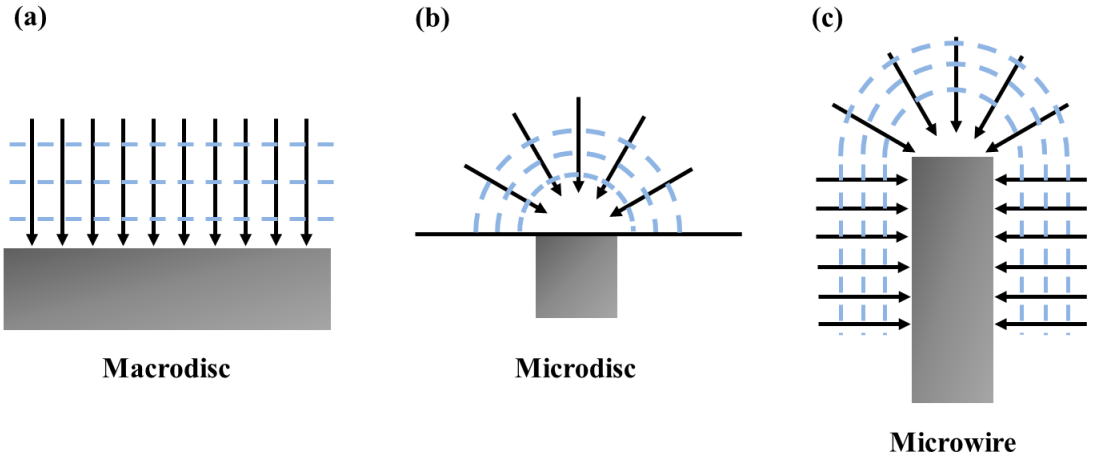


Figure 1.9. Diffusion at macrodisc (a), microdisc (b) and microwire (c) electrodes. Arrows: diffusion of electroactive species. Dashed line: the diffusion layers.

1.7 Electrochemical Techniques

Two powerful electrochemical techniques are used in this thesis: cyclic voltammetry and chronoamperometry. In both techniques, the potentials of the working electrode is controlled in a predetermined manner (either varied with time or held constant) and the resulting currents attributed to the redox reactions of interest are measured. Voltammetry is usually employed to investigate the interplay between reaction kinetics and mass transport in solution, while chronoamperometry is often applied to explicitly study the latter.

1.7.1 Cyclic Voltammetry

Cyclic voltammetry is conducted by linearly sweeping the potential of the working electrode from an initial potential, E_1, to a reversed potential, *E2*, and sweeping back to the initial potential.[39,40] The potential is swept negatively for the study of a reduction process, and positively for an oxidation process. The sweeping rate of the potential is the scan rate, v (V s^{-1}), where $v = \delta E/\delta t$. Typically, the initial potential (E_1) where the scan starts in voltammetric measurements begins at a potential where no *Faradaic* – oxidation or reduction – process takes place. The current at this point is near-zero and predominantly attributed to the non-Faradaic or capacitative current due to the buildup of charges at the electrode surface, as discussed in section 1.4.[41] The reversal potential (E_2) is usually chosen at a high overpotential ($\eta = |E - E^0_f|$), where the reaction of interest is 'fully driven' – the electron transfer occurs almost instantaneously when the electroactive species diffuses to the electrode surface. In practice, rather than true 'linear' sweeping, cyclic voltammetry is performed using a large number of digitally generated small potential steps ('staircase') as shown in Figure 1.10. The current is measured at a certain point of each potential step where gives a close equivalence to true linear sweep voltammetry.[42] The plot of the resultant current against the sweeping potential is known as a cyclic voltammogram.

The shape of a voltammogram reflects an interplay of electrode kinetics, scan rates and mass transport (diffusion).The latter depends on both the nature of the electroactive species and the size-determined diffusion at the working electrode, as discussed in Section 1.6. Herein, the voltammetric characteristics of both macro- and microelectrodes are considered. The cyclic voltammetric features of simple one-electron reaction $A + e^- \rightleftharpoons B$ with only reactant *A* present in bulk solution is discussed below.

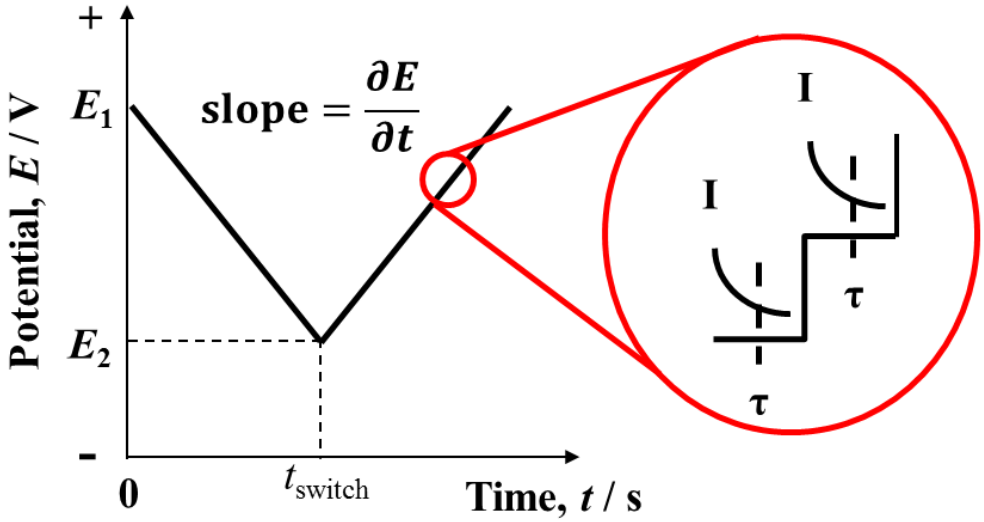


Figure 1.10. The potential-time profile of a cyclic voltammogram for a reduction reaction. Zoom-in image shows the steps at each of which current is recorded at $t = \tau$.

1.7.1.1. Voltammetry at Macroelectrodes

For macrodisc electrodes, *peak-shaped* voltammetric responses are typically observed in the current-voltage plot, attributed to the relative rates of electron transfer and mass transport. At the initial potential E_1, which is more positive than the formal potential E^0_f, no electron transfer occurs and no Faradaic current is observed. As the potential sweeps more negative than E^0_f, the reduction of *A* takes place leading to a reductive current flow. The electrochemical reaction rates at each potentials follow the *Butler-Volmer equation* (Eqn.(1.26)). The further increase in the potential makes reaction more favourable and the consumption of *A* becomes faster, corresponding to a higher current flux, in the region

near the electrode. Meanwhile, the concentration of *B* builds up near the electrode surface. The current flux reaches a peak where the surface concentration of *A* becomes close to zero and when the electron transfer rate is balanced by the diffusion rate of *A*. As the voltammetry continues to sweep, the current falls off as the diffusion of *A* is not sufficient to replenish the consumption at the electrode surface, bringing a *peak-shaped* response to the voltammogram. In the reverse sweep, a similar principle applies to the oxidation of *B*, which is accumulated in the electrode's vicinity during the forward sweep, and a backward anodic peak is observed.

There are three general voltammetric profiles regarding the reversibility of a process, corresponding to the electrode kinetics, namely, reversible, quasi-reversible and irreversible features. This reversibility at macroelectrodes can be quantified by comparing the standard electrochemical rate constant, k^0, with the diffusional mass transport coefficient m_T (m s^{-1}), defined as

$$m_T = \frac{D}{\delta} \tag{1.45}$$

where δ is the time-dependent diffusion layer thickness ($\delta \sim \sqrt{2Dt}$, as shown in Eqn.(1.39)). The sweep time t (s) is related to the scan rate, *v*, as

$$t \sim \frac{RT}{Fv} \tag{1.46}$$

Thus for a cyclic voltammetric experiment

$$m_T \sim \sqrt{\frac{FDv}{RT}} \tag{1.47}$$

For *fast* electrode kinetics, $k^0 >> m_T$, the process is *reversible* and for relatively *slow* electrode kinetics, $k^0 << m_T$, the process is *irreversible*. The process in between these two limits is referred to as *quasi-reversible*.

These three classifications can be more precisely characterised according to the parameter, Λ, introduced by Matsuda and Ayabe, defined as[43]

$$\Lambda = \frac{k_0}{\sqrt{\frac{DFv}{RT}}} \tag{1.48}$$

This parameter compares the standard electrochemical rate constant, k^0, and the mass transport coefficient ($\sqrt{\frac{DFv}{RT}}$). The following ranges for the three classifications at macroelectrodes are suggested:

$$\text{Reversible, } \Lambda \geq 15,\ k^0 \geq 0.3v^{0.5}\ \text{cm s}^{-1} \tag{1.49}$$

$$\text{Quasi-Reversible, } 15 > \Lambda > 10^{-3},\ 0.3v^{0.5} > k^0 > 2\times10^{-5}v^{0.5}\ \text{cm s}^{-1} \tag{1.50}$$

$$\text{Irreversible, } \Lambda \leq 10^{-3},\ k^0 \leq 2\times10^{-5}v^{0.5}\ \text{cm s}^{-1} \tag{1.51}$$

where numerical values relate to 298 K and the transfer coefficient α is assumed to be 0.5.

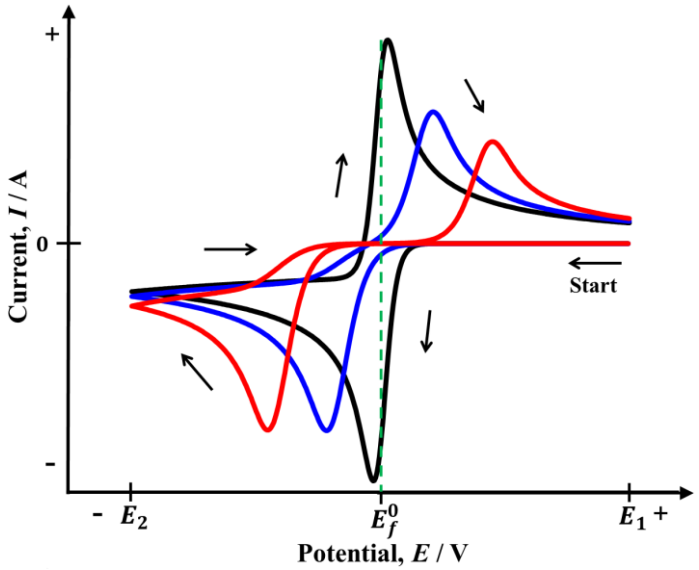


Figure 1.11. Cyclic voltammograms at a macrodisc electrode corresponding to reversible (black line), quasi-reversible (blue line), and irreversible systems (red line). Arrows show the starting point and scan direction.

For an electrochemically reversible system, as the electron transfer rate sufficiently outweighs the mass transport coefficient ($k^0 >> m_T$), the concentrations of the electroactive species at the electrode surface obey the *Nernst equation* (Eqn.(1.13)). According to the

Nernst equation, the peak-to-peak separation (ΔE_p, the difference between the anodic and cathodic peak potentials) is expected to be around 57 mV at 298K and is independent of scan rate, as shown in Figure 1.12. For an irreversible system, where the electron transfer rate is smaller than the rate of mass transport, this peak-to-peak separation is larger than 57 mV of the reversible limit (298K). This is because the rate of the electroactive species being consumed at the electrode is relatively small at low overpotentials attributed to the small k_0, leading to a higher overpotential required to drive the electrode reaction—the potential has to be applied in excess of the thermodynamic threshold, E^0_f. This applies for both oxidation and reduction processes giving a larger ΔE_p. Moreover, the peak-to-peak separation of the irreversible system depends on the scan rate. At fast scan rates, the diffusion layer is relatively thin attributed to short reaction time. Therefore, the mass transport is more 'efficient' relative to the electrode kinetics (*vs.* at low scan rates) and the system is more irreversible bringing a larger peak-to-peak separation. In practice, many systems are *quasi-reversible*, in between these two limits, as defined in Eqn(1.50). These systems behave more 'reversible-like' at very slow scan rates while are 'irreversible-like' at very fast scan rates.

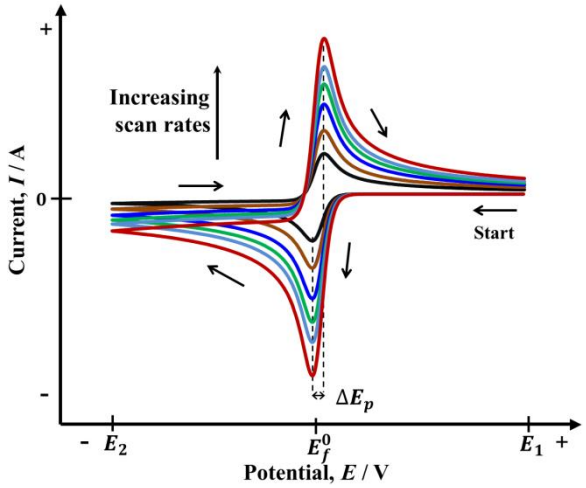


Figure 1.12. Cyclic voltammogram at a macrodisc electrode of a one-electron transfer reduction process ($A + e^- \rightleftharpoons B$; $E^0_f = 0$ V, $C_A = 1$ mM, $C_B = 0$ mM, $D_A = D_B = 1\times10^{-5}$ cm^2 s^{-1}) at a range of scan rates (10-400 mV s^{-1}) for a *reversible* process (large $k^0 = 1\times10^4$ cm s^{-1}) showing constant peak to peak separation as the scan rate increases.

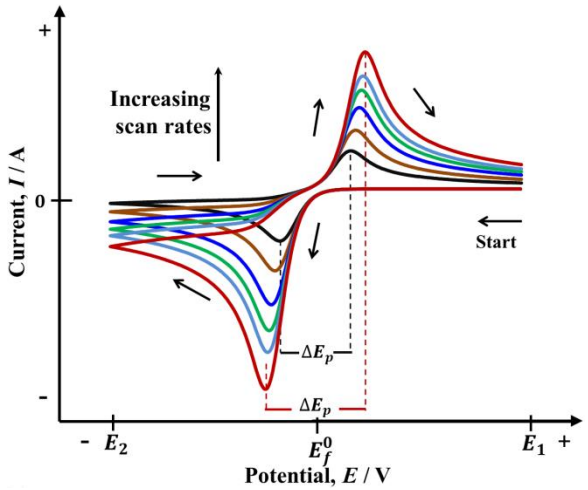


Figure 1.13. Cyclic voltammogram at a macrodisc electrode of a one-electron transfer reduction process ($A + e^- \rightleftharpoons B$; E^0_f = 0 V, C_A = 1 mM, C_B = 0 mM, $D_A = D_B = 1\times10^{-5}$ cm^2 s^{-1}) at a range of scan rates (10-400 mV s^{-1}) for an *irreversible* process (small $k^0 = 1\times10^{-4}$ cm s^{-1}) showing larger peak to peak separation as the scan rate increases.

The mid-point potential of the forward and back peaks, ($E_{mid} = \frac{1}{2}\left(E_{p,f} + E_{p,b}\right)$, for both reversible and irreversible processes can be related to the formal potential E^0_f.[2]

For a reversible process

$$E_{mid} = E^0_f + \frac{RT}{2F} ln\left(\frac{D_B}{D_A}\right) \tag{1.52}$$

For an irreversible process assuming both transfer coefficients is 0.5 ($\alpha = \beta = 0.5$)

$$E_{mid} = E^0_f + \frac{RT}{F} ln\left(\frac{D_B}{D_A}\right) \tag{1. 53}$$

From above, it is evident that $E_{mid} = E^0_f$ when the diffusion coefficients of *A* and *B* are identical ($D_A = D_B$) regardless of the reversibility of the process. Therefore, in practice, the mid-point potential is a good indication or an approximation for the formal potential. In Chapter 11, the mid-point potential of $[Ru(NH_3)_6]^{3+}/[Ru(NH_3)_6]^{2+}$ redox reaction is used as an indicator to examine the stability of the newly invented reference electrodes.

In addition to the peak potentials and peak-to-peak separation, the peak currents (I_p) of the voltammetric response contain insightful information related to the bulk concentration (c^*) and diffusion coefficient (D) of the redox species. The peak currents increase with the square roof of the scan rate. This transport-controlled peak signal can be determined by the *Randles-Ševčík equations*:

$$\text{Reversible, } I_p = 0.446FAc^* \sqrt{\frac{FDv}{RT}} \tag{1.54}$$

$$\text{Irreversible, } I_p = 0.496\sqrt{\alpha}FAc^* \sqrt{\frac{FDv}{RT}} \tag{1.55}$$

where α is the transfer coefficient, and A is the electrode surface area. The rest of the terms have been defined previously.

For a more general electrochemical reaction involving n-electron transfer, Eqn.(1.54) and Eqn.(1.55) can be generalised as:

$$\text{Reversible, } I_p = 0.446nFAc^* \sqrt{\frac{nFDv}{RT}} \tag{1.56}$$

$$\text{Irreversible, } I_p = 0.496\sqrt{n' + \alpha_{n'+1}}nFAc^* \sqrt{\frac{FDv}{RT}} \tag{1.57}$$

where n' is the total number of electrons transferred before the rate-determining step. $\alpha_{n'+1}$ is the transfer coefficient of the rate-determining step.

1.7.1.2 Surface bound and thin layer voltammetry

Hitherto, the discussion on voltammetry has focused on diffusional process in which the reactants and products are in solution and diffuse towards and away from the electrode. If the species can adsorb onto the electrode surface so eliminating diffusion or a very thin layer of solution containing the electroactive species contained in the space above the electrode surface, a distinctive voltammetry compared to that of the diffusing species can

be obtained.[44-46] As depicted in Figure 1.14, the characteristics are different to the diffusional scenario but the same principles can be applied.

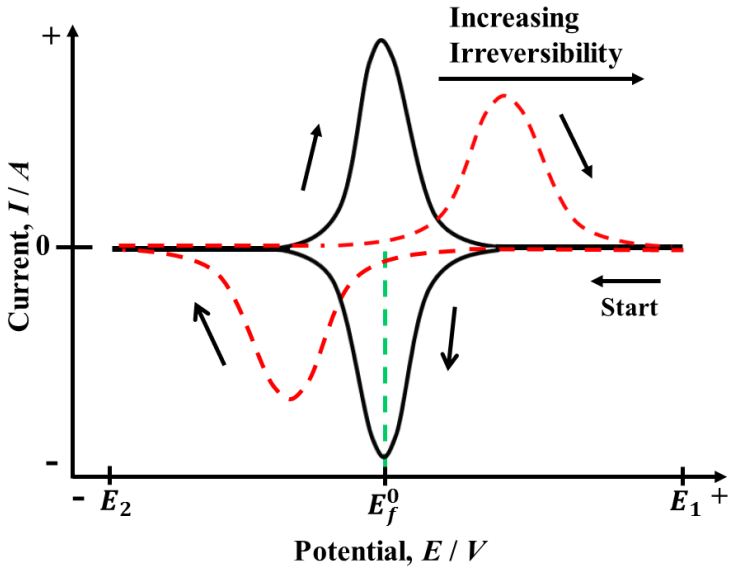


Figure 1.14. Reversible (solid) and irreversible (dashed) cyclic voltammetry profiles of surface bound species or thin layer effect.

For ideal behaviour of a surface bound species and the thin layer effect, the forward and backward peak are symmetrical (ΔE_p=0) when the process is electrochemically reversible and both of peaks are located at the formal potential of the redox couple. Due to the finite amount of electroactive species on/near the electrode surface, the current drops to zero after the peak. Therefore the wave shape is controlled only by the rate of electron transfer. In the electrochemically irreversible case (slow electron transfer), the same principle applies but a peak-to-peak separation appears. The forward and backward peaks become more separated at either side of the formal potential attributed to slower kinetics and hence requiring a larger overpotential to drive the reaction, as discussed above for the diffusional systems. The peak currents are is given as:[47]

$$\text{Reversible, } I_p = \frac{F^2}{4RT} A\Gamma_A \nu \tag{1.58}$$

$$\text{Irreversible, } I_p = \frac{\alpha F^2}{2.718RT} A\Gamma_A \nu \tag{1.59}$$

where Γ_A the surface coverage (mol m^{-2}) of reactant *A* at the electrode surface and other terms have been defined previously. A reductive process is assumed. The peak current is directly proportional to the scan rate in contrast to the observation of the diffusional systems. This also provides a diagnostic test to determine if the process is surface-limited or diffusion-controlled.

In Chapter 9, classical thin layer behaviour is observed, as described above, where inactive particles are deposited on a macroelectrode and partially 'block' the mass transport of the electroactive species.

1.7.1.3 Voltammetry at Microelectrodes

In the case of microdisc electrodes, the voltammetry differs from that of macroelectrodes due to the convergent diffusion pattern, as described in Section 1.6. As a result of this convergent diffusion, the diffusion layer is approximately hemispherical in shape, as illustrated in Figure 1.9, allowing the attainment of a constant mass transport flux of the species from bulk solution to the electrode surface.[48] A *steady-state current*, I_{ss}, thus is observed in the cyclic voltammetry at a microdisc electrode when the scan rate is slow enough for the convergent diffusion to be fully established.[49-51]

Similar to the above discussion on macroelectrodes, the shape of the voltammetry reflects the reversibility and irreversibility of the process. A parameter *K* is introduced to quantify the kinetic transition between the two extremes:[3]

$$K = \frac{r_e k^0}{D} \tag{1.60}$$

The boundaries of the three kinetic regimes at microelectrodes are suggested as:

$$\text{Reversible, } K > 10 \tag{1.61}$$

$$\text{Quasi-Reversible, } 10 \geq K \geq 10^{-2\alpha} \tag{1.62}$$

$$\text{Irreversible, } K < 10^{-2\alpha} \tag{1.63}$$

Therefore, the half-wave potential ($E_{1/2}$, the potential where the current is half of the steady-state current, $I = \frac{1}{2} I_{ss}$) can be related to the formal potential E^0_f as:[3]

$$\text{Reversible, } E_{1/2} = E_f^0 + \frac{RT}{2F} ln\left(\frac{D_B}{D_A}\right) \tag{1.64}$$

$$\text{Irreversible, } E_{1/2} = E_f^0 + \frac{RT}{\alpha F} ln\left(\frac{r_e k^0}{D_A}\right) \tag{1.65}$$

For a reversible process, $E_{1/2} = E_f^0$ when $D_A = D_B$ while for an irreversible process the the half-wave potential is dependent on the electrochemical rate constant. As illustrated in Figure 1.15, higher overpotentials are required to induce the current at electrode for a small k^0.

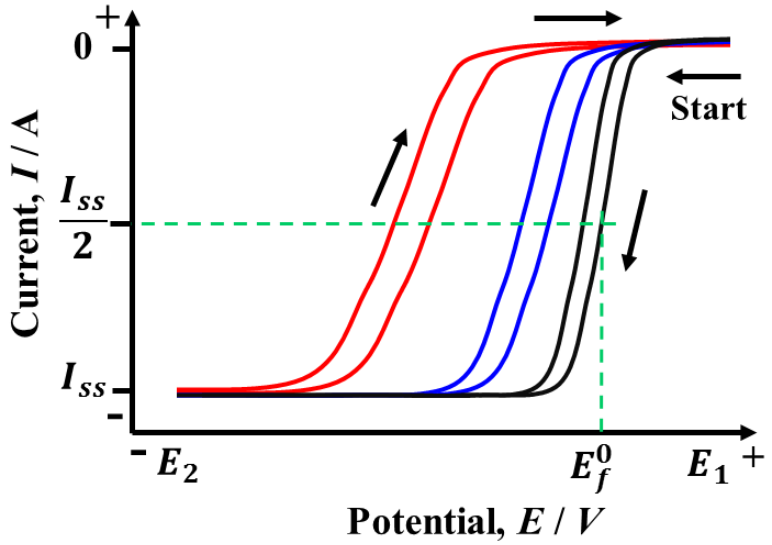


Figure 1.15. Microdisc electrodes: sigmoidal responses for the reduction $A + e^- \leftrightharpoons B$ corresponding to reversible (black line), quasi-reversible (blue line), and irreversible systems (red line). Arrows show the starting point and scan direction.

At sufficient slow rates where the steady-state is attained, the steady-state current, I_{ss}, at a microdisc electrode is expressed as:[52]

$$I_{ss} = 4nFc^* Dr_e \tag{1.66}$$

where the terms have been defined previously. Note from Figure 1.15 the absence of a back peak on the reverse scan due to the efficient loss of B from the electrode.

1.7.2 Chronoamperometry

Chronoamperometry is another powerful electrochemical technique, in which the potential applied at the working electrode is instantaneously stepped from an initial potential, E_1, where usually no reaction takes place (no Faradaic current) to a second potential, E_2, at which electrolysis of interest occurs. The potential E_2 usually provides a significantly high overpotential ($\eta = |E - E^0_f|$) such that the rate of electron transfer is fast enough to consume all the electroactive species which diffuse towards the electrode. Thus the chronoamperometric scan detects exclusively the mass transport of the species of interest from the bulk solution towards the electrode. As shown in Figure 1.16, a large current arises after the potential steps from E_1 to E_2 and the current steadily decreases with time attributed to the continuous consumption of the reactants in the vicinity of electrode.

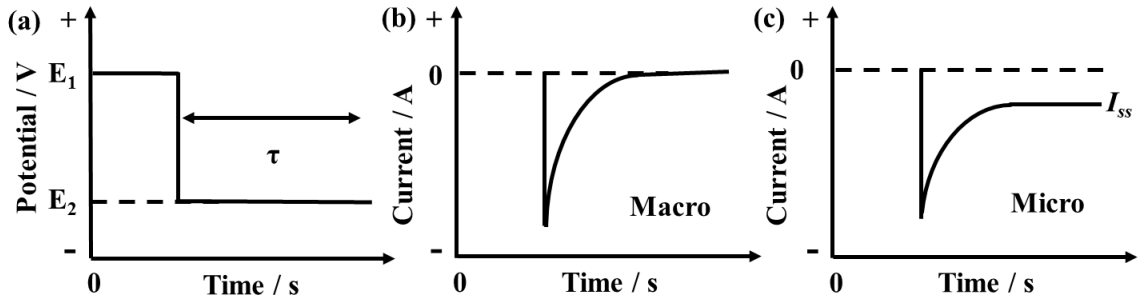


Figure 1.16. (a) The potential-time profile for a single-step chronoamperometry experiment. The resulting chronoamperometric responses at (b) macroelectrodes and (c) microelectrodes.

For a macrodisc electrode where the diffusional transport to the electrode is one-dimensional or linear, the current decreases gradually and ultimately approaches zero. The current-time response (*I*-*t*) when a sufficient potential is applied is described by the Cottrell equation:

$$I = \frac{nFAc^* \sqrt{D}}{\sqrt{\pi t}} \tag{1.67}$$

where n is the number of electrons transferred in $A + ne^- \leftrightharpoons B$ and A is the electrode area. From Eqn.(1.67) the current approaches zero when t is infinite, attributed to the inefficient diffusion leading to a ultimate depletion of reactants throughout the electrochemical cell.

For a microdisc electrode where the *convergent* diffusion occurs, the transient current can be expressed by *Shoup and Szabo Equation*:

$$I = 4nFc^* Dr_e f(\tau) \tag{1.68}$$

where c^* is the bulk concentration of electroactive species and r_e is the radius of the electrode.

$$f(\tau) = 0.7854 + 0.8862\tau^{-0.5} + 0.2146 exp\left(-0.7823\tau^{-0.5}\right) \tag{1.69}$$

where the dimensionless time parameter, τ, is expressed as:

$$\tau = \frac{4Dt}{r_e^2} \tag{1.70}$$

At a long experimental time scale, the steady state current, I_{ss}, is recorded and has an expression as Eqn(1.66).

In this thesis, a current-time transient is employed to study the electrochemistry at individual nanoparticles. This method is known as 'nano-impacts', which will be further elaborated in the next section.

1.8 Single Nanoparticle Electrochemistry

1.8.1 Nanomaterials

The physical and chemical properties of a material can change dramatically when its dimensions decrease from the macroscale to the nanoscale, leading to potential application in the fields of catalysis, energy and biotechnology.[53-56] Nanoparticles (NPs), defined by IUPAC (International Union of Pure and Applied Chemistry), refer to a specific class of

material of any shape with at least one dimension in the range of 1-100 nm.[57] They have received a tremendous amount of attention in recent decades owing to the special structure-dependent properties they exhibit at the nanoscale, such as a much higher percentage of surface atoms compared to bulk atoms bringing more catalytic sites hence boosting the catalytic efficiency.[58]

Graphene and Nafion polymer nanoparticles are studied in this thesis. The interest in graphene and related carbon materials has boomed over the last decade, ever since the discovery of graphene by Novoselov and Geim in 2004.[59] The high thermal and electronic conductivity, large surface area, high charge and carrier mobility and strong mechanical strength encourage the application of graphene and its derivatives in a variety of contexts, from electronics to medicine.[60-75] Two particularly interesting branches are the production of new and advanced catalytic materials,[73] where graphene features extensively both as catalyst support and as catalyst itself, and the development of ultra-sensitive graphene-based chemical detectors[64] and biological molecule sensors,[75] which are capable of detecting individual molecules adsorbed on graphene. Accordingly, it is of fundamental importance to quantify and understand the behaviour of molecules on graphene surfaces (Chapters 4-7).

Nafion, a sulfonated tetrafluoroethylene based fluoropolymer-copolymer, has a broad range of applications such as fuel cells, batteries, sensors, superacid catalysis, owing to its high selectivity and permeability to protons and water as well as a superior resistance to chemical attack.[76-78] In this thesis, Nafion in the forms of both nanoparticles and films are investigated as supports for authentic electrocatalysts (Chapter 8), as well as for the study of 'fake' catalysis more correctly attributed to retarded mass transport (Chapter 9). Ion transport in the films and particles is assessed (Chapter 10), which leads to their use in novel improved reference electrodes for real applications (Chapter 11).

1.8.2 Nano-impacts

Most published electrochemical studies on nanoparticles are based on ensemble measurements in which the nanoparticles are immobilised, usually via drop-casting or adsorption, on an electrode surface. The measurements, therefore, are inevitably averaged over a large population of nanoparticles so that the properties of single entities, such as size, morphology and catalytic ability, are inaccessible. Moreover, the results sometimes are difficult to interpret due to poly-dispersity, uncontrollable orientations, and possible agglomeration of the nanoparticles associated with the immobilisation techniques. In addition, Chapter 9 demonstrates that the deposited nanoparticle layers may retard the mass transport of the electroactive species to an electrode surface leading to a 'fake' (either positive or negative) catalysis. Electrochemical techniques at single nanoparticle level therefore are highly desirable.

'Impact electrochemistry' or 'nano-impacts' has recently become a popular electroanalytical technique to characterise the individual particles and probe their catalytic activities in a simple, reliable and efficient manner.[79-82] This technique involves the detection of enhanced current signals resulting from individual nanoparticles randomly colliding, by virtue of their Brownian motion, on a potentiostated microelectrode which is immersed in their suspension. These measured current signals may result from Faradaic processes or non-Faradaic processes, as described in Section 1.4, while the former can arise from *direct* or *indirect* (mediated) electron transfer. As shown in Figure 1.17a, in a so-called direct electron transfer reaction, the impacting nanoparticles are consumed (reduced or oxidized) during the measurement.[83] In contrast, during the indirect processes, redox reactions of solution phase species are mediated by the catalytically active nanoparticles and the latter remain unchanged.[84-86] The current responses of these catalytic collisions may adopt one of two general forms: a current spike or a current step, as

schematically illustrated in Figures 1.17b&c. This difference results from the the residence time of impacting nanoparticles on the electrode surface. If the nanoparticles quickly (ca. 20-50 ms) diffuse away from the electrode after collision, a sharp current spike is usually seen, while if the particles can stick or adsorb on the electrode surface, a 'step on' in the current-time response is expected to appear as the solution phase reactant diffuse continuously towards the catalytic particles.

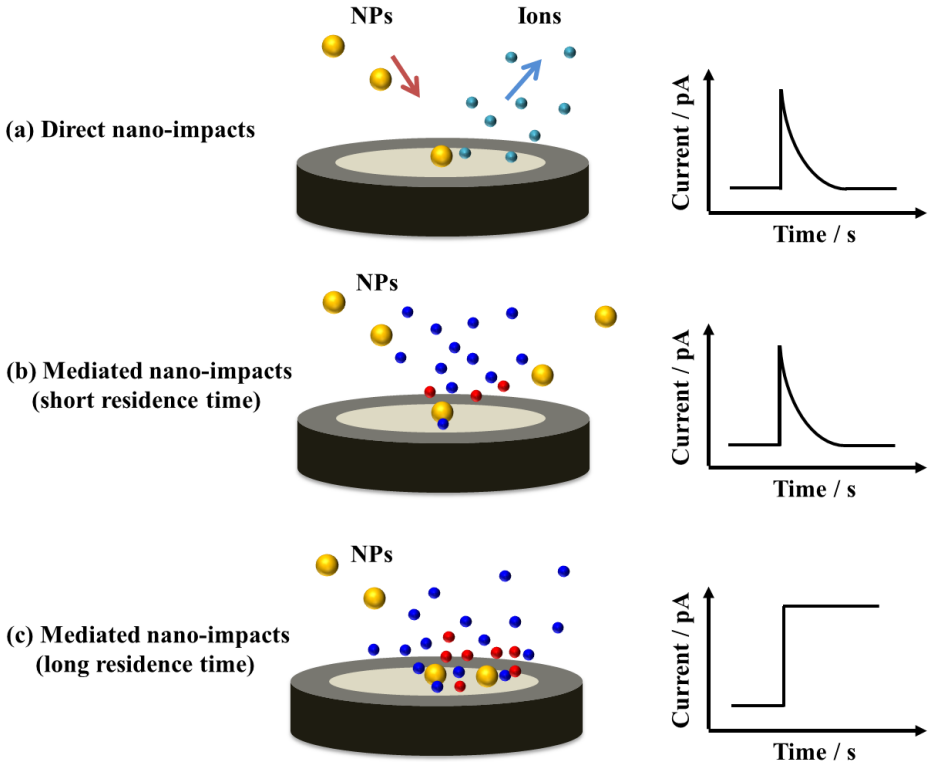


Figure 1.17. The three main scenarios of impact experiments. The current-time transient generated by each mechanism is shown next to the schematic diagram. (a) direct nano-impact, (b) mediated nano-impact with short residence time and (c) mediated nano-impact with long residence time.

Capacitative (non-Faradaic) impacts arise from either the displacement of charge from the electrode/solution interface (double layer) or the charging of an impacting nanoparticle.[79] Importantly, no redox reaction occurs in either of the processes. In order to maintain the electrical neutrality, electrons can either enter or leave the electrode in response to any change in the ionic charge distribution at the interface. Oxidative or

reductive current responses can be observed if the applied potential at the working electrode is positive or negative to the potential of zero charge (PZC), respectively.[87,88] As shown in Figure 1.18a, the double layer is disturbed and reforms upon impact of a particle with the electrode surface and 1.18b shows a second type of capacitive impact caused by the charging of the impacting particle.

Note that nano-impact experiments are usually performed with a microelectrode rather than macroelectrode, in order to reduce the particle collision frequency and the background noise, thereby resulting in clear resolution of *single* impact events. The faster response time and lower capacitance also allow better time resolution.

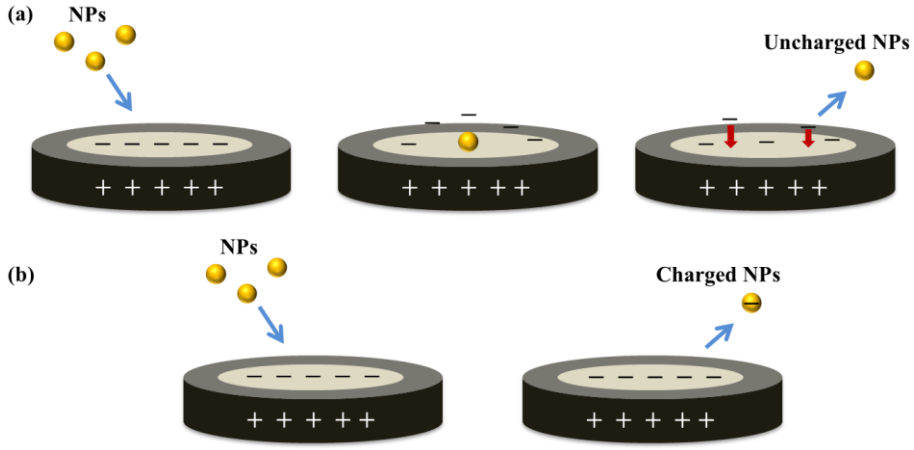


Figure 1.18. Two types of capacitive impacts. (a) Initially the impacting particle causes perturbation of the electrode double layer, after the particle leaves the double layer is restored. (b) Impacting particle is charged as it approaches an electrode and leaves the electrode surface.

Bibliography

(1) Compton, R. G.; Sanders, G. H. W. *Electrode Potentials*; Oxford University Press: Oxford, 1996.
(2) Compton, R. G.; Banks, C. E. *Understanding Voltammetry*, 2nd ed.; Imperial College Press: London, 2011.
(3) Bard, A. J.; Faulkner, L. R. *Electrochemical Methods: Fundamentals and Applications*; Wiley, 2000.
(4) Gamsjäger, H.; Lorimer, J. W.; Scharlin, P.; Shaw, D. G. *Pure and Applied Chemistry* **2008**, *80*, 233-276.
(5) Albery, J. *Electrode Kinetics*, 1st ed.; Clarendon Press: Oxford, 1975.
(6) Truhlar, D. G.; Hase, W. L.; Hynes, J. T. *Journal of Physical Chemistry* **1983**, *87*, 2664-2682.
(7) Truhlar, D. G.; Garrett, B. C.; Klippenstein, S. J. *Journal of Physical Chemistry* **1996**, *100*, 12771-12800.

(8) Guidelli, R.; Compton, R. G.; Feliu, J. M.; Gileadi, E.; Lipkowski, J.; Schmickler, W.; Trasatti, S. *Pure and Applied Chemistry* **2014**, *86*, 245-258.
(9) Guidelli, R.; Compton, R. G.; Feliu, J. M.; Gileadi, E.; Lipkowski, J.; Schmickler, W.; Trasatti, S. *Pure and Applied Chemistry* **2014**, *86*, 259-262.
(10) Fisher, A. C. *Electrode Dynamics*; Oxford University Press: Oxford, 1996.
(11) Marcus, R. A. *Journal of Physical Chemistry* **1963**, *67*, 853-857.
(12) Butler, J. A. V. *Transactions of the Faraday Society* **1924**, *19*, 729-733.
(13) Butler, J. A. V. *Transactions of the Faraday Society* **1924**, *19*, 734-739.
(14) Butler, J. A. V. *Transactions of the Faraday Society* **1924**, *19*, 659-665.
(15) Agar, J. N. *Discussions of the Faraday Society* **1947**, *1*, 26-37.
(16) Fick, A. *Annalen der Physik* **1855**, *170*, 59-86.
(17) Fick, A. *The London, Edinburgh, and Dublin Philosophical Magazine and Journal of Science* **1855**, *10*, 30-39.
(18) Bockris, J. *Modern Electrochemistry: An Introduction to an Interdisciplinary Area*; Springer: US, 2012.
(19) Islam, M. A. *Physica Scripta* **2004**, *70*, 120.
(20) Von Smoluchowski, M. *Annalen der Physik* **1906**, *326*, 756-780.
(21) Einstein, A. *Annalen der Physik* **1905**, *322*, 549-560.
(22) Novev, J. K.; Compton, R. G. *Current Opinion in Electrochemistry* **2018**, *7*, 118-129.
(23) Ngamchuea, K.; Eloul, S.; Tschulik, K.; Compton, R. G. *Analytical Chemistry* **2015**, *87*, 7226-7234.
(24) Montenegro, I.; Queirós, M. A.; Daschbach, J. L. *Microelectrodes: theory and applications*; Springer Science & Business Media, 2012; Vol. 197.
(25) Belding, S. R.; Limon-Petersen, J. G.; Dickinson, E. J. F.; Compton, R. G. *Angewandte Chemie International Edition* **2010**, *49*, 9242-9245.
(26) Pletcher, D. *A First Course in Electrode Processes*; Royal Society of Chemistry, 2009.
(27) Oldham, K. B.; Zoski, C. G. In *Comprehensive Chemical Kinetics*, Bamford, C. H.; Compton, R. G., Eds.; Elsevier, 1986, pp 79-143.
(28) Toh, H. S.; Batchelor-McAuley, C.; Tschulik, K.; Uhlemann, M.; Crossley, A.; Compton, R. G. *Nanoscale* **2013**, *5*, 4884-4893.
(29) Ward Jones, S. E.; Campbell, F. W.; Baron, R.; Xiao, L.; Compton, R. G. *Journal of Physical Chemistry C* **2008**, *112*, 17820-17827.
(30) Batley, G. E. *Marine Chemistry* **1983**, *12*, 107-117.
(31) Wang, J.; Lu, J.; Hocevar, S. B.; Farias, P. A. M.; Ogorevc, B. *Analytical Chemistry* **2000**, *72*, 3218-3222.
(32) Dai, X.; Nekrassova, O.; Hyde, M. E.; Compton, R. G. *Analytical Chemistry* **2004**, *76*, 5924-5929.
(33) Dickinson, E. J. F.; Limon-Petersen, J. G.; Rees, N. V.; Compton, R. G. *Journal of Physical Chemistry C* **2009**, *113*, 11157-11171.
(34) Faraday, M. *Philosophical Transactions of the Royal Society of London* **1834**, 77-122.
(35) Rogers, E. I.; Streeter, I.; Aldous, L.; Hardacre, C.; Compton, R. G. *Journal of Physical Chemistry C* **2008**, *112*, 10976-10981.
(36) Fleischmann, M.; Lasserre, F.; Robinson, J.; Swan, D. *Journal of Electroanalytical Chemistry and Interfacial Electrochemistry* **1984**, *177*, 97-114.
(37) Ngamchuea, K.; Eloul, S.; Tschulik, K.; Compton, R. G. *Journal of Solid State Electrochemistry* **2014**, *18*, 3251-3257.
(38) Ellison, J.; Batchelor-McAuley, C.; Tschulik, K.; Compton, R. G. *Sensors and Actuators B: Chemical* **2014**, *200*, 47-52.
(39) Nicholson, R. S.; Shain, I. *Analytical Chemistry* **1964**, *36*, 706-723.
(40) Nicholson, R. S.; Shain, I. *Analytical Chemistry* **1965**, *37*, 178-190.
(41) Cinková, K.; Clark, M.; Sokolov, S. V.; Batchelor-McAuley, C.; Švorc, Ľ.; Compton, R. G. *Electroanalysis* **2017**, *29*, 1006-1013.
(42) Batchelor-McAuley, C.; Yang, M.; Hall, E. M.; Compton, R. G. *Journal of Electroanalytical Chemistry* **2015**, *758*, 1-6.

(43) Matsuda, H.; Ayabe, Y. *Zeitschrift für Elektrochemie, Berichte der Bunsengesellschaft für physikalische Chemie* **1955**, *59*, 494-503.
(44) Henstridge, M. C.; Dickinson, E. J. F.; Aslanoglu, M.; Batchelor-McAuley, C.; Compton, R. G. *Sensors and Actuators B: Chemical* **2010**, *145*, 417-427.
(45) Henstridge, M. C.; Dickinson, E. J. F.; Compton, R. G. *Russian Journal of Electrochemistry* **2012**, *48*, 629-635.
(46) Gonçalves, L. s. M.; Batchelor-McAuley, C.; Barros, A. A.; Compton, R. G. *Journal of Physical Chemistry C* **2010**, *114*, 14213-14219.
(47) Compton , R. G.; Batchelor-mcauley, C.; Dickinson, E. J. F. *Understanding Voltammetry: Problems And Solutions*; Imperial College Press: London, 2012.
(48) Bond, A. M.; Oldham, K. B.; Zoski, C. G. *Journal of Electroanalytical Chemistry and Interfacial Electrochemistry* **1988**, *245*, 71-104.
(49) Oldham, K. B.; Zoski, C. G. *Journal of Electroanalytical Chemistry and Interfacial Electrochemistry* **1988**, *256*, 11-19.
(50) Wightman, R. M. *Analytical Chemistry* **1981**, *53*, 1125A-1134A.
(51) Bond, A. M.; Oldham, K. B.; Zoski, C. G. *Analytica Chimica Acta* **1989**, *216*, 177-230.
(52) Saito, Y. *Review of Polarography* **1968**, *15*, 177-187.
(53) Raimondi, F.; Scherer, G. G.; Kötz, R.; Wokaun, A. *Angewandte Chemie International Edition* **2005**, *44*, 2190-2209.
(54) Tong, R.; Hemmati, H. D.; Langer, R.; Kohane, D. S. *Journal of the American Chemical Society* **2012**, *134*, 8848-8855.
(55) Kim, T.; Hyeon, T. *Nanotechnology* **2013**, *25*, 012001.
(56) Bandaru, P. R.; Yamada, H.; Narayanan, R.; Hoefer, M. *Materials Science and Engineering: R: Reports* **2015**, *96*, 1-69.
(57) Vert, M.; Doi, Y.; Hellwich, K.-H.; Hess, M.; Hodge, P.; Kubisa, P.; Rinaudo, M.; Schué, F. *Pure and Applied Chemistry* **2012**, *84*, 377-410.
(58) Nützenadel, C.; Züttel, A.; Chartouni, D.; Schmid, G.; Schlapbach, L. *European Physical Journal D* **2000**, *8*, 245-250.
(59) Novoselov, K. S.; Geim, A. K.; Morozov, S. V.; Jiang, D.; Zhang, Y.; Dubonos, S. V.; Grigorieva, I. V.; Firsov, A. A. *Science* **2004**, *306*, 666-669.
(60) Morozov, S. V.; Novoselov, K. S.; Katsnelson, M. I.; Schedin, F.; Elias, D. C.; Jaszczak, J. A.; Geim, A. K. *Physical Review Letters* **2008**, *100*, 016602.
(61) Park, C. H.; Giustino, F.; Spataru, C. D.; Cohen, M. L.; Louie, S. G. *Nano Lett* **2009**, *9*, 4234-4239.
(62) Ambrosi, A.; Chua, C. K.; Bonanni, A.; Pumera, M. *Chemical Reviews* **2014**, *114*, 7150-7188.
(63) Stankovich, S.; Dikin, D. A.; Dommett, G. H. B.; Kohlhaas, K. M.; Zimney, E. J.; Stach, E. A.; Piner, R. D.; Nguyen, S. T.; Ruoff, R. S. *Nature* **2006**, *442*, 282-286.
(64) Schedin, F.; Geim, A. K.; Morozov, S. V.; Hill, E. W.; Blake, P.; Katsnelson, M. I.; Novoselov, K. S. *Nature Materials* **2007**, *6*, 652-655.
(65) Balandin, A. A.; Ghosh, S.; Bao, W.; Calizo, I.; Teweldebrhan, D.; Miao, F.; Lau, C. N. *Nano Lett* **2008**, *8*, 902-907.
(66) Li, D.; Müller, M. B.; Gilje, S.; Kaner, R. B.; Wallace, G. G. *Nature Nanotechnology* **2008**, *3*, 101-105.
(67) Castro Neto, A. H.; Guinea, F.; Peres, N. M. R.; Novoselov, K. S.; Geim, A. K. *Reviews of Modern Physics* **2009**, *81*, 109-162.
(68) Kim, K. S.; Zhao, Y.; Jang, H.; Lee, S. Y.; Kim, J. M.; Kim, K. S.; Ahn, J. H.; Kim, P.; Choi, J. Y.; Hong, B. H. *Nature* **2009**, *457*, 706-710.
(69) Geim, A. K. *Science* **2009**, *324*, 1530-1534.
(70) Dreyer, D. R.; Park, S.; Bielawski, C. W.; Ruoff, R. S. *Chemical Society Reviews* **2010**, *39*, 228-240.
(71) Bae, S.; Kim, H.; Lee, Y.; Xu, X.; Park, J. S.; Zheng, Y.; Balakrishnan, J.; Lei, T.; Ri Kim, H.; Song, Y. I.; Kim, Y. J.; Kim, K. S.; Özyilmaz, B.; Ahn, J. H.; Hong, B. H.; Iijima, S. *Nature Nanotechnology* **2010**, *5*, 574-578.
(72) Schwierz, F. *Nature Nanotechnology* **2010**, *5*, 487-496.

(73) Liang, Y.; Li, Y.; Wang, H.; Zhou, J.; Wang, J.; Regier, T.; Dai, H. *Nature Materials* **2011**, *10*, 780-786.
(74) Novoselov, K. S.; Fal'Ko, V. I.; Colombo, L.; Gellert, P. R.; Schwab, M. G.; Kim, K. *Nature* **2012**, *490*, 192-200.
(75) Bonanni, A.; Chua, C. K.; Zhao, G.; Sofer, Z.; Pumera, M. *ACS Nano* **2012**, *6*, 8546-8551.
(76) Mauritz, K. A.; Moore, R. B. *Chemical Reviews* **2004**, *104*, 4535-4586.
(77) Maldonado, L.; Perrin, J.-C.; Dillet, J.; Lottin, O. *Journal of Membrane Science* **2012**, *389*, 43-56.
(78) Kusoglu, A.; Weber, A. Z. *Chemical Reviews* **2017**, *117*, 987-1104.
(79) Sokolov, S. V.; Eloul, S.; Katelhon, E.; Batchelor-McAuley, C.; Compton, R. G. *Physical Chemistry Chemical Physics* **2017**, *19*, 28-43.
(80) Pumera, M. *ACS Nano* **2014**, *8*, 7555-7558.
(81) Rees, N. V. *Electrochemistry Communications* **2014**, *43*, 83-86.
(82) Cheng, W.; Compton, R. G. *TrAC Trends in Analytical Chemistry* **2014**, *58*, 79-89.
(83) Zhou, Y. G.; Rees, N. V.; Compton, R. G. *Angewandte Chemie International Edition* **2011**, *50*, 4219-4221.
(84) Xiao, X.; Bard, A. J. *Journal of the American Chemical Society* **2007**, *129*, 9610-9612.
(85) Kahk, J. M.; Rees, N. V.; Pillay, J.; Tshikhudo, R.; Vilakazi, S.; Compton, R. G. *Nano Today* **2012**, *7*, 174-179.
(86) Guo, Z.; Percival, S. J.; Zhang, B. *Journal of the American Chemical Society* **2014**, *136*, 8879-8882.
(87) Banks, C. E.; Rees, N. V.; Compton, R. G. *Journal of Physical Chemistry B* **2002**, *106*, 5810-5813.
(88) Rees, N. V.; Banks, C. E.; Compton, R. G. *Journal of Physical Chemistry B* **2004**, *108*, 18391-18394.

Chapter 2

Introduction to UV-visible Spectroscopy

This Chapter describes the principles underlying UV-vis spectroscopy. This technique allows the characterisation, identification and quantification of analytes in a quick, accurate, and reliable manner. The measurement is concerned with the adsorption of near-ultraviolet (190–390 nm) or visible (390–800 nm) electromagnetic radiation by the species of interest in the solution or gas phases. These measurements are used throughout the thesis.

2.1 Properties of UV and visible Radiation

Ultraviolet (UV) and visible radiation is a small part of electromagnetic spectrum, which are viewed as either waves of coupled electric and magnetic fields or as particles of light (*photons*) in the so-called *wave-particle duality*.[1] Therefore, the electromagnetic radiation, as a '*wave*', can be expressed by a frequency (f), a wavelength (λ) and a velocity (v) of the wave:[2]

$$f = \frac{v}{\lambda} \tag{2.1}$$

In addition, for electromagnetic radiation, seen as *photons*, a stream of zero rest mass particles or packages of radiation, can be associated with the energy of the radiation (E_{photon}):

$$E_{photon} = hf \tag{2.2}$$

where h is Plank's constant (6.626176×10^{-34} J s).

Combining these two equations gives:

$$E_{photon} = \frac{hv}{\lambda} \tag{2.3}$$

which shows that the energy is inversely proportional to wavelength.

2.2 Absorption of Electromagnetic Radiation

Electromagnetic radiation can interact with matter via several processes including absorption, scattering and fluorescence. In UV-vis spectroscopic measurements, only the absorption of photons plays a significant role, and relates to the excitation of electrons from lower to higher energy levels of the absorbing species. As the energy orbitals are discrete, only the photons with the 'correct' energy will trigger the electronic transitions and therefore be absorbed,[3] as schematically shown in Figure 2.1. For radiation in the UV and visible range (λ = 200-800 nm),the transition typically involves bonding electrons, for example, $\pi \rightarrow \pi^*$ transitions in molecular species.

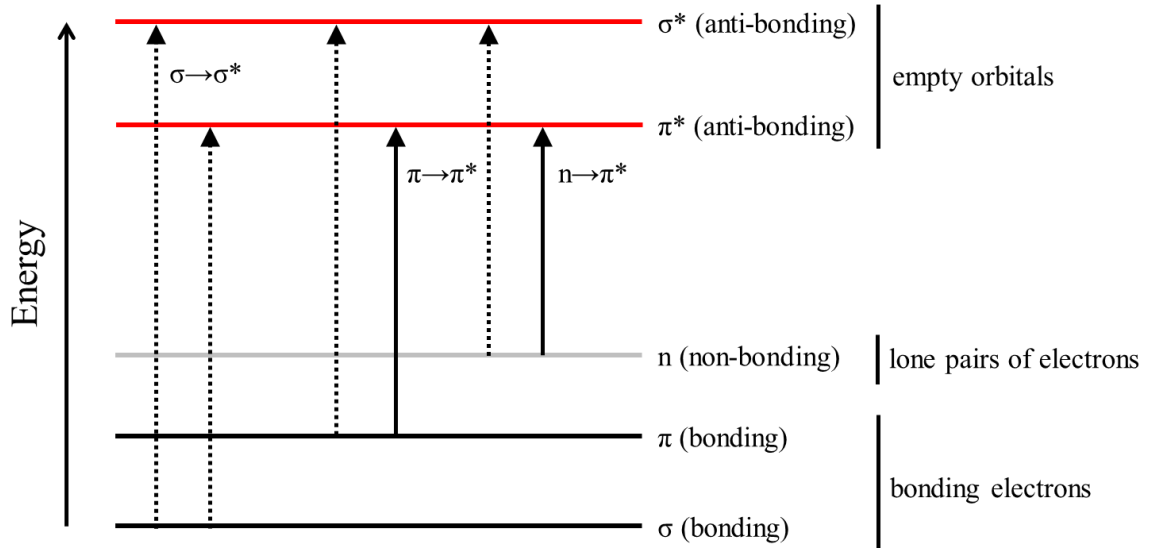


Figure 2.1. Diagram of possible electron excitation in an atom or molecule associated with the absorption of radiation. The solid arrows indicate the possible electron promotions via UV-vis radiation ($\pi \rightarrow \pi^*, n \rightarrow \pi^*$). The dotted arrows depict energy jumps outside the spectrum range and therefore cannot be detected. Relative energies are illustrated for each orbital.

In spectroscopic measurements, the amount of radiation adsorbed by the species of interest can be quantified from the intensity difference between the incident radiation, I_0, (W m^{-2}) and the transmitted radiation, I, after passing through the sample, as shown in

Figure 2.2. This change can be related to the concentration of the absorbing species as follows.

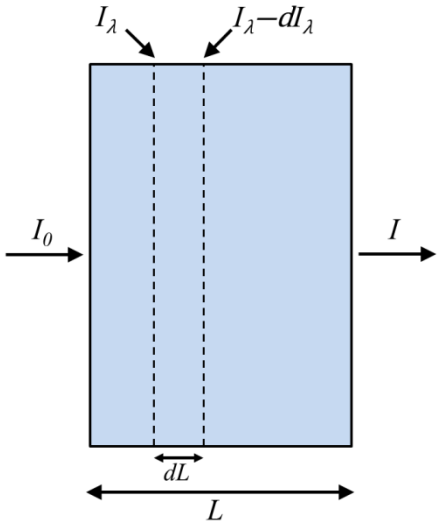


Figure 2.2. An illustration showing the path of the radiation and the intensities of radiation at different points in the sample.

Considering a beam of monochromatic radiation of intensity I_λ which passes through a sample of length dL with an intensity change of dI_λ. The rate of decrease in the radiation intensity is expected to be proportional to the intensity of the incident radiation, as proposed by Lambert.[4] Hence,

$$\frac{dI_\lambda}{I_\lambda} = -k' dL \tag{2.4}$$

where k' is a wavelength-dependant proportionality constant. Note that the *negative* sign in the equation reflects the *decrease* in intensity.

Therefore, the total change in intensity across a sample thickness of L is:

$$\int_{I_0}^{I} \frac{dI_\lambda}{I_\lambda} = -k' \int_0^L dL \tag{2.5}$$

$$\left[ln\left(I_\lambda\right) \right]_{I_0}^{I} = -k' \left[L \right]_0^L \tag{2.6}$$

$$ln \frac{I}{I_0} = -k' L \tag{2.7}$$

$$log_{10}\frac{I_0}{I} = \frac{k'L}{2.303} \tag{2.8}$$

Similar to the dependence on the sample length, Beer demonstrated that the radiation intensity decreases *exponentially* with the number of absorbing species, corresponding to the concentration, *c*:[4]

$$log_{10}\frac{I_0}{I} = \frac{k''c}{2.303} \tag{2.9}$$

where *k''* is also a wavelength-dependant proportionality constant.

By defining the absorbance, *A*, as $log_{10}(I_0/I)$, the *Beer-Lambert law*[5] is derived as :

$$A = \varepsilon Lc \tag{2.10}$$

where ε is the extinction coefficient (m^2 mol^{-1}) of the species. The parameter I/I_0 is also known as transmittance. The Beer-Lambert law is generally true for sufficiently dilute solution (typically <0.01 M).[6]

2.3 Instrumentation

A classical single beam UV-vis spectrometer is schematically illustrated in Figure 2.3. Typically, the radiation sources of the UV-vis spectrometer are a deuterium lamp employed to cover the 190-390 nm interval and a halogen filament lamp for the 340-800 nm range. The radiation from the sources is passed through a monochromator (typically a diffraction grating) to restrict the radiation source to a specific wavelength. The radiation source is first projected onto a prism to provide continuous and well-dispersed spectrum, then filtered by an exit silt. The filtered homochromic beam is then split into two *equal* beams passing through the test and the reference samples. The use of a reference sample can much enhance the accuracy of the measurement and minimise the uncertain variations

such as absorption of radiation by the cuvette, intensity variation of the radiation source, etc. Finally, the intensity of the resulting radiation is measured and analysed by a detector.

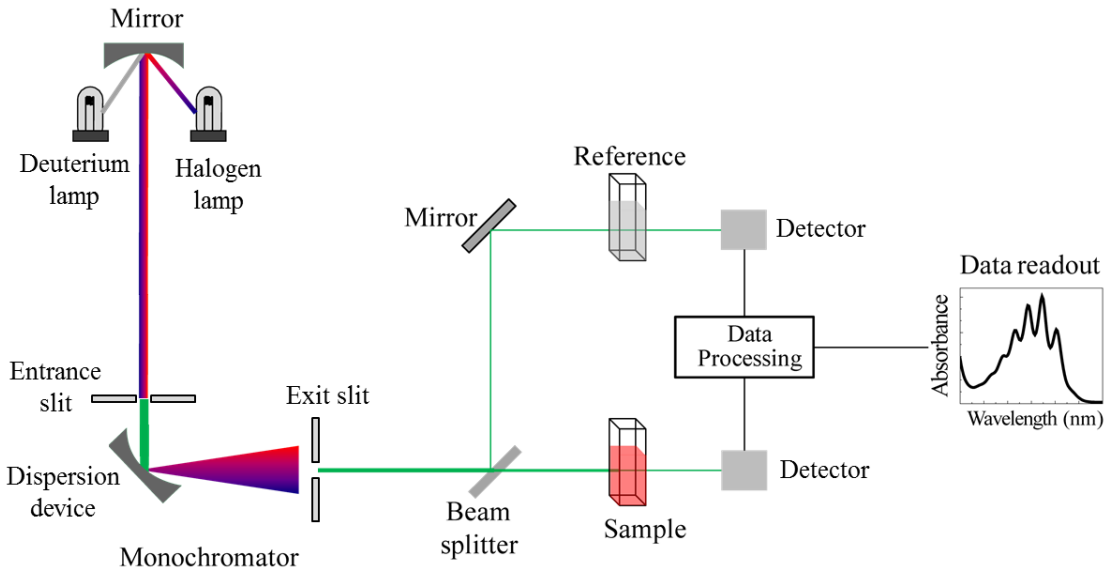


Figure 2.3. Scheme showing the major components of a UV-vis spectrometer.

Bibliography

(1) Cassidy, D. C. *Annalen der Physik* **2005**, *14*, 15-22.
(2) Atkins, P. W.; De Paula, J.; Keeler, J. *Atkins' physical chemistry*; Oxford university press, 2018.
(3) Einstein, A. *Annalen der Physik* **1906**, *325*, 199-206.
(4) Ball, D. W.; SPIE-The International Society for Optical Engineering.
(5) Clark, B. J.; Frost, T.; Russell, M. A. *UV Spectroscopy: Techniques, instrumentation and data handling*; Springer Science & Business Media, 1993; Vol. 4.
(6) Harris, D. C. *Quantitative chemical analysis*; Macmillan, 2010.

Chapter 3

Experimental

This Chapter outlines general experimental details including the chemical reagents, experimental method and instrumentation used in the work presented in this thesis; specific descriptions of each experiment and/or reagents can be found in the relevant experimental sections of Chapters 4-11.

3.1 Chemicals and Reagents

All chemicals, reagents and materials described in this thesis are listed in Table 3.1 and were used as received without further purification. All solutions were prepared using deionised water (Millipore, UK) with a resistivity of 18.2 MΩ cm at 298 K.

Table 3.1 List of chemicals, reagents and materials used in this thesis. The chemical structures of large and complex organic molecules are provided in the relevant Chapters.

Chemical Name	**Formula**	**Purity**	**Supplier**
Graphene nanoplatelets (GNPs)	–	–	Strem Chemicals
Catechol	$C_6H_6O_2$	≥99.0%	Aldrich
Citric acid monohydrate	$C_6H_8O_7 \cdot H_2O$	≥99%	Sigma-Aldrich
Sodium citrate tribasic dihydrate	$Na_3C_6H_5O_7 \cdot 2H_2O$	≥99.0%	Sigma-Aldrich
Phenyl hydroquinone	$C_6H_5C_6H_3(OH)_2$	97%	Sigma-Aldrich
Hydrochloric acid	HCl	37%	Fisher Scientific
Methanol	CH_3OH	≥99.9%	Sigma-Aldrich
Dopamine hydrochloride	$C_8H_{11}NO_2 \cdot HCl$	≥98%	Sigma-Aldrich
Methylene blue	$C_{16}H_{18}ClN_3S$	≥98%	Aldrich
Methyl viologen dichloride	$C_{12}H_{14}Cl_2N_2$	≥98%	Aldrich
Nafion perfluorinated resin solution	–	5 wt%	Sigma-Aldrich
Sodium chloride	NaCl	≥99.5%	Sigma-Aldrich

Chemical Name	Formula	Purity	Supplier
Potassium chloride	KCl	≥99.0%	Sigma-Aldrich
Sodium phosphate dibasic dihydrate	$Na_2HPO_4 \cdot 2H_2O$	≥99.95%	Sigma-Aldrich
Potassium phosphate monobasic	KH_2PO_4	≥99.0%	Sigma-Aldrich
Polybead® carboxylate microspheres 0.50 μm	–	2.5 wt%	Polysciences Inc.
Polybead® carboxylate microspheres 4.50 μm	–	2.5 wt%	Polysciences Inc.
Polybead® carboxylate microspheres 20.00 μm	–	2.5 wt%	Polysciences Inc.
Ferrocenemethanol	$C_{11}H_{12}FeO$	≥97%	Santa Cruz Biotechnology
Ferrocenium hexafluorophosphate	$FcPF_6$	≥97%	Aldrich
Poly(vinylferrocene) (PVFc, molecular weight of ca. 50 000)	–	≥99%	Polysciences Inc.
Hexaammineruthenium(III) chloride	$[Ru(NH_3)_6]Cl_3$	≥98.3%	Alfa Aesar
Tris(2,2'-bipyridyl)dichloro-ruthenium(II) hexahydrate	$Ru(bpy)_3Cl_2 \cdot 6H_2O$	≥99.95%	Sigma-Aldrich
Nitrogen gas	N_2	≥99.99%	BOC
Argon gas	Ar	≥99.99%	BOC

3.1.1 Graphene Nanoplatelets

Graphene nanoplatelets (GNPs, 15 μm in width, 6-8 nm in thickness) from Strem Chemicals (MA, USA) were used in Chapters 4-7. The GNPs were characterised previously[1] *via* scanning electron microscopy (SEM) having an average width of 16.5 ± 5 μm whereas an average surface area of 297 ± 152 μm^2. The thickness of the graphene nanoplatelets is 7.1 ± 2 nm, in concordance with supplier's specification sheet.[2] Using the experimentally derived thickness of 0.37 nm/graphene layer[3] (*cf.* 0.34 nm/layer in graphite[4]), each GNP consists of ca. 16–22 graphene layers.

3.1.2 Preparation of GNP Suspensions

Stock suspensions of 3.3×10^{-13} M of unmodified GNPs were prepared by adding 2.8 mg of GNPs into 5 mL buffer solution (details of buffer solution can be found in the relevant Chapters). To generate evenly dispersed suspensions, the mixtures were sonicated (FB15050, Fisher Scientific, 50/60 Hz, 80W, Germany) for 25 min. The above suspension was used as a stock solution, and diluted for nano-impact experiments. Fresh suspensions were prepared daily. The preparation procedures of modified GNP suspensions used in Chapters 4-6 are different and will be described in detail in the relevant Chapters.

3.1.3 Synthesis of Nafion Particles

Nafion particles used in Chapters 8-11 were synthesised by the re-precipitation method.[5] Nafion perfluorinated resin solution (5 wt% in lower aliphatic alcohol and water with a water content of 45%, Sigma-Aldrich) was heated in a water bath at 52 ± 0.5°C to obtain a concentrated 12.5 wt% Nafion solution. For the synthesis of Nafion particles doped with methyl viologen (MV^{2+}), 5 μL aqueous solution of MV^{2+} was added into 50 μL concentrated 12.5 wt% Nafion, followed by stirring with a pipette tip for 200 circles. The mixture was injected dropwise over 10 s into 1 mL deionised water under stirring by magnetic vortexing at 600 rpm for 5 minutes. The resulting mixture was subjected to sonication (FB15050, Fisher Scientific, 50/60 Hz, Germany) for 30 min at room temperature. The suspension was then centrifuged (Eppendorf Centrifuge 5430 R) at 14000 rpm for 10 min and the precipitate was washed with water thoroughly to remove excess MV^{2+}. This washing-step was repeated three times. The obtained MV-Nafion particles were characterised as previously described giving an average radius of 0.43 ± 0.26 μm.[6] The MV-Nafion particles were re-dispersed evenly in 0.5 mL water by sonication for 5 min. Fresh stock suspensions were prepared daily.

For the synthesis of pure Nafion particles, 50 μL concentrated 12.5 wt% Nafion was directly injected into 1 mL deionised water under stirring by magnetic vortexing at 600 rpm for 5 minutes, followed by sonication for 30 min at room temperature. The suspension was then centrifuged at 14000 rpm for 10 min and the precipitate was re-suspended in 0.5 mL water by sonication for 5 min.

3.2 Electrochemical Instrumentation

Electrochemical experiments were performed using a μAutolab II potentiostat (Metrohm-Autolab BV, Netherlands) and a three-electrode set-up inside a grounded and thermostatted (25.0 ± 0.2 °C) Faraday cage. A Saturated Calomel Electrode (SCE, +0.244 V *vs.* SHE, BASi Inc., Japan) and a graphite rod were used as reference electrode and counter electrode, respectively. A glassy carbon macroelectrode (GC, 3 mm diameter, CH Instrument), an edge-plane pyrolytic graphite (EPPG, 3 mm diameter, IJ Cambria Scientific Ltd, UK) electrode, a basal-plane pyrolytic graphite (BPPG, Le Carbone, Sussex, UK) electrode, a carbon microdisc electrode (IJ Cambria Scientific Ltd, UK) or a home-fabricated carbon fibre micro electrode (7.0 μm diameter, ca. 1 mm length; fabrication method see below) were used as working electrodes. The details of the working electrodes used differ from Chapter to Chapter and will be discussed in the relevant Chapters.

3.2.1 Carbon Macro- and Micro- electrode Preparations

Prior to all electrochemical experiments, the glassy carbon macroelectrode, the EPPG electrode, and microdisc electrode were polished using micropolish alumina (Buehler, IL, UK) of decreasing particle sizes (1.0, 0.3 and 0.05 μm) on a polishing pad, followed by sonication in water and drying with nitrogen. The radius of the microdisc electrode was calibrated as 26.5 μm electrochemically by analysing the steady state voltammetry of 1.0

mM hexaaminеruthenium(III) chloride in aqueous solution containing 0.1 M KCl, using a diffusion coefficient for $[Ru(NH_3)_6]^{3+}$ of 8.4×10^{-10} m^2s^{-1} at 298 K.[7]

3.2.2 Carbon Fibre Micro Electrode Fabrication

The method of carbon fibre micro electrode fabrication follows that developed by Ellison *et al*.[8] Specifically, a carbon fibre (diameter 7.0 μm, Goodfellow, Cambridge, UK) was adhered to a metal wire *via* silver epoxy conductive adhesive (RS Components Ltd.), which was then placed in an oven at approximately 60 °C for 15 min to set the adhesive. Next, the wire was threaded through a plastic pipette tip. The interstice between wire and tip was sealed using cyanoacrylate adhesive and the wire slowly pulled down, leaving only the carbon fibre extended out of the end, and left overnight to set the cyanoacrylate adhesive. Finally, the carbon fibre was cut to approximate 1 mm length.

3.3 Non-electrochemical Instrumentation

All ultraviolet-visible (UV-vis) measurements were performed using a Shimadzu UV-1800 UV-vis spectrometer and quartz cells with a 10 mm optical path length. The quartz cells were cleaned *via* sonication in acetone before use. In all cases, a baseline correction was conducted prior to any measurement.

Bibliography

(1) Poon, J.; Batchelor-McAuley, C.; Tschulik, K.; Compton, R. G. *Chemical Science* **2015**, *6*, 2869-2876.
(2) *Strem Product Catalog - Graphene Nanoplatelets* **2012**.
(3) Koh, Y. K.; Bae, M.-H.; Cahill, D. G.; Pop, E. *ACS Nano* **2011**, *5*, 269-274.
(4) Chung, D. D. L. *Journal of Materials Science* **2004**, *39*, 2645-2661.
(5) Horn, D.; Rieger, J. *Angewandte Chemie International Edition* **2001**, *40*, 4330-4361.
(6) Yang, H.; Li, X.; Batchelor-McAuley, C.; Sokolov, S. V.; Compton, R. G. *Physical Chemistry Chemical Physics* **2018**, *20*, 682-689.
(7) Wang, Y.; Limon-Petersen, J. G.; Compton, R. G. *Journal of Electroanalytical Chemistry* **2011**, *652*, 13-17.
(8) Ellison, J.; Batchelor-McAuley, C.; Tschulik, K.; Compton, R. G. *Sensors and Actuators B: Chemical* **2014**, *200*, 47-52.

Chapter 4

Catechol Adsorption on Graphene Nanoplatelets: Isotherm, Flat to Vertical Phase Transition and Desorption Kinetics

As an important material widely applied in advanced catalysts and ultra-sensitive sensors, the first aim of this thesis is to quantify and understand the behaviour of large organic molecules on the surface of graphene. In this Chapter, the adsorption of catechol (1,2-dihydroxybenzene) on graphene nanoplatelets (GNPs) is investigated electrochemically and spectroscopically. The reversible adsorption of catechol on GNPs is shown to be Langmuirian with an adsorption constant of (0.2 ± 0.002) mM^{-1} at low adsorbate concentrations (≤100 mM). At higher concentrations (>100 mM) the adsorption of catechol on GNPs is shown to undergo a flat to vertical concentration driven phase transition. The kinetics of desorption are measured with a single particle electrochemical technique. The study of individual impacts allows the determination of the rate constant of catechol desorption from GNPs to be k = 0.08 ± 0.01 s^{-1} with first order kinetics. The method provides a powerful and efficient generic approach to study adsorption and, importantly, desorption of molecules on nanomaterials, as well as giving insight into the modification process.

The work presented in this Chapter has been published in *Chemical Science*.[1]

4.1 Introduction

Graphene, due to its large thermal and electronic conductivity, high electron and carrier mobility, great surface area and strong intrinsic mechanical strength, has been actively investigated over recent decades.[2-7] A broad range of potential applications have been extensively reported,[7-26] of which two particularly interesting branches are the development of highly sensitive graphene-based chemical[15] and biological[23,24] sensors, and the use of graphene as a catalyst.[25,26] To underpin such studies, it is of fundamental interest to quantify and gain further understanding of the adsorption of diverse molecules on graphene.

Hitherto, the adsorption of various types of small molecules or atoms on graphene have been studied, notably metal atoms (Li,[27] Zn,[28] etc.), gas molecules (CO_2,[29] N_2,[30] H_2,[31] H_2S,[32] etc.), halogens[33-35] and organic molecules (methane,[36] dibenzothiophene,[37] methanol,[38] etc.) where most of the work was theoretically investigated using quantum mechanical calculations based on density functional theory (DFT).[27,28,30-36,38] The experimental data was usually attained using scanning electron microscopy (SEM), Raman spectroscopy and X-ray spectroscopy (XPS).[39-41] In contrast, little is known about the adsorption of larger, especially organic, molecules on graphene. This Chapter focuses on the adsorption of 1,2-dihydroxybenzene ('catechol') on graphene from aqueous solution making use of a relatively new electrochemical method—that of nano-impacts—here novelly applied to the measurement of adsorption and desorption phenomena as well as complementary spectroscopic data.

Graphene nanoplatelets (GNPs), belonging to the family of graphene materials, preserve many of the appealing properties but circumvent the poor stability of single-layer graphene[21,42] due to the structural distortion of rippling at 1 nm width.[43] Meanwhile, GNPs

are more commercially available and easier to produce and handle,[21,44] which makes them an attractive alternative.

The molecular orientation of aromatic compounds adsorbed at platinum electrodes, including an assortment of 40 quinones and phenols, have been extensively studied by Hubbard's group.[45-51] There are two orientation states, namely horizontal orientation with the aromatic ring parallel to the adsorbent surface and vertical orientation with a perpendicular aromatic ring. For instance, adsorption of hydroquinone at low adsorbate concentrations adopts a horizontal orientation but reorients to the vertical form when exposed to a solution containing higher concentrations.[51]

Herein, the adsorption and desorption of catechol molecules on GNPs were studied *via* nano-impacts, as introduced in Chapter 1, which detects stochastic collisions of *individual* nanoparticles with a carbon wire microelectrode by virtue of their Brownian motion in solution. By potentiostatting the electrode at a suitable potential, mediated electron transfer occurs on the surface of the impacting nanoparticle during collision,[52-56] giving rise to a current spike in chronoamperometry. In this work, GNPs are modified with different concentrations of catechol and studied using the nano-impact method. In the latter, suspended particles collide randomly with an electrode. The surface coverage of the electroactive catechol on Faradaically non-active GNPs can be obtained, based on the charge passed per spike leading to the number of adsorbed catechol molecules at the *single* GNP entity level. Therefore, it can be used to probe the kinetics of desorption of catechol from GNPs as the surface progressively depletes when in contact with a solution which does not contain catechol. UV-vis measurements are conducted to investigate the catechol adsorption isotherm for GNPs and determine the orientation state of catechol molecules on the GNPs: at low coverage, a reversible Langmuirian adsorption is seen but with a flat to vertical phase transition driven at high concentrations of catechol in solution. The

approach is generic and can be applied to study the adsorption and desorption of various kinds of molecules on nanomaterials, such as GNPs, carbon nanotubes (CNTs) and nanodots, among others.

4.2 Experimental

4.2.1 Buffer Solution

The pH 3.0 buffer solution was freshly prepared from 0.1 M citric acid/sodium citrate with 0.1 M KCl supporting electrolyte, and measured using a Hannah pH231 pH meter (Hannah, Bedfordshire, UK). It has been reported that catechol is more stable in a pH 3.0 environment,[57] and thus all the following experiments were conducted in pH 3.0. The pH buffer was degassed thoroughly with pure nitrogen (BOC Gases plc, UK) for 20 min prior to the addition of catechol to prevent degradation of the solution by atmospheric oxygen.

4.2.2 Preparation of GNP Suspensions

The stock suspension of unmodified GNPs was prepared as described in Chapter 3. To prepare suspensions of 3.3×10^{-13} M catechol modified GNPs, 2.8 mg of GNPs was added to 10 mL of catechol solution followed by sonication for 25 min. The mixture was then centrifuged (Eppendorf Centrifuge 5702) at 3000 rpm for 13 min. The precipitates were washed thoroughly after settling with 10 mL of pH 3.0 buffer solution, followed by centrifugation, to remove excess catechol. This washing-step was repeated 3 times. Further centrifugation was applied and the settled modified GNPs powders were added into 5 mL of pH 3.0 aqueous buffer solution. The mixture was shaken on a vortex (Whirlmixer, Loughbough, UK) for 30 s and sonicated for 20 s. This dispersion procedure was repeated 3 times to get an even suspension. The above stock suspension was freshly prepared every day.

Two different concentrations of catechol solutions were used to modify GNPs in this work. The GNPs that were modified with 100 mM catechol solution are noted as 100-catechol GNPs and GNPs modified with 300 mM catechol solution are to be noted as 300-catechol GNPs in the following sections.

4.2.3 Cyclic Voltammetry at EPPG Electrodes

For the cyclic voltammetry (CV) measurements, an edge-plane pyrolytic graphite (EPPG, 3 mm diameter) electrode was used as the working electrode. 10 μg of modified or unmodified GNPs was drop-casted on the EPPG electrode and left under a N_2 environment to dry fully. For comparison, the same experiment was conducted by drop-casting 5 μL of 2 mM catechol solution on the EPPG electrode. Cyclic voltammograms were then recorded at the scan rate of 25 mV s^{-1} in a degassed pH 3.0 buffer solution.

4.2.4 Nano-impact Experiments

In nano-impact experiments, chronoamperometry was recorded at a home-fabricated carbon fibre wire microelectrode (fabrication procedure described in Chapter 3). Note the potentiostat used in this work accurately conserves the charge transferred during a particle-impact process despite possible alteration in the spike shape.[58,59] 4.5 mL of pH 3.0 buffer solution was bubbled with nitrogen thoroughly for 5 min to remove dissolved electroactive oxygen and 500 μL of modified or unmodified GNPs stock suspension was then added while the nitrogen was kept bubbling for further 10 s to get an even suspension, followed by immediate chronoamperometric scans. Chronoamperograms were recorded for 20 s at different potentials from +0.2 to +1.1 V.

4.2.5 UV-vis Experiments

A wide range of concentrations of catechol in the buffer solution were prepared. A known amount of GNPs were then mixed with 1 mL of different concentrations of catechol solutions. The amount of GNPs used for each catechol solution was determined by theoretical calculation such that the GNPs used must reduce at least 20% of catechol concentration, assuming a full monolayer coverage of catechol on GNPs. The mixture of GNPs and catechol solution was then sonicated (FB15050, Fisher Scientific, 50/60 Hz, 80W, Germany) for 30 min to promote adsorption, followed by centrifugation (Eppendorf Centrifuge 5430 R) for 15 min at 14000 rpm. The original catechol solution before adsorption and the supernatant after adsorption were both diluted into calibration region then measured by UV-vis spectroscopy. The absorbance was recorded from 500–200 nm.

4.3 Results and Discussion

This section first reports the adsorption of catechol onto GNPs, which is evidenced by the cyclic voltammetry of an ensemble of catechol-GNPs on a macro EPPG electrode. Second, complementary UV-vis measurements are conducted to study the adsorption isotherm of catechol on GNPs. Finally, chronoamperometry of a wire microelectrode in catechol-GNPs suspensions is measured. The charge transfer of single catechol-GNPs at different applied potentials is investigated and individual current spikes are analysed.

4.3.1 Cyclic Voltammetry of Catechol Modified GNPs

First, a cyclic voltammogram of a catechol modified EPPG electrode was measured to evidence the electroactivity of the catechol. The EPPG electrode was modified by drop-casting with 5 μL of 2 mM catechol solution and dried under a nitrogen atmosphere. The modified electrode was then immersed in a degassed pH 3.0 buffer solution and CV was

recorded from −0.20 to +1.10 V *vs.* SCE and reversed back to −0.20 V at a scan rate of 25 mV s^{-1} (Figure 4.1a, green line). For comparison, the CV of a bare EPPG was also recorded under the same conditions (Figure 4.1a, grey line). In the presence of catechol, a single oxidation peak was observed at ca. +0.43 V *vs.* SCE, which is consistent with previous reports on the catechol oxidation.[57,60] Note that the oxidation of catechol (C) forms *o*-benzoquinone (Q) at these potentials and at the pH studied is understood to follow the mechanism below:

$$C - e^{-} \rightleftarrows S \tag{4.1}$$

$$2S \rightarrow Q + C \tag{4.2}$$

in which there is disproportionation between the semiquinone (S) radicals and the states of protonation of S are neglected in the above scheme.[57]

Next, in order to investigate the adsorption of catechol on GNPs, an EPPG electrode was modified by drop-casting with 10 μg of 100-catechol GNPs and cyclic voltammograms were recorded between −0.20 and +1.10 V *vs.* SCE at a scan rate of 25 mV s^{-1} (Figure 4.1b, blue line). This experiment was repeated for 300-catechol GNPs (Figure 4.1b, red line), which showed a higher oxidative peak suggesting greater adsorption of catechol on the GNPs. Well-defined oxidative and reductive peaks, for both concentrations of catechol modified GNPs, were observed at ca. +0.46 V and +0.32 V *vs.* SCE, respectively, close to the peak potentials of the drop-cast catechol on the EPPG (Figure 4.1a, green line). This is in good agreement with literature,[57,61] confirming that the GNPs were successfully modified with catechol. A control experiment for unmodified-GNPs drop-casted onto an EPPG was also conducted in the same solution and no redox signal was detected (Figure 4.1a&b, black line). Note that the enlarged background current in the presence of unmodified GNPs is a result of increased electrode capacitance.

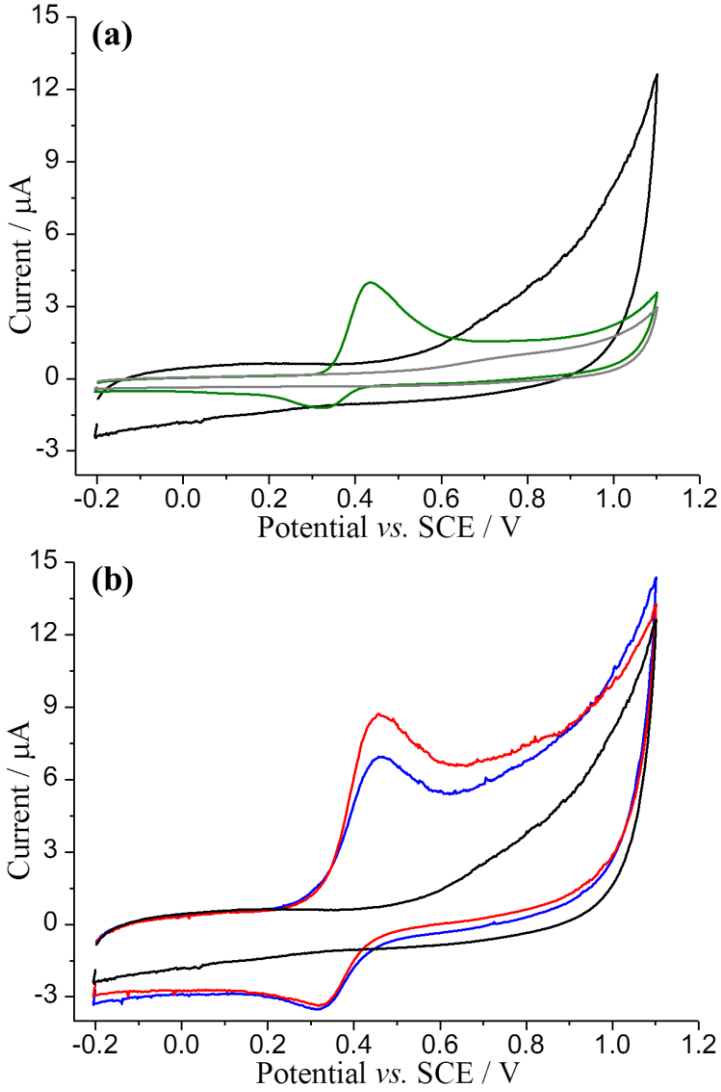


Figure 4.1. (a) Voltammograms of an EPPG electrode drop-casted with 5 μL of 2 mM catechol (green line), 10 μg of unmodified GNPs (black line), and a bare EPPG electrode (grey line) in pH 3.0 buffer solution supported with 0.1 M KCl. Scan rate = 25 mV s^{-1}. (b) Voltammograms of an EPPG electrode drop-casted with 10 μg of 300-catechol GNPs (red line), 100-catechol GNPs (blue line), unmodified GNPs (black line) in pH 3.0 buffer solution supported with 0.1 M KCl. Scan rate = 25 mV s^{-1}.

4.3.2 UV-vis Studies of Catechol Adsorption on GNPs

To study the adsorption of catechol on GNPs, UV-vis experiments were performed. 1 mL of catechol solutions over a wide range of concentrations in the pH 3.0 buffer were mixed with GNPs and then sonicated for 30 min to promote adsorption, followed by centrifugation. The original catechol solutions and supernatants after adsorption were both

examined using UV-vis spectroscopy, allowing the determination of the amount of catechol adsorbed by GNPs. A linear Beer–Lambert plot was obtained with the extinction coefficient (ε) of 0.224 ± 0.002 M^{-1} m^{-1} illustrating the relationship between absorbance and catechol concentration, as shown in Figure 4.2.

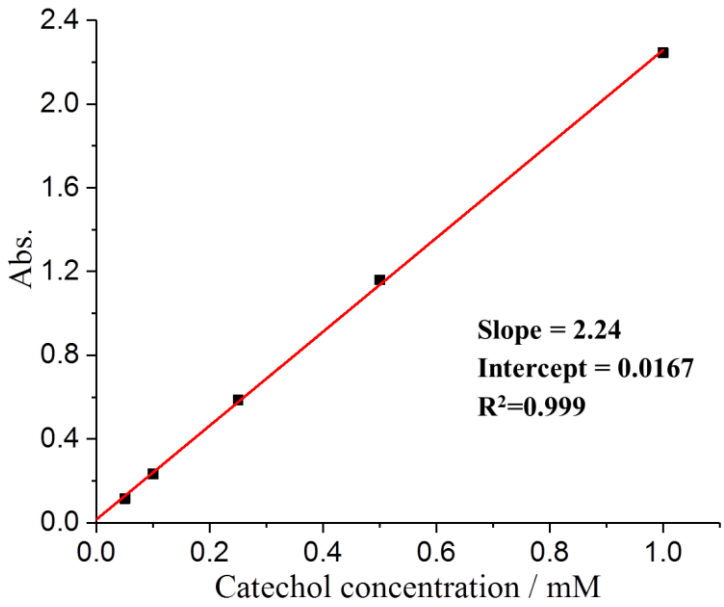


Figure 4.2. Beer–Lambert plot of catechol in citric acid/sodium citrate buffer solution (pH 3.0).

As shown in Figure 4.3a, the absorbance peak is at 276 nm, consistent with prior literature.[62,63] The reduction in the magnitude of the catechol absorbance peak is evidently due to the adsorption of GNPs. The amount of catechol adsorbed by unit amount (1 mg) of GNPs was quantified and the catechol adsorption isotherm for GNPs in pH 3.0 buffer solution was then plotted (Figure 4.3b), where two clear plateaux can be observed. As the concentration of catechol increases, the amount of catechol adsorbed by 1 mg of GNPs (n) increases and reaches the first plateau at catechol concentrations of between ca. 50 and 100 mM with n_{max} = 1.6 × 10^{-7} mol mg^{-1}, giving the maximum surface coverage (Γ_{max}) of (2.5 ± 0.8) × 10^{-10} mol cm^{-2}, and reaches the second plateau at concentrations around ca. 250 and 400 mM with n'_{max} = 3.2 × 10^{-7} mol mg^{-1}, giving Γ'_{max} of (5.1 ± 1.7) × 10^{-10} mol cm^{-2} (see Appendix A for detailed calculation). The molecular area of catechol ($S_{catechol}$) can be

estimated by approximating catechol as a rectangular box with all side lengths estimated by trigonometry for bond lengths, bond angles and van de Waals radii of terminating atoms[64] (Scheme 4.1). $S_{catechol}$ of flat view and $S'_{catechol}$ of edgewise view hence can be estimated as 5.6×10^{-15} cm^2 and 2.8×10^{-15} cm^2, respectively, in good agreement with literature.[45,47,61]

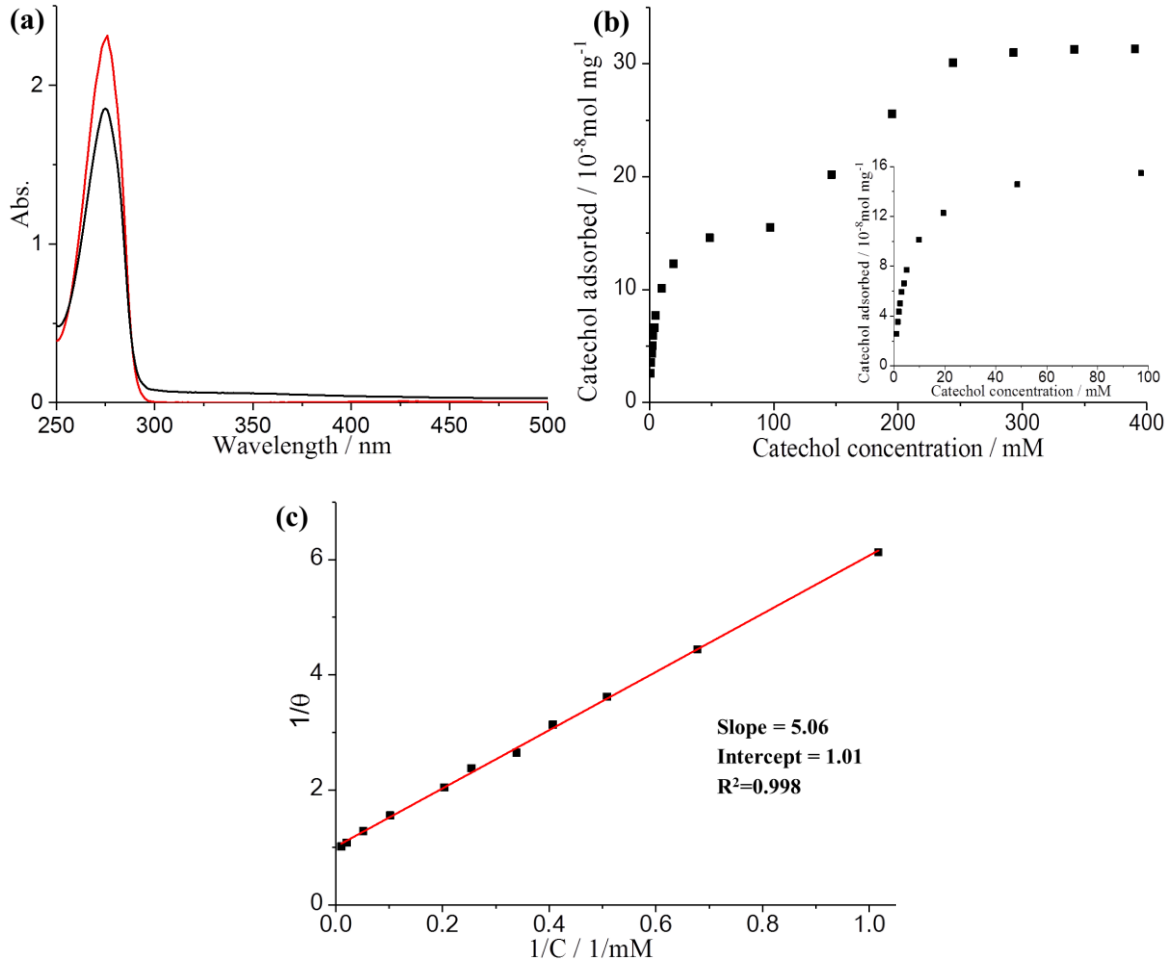
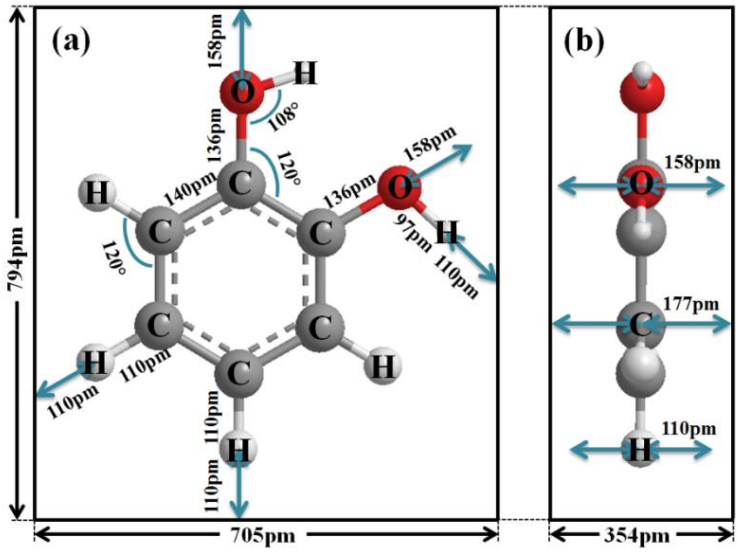


Figure 4.3. (a) UV-vis absorption of a pH 3.0 solution containing 5 mM catechol before GNPs adsorption (red line) and after adsorption (blue line); dilution factor = 5. (b) Catechol adsorption isotherm on GNPs in pH 3.0 buffer solution. Inset: zoom-in of the adsorption isotherm when catechol concentration below than 100 mM. (c) Langmuir plot of catechol adsorption on GNPs in pH 3.0 buffer solution, where Θ is the fractional surface coverage and C is the adsorbate concentration; Langmuir adsorption model applies when the catechol concentration is lower than 100 mM.

Scheme 4.1. Rectangular box model of catechol molecule for both (a) flat view and (b) edgewise view.



The area occupied by each individual catechol molecule ($S_{R\text{-}Ct}$) on GNP from UV-vis measurements can thus be determined as $S_{R\text{-}Ct} = (6.7 \pm 1.7) \times 10^{-15}$ cm^2 in 100 mM catechol and $S_{R\text{-}Ct} = (3.3 \pm 0.8) \times 10^{-15}$ cm^2 in 300 mM catechol, consistent with the flat catechol molecule area of 5.6×10^{-15} cm^2 (Scheme 4.1a) and edgewise catechol molecule area of 2.8×10^{-15} cm^2 (Scheme 4.1b), respectively. This gives the physical insight that at low concentrations (≤100 mM), catechol molecules adopt a flat orientation adsorbed on the GNP surface, while at high concentrations (≥150 mM) they adopt an edgewise orientation. At intermediate concentrations, it remains an open question if the different oriented molecules are locally organised or randomly distributed.

Last, as shown in Figure 4.3c, the low concentration data (≤100 mM) were analysed in terms of the Langmuir model, which predicts the fractional coverage Θ to vary with adsorbate concentration, C,

$$\theta = \frac{KC}{1+KC} \tag{4.3}$$

where $\Theta = \Gamma/\Gamma_{max}$ and Γ is the surface coverage corresponding to the concentration, C. $1/\Theta$ was plotted *versus* $1/C$, giving a straight line with a slope of 5.06, intercept of 1.01 and R^2 = 0.998, which indicates excellent agreement with the Langmuir model. Therefore, the adsorption constant (K) can be determined from the reciprocal of the slope giving (0.2 ± 0.002) mM^{-1} .The success of the Langmuir model also suggests that the adsorption for catechol onto GNPs is reversible, hence a desorption process might be expected to occur when modified GNPs are transferred into a solution which contains no catechol. The latter is next further explored through analysis of the nano-impact data.

4.3.3 Nano-impacts of Catechol-GNPs and Unmodified-GNPs

Having evidenced the adsorption of catechol on the GNPs electrochemically and spectroscopically, nano-impact experiments of catechol-GNPs were conducted to study *individual* catechol modified GNPs. From the cyclic voltammetry, oxidation of catechol may occur when the applied potential on the electrode is held at or more positive than ca. +0.43 V. A clean carbon fibre microelectrode was first immersed in solution and after the addition of a stock GNPs suspension with a known concentration (0.33 pM), chronoamperograms were immediately recorded at +0.5 and +0.9 V *vs.* SCE. For comparison, chronoamperograms were also recorded for unmodified GNPs in the same conditions. As shown in Figure 4.4, oxidative spikes were observed for both catechol-modified GNPs and unmodified GNPs, with each spike corresponding to an individual collision between single GNP and the electrode. The average charge passed per spike (Q) at each potential was quantified by averaging the integration of each individual spike and a slow decrease in the size of the spikes from the modified GNPs was seen with time. This is discussed below and attributed to slow desorption of catechol.

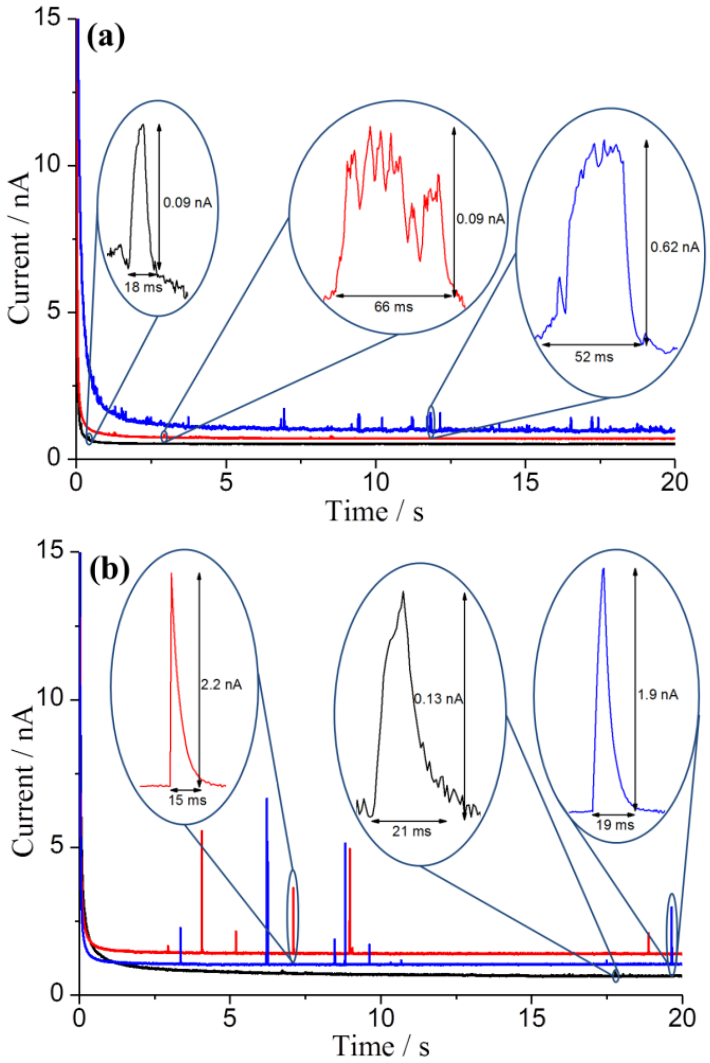


Figure 4.4. Chronoamperograms recorded at a carbon fibre wire microelectrode in a 3.33×10^{-14} M GNP suspension containing pH 3.0 buffer solution and 0.1 M KCl, (a) at +0.50 V and (b) at +0.90 V. Red line: suspension of 100-catechol GNPs. Blue line: suspension of 300-catechol GNPs. Black line: suspension of unmodified GNPs. For clarity, baselines are vertically shifted.

Two possible types of charge transfer process may be involved in a collision between a GNP and the microelectrode, namely Faradaic and capacitative. The corresponding physical origins of these two processes have been elaborated in previous work.[65-67] Briefly, a threshold potential is required to be applied in Faradaic impacts to drive the redox reaction, leading to a sharp increase in the charge transferred during the impact timescale. In contrast, when the applied potential deviates from the potential zero charge (PZC) of the electrode/electrolyte interface, a steady increase in charge transferred is shown for

capacitative impacts. Upon elevation of the applied potential, the average charge (*Q*) for unmodified GNPs increases slightly (Figure 4.4, black line), consistent with capacitative behaviour. In contrast, a large increase in *Q* for 100-catechol GNPs (Figure 4.4, red line) and 300-catechol GNPs (Figure 4.4, blue line), respectively, is observed between +0.5 and +0.9 V. This implies that Faradaic current from the oxidation of catechol on the individual impacting catechol-GNPs plays a dominant role in the observed current spikes while the simultaneous capacitative charge transfer caused by the GNPs is negligible. Figure 4.4 also shows that the impact features are either in the form of 'sharp spikes' (short transient times) or 'flat topped spikes' (long transient times) and the spikes at low potentials are of significantly longer duration with altered spike shapes.

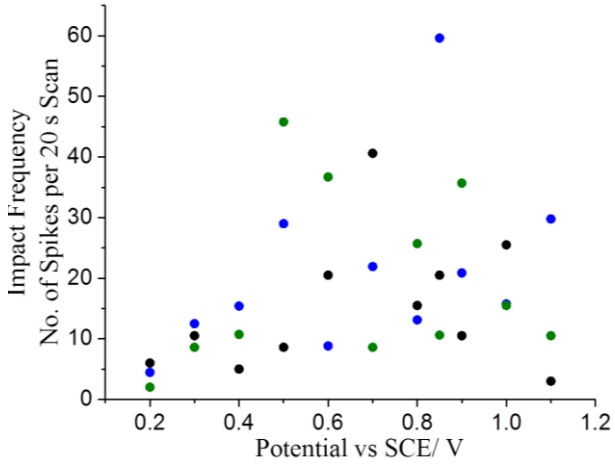


Figure 4.5. Plot of average impact frequency (number of spikes per 20 s scan) against potential applied (vs. SCE). Green dots: 300-catechol GNPs. Blue dots: 100-catechol GNPs. Black dots: unmodified GNPs.

In order to better understand the difference in the charge per spike between the two different concentrations of catechol modified GNPs, a potential variation study was performed. 0.28 mg of catechol-modified or unmodified GNPs was well dispersed in 5 mL of nitrogen saturated pH 3.0 buffer solutions. Chronoamperograms were then recorded at different potentials, from +0.2 to +1.1 V. The experiment at each potential was repeated to obtain a large sample size. Figure 4.5 show the average number of spikes in one

chronoamperometry scan (20 s) when different potentials are applied to the electrode. The impact frequency follows a random distribution, consistent with the fact that particle diffusion is independent of the applied potential or modification of GNP. The average charge transferred per individual impact spike (Q) was plotted against the applied potential, as shown in Figure 4.6.

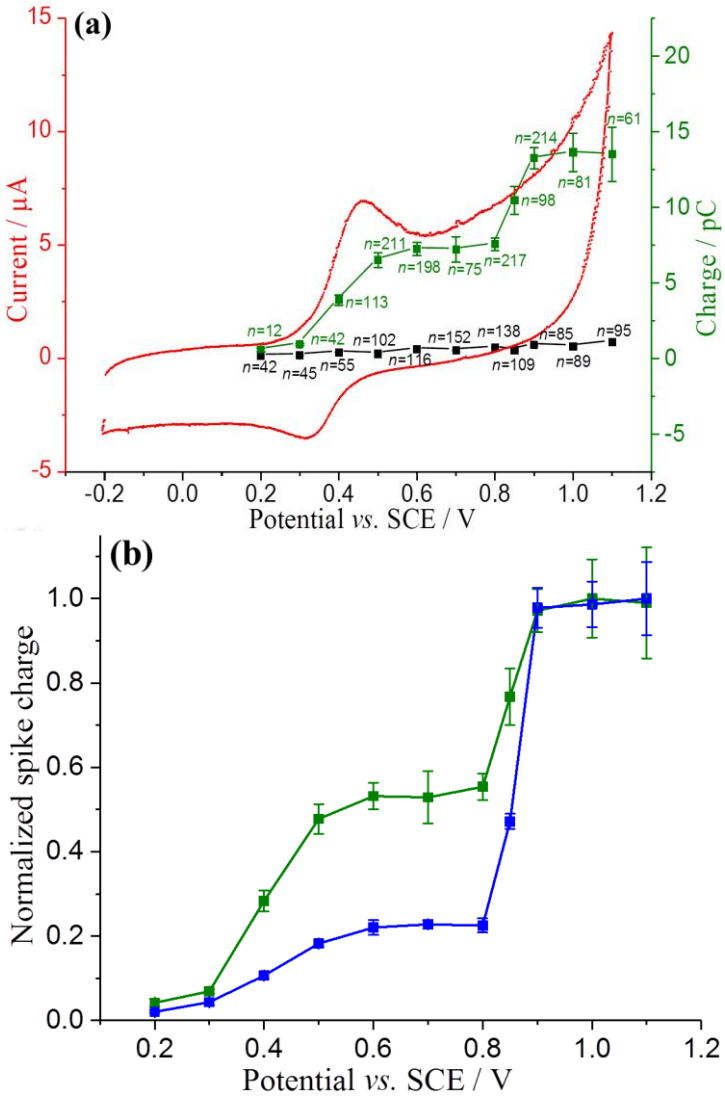


Figure 4.6. (a) Voltammogram of 100-catechol GNPs modified EPPG electrode in a pH 3.0 buffer solution supported with 0.1 M KCl, recorded at 25 mV s^{-1}. Overlayed squares are the average charge transferred per individual impact spike of 300-catechol GNPs (green) and unmodified GNPs (black) at a carbon fibre wire microelectrode. The error bars are derived from SD/$(n)^{1/2}$, where SD is the standard deviation and n is the number of the spikes. (b) The relative size of the charge passed as a function of potential for 100-catechol GNPs (blue) and 300-catechol GNPs (green). The data are normalised relative to the maximum charge seen at high potentials.

The charge transferred per spike of unmodified GNPs (black squares) shows a steady small increase with a higher applied potential, consistent with capacitative behaviour as previously reported.[65,66] It is clear that there are two onsets of potential at ca. +0.43 V and +0.85 V, respectively, and both are quinone related. The two features are reminiscent of the oxidation of catechol adsorbed on alumina.[61] Similarly it can be concluded that the first feature relates to incomplete catechol oxidation since the duration of the impact is too short to allow for full charge propagation over the surface and for the disproportionation kinetics of S to form C and Q to take place. The feature at the more positive potentials is likely related to catechol oxidation *via* a direct two electron process:

$$C - 2e^- \rightleftarrows Q \tag{4.4}$$

The difference in spike shapes suggest that at the low potentials, the oxidation is kinetically limited consistent with the flat topped spikes seen, whereas the faster, high potential process leads to sharper peaks and more complete oxidation of the adsorbed species. Experiments conducted with different levels of adsorbate (100-catechol GNP and 300-catechol GNP) showed the relative size of two features to vary: the higher coverage leads to a relatively larger signal consistent with the second order kinetics of the S disproportionation influencing the rate (Figure 4.6b).

The surface coverage (Γ) of 300-catechol GNPs can be quantified based on Figure 4.6. At +1.0 V, the average charge passed per spike due to the Faradaic process ($Q_{Faradaic}$) can be determined *via* $Q_{Total} = Q_{Faradaic} + Q_{capacitative}$, where Q_{Total} = (13.6 ± 1.3) pC and $Q_{capacitative}$ = (0.81 ± 0.05) pC. $Q_{Faradaic}$ can be related to the number of catechol molecules adsorbed per GNP (N) by $Q_{Faradaic} = nNe$, where n is the number of electrons transferred during the oxidation of catechol (n = 2) and e is the charge per electron. The area occupied by each individual catechol molecule ($S_{R\text{-}Ct}$) on the surface of GNP can be obtained *via* $S_{R\text{-}Ct} = S_{GNP}/N$, where S_{GNP} is the area of GNP (equivalent to 297 ± 152 μm^2).[65] Moreover, Γ

can be determined *via* $\Gamma = N/(N_A S_{GNP})$, where N_A is the Avogadro constant. Therefore, at +1.0 V, N, $S_{R\text{-}Ct}$ and Γ can be calculated as $(4.0 \pm 0.4) \times 10^7$, $(7.4 \pm 4.1) \times 10^{-14}$ cm^2 per molecule, and $(2.2 \pm 0.9) \times 10^{-11}$ mol cm^{-2}, respectively.

The theoretical number of catechol molecules for monolayer adsorption per GNP (N') can be estimated from $N' = S_{GNP}/S_{catechol}$ assuming a close packed coverage, hence N' can be calculated as $(5.3 \pm 2.6) \times 10^8$. N obtained from nano-impacts at +1.0 V is $(4.0 \pm 0.4) \times 10^7$, which indicates a submonolayer coverage of catechol on the GNP. The reason for this submonolayer coverage and lower coverage relative to those inferred *via* UV-vis spectroscopy might be the progressive desorption of catechol molecules from GNPs before and during the nano-impact experiment following immersion into a solution containing no catechol, which is further confirmed by analysis of the spike charge with time, as next discussed.

Fifteen representative chronoamperometric scans with large spike sample size from both 100-catechol and 300-catechol GNPs, and different potentials were selected and single first order analysis of each spike was made. The average spike charge, Q, decreased with time. As the catechol adsorbed on a GNP is proportional to the charge, a clear steady decrease in the amount of catechol on GNP was inferred and attributed to the desorption process. Assuming first order desorption kinetics, plots of Ln(Q) against time were made and are shown in Figure 4.7. Although the data is scattered, a reasonable linear dependence is seen. It can be concluded that the desorption of catechol on GNPs during chronoamperometric scans undergoes first order kinetics with a rate constant of $k = 0.08 \pm 0.01$ s^{-1}.

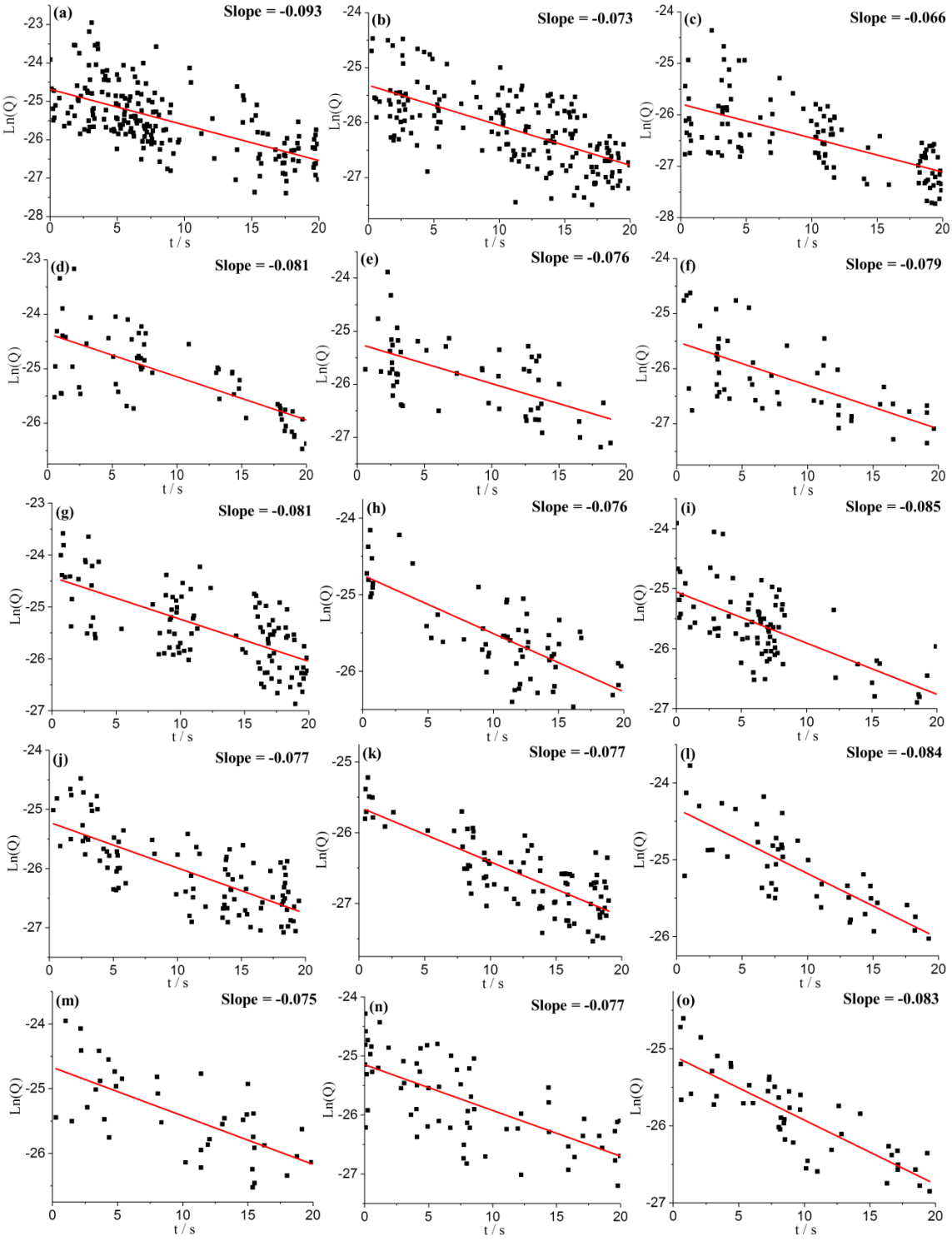


Figure 4.7. The natural logarithm of individual spike charge (*Q*) against time. (a) 100-catechol GNPs at +0.9 V; (b) 100-catechol GNPs at +0.85 V; (c) 100-catechol GNPs at +0.7 V; (d) 300-catechol GNPs at +0.9 V; (e) 300-catechol GNPs at +0.6 V; (f) 300-catechol GNPs at +0.5 V; (g) 100-catechol GNPs at +1.1 V; (h) 100-catechol GNPs at +1.0 V; (i) 100-catechol GNPs at +0.9 V; (j) 100-catechol GNPs at +0.85 V; (k) 100-catechol GNPs at +0.5 V; (l) 300-catechol GNPs at +0.9 V; (m) 300-catechol GNPs at +0.85 V; (n) 300-catechol GNPs at +0.8 V; (o) 300-catechol GNPs at +0.5 V.

In summary, the adsorption of catechol on GNPs is reversible and, at low concentrations, Langmuirian. At high concentrations, a flat to vertical phase transition change is inferred. In the absence of catechol in bulk solution there is a slow first order desorption of the adsorbate.

4.4 Conclusions

The adsorption of catechol on GNPs follows the Langmuir model with the adsorption constant (K) of (0.2 ± 0.002) mM^{-1} at a low catechol concentration but with a flat to vertical phase transition occurring at high concentrations. The desorption process follows a slow first order kinetics with a rate constant of k = 0.08 ± 0.01 s^{-1}. A powerful new strategy is thus demonstrated to study adsorption and desorption of catechol on GNPs, and better understand the modification process, whose use can also be extended to the characterisation of various kinds of molecules on nanomaterials of industrial interest. This may significantly assist the potential environmental, biological and medical applications of GNPs and other similar nanomaterials.

Bibliography

(1) Chen, L.; Li, X.; Tanner, E. E.; Compton, R. G. *Chemical Science* **2017**, *8*, 4771-4778.
(2) Novoselov, K. S.; Geim, A. K.; Morozov, S. V.; Jiang, D.; Zhang, Y.; Dubonos, S. V.; Grigorieva, I. V.; Firsov, A. A. *Science* **2004**, *306*, 666-669.
(3) Morozov, S. V.; Novoselov, K. S.; Katsnelson, M. I.; Schedin, F.; Elias, D. C.; Jaszczak, J. A.; Geim, A. K. *Physical Review Letters* **2008**, *100*, 016602.
(4) Kudin, K. N.; Ozbas, B.; Schniepp, H. C.; Prud'homme, R. K.; Aksay, I. A.; Car, R. *Nano Lett* **2008**, *8*, 36-41.
(5) Park, C. H.; Giustino, F.; Spataru, C. D.; Cohen, M. L.; Louie, S. G. *Nano Lett* **2009**, *9*, 4234-4239.
(6) Ambrosi, A.; Chua, C. K.; Bonanni, A.; Pumera, M. *Chemical Reviews* **2014**, *114*, 7150-7188.
(7) Castro Neto, A. H.; Guinea, F.; Peres, N. M. R.; Novoselov, K. S.; Geim, A. K. *Reviews of Modern Physics* **2009**, *81*, 109-162.
(8) Geim, A. K.; Novoselov, K. S. *Nature Materials* **2007**, *6*, 183-191.
(9) Stankovich, S.; Dikin, D. A.; Dommett, G. H. B.; Kohlhaas, K. M.; Zimney, E. J.; Stach, E. A.; Piner, R. D.; Nguyen, S. T.; Ruoff, R. S. *Nature* **2006**, *442*, 282-286.
(10) Geim, A. K. *Science* **2009**, *324*, 1530-1534.

(11) Kim, K. S.; Zhao, Y.; Jang, H.; Lee, S. Y.; Kim, J. M.; Kim, K. S.; Ahn, J. H.; Kim, P.; Choi, J. Y.; Hong, B. H. *Nature* **2009**, *457*, 706-710.
(12) Li, D.; Müller, M. B.; Gilje, S.; Kaner, R. B.; Wallace, G. G. *Nature Nanotechnology* **2008**, *3*, 101-105.
(13) Balandin, A. A.; Ghosh, S.; Bao, W.; Calizo, I.; Teweldebrhan, D.; Miao, F.; Lau, C. N. *Nano Lett* **2008**, *8*, 902-907.
(14) Dreyer, D. R.; Park, S.; Bielawski, C. W.; Ruoff, R. S. *Chemical Society Reviews* **2010**, *39*, 228-240.
(15) Schedin, F.; Geim, A. K.; Morozov, S. V.; Hill, E. W.; Blake, P.; Katsnelson, M. I.; Novoselov, K. S. *Nature Materials* **2007**, *6*, 652-655.
(16) Bae, S.; Kim, H.; Lee, Y.; Xu, X.; Park, J. S.; Zheng, Y.; Balakrishnan, J.; Lei, T.; Ri Kim, H.; Song, Y. I.; Kim, Y. J.; Kim, K. S.; Özyilmaz, B.; Ahn, J. H.; Hong, B. H.; Iijima, S. *Nature Nanotechnology* **2010**, *5*, 574-578.
(17) Zhu, Y.; Murali, S.; Cai, W.; Li, X.; Suk, J. W.; Potts, J. R.; Ruoff, R. S. *Advanced Materials* **2010**, *22*, 3906-3924.
(18) Reina, A.; Jia, X.; Ho, J.; Nezich, D.; Son, H.; Bulovic, V.; Dresselhaus, M. S.; Jing, K. *Nano Lett* **2009**, *9*, 30-35.
(19) Dikin, D. A.; Stankovich, S.; Zimney, E. J.; Piner, R. D.; Dommett, G. H. B.; Evmenenko, G.; Nguyen, S. T.; Ruoff, R. S. *Nature* **2007**, *448*, 457-460.
(20) Hernandez, Y.; Nicolosi, V.; Lotya, M.; Blighe, F. M.; Sun, Z.; De, S.; McGovern, I. T.; Holland, B.; Byrne, M.; Gun'ko, Y. K.; Boland, J. J.; Niraj, P.; Duesberg, G.; Krishnamurthy, S.; Goodhue, R.; Hutchison, J.; Scardaci, V.; Ferrari, A. C.; Coleman, J. N. *Nature Nanotechnology* **2008**, *3*, 563-568.
(21) Novoselov, K. S.; Fal'Ko, V. I.; Colombo, L.; Gellert, P. R.; Schwab, M. G.; Kim, K. *Nature* **2012**, *490*, 192-200.
(22) Schwierz, F. *Nature Nanotechnology* **2010**, *5*, 487-496.
(23) Bonanni, A.; Chua, C. K.; Zhao, G.; Sofer, Z.; Pumera, M. *ACS Nano* **2012**, *6*, 8546-8551.
(24) Loo, A. H.; Bonanni, A.; Pumera, M. *Nanoscale* **2013**, *5*, 7844-7848.
(25) Liang, Y.; Li, Y.; Wang, H.; Zhou, J.; Wang, J.; Regier, T.; Dai, H. *Nature Materials* **2011**, *10*, 780-786.
(26) Qu, L.; Liu, Y.; Baek, J. B.; Dai, L. *ACS Nano* **2010**, *4*, 1321-1326.
(27) Krepel, D.; Hod, O. *Journal of Physical Chemistry C* **2013**, *117*, 19477-19488.
(28) Hu, L.; Hu, X.; Wu, X.; Du, C.; Dai, Y.; Deng, J. *Physica B: Condensed Matter* **2010**, *405*, 3337-3341.
(29) Mishra, A. K.; Ramaprabhu, S. *AIP Advances* **2011**, *1*, 032152.
(30) Rani, B.; Dharamvir, K. *International Journal of Quantum Chemistry* **2014**, *114*, 1619-1629.
(31) Ivanovskaya, V. V.; Zobelli, A.; Teillet-Billy, D.; Rougeau, N.; Sidis, V.; Briddon, P. R. *European Physical Journal B* **2010**, *76*, 481-486.
(32) Sharma, S.; Verma, A. S. *Physica B: Condensed Matter* **2013**, *427*, 12-16.
(33) Widjaja, H.; Jiang, Z. T.; Altarawneh, M.; Yin, C. Y.; Goh, B. M.; Mondinos, N.; Dlugogorski, B. Z. *Applied Surface Science* **2015**, *356*, 370-377.
(34) Şahin, H.; Ciraci, S. *Journal of Physical Chemistry C* **2012**, *116*, 24075-24083.
(35) Widjaja, H.; Jiang, Z. T.; Altarawneh, M.; Yin, C. Y.; Goh, B. M.; Mondinos, N.; Amri, A.; Dlugogorski, B. Z. *Applied Surface Science* **2016**, *373*, 65-72.
(36) Thierfelder, C.; Witte, M.; Blankenburg, S.; Rauls, E.; Schmidt, W. G. *Surface Science* **2011**, *605*, 746-749.
(37) Song, H. S.; Ko, C. H.; Ahn, W.; Kim, B. J.; Croiset, E.; Chen, Z.; Nam, S. C. *Industrial and Engineering Chemistry Research* **2012**, *51*, 10259-10264.
(38) Schröder, E. *Journal of Nanomaterials* **2013**, *2013*, 6.
(39) Pinto, A. M.; Moreira, J. A.; Magalhães, F. D.; Gonçalves, I. C. *Colloids and Surfaces B: Biointerfaces* **2016**, *146*, 818-824.
(40) Wang, J.; Chen, Z.; Chen, B. *Environmental Science and Technology* **2014**, *48*, 4817-4825.
(41) Mabayoje, O.; Seredych, M.; Bandosz, T. J. *ACS Applied Materials and Interfaces* **2012**, *4*, 3316-3324.

(42) Liu, L.; Ryu, S.; Tomasik, M. R.; Stolyarova, E.; Jung, N.; Hybertsen, M. S.; Steigerwald, M. L.; Brus, L. E.; Flynn, G. W. *Nano Lett* **2008**, *8*, 1965-1970.
(43) Meyer, J. C.; Geim, A. K.; Katsnelson, M. I.; Novoselov, K. S.; Booth, T. J.; Roth, S. *Nature* **2007**, *446*, 60-63.
(44) Shen, J.; Hu, Y.; Li, C.; Qin, C.; Shi, M.; Ye, M. *Langmuir* **2009**, *25*, 6122-6128.
(45) Soriaga, M. P.; Hubbard, A. T. *Journal of the American Chemical Society* **1982**, *104*, 2735-2742.
(46) Soriaga, M. P.; Hubbard, A. T. *Journal of the American Chemical Society* **1982**, *104*, 2742-2747.
(47) Soriaga, M. P.; Hubbard, A. T. *Journal of the American Chemical Society* **1982**, *104*, 3937-3945.
(48) Chia, V. K. F.; Soriaga, M. P.; Hubbard, A. T. *Journal of Physical Chemistry* **1983**, *87*, 232-235.
(49) Song, D.; Soriaga, M. P.; Vjeira, K. L.; Zapien, D. C.; Hubbard, A. T. *Journal of Physical Chemistry* **1985**, *89*, 3999-4002.
(50) Soriaga, M. P.; Binamira-Soriaga, E.; Hubbard, A. T.; Benziger, J. B.; Pang, K. W. P. *Inorganic Chemistry* **1985**, *24*, 65-73.
(51) Ren, D.; Hubbard, A. T. *J Colloid Interface Sci* **1999**, *209*, 435-441.
(52) Xiao, X.; Bard, A. J. *Journal of the American Chemical Society* **2007**, *129*, 9610-9612.
(53) Bard, A. J.; Zhou, H.; Kwon, S. J. *Israel Journal of Chemistry* **2010**, *50*, 267-276.
(54) Cheng, W.; Compton, R. G. *TrAC Trends in Analytical Chemistry* **2014**, *58*, 79-89.
(55) Pumera, M. *ACS Nano* **2014**, *8*, 7555-7558.
(56) Rees, N. V. *Electrochemistry Communications* **2014**, *43*, 83-86.
(57) Lin, Q.; Li, Q.; Batchelor-McAuley, C.; Compton, R. G. *Journal of Physical Chemistry C* **2015**, *119*, 1489-1495.
(58) Kätelhön, E.; Tanner, E. E. L.; Batchelor-McAuley, C.; Compton, R. G. *Electrochimica Acta* **2016**, *199*, 297-304.
(59) Sokolov, S. V.; Eloul, S.; Katelhon, E.; Batchelor-McAuley, C.; Compton, R. G. *Physical Chemistry Chemical Physics* **2017**, *19*, 28-43.
(60) Ghadimi, H.; Ali, A. S. M.; Mohamed, N.; Ab Ghani, S. *Journal of the Electrochemical Society* **2012**, *159*, E127-E131.
(61) Lin, Q.; Compton, R. G. *Journal of Physical Chemistry C* **2015**, *119*, 23463-23469.
(62) Dewar, M. J. S.; Kubba, V. P.; Pettit, R. *Journal of the Chemical Society* **1958**, 3076-3079.
(63) Jha, P. K.; Halada, G. P. *Chemistry Central Journal* **2011**, *5*, 12-12.
(64) Batsanov, S. S. *Inorganic Materials* **2001**, *37*, 871-885.
(65) Poon, J.; Batchelor-McAuley, C.; Tschulik, K.; Compton, R. G. *Chemical Science* **2015**, *6*, 2869-2876.
(66) Wu, H.; Lin, Q.; Batchelor-McAuley, C.; Goncalves, L. M.; Lima, C. F.; Compton, R. G. *Analyst* **2016**, *141*, 2696-2703.
(67) Lin, Q.; Lin, C.; Wu, H.; Batchelor-McAuley, C.; Compton, R. G. *Journal of Physical Chemistry C* **2016**, *120*, 20216-20223.

Chapter 5

Adsorption on Graphene: Flat to Edge to End Transitions of Phenyl Hydroquinone

The adsorption of phenyl hydroquinone (PHQ) on graphene surfaces at the liquid/solid interface is investigated revealing a flat orientation and two different vertically adsorbed states of PHQ on graphene nanoplatelets (GNPs), namely edgewise or endwise adsorption. The transition between these states is driven by increasing concentrations of PHQ in solution leading to increased absolute coverages on the graphene surface. At low adsorbate concentrations (≤21 mM), the adsorption process is shown to be Langmuirian with an adsorption constant of (9.5 ± 0.2) mM^{-1}. Independent measurements are conducted using a single particle electrochemical technique to confirm the surface coverage of PHQ on GNPs at low concentrations, showing excellent agreement with the UV-vis measurements.

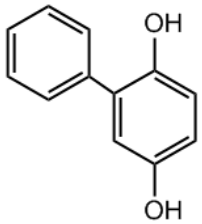
The work presented in this Chapter has been published in *Physical Chemistry Chemical Physics*.[1]

5.1 Introduction

As discussed in the previous Chapter, the applications of graphene and its derivatives lie in a variety of contexts, from electronics to medicine owing to its outstanding properties.[2-20] Understanding the behaviour of molecules on graphene surfaces is fundamentally important to underpin the applications in advanced catalysts and ultra-sensitive sensors.

The previous Chapter has focused on the adsorption and desorption of organic molecules on individual graphene nanoplatelets (GNPs), a graphene derivative which has the advantageous properties of graphene, but circumvents the poor stability traditionally experienced.[19,21] Specifically, adsorption of 1,2-dihydroxybenzene (catechol) on the GNPs was shown to be reversible and at low concentrations to follow the Langmuir isotherm. At higher concentrations the adsorbate is inferred to undergo a flat to vertical concentration driven phase transition. To seek new insights into such adsorption processes, the possibility of two different vertically adsorbed states reflecting the edge or end adsorption of a 'box' shaped molecule are considered. In particular, this Chapter focuses on the adsorption of phenyl hydroquinone (chemical structure given in Scheme 5.1) on GNPs from aqueous solutions.

Scheme 5.1. Chemical structure of phenyl hydroquinone (PHQ).



A wide range of concentrations of PHQ solutions are used to modify the GNPs. The uptake of PHQ is followed by UV-vis spectroscopy—hence allowing the accurate amount of PHQ molecules adsorbed by GNPs to be determined. The adsorption isotherm then can be constructed and three plateaux are observed, indicating that three molecular orientation

states of PHQ on GNPs exist. By comparing the area occupied by each individual PHQ molecule on GNPs, corresponding to each plateau, with the theoretical molecular area of different orientations, the orientation states of PHQ on GNPs can be determined. To confirm this orientation state and enable single PHQ-GNPs measurements, the nano-impact method is applied. In this method, as described in Chapter 1, the nanoparticles in a suspension move by virtue of their Brownian motion which undergo stochastic collisions with a potentiostatted microelectrode, resulting in a 'spike' in the current that corresponds to the Faradaic electron transfer of the adsorbed molecules. The spike in current has been shown to directly relate to the amount of materials undergoing electron transfer due to Faraday's first law and has been applied in a variety of contexts.[22-25] The surface coverage of electroactive species (PHQ) on GNPs could then be attained based on the charge passed per individual impact, allowing the molecular orientation of PHQ to be inferred.

5.2 Experimental

5.2.1 Buffer Solution

The buffer solution, consisting of 19.75M methanol and 0.2 M HCl, was freshly prepared from pure methanol (99.8%) and 1 M HCl. This amount of methanol was determined experimentally for the minimal amount of methanol required to make a 300 mM PHQ aqueous solution, and all following experiments were conducted in this buffer.

5.2.2 UV-vis Spectroscopy

A wide range of concentrations (from 0.1 mM to 300 mM) of PHQ in the buffer solution were made. A known amount of GNPs were then added into and mixed with 1 mL of different concentrations of PHQ solutions. The amount of GNPs used for each PHQ solution was determined by calculation such that the GNPs used must reduce at least 20%

of PHQ concentration, assuming a full monolayer coverage of PHQ on GNPs. The mixture of GNPs and PHQ solution was then sonicated (FB15050, Fisher Scientific, 50/60 Hz, 80W, Germany) for 35 min to realise maximum adsorption, followed by centrifugation (Eppendorf Centrifuge 5430 R) at 14000 rpm for 15 min. The original PHQ solution before adsorption and the supernatant after adsorption were both diluted then measured by UV-vis spectroscopy. The UV-vis absorbance was recorded from 600–220 nm.

5.2.3 Preparation of PHQ-GNP Stock Suspensions

A suspension of 3.3×10^{-13} M of PHQ-GNPs was prepared by mixing 2.8 mg of GNPs with 10 mL of 3 mM PHQ in buffer solution and then sonicated (FB15050, Fisher Scientific, 50/60 Hz, 80W, Germany) for 35 min to allow the full adsorption of PHQ onto GNPs. The well dispersed mixture was then divided into ten portions by being transferred into ten microcentrifuge tubes (1.5mL, Fisherband) equally, followed by centrifugation (Eppendorf Centrifuge 5430 R) for 15 min in 14000 rpm. 1 mL of buffer solution was then added into modified GNPs powder. The mixture was shaken on a vortex (Whirlmixer, Loughbough, UK) for 30 s and sonicated for 20 s. This dispersion procedure was repeated 3 times to get an even suspension. The above stock suspension was freshly prepared daily and diluted for nano-impact experiments.

5.2.4 Electrochemical Measurements

For the cyclic voltammetry measurements, a basal-plane pyrolytic graphite (BPPG) electrode was used as the working electrode. The BPPG electrode was produced from pieces of the highly ordered pyrolytic graphite (HOPG) (Le Carbone, Sussex, UK). Prior to each measurement, the surface of BPPG electrode was renewed via polishing on sand papers P2500 and P4000 grade, respectively, followed by repeatedly pressing with cellotape (Henkel AG, Dusseldorf, Germany) 10-15 times. The electrode was subsequently

rinsed with acetone and dried with nitrogen. Cyclic voltammograms were then recorded at different scan rates in a degassed 3 mM PHQ solution containing 19.75 M methanol and 0.2 M HCl.

In nano-impact experiments, chronoamperometry was conducted at a home-fabricated carbon fibre wire microelectrode (see Chapter 3 for fabrication procedures). Note that the potentiostat used in this work accurately conserves the charge transferred due to a particle-impact process despite possible alteration in the spike shape.[26,27] 4 mL of buffer solution was bubbled thoroughly with nitrogen for 5 min and then 1 mL of the PHQ-GNPs stock suspension was added while the nitrogen was kept bubbling for further 5 s to get an even suspension, followed by immediate chronoamperometric scans at + 1.0 V for 20s.

5.3 Results and Discussion

5.3.1 Adsorption Isotherm of Phenyl Hydroquinone on Graphene

First, to maximise the solubility of PHQ in aqueous solution, a buffer solution containing 19.75 M methanol and 0.2 M HCl was chosen. Buffer solutions containing a range of concentrations of PHQ were then prepared and examined by UV-vis spectroscopy, correlating the relationship between PHQ concentration and absorbance. A linear Beer-Lambert plot was obtained with the extinction coefficient (ε) of 0.482 ± 0.002 M^{-1} m^{-1}, as shown in Figure 5.1. Next, the GNPs were modified by mixing 1 mL of known concentrations of PHQ in buffer solution with GNPs. They were then sonicated for 35 min to allow maximum adsorption, followed by centrifugation. The absorbance of the original PHQ solution before adsorption and the supernatant after adsorption were both measured by UV-vis spectroscopy. As shown in Figure 5.2, the absorbance of phenyl hydroquinone in aqueous solution reaches a maximum at 301 nm, consistent with prior literature.[28] An

obvious reduction in magnitude of the absorbance peak can be observed, evidently attributed to the adsorption onto the GNPs, allowing the accurate assessment of adsorbed amount of PHQ by GNPs. These results were then used to plot the adsorption isotherm of PHQ on GNPs in buffer solution, as shown in Figure 5.3a, where three distinct plateaux can be observed. A semi-logarithmic plot was also constructed (Figure 5.3b) to more clearly examine the first plateau.

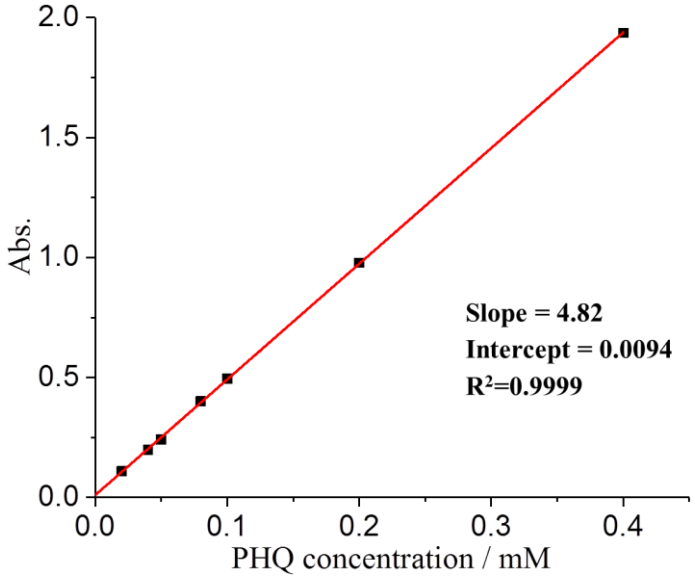


Figure 5.1. Beer-Lambert plot of phenyl hydroquinone in buffer solution (19.75 M methanol and 0.2 M HCl).

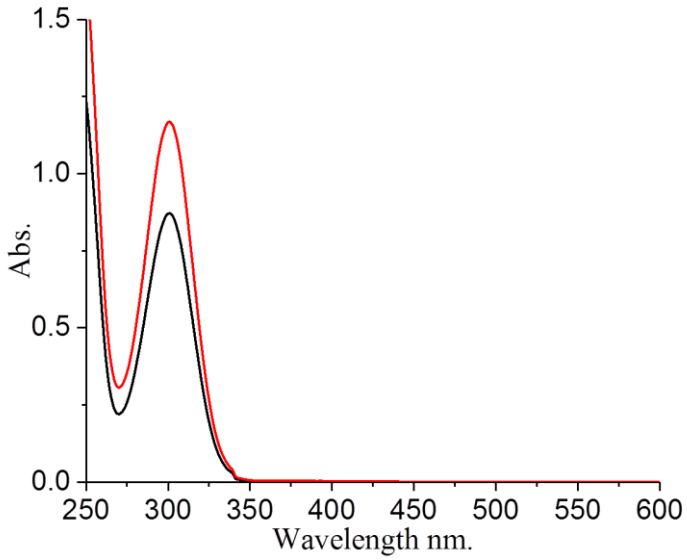


Figure 5.2. UV-visible spectra of a buffer solution (19.75 M methanol and 0.2 M HCl) containing 5 mM phenyl hydroquinone before GNPs adsorption (red line) and after adsorption (black line); Dilution factor = 20.

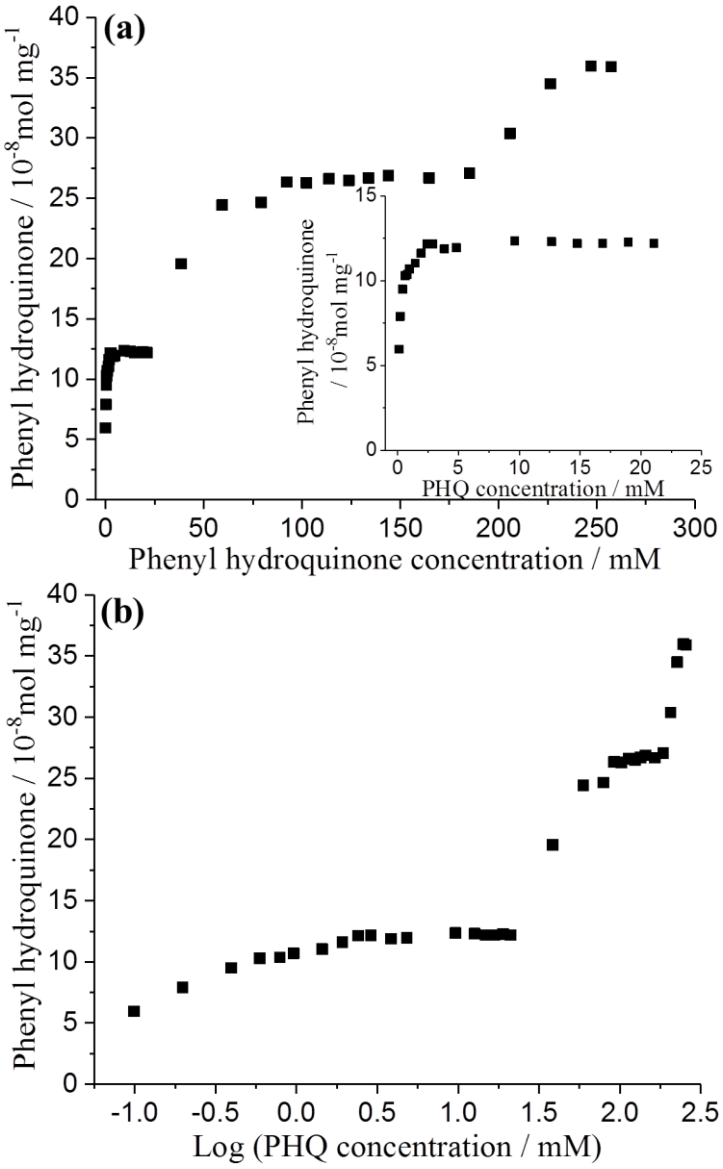
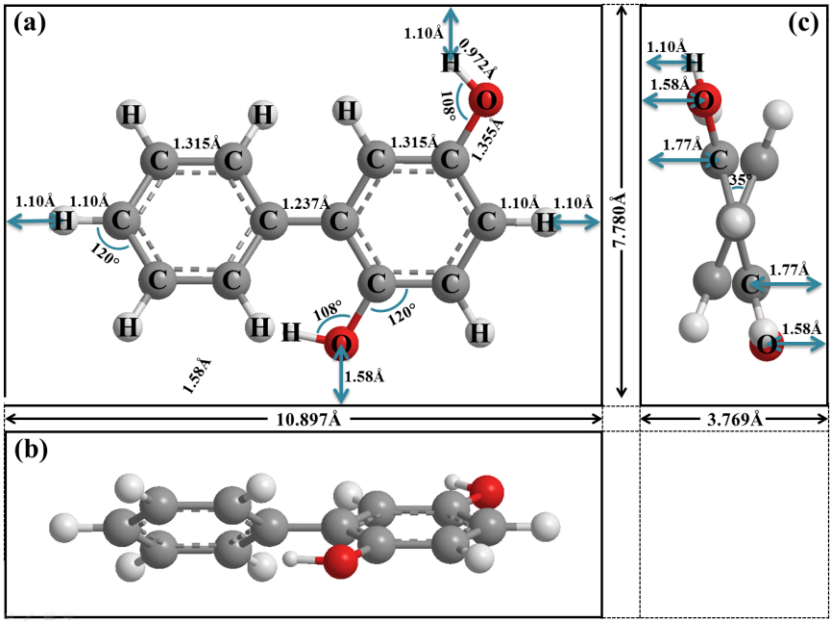


Figure 5.3. (a) Phenyl hydroquinone adsorption isotherm for GNPs in buffer solution (19.75 M methanol and 0.2 M HCl). Inset: zoom-in of PHQ adsorption isotherm for GNPs when concentration below than 21 mM. (b) Log PHQ concentration plot.

With an increasing of PHQ concentration, the amount of PHQ adsorbed by a unit amount (1 mg) of GNPs (n) increases progressively and reaches the first plateau at a PHQ concentration between ca. 2 and 21 mM with n_{max} = 1.2 × 10^{-7} mol mg^{-1}, giving the maximum surface coverage (Γ_{max}) of (1.9 ± 0.6) × 10^{-10} mol cm^{-2} (see Appendix A for sample calculation). The second plateau is reached at an adsorbate concentration of ca. 92 to 185 mM with n'_{max} = 2.7 × 10^{-7} mol mg^{-1} and Γ'_{max} = (4.3 ± 1.5) × 10^{-10} mol cm^{-2},

while the third plateau occurs at concentrations between ca. 240 and 260 mM with n''_{max} = 3.6 × 10^{-7} mol mg^{-1}, giving Γ''_{max} = (5.8 ± 1.9) × 10^{-10} mol cm^{-2}. The increasing Γ at higher adsorbate concentrations is inferred to result from a molecular phase transition to a more densely packed layer corresponding to a different orientation rather than multilayer adsorption, as the coverage for both catechol[23] and PHQ eventually reaches a plateau, that the coverages for the different orientations are consistent with the known molecular geometry. That said the possible formation of multilayers cannot be completely ruled out.

Scheme 5.2. Rectangular box model of phenyl hydroquinone molecule for both (a) flat view, (b) edgewise view and (c) endwise view.



In order to confirm the molecular orientation, it is necessary to obtain the theoretical areas of the molecule in each possible orientation. This can be achieved by approximating the PHQ molecule as a rectangular box with all side lengths estimated by trigonometry for bond lengths, bond angles and van de Waals radii of terminating atoms (Scheme 5.2). The data for bond lengths, bond angles were obtained from ChemDraw 15.1 and van de Waals radii of terminating atoms tabulated by Rowland were used.[29] S_{PHQ} of flat view, S'_{PHQ} of edgewise view, and S''_{PHQ} of endwise view hence can be estimated as 8.5 × 10^{-15} cm^2, 4.1

$\times 10^{-15}$ cm^2, and 2.9 $\times 10^{-15}$ cm^2, respectively, which are in excellent agreement with literature.[30,31] The average area occupied by each individual PHQ molecule ($S_{\text{R-PHQ}}$) on GNPs can be obtained from the surface coverage, Γ, *via* $S_{\text{R-PHQ}} = 1/(N_A\Gamma)$, where N_A is the Avogadro constant. Therefore, $S_{\text{R-PHQ}}$ can be determined as (8.5 ± 2.1) $\times 10^{-15}$ cm^2 at the first plateau, (3.8 ± 0.9) $\times 10^{-15}$ at the second plateau, and (2.9 ± 0.7) $\times 10^{-15}$ at the third plateau, consistent with the flat PHQ molecule area of 8.5 $\times 10^{-15}$ cm^2 (Scheme 5.2a), edgewise PHQ molecule area of 4.1 $\times 10^{-15}$ cm^2 (Scheme 5.2b) and endwise PHQ molecule area of 2.9 $\times 10^{-15}$ cm^2 (Scheme 5.2c), respectively. This gives insight into the orientation states and phase transitions of large organic molecules adsorbed on graphene. The PHQ molecules adopt a flat orientation adsorbed on the graphene surface at low concentrations (≤21 mM), while they adopt an edgewise orientation at medium concentrations (92<C<185 mM). At intermediate concentrations, a flat to edgewise phase transition is inferred to occur, but it remains an open question if the different oriented molecules are locally organised or randomly distributed. Similarly, PHQ molecules adopt an endwise orientation at high concentrations (≥240 mM) and an edgewise to endwise phase transition is inferred to take place when the adsorbate concentration increases from a medium concentration region to a high concentration region.

Last, the low concentration region below the onset of the second plateau (≤ 21 mM) was analysed in terms of the Langmuir model, which predicts the fractional coverage, Θ, to vary with adsorbate concentration, C,

$$\theta = \frac{KC}{1+KC} \tag{5.1}$$

where $\Theta = \Gamma/\Gamma_{\max}$ and Γ is the coverage corresponding to the adsorbate concentration. As shown in Figure 5.4, $1/\Theta$ was plotted against $1/C$, giving a straight line with intercept of 0.999 and R^2 = 0.99. This indicates that the adsorption of PHQ onto GNPs before the

phase transition is in good agreement with the Langmuir model. Meanwhile, the adsorption constant (K) can be determined from the reciprocal of the slope, which is 0.11, giving value of (9.5 ± 0.2) mM^{-1}. The success of the Langmuir model also suggests that the adsorption for PHQ onto GNPs is reversible.

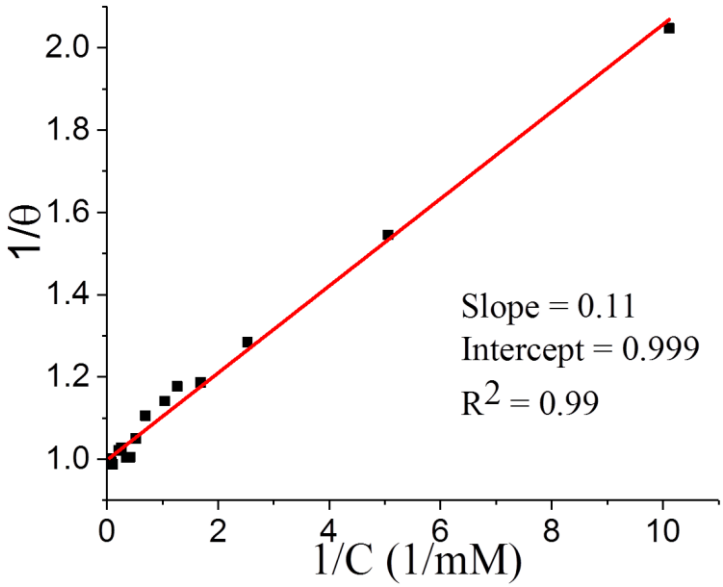


Figure 5.4. Langmuir plot of PHQ adsorption on GNPs in buffer solution (19.75 M methanol and 0.2 M HCl), where Θ is the fractional surface coverage and C is the adsorbate concentration, Langmuir adsorption model applies when the PHQ concentration is lower than 21 mM.

5.3.2 Cyclic Voltammetry of Phenyl Hydroquinone

Having evidenced the adsorption of PHQ on the GNPs spectroscopically, an electrochemical method was then used to confirm the surface coverage of PHQ on GNPs and the orientation in the horizontal state. To determine the approximate oxidation potentials required for subsequent nano-impact experiments, cyclic voltammetry (CV) was conducted using a BPPG electrode. Cyclic voltammograms were recorded on a bare BPPG macroelectrode in a buffer solution containing 3 mM PHQ and saturated with nitrogen by sweeping the potential from −0.10 to +1.00 V *vs.* SCE and reversed back to −0.10 V at a scan rate of 25 mV s^{-1} (Figure 5.5, brown line). The resultant voltammogram showed an

single oxidative peak at *ca.* +0.52 V *vs.* SCE and a reductive peak at *ca.* +0.24 V *vs.* SCE. The peak current is also found to be proportional with the square root of scan rate (Figure 5.5 inset) indicating that it is a diffusion controlled electrochemical process.

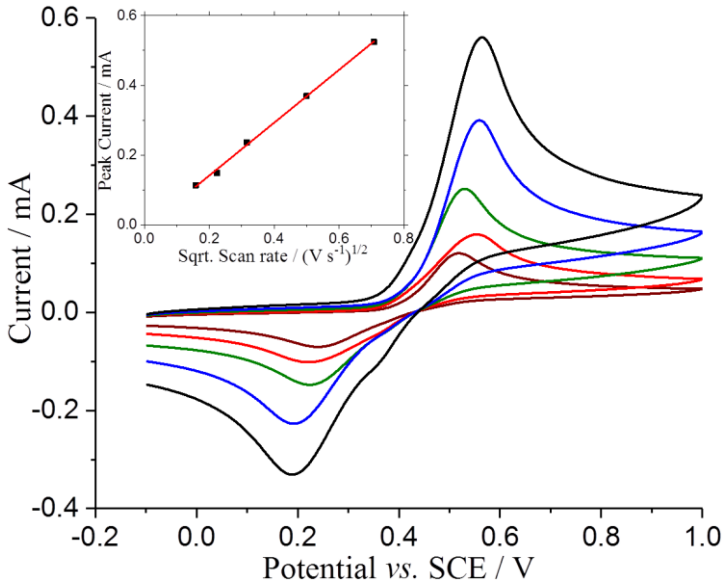


Figure 5.5. Cyclic voltammograms of 3 mM PHQ in buffer solution (19.75 M methanol and 0.2 M HCl) on a BPPG electrode at scan rate of 25 mV s^{-1} (brown), 50 mV s^{-1} (red), 100mV s^{-1} (green), 250 mV s^{-1} (blue) and 500 mV s^{-1} (black). Inset: Oxidative peak current as a function of the square root of scan rate. A red line indicates the best-fit line.

5.3.3 Nano-impacts of Individual PHQ-GNPs

Next, a clean cylindrical carbon fibre wire microelectrode (of length *ca.* 1 mm and diameter 7 μm) was first immersed in buffer solution and a known concentration (0.33 pM) of dispersed PHQ-GNPs suspension was added. The oxidative potential used for nano-impact experiments was +1.0 V *vs.* SCE, a potential value more positive than the oxidative peak potential in cyclic voltammetry—chosen to ensure that the complete oxidation of PHQ would occur, as previous studies have shown that at low overpotentials an incomplete oxidation may occur.[22,25] Under potentiostatted conditions, +1.0 V *vs.* SCE, clear and sharp oxidative spikes with a short duration (10-25 ms) from individual PHQ-

GNPs were observed as shown in Figure 5.6. For comparison, a control experiment was conducted in the same conditions without addition of PHQ-GNPs suspension. As depicted Figure 5.7, no spikes were detected confirming that each individual spike results from the random collisions between the single PHQ-GNPs and the electrode, and subsequent two-electron, two-proton oxidation of PHQ[32] and electron transfer to the electrode (Scheme 5.3).

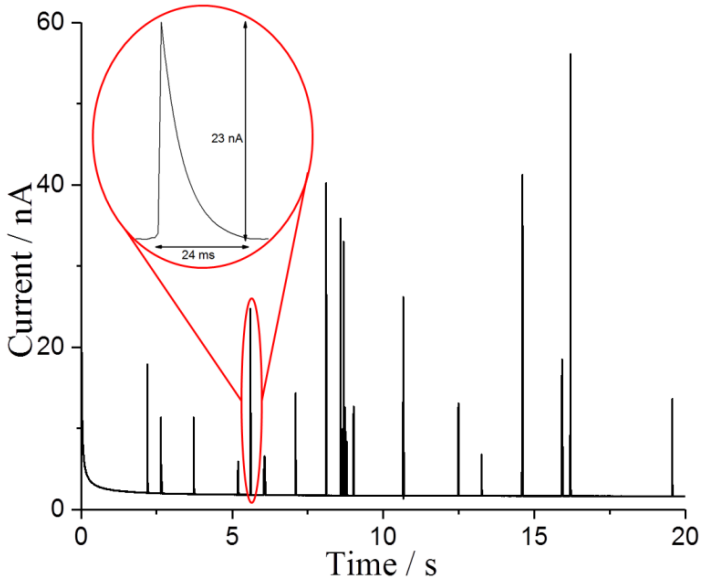


Figure 5.6. Representative chronoamperometric profiles of a 3.33×10^{-14} M suspension of PHQ-GNPs containing 19.75 M methanol and 0.2 M HCl buffer solution at +1.0 V *vs.* SCE.

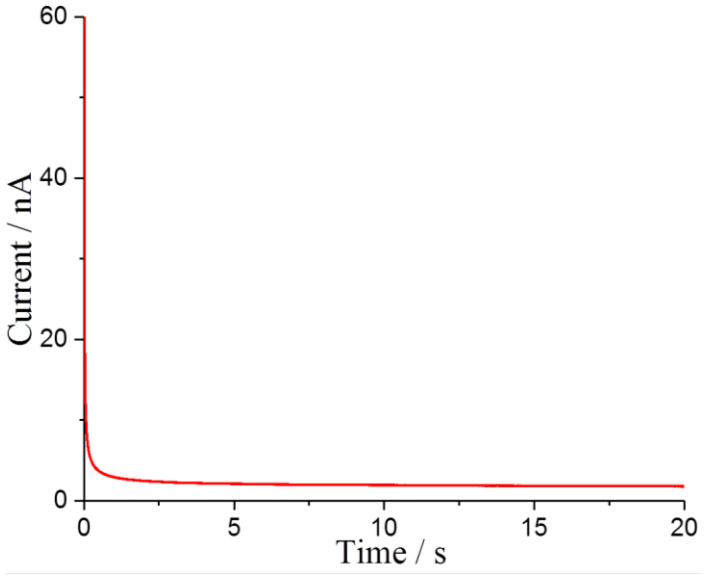
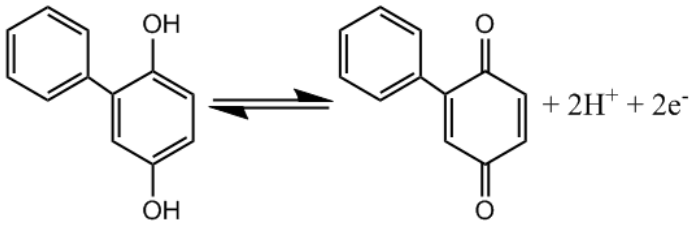


Figure 5.7. Representative chronoamperometric profiles of buffer solution containing 19.75 M methanol and 0.2 M HCl without addition of PHQ-GNPs suspension at +1.0 V *vs.* SCE.

Scheme 5.3. Two-electron, two-proton oxidation of adsorbed PHQ.



A total of 146 single spikes were detected from ten 20s chronoamperometric scans. The charge passed per spike (Q) was then quantified by integrating the area underneath the individual spikes. Figure 5.8 shows the distribution of charge of spikes only with a single-peak, sharp shape. This distribution reflects the range of size of GNP present.[33] The multi-peak spikes might result from collision between multi PHQ-GNPs and the electrode simultaneously, and hence were not included in the analysis. The duration of impacts were analysed in Figure 5.9. The average charge was determined to be (94.4 ± 7.4) pC. The error bar was derived from SD/$(n)^{1/2}$, where SD is the standard deviation and n is the number of the spikes.

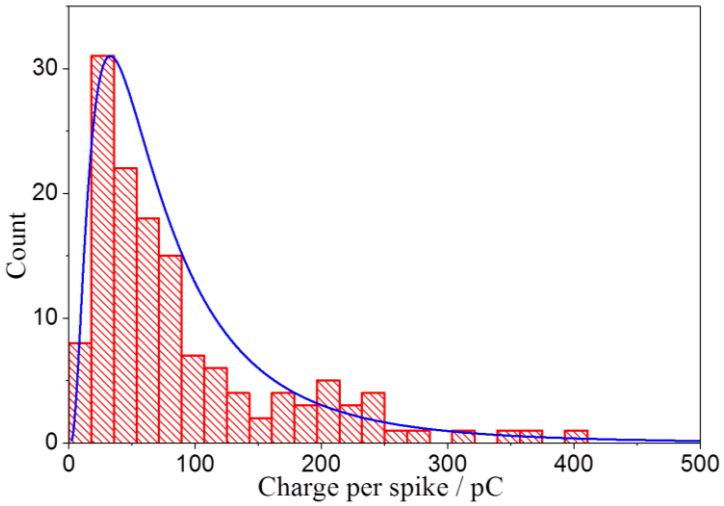


Figure 5.8. Distribution of charge from oxidation of single PHQ-GNPs by analysis of the 146 current spikes at + 1.0 V *vs*. SCE. The log-normal distribution is plotted in the blue curve.

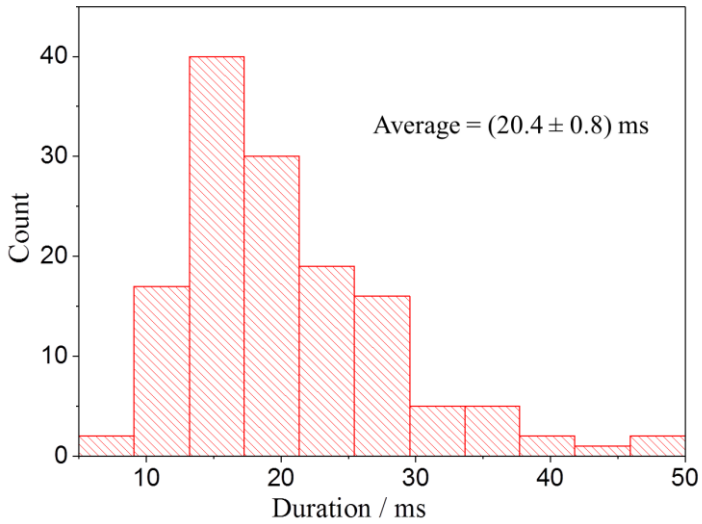


Figure 5.9. Distribution of spike duration from oxidation of single PHQ-GNPs by analysis of the 146 current spikes at + 1.0 V *vs*. SCE. Average duration = (20.4 ± 0.8) ms.

If the charge passed (Q) is as a result of complete oxidation of PHQ on single GNPs as the simultaneous capacitative charge transfer caused by the GNPs is negligible,[22] then Q can be related to the number of PHQ molecules adsorbed per GNP (N) *via* $Q = nNe$, where n is the number of electrons transferred during oxidation of PHQ (n = 2), and e is the charge per electron. The surface coverage (Γ) and the area occupied by each individual PHQ molecule ($S_{R\text{-}PHQ}$) on the GNP can be determined as $(1.6 \pm 0.6) \times 10^{-10}$ mol cm^{-2} and $(10.1 \pm 4.1) \times 10^{-15}$ cm^2 per molecule, respectively. Comparing Γ of GNP modified by 3mM PHQ buffer solution from nano-impact method, which is $(1.6 \pm 0.6) \times 10^{-10}$ mol cm^{-2}, with Γ_{max} at the first plateau obtained from UV-vis with value of $(1.9 \pm 0.6) \times 10^{-10}$ mol cm^{-2} shows excellent agreement and suggests a flat orientation of PHQ molecules on GNPs at this concentration. The nano-impact method is most useful at low PHQ concentrations. At higher concentrations, the excess modifier molecules introduce an extremely high background current leading to no spikes being detected. Previous work[23] applied a wash-step to remove excess modifier molecules to investigate GNPs modified with higher adsorbate concentrations. However, the reversible Langmuirian adsorption

results in an inevitable desorption process which occurs during the washing leading to an underestimated surface coverage at high concentrations.

5.4 Conclusions

In conclusion, the present method allows the accurate measurements of the amount of large organic molecules adsorbed on GNPs, hence probing the orientation states and concentration driven phase transition of adsorbed molecules on the adsorbent. The adsorption of PHQ on GNPs is reversible and, at low concentrations Langmuirian. With the increase of adsorbate concentrations, first a flat to edgewise then an edgewise to endwise phase transition change is inferred.

Bibliography

(1) Chen, L.; Tanner, E. E.; Compton, R. G. *Physical Chemistry Chemical Physics* **2017**, *19*, 17521-17525.
(2) Kudin, K. N.; Ozbas, B.; Schniepp, H. C.; Prud'homme, R. K.; Aksay, I. A.; Car, R. *Nano Lett* **2008**, *8*, 36-41.
(3) Morozov, S. V.; Novoselov, K. S.; Katsnelson, M. I.; Schedin, F.; Elias, D. C.; Jaszczak, J. A.; Geim, A. K. *Physical Review Letters* **2008**, *100*, 016602.
(4) Park, C. H.; Giustino, F.; Spataru, C. D.; Cohen, M. L.; Louie, S. G. *Nano Lett* **2009**, *9*, 4234-4239.
(5) Ambrosi, A.; Chua, C. K.; Bonanni, A.; Pumera, M. *Chemical Reviews* **2014**, *114*, 7150-7188.
(6) Stankovich, S.; Dikin, D. A.; Dommett, G. H. B.; Kohlhaas, K. M.; Zimney, E. J.; Stach, E. A.; Piner, R. D.; Nguyen, S. T.; Ruoff, R. S. *Nature* **2006**, *442*, 282-286.
(7) Geim, A. K.; Novoselov, K. S. *Nature Materials* **2007**, *6*, 183-191.
(8) Schedin, F.; Geim, A. K.; Morozov, S. V.; Hill, E. W.; Blake, P.; Katsnelson, M. I.; Novoselov, K. S. *Nature Materials* **2007**, *6*, 652-655.
(9) Dikin, D. A.; Stankovich, S.; Zimney, E. J.; Piner, R. D.; Dommett, G. H. B.; Evmenenko, G.; Nguyen, S. T.; Ruoff, R. S. *Nature* **2007**, *448*, 457-460.
(10) Balandin, A. A.; Ghosh, S.; Bao, W.; Calizo, I.; Teweldebrhan, D.; Miao, F.; Lau, C. N. *Nano Lett* **2008**, *8*, 902-907.
(11) Li, D.; Müller, M. B.; Gilje, S.; Kaner, R. B.; Wallace, G. G. *Nature Nanotechnology* **2008**, *3*, 101-105.
(12) Castro Neto, A. H.; Guinea, F.; Peres, N. M. R.; Novoselov, K. S.; Geim, A. K. *Reviews of Modern Physics* **2009**, *81*, 109-162.
(13) Kim, K. S.; Zhao, Y.; Jang, H.; Lee, S. Y.; Kim, J. M.; Kim, K. S.; Ahn, J. H.; Kim, P.; Choi, J. Y.; Hong, B. H. *Nature* **2009**, *457*, 706-710.
(14) Geim, A. K. *Science* **2009**, *324*, 1530-1534.

(15) Dreyer, D. R.; Park, S.; Bielawski, C. W.; Ruoff, R. S. *Chemical Society Reviews* **2010**, *39*, 228-240.
(16) Bae, S.; Kim, H.; Lee, Y.; Xu, X.; Park, J. S.; Zheng, Y.; Balakrishnan, J.; Lei, T.; Ri Kim, H.; Song, Y. I.; Kim, Y. J.; Kim, K. S.; Özyilmaz, B.; Ahn, J. H.; Hong, B. H.; Iijima, S. *Nature Nanotechnology* **2010**, *5*, 574-578.
(17) Schwierz, F. *Nature Nanotechnology* **2010**, *5*, 487-496.
(18) Liang, Y.; Li, Y.; Wang, H.; Zhou, J.; Wang, J.; Regier, T.; Dai, H. *Nature Materials* **2011**, *10*, 780-786.
(19) Novoselov, K. S.; Fal'Ko, V. I.; Colombo, L.; Gellert, P. R.; Schwab, M. G.; Kim, K. *Nature* **2012**, *490*, 192-200.
(20) Bonanni, A.; Chua, C. K.; Zhao, G.; Sofer, Z.; Pumera, M. *ACS Nano* **2012**, *6*, 8546-8551.
(21) Liu, L.; Ryu, S.; Tomasik, M. R.; Stolyarova, E.; Jung, N.; Hybertsen, M. S.; Steigerwald, M. L.; Brus, L. E.; Flynn, G. W. *Nano Lett* **2008**, *8*, 1965-1970.
(22) Wu, H.; Lin, Q.; Batchelor-McAuley, C.; Goncalves, L. M.; Lima, C. F.; Compton, R. G. *Analyst* **2016**, *141*, 2696-2703.
(23) Chen, L.; Li, X.; Tanner, E. E. L.; Compton, R. G. *Chemical Science* **2017**.
(24) Cheng, W.; Compton, R. G. *TrAC Trends in Analytical Chemistry* **2014**, *58*, 79-89.
(25) Lin, Q.; Compton, R. G. *Journal of Physical Chemistry C* **2015**, *119*, 23463-23469.
(26) Kätelhön, E.; Tanner, E. E. L.; Batchelor-McAuley, C.; Compton, R. G. *Electrochimica Acta* **2016**, *199*, 297-304.
(27) Sokolov, S. V.; Eloul, S.; Katelhon, E.; Batchelor-McAuley, C.; Compton, R. G. *Physical Chemistry Chemical Physics* **2017**, *19*, 28-43.
(28) Yoshio, N.; Sumiko, T.; Moore, G.; Moldéus, P. *Biochemical Pharmacology* **1993**, *45*, 1959-1965.
(29) Batsanov, S. S. *Inorganic Materials* **2001**, *37*, 871-885.
(30) Soriaga, M. P.; Hubbard, A. T. *Journal of the American Chemical Society* **1982**, *104*, 2735-2742.
(31) Soriaga, M. P.; Wilson, P. H.; Hubbard, A. T.; Benton, C. S. *Journal of Electroanalytical Chemistry and Interfacial Electrochemistry* **1982**, *142*, 317-336.
(32) Kwok, E. S. C.; Eastmond, D. A. *Chemical Research in Toxicology* **1997**, *10*, 742-749.
(33) Poon, J.; Batchelor-McAuley, C.; Tschulik, K.; Compton, R. G. *Chemical Science* **2015**, *6*, 2869-2876.

Chapter 6

Impact Electrochemistry Reveals that Graphene Nanoplatelets Catalyse the Oxidation of Dopamine *via* Adsorption

Graphene nanoplatelets are shown to electrocatalyse the oxidation of dopamine. Single entity measurements (‘nano-impacts’) coupled with *micro*disc voltammetry and UV-visible spectroscopy reveal that adsorption of dopamine and its oxidised product on the graphene nanoplatelets is the key factor causing the observed catalysis. Generic implications are drawn both for the study of catalysts in general and for graphene nanoplatelets in particular.

The work presented in this Chapter has been published in *Chemical Science*.[1]

6.1 Introduction

Graphene nanoplatelets (GNPs) have been proposed as effective electrocatalysts for various redox processes including some which lie near the heart of energy transformation technology such as solar cells.[2-8] The GNPs are typically applied as layers or ensembles on other electrodes acting as a substrate with the observed electrochemistry showing decreases in the potential required for the oxidation or reduction process of interest.[9] However, the mechanism for GNP catalysis or electrocatalysis has received relatively little attention hitherto.

In the present Chapter, the oxidation of dopamine in aqueous acid in the presence and absence of GNPs is examined with the aim of identifying any catalysis and understanding the origin of this effect in physicochemical terms. Dopamine is used as a model redox active adsorbate which plays important roles in biomedical applications[10] and dye-sensitized solar cells.[11] To this end, the nano-impacts technique is utilised so as to allow the observation of the electrochemistry of dopamine at single GNPs. In this method[12-15] the particles are suspended in solution but from time to time collide with (impact) a microelectrode held at a suitable electrical potential. For the duration of the impact, the conducting particle may act as a tiny electrode with the same potential of the impacted microelectrode and hence electrochemistry can be observed *exclusively* during the duration of the impact if the redox process studied occurs *selectively* on the particle rather than the electrode.[16,17] Thus by careful choice of the electrode material, the electrochemistry at single particles can be observed. In particular if an electrochemical response is seen during the 'nano-impact' and not on the substrate electrode then clearly the process is more favoured—thermodynamically and/or kinetically—on the material of the particle than that of the electrode so providing a very easy, qualitative assessment of the relative catalytic behaviour of the two materials for the process of interest.

Herein the oxidation of dopamine at single entity GNPs with that at glassy carbon (GC) are compared. Further, building on previous work,[6] this Chapter explores the role of adsorption in the observed apparent catalysis and investigates possible causes of this using the nano-impacts technique as already applied to GNPs[18,19] for the observation of their properties including their potential of zero charge (PZC) and their diffusion coefficient in aqueous solution.

6.2 Experimental

6.2.1 Buffer Solution

The buffer solution (pH=0) consisting of 1 M HCl was freshly prepared from hydrochloric acid (37%) and confirmed using a Hannah pH231 pH meter (Hannah, Bedfordshire, UK). It has been reported that dopamine is more stable and water-soluble in the protonated form in acidic environments (pH<2.0),[20] hence all the following experiments were conducted at a pH 0 condition. The buffer was degassed thoroughly with pure nitrogen for 15 min prior to the addition of dopamine to prevent degradation of the solution by atmospheric oxygen.

6.2.2 UV-vis Spectroscopy and Adsorption Measurements

To attain the adsorption isotherm of dopamine on GNPs, UV-vis studies were performed to accurately measure the uptake of dopamine by the GNPs. A known amount of GNPs were mixed with a defined unit volume (1.0 mL) of different concentrations of dopamine solutions. The amount of GNPs used for each dopamine solution was estimated by calculation such that the GNPs used must adsorb at least 20% of dopamine in solution, assuming a full monolayer coverage of dopamine on GNPs. The mixture of GNPs and dopamine solution was then sonicated (FB15050, Fisher Scientific, 50/60 Hz, 80W, Germany) for 35 min to allow full adsorption, followed by centrifugation (Eppendorf

Centrifuge 5430 R) for 10 min at 14000 rpm. The original dopamine solution prior to adsorption and the supernatant after adsorption were both diluted and examined by UV-vis spectroscopy. The UV-vis absorbance was recorded from 400–220 nm.

6.2.3 Preparation of GNP Suspensions for Nano-impact Experiments

The suspension of 3.3×10^{-13} M unmodified GNPs was prepared as described in Chapter 3. Dopamine modified GNPs suspensions were also prepared. For modified GNP suspensions *via* pre-exposure, the unmodified GNPs were first sonicated in the buffer solution prior to the addition of dopamine and left for different time for exposure. For modified GNP suspensions *via* sonication, the unmodified GNPs were sonicated in dopamine solutions for 25 mins to generate evenly dispersed suspensions and promote the adsorption. The above suspensions were used as stock suspensions, and diluted for nano-impact experiments. Fresh stock suspensions were prepared daily.

6.2.4 Electrochemical Measurements

For voltammetric measurements, a carbon *micro*disc electrode (26.5 μm radius, calibrated electrochemically as described in Chapter 3) or a glassy carbon *macro*electrode (GC, 3 mm diameter) was used as the working electrode. Cyclic voltammetry (CV) was conducted at selected scan rates of between 25 mVs^{-1} to 1000 mVs^{-1} in degassed pH 0 buffer solutions containing variable concentrations of dopamine.

For nano-impact and chronoamperometry, the same carbon *micro*disc electrode was used as a working electrode. Note that the potentiostat used in this work accurately conserves the charge transferred due to a particle-impact process.[14,21] 4.5 mL of buffer solution was nitrogen degassed for 5 min to remove dissolved oxygen and 500 μL of unmodified GNPs stock suspension was then added while the nitrogen was kept bubbling for further 5 s to get an even suspension, followed by immediate chronoamperometric

scans. For catalytic nano-impact experiments with the present of dopamine, a known concentration of dopamine was used with adding of unmodified or modified GNPs.

6.3 Results and Discussion

This section first reports the adsorption of dopamine (DA) on graphene nanoplatelets (GNPs), characterised by UV-vis spectroscopy. Second, solution phase voltammetry of DA on carbon electrodes was undertaken, followed third, by use of the nano-impact methodology to investigate the oxidation of DA at single GNPs.

6.3.1 Adsorption of Dopamine on GNPs

The adsorption of DA on GNPs was first studied by UV-vis spectroscopy. 1 mL of DA solution was mixed with GNPs and sonicated for 35 min to realise a full adsorptive uptake, followed by centrifugation. The amount of DA immobilized on the GNPs was quantified by examining the original DA solution before adsorption and the supernatant after adsorption *via* UV-vis spectroscopy. A linear Beer–Lambert plot was obtained with the extinction coefficient (ε) of (0.25 ± 0.004) M^{-1} m^{-1} illustrating the relationship between absorbance and DA concentration, as shown in Figure 6.1.

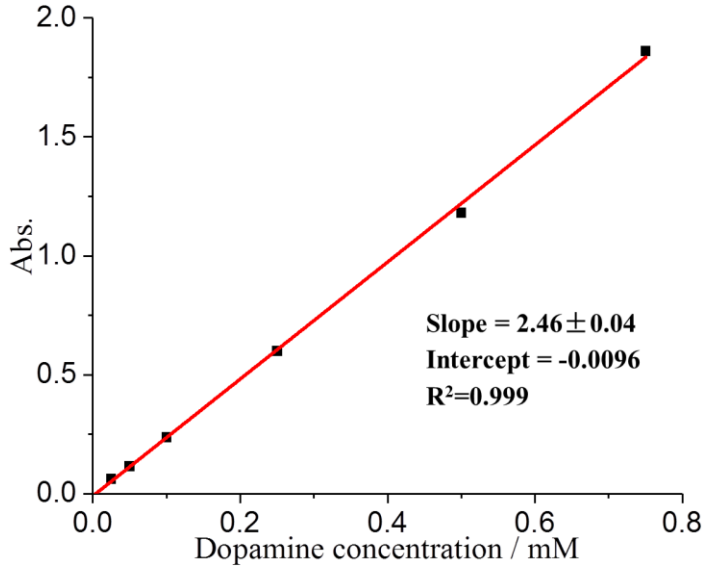


Figure 6.1. Beer–Lambert plot of dopamine in buffer (pH=0).

As shown in Figure 6.2a, the absorbance peak of dopamine in aqueous solution is at 279 nm, in good agreement with literature.[22] It is evident that the reduction in magnitude of absorbance peak results from the adsorption onto GNPs. The adsorption isotherm of dopamine for GNPs in aqueous buffer was then plotted as shown in Figure 6.2b. The presence of two distinct plateaux suggests a flat to vertical concentration driven phase transition[23,24] of DA molecules adsorbed on GNPs, corresponding respectively to a flat molecular orientation at low concentrations (≤200 mM), and a vertical orientation of DA molecules at higher concentrations (≥353 mM). This was confirmed by comparing the average area occupied by each individual molecule ($S_{R\text{-}DA}$) on GNPs with the theoretical estimated area of the molecule in each possible orientation. As illustrated in Figure 6.2c, the theoretical areas of DA were determined by approximating the DA molecule as a rectangular box with all side lengths estimated by trigonometry for bond lengths, bond angles (obtained from ChemDraw 15.1) and van de Waals radii of terminating atoms (tabulated by Rowland).[25] The molecule area of flat view (S_{DA}) and of edgewise view (S'_{DA}) hence are estimated as 6.5×10^{-15} cm^2 and 3.6×10^{-15} cm^2, respectively, in agreement with literature.[26] In the dopamine isotherm, the amount of DA adsorbed by a unit amount of GNPs reaches the first plateau at adsorbate concentrations approaching 200 mM with a limiting uptake of 1.7×10^{-7} mol mg^{-1}, giving the maximum surface coverage (Γ_{max}) of $(2.6 \pm 0.8) \times 10^{-10}$ mol cm^{-2} and the average area occupied by each individual molecule ($S_{R\text{-}DA}$) of $(6.4 \pm 1.5) \times 10^{-15}$ cm^2 consistent with the flat dopamine molecule area. The second plateau occurs at concentrations approaching 400 mM with a limiting uptake of 2.7×10^{-7} mol mg^{-1}, $\Gamma'_{max} = (4.3 \pm 1.3) \times 10^{-10}$ mol cm^{-2} and $S'_{R\text{-}DA} = (3.8 \pm 0.9) \times 10^{-15}$ cm^2, in good agreement with the edgewise (vertical) molecule area. It is also notable that the phase transition of dopamine is less abrupt and the second plateau is reached only

at considerably higher adsorbate concentrations as compared with catechol,[23] in excellent agreement with Hubbard's observation of the adsorption of dopamine on platinum.[27]

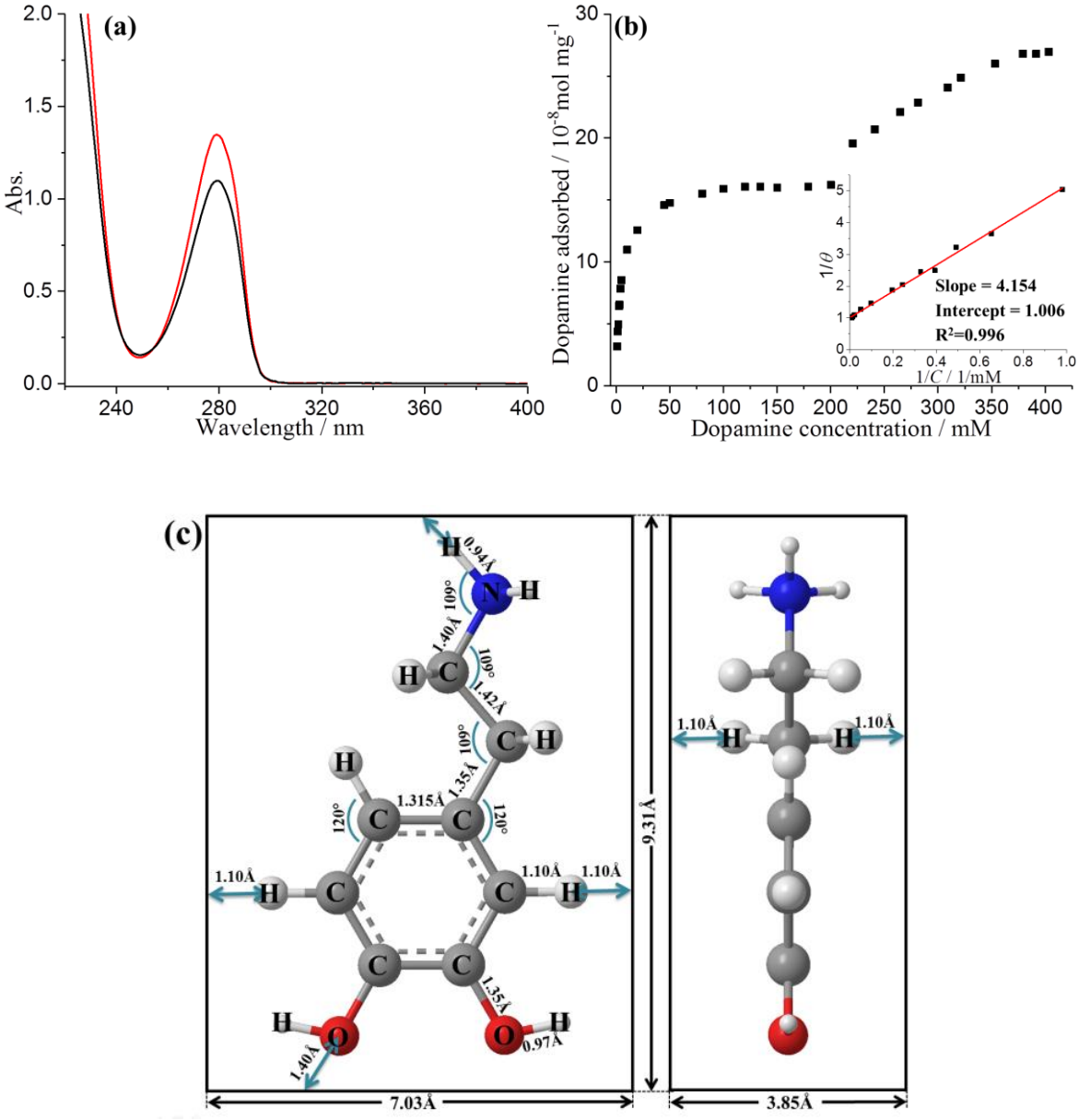


Figure 6.2. (a) UV-vis absorption of a pH 0 solution containing 5 mM dopamine before GNPs adsorption (red line) and after adsorption (black line); Dilution factor = 10. (b) Dopamine adsorption isotherm for GNPs in pH 0 buffer. Inset: Langmuir plot of dopamine on GNPs in pH 0 buffer, where Θ is the fractional surface coverage and C is the adsorbate concentration, Langmuir adsorption model applies when the DA concentration is lower than 200 mM. (c) Rectangular box model of dopamine molecule for flat view (left) and edgewise view (right).

The low concentration region (≤ 200 mM) was then analysed in terms of Langmuir model, which predicts the fractional coverage, Θ, to vary with adsorbate concentration, C,

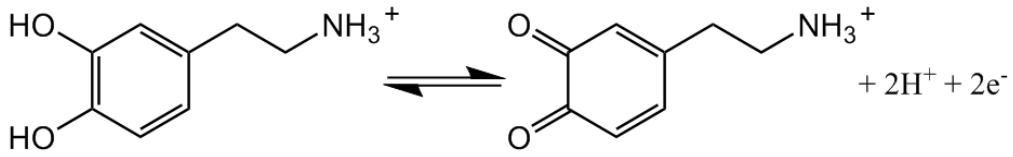
$$\theta = \frac{KC}{1+KC} \tag{6.1}$$

where $\Theta = \Gamma/\Gamma_{max}$ and Γ is the coverage corresponding to the adsorbate concentration. As shown in Figure 6.2b inset, a straight line with intercept of 1.006 and R^2 = 0.996 is obtained indicating excellent agreement with the Langmuir model, suggesting that the adsorption is reversible. Furthermore, the adsorption constant (K) was estimated from the reciprocal of the slope, giving (0.24 ± 0.004) mM^{-1}.

6.3.2 Oxidation of Dopamine on *Micro* and *Macro* Carbon Electrodes

Next, the oxidation of DA in aqueous acid in the presence and absence of GNPs was examined electrochemically. The cyclic voltammetric responses of bare *micro*disc carbon electrodes (radius 26.5 μm) were first recorded in pH 0 buffer solution (1.0 M HCl) containing variable DA concentrations (from 0 to 10 mM) at scan rates of 25 mV s^{-1} to 1000 mV s^{-1}. As depicted in Figure 6.3, the half-wave potential ($E_{1/2}$) of the voltammograms is independent of DA concentration with a constant value of ca. +0.64 V *vs.* SCE across the range of scan rates, suggesting the electrochemical reversibility of the process. Moreover, literature suggests that the voltammetric responses likely correspond to a two-electron, two-proton oxidation of DA[28] (Scheme 6.1). Note that the amine group is protonated in the pH 0 environment.[29]

Scheme 6.1. Two-electron, two-proton oxidation of dopamine.



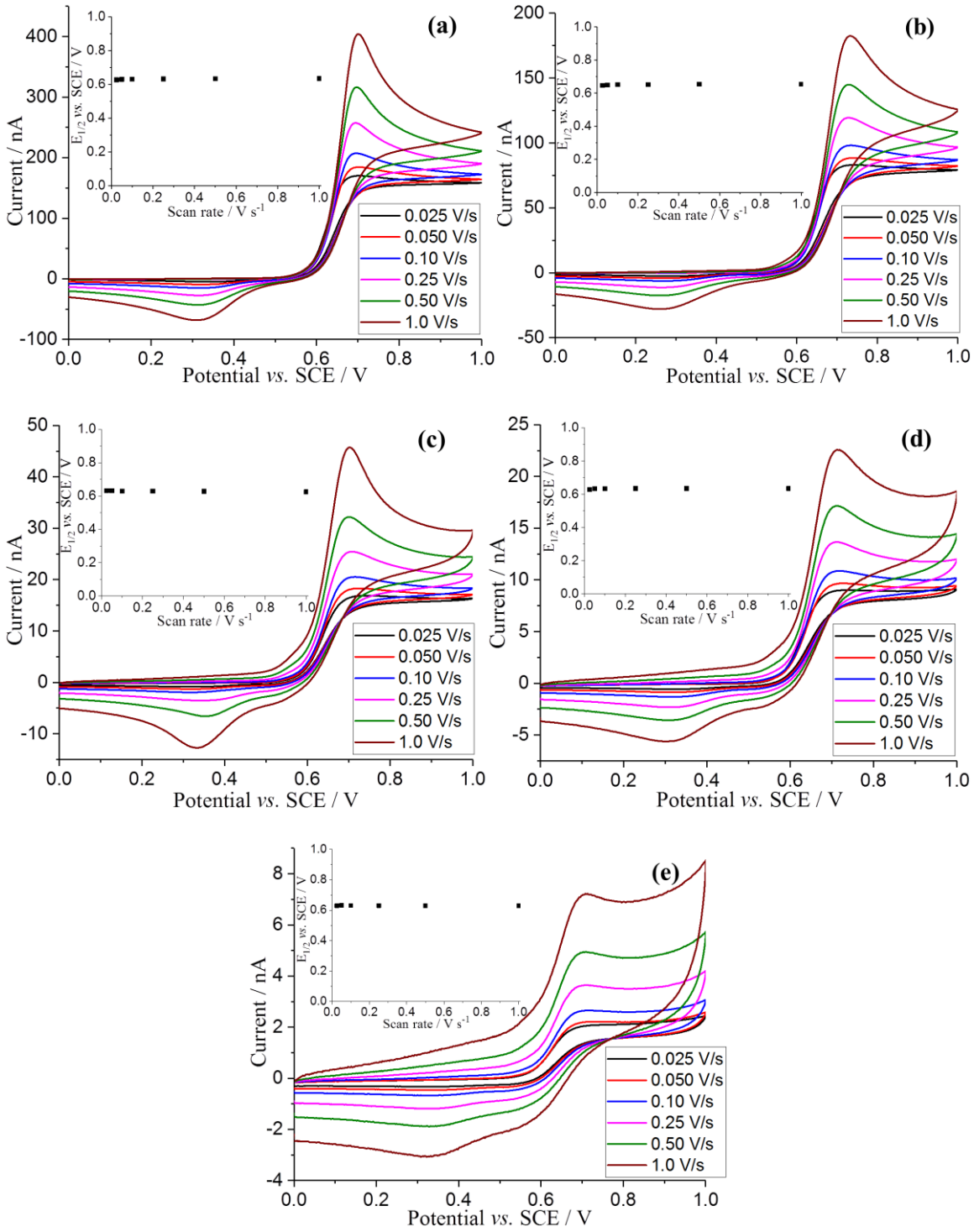


Figure 6.3. Cyclic voltammograms of a bare *micro*disc carbon electrode in pH 0 buffer solution containing variable concentrations of dopamine recorded as a function of scan rate from 25 mV s^{-1} to 1000 mV s^{-1}. Inset: the plot of half-wave potential as a function of the scan rate. (a) 10 mM DA, (b) 5 mM DA, (c) 1 mM DA, (d) 0.5 mM DA and (e) 0.1 mM DA.

Figure 6.4a compares the *micro*disc voltammetric responses in variable concentrations of DA solutions. The magnitude of the steady-state limiting current (I_{ss}) of a diffusion-

controlled process, assuming that all of DA molecules that diffuse to the electrode surface undergo oxidation, is described by:

$$I_{ss} = 4nFDCr \tag{6.2}$$

where n = 2 (the number of electrons transferred), F is the Faraday constant, D is the diffusion coefficient of DA, C is the bulk concentration of DA, and r is the radius of the working electrode.

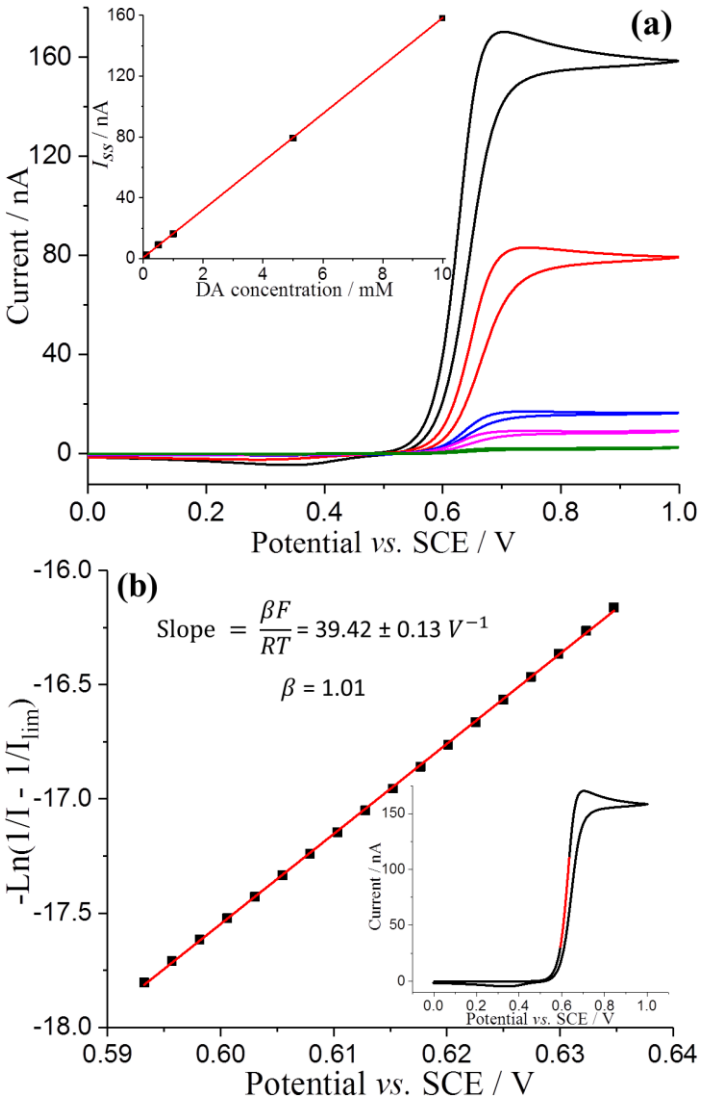


Figure 6.4. (a) Voltammograms of a bare *micro*disc carbon electrode in pH 0 buffered solution containing variable concentration of DA (10 mM, black; 5 mM red; 1 mM blue; 0.5 mM magenta; 0.1 mM green) at a scan rate of 25 mV s^{-1}. Inset shows the linear correlation of limiting current (I_{ss}) as a function of DA concentration. (b) Mass-transfer corrected Tafel analysis for voltammogram of a bare *micro*disc carbon electrode in 10 mM dopamine at scan rate of 25 mV s^{-1}. The highlighted red region in inset voltammograms was selected as the Tafel analysis region.

Study of the recorded I_{ss} as a function of DA concentration allows a good estimation of the DA diffusion coefficient. From the slope of the limiting current (I_{ss}) against DA concentration (Figure 6.4a inset), the diffusion coefficient of DA was determined as (7.70 ± 0.02) × 10^{-10} $m^2 s^{-1}$, in good agreement with previous reports.[30,31]

The experimental voltammetry was next analysed using Tafel analysis.[32,33] To enable an accurate measurement of the apparent oxidative transfer coefficient (β), a mass transport corrected analysis[34,35] for the voltammetry measured on the *micro*disc was performed by taking the reciprocal of the experimental current with the reciprocal of the limiting current subtracted $(\frac{1}{I} - \frac{1}{I_{lim}})$, as shown in Figure 6.4b. It is necessary to correct the Tafel analysis to take into account mass transport for the voltammetry on a *micro*electrode to separate out the electron transfer kinetics from the diffusion. The apparent β value determined from the slope is close to unity, suggesting, at first sight, that the process is a one electron reversible reaction.[36]

To reconcile the *micro*electrode observations, analogous experiments were then conducted with a glassy carbon *macro*electrode. The resultant voltammogram showed a single oxidative peak at ca. +0.61 V *vs.* SCE and a reductive peak at ca. +0.41 V *vs.* SCE (Figure 6.5a black line). The peak current was found to be directly proportional to the square root of scan rate, as shown in Figure 6.5a inset, suggesting again that the electrochemical process is diffusion controlled. Note that the peak to peak separation is not consistent with a simple one or two electron transfer, reversible or irreversible, suggesting more complex chemistry on the longer timescale of the *macro*electrode experiments. In particular the oxidative peak potential shows only a weak scan rate dependence suggesting a reversible process while the reductive peak looks irreversible in character. The existence of follow up chemistry is also indicated by the less positive oxidative peak potential seen

on the *macro*electrode as compared to the half-wave potential on the *micro*electrode. This indicates a reversible electron transfer followed by a fast irreversible chemical reaction. Below the *macro*electrode voltammetry is interpreted in terms of an ECE process so that the back peak is unrelated to the DA/DA^{2+} couple and the lowered potential on the *macro*electrode is consistent with a fast chemical reaction following an electrochemically reversible process.

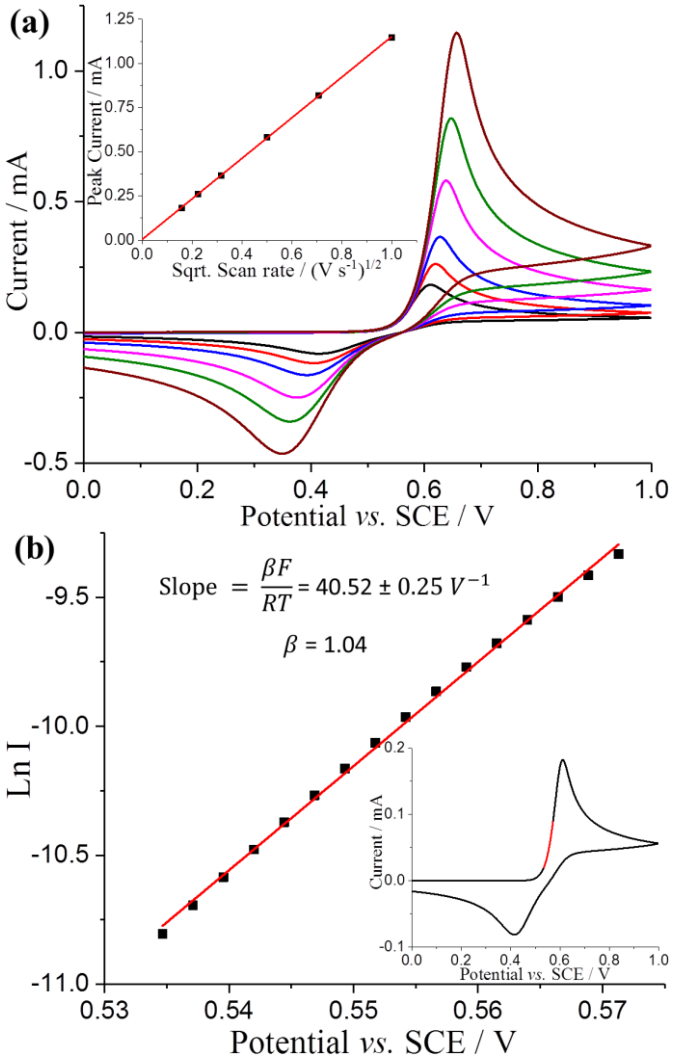


Figure 6.5. (a) Voltammograms of a bare glassy carbon *macro*electrode in pH 0 buffer solution containing 10 mM DA recorded as a function of scan rate (25 mV s^{-1}, black line; 50 mV s^{-1}, red line; 100 mV s^{-1}, red line; 250 mV s^{-1}, magenta line; 500 mV s^{-1}, green line; 1000 mV s^{-1}, brown line). Inset: the plot of peak current as a function of the square root of the scan rate from 25 mV s^{-1} to 1000 mV s^{-1}. (b) Tafel analysis for voltammogram of a bare glassy carbon *macro*electrode in 10 mM dopamine at a scan rate of 25 mV s^{-1}. The highlighted red region in inset voltammograms was selected as the Tafel analysis region.

The voltammetry on the *macro*electrode is peak shaped, hence a simple Tafel analysis of *Ln I* versus *E* was performed, but using the part of voltammogram where diffusion plays a near negligible role (Figure 6.5b and inset). β from Figure 6.5b also has value close to unity, suggesting again that the rate determining step comprises a one electron reversible process. This leads the conclusion that overall the oxidation of dopamine is an $E_{rev}CE$ process, whereby the first electron transfer is electrochemically reversible and the second electron is fully "driven". This mechanism has been fully explored in the follow-up work[37] *via* experiment and simulation concluding that oxidation of dopamine in strongly acidic (pH = 0) condition shows a behaviour consistent with an ECE process with a fast chemical step and in which the second electron transfer is thermodynamically more favourable than the first step.

6.3.3 Oxidation of Dopamine on Single GNPs

The nano-impact method was applied to enable the investigation of the oxidation of dopamine at single GNPs. A carbon *micro*disc electrode was immersed in a degassed pH 0 buffer solution (1.0 M HCl), and known amounts of dispersed GNPs were added. In the absence of DA, under potentiostatted conditions, clear but small oxidative (capacitative) current spikes at +0.55 V *versus* SCE were detected (Figure 6.6a, black). The polarity of the GNPs current spikes[18] was found to be changed upon alteration of the applied potential to +0.40 V (Figure 6.7), confirming the spikes correspond to capacitative impacts of GNPs. Another control experiment was conducted with no GNPs in the solution; no spikes were detected, further confirming that the occurrence of spikes results from collisions of GNPs with the electrode (Figure 6.8). A potential variation study was then performed and chronoamperograms were recorded at different potentials, from +0.35 to +0.60 V. A plot of average charge of individual capacitative impacts as a function of potential was obtained, as illustrated in Figure 6.6b (black squares). The polarity of the spikes changes as

a function of potential, consistent with capacitative behaviour. The potential of zero charge (PZC) of GNPs in pH 0 buffer was determined as +0.51 V, as shown in Figure 6.9. The PZC of GNPs in pH 0 buffer is larger than in 0.1 M KCl, 50 mM KH_2PO_4, 50 mM K_2HPO_4 PBS buffer (−0.14 V, pH=6.8),[18] consistent with the pH dependence of the PZC.[38]

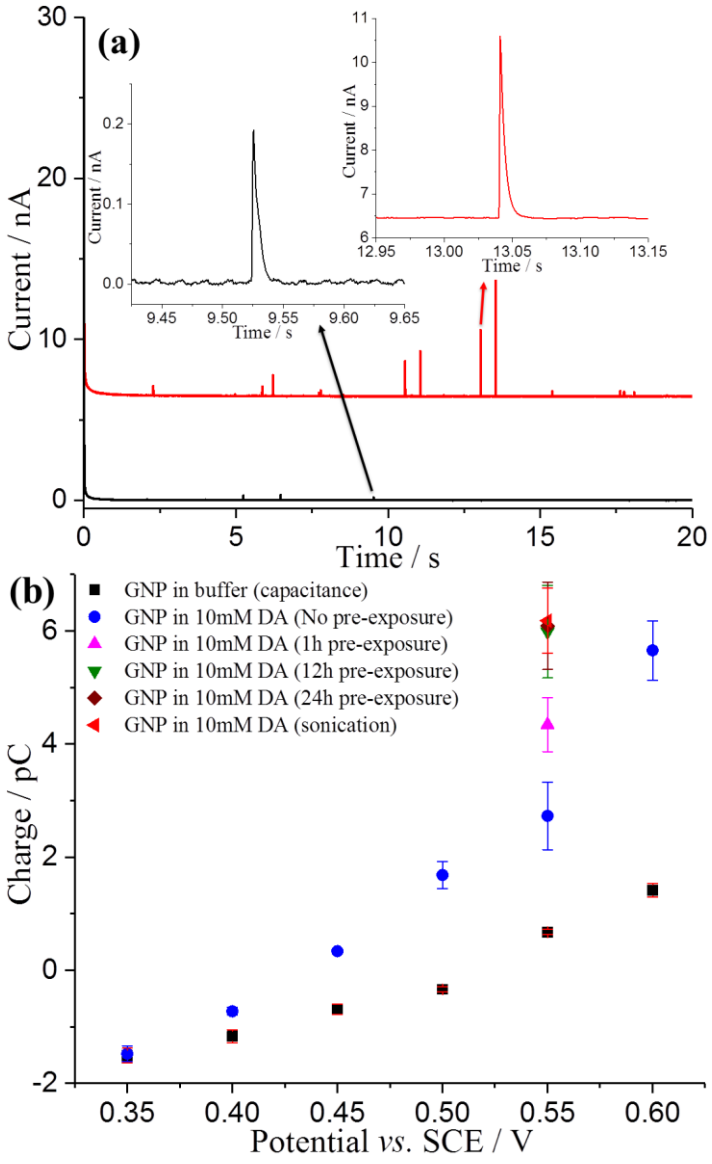


Figure 6.6. (a) Representative chronoamperometric profiles of nano-impact at +0.55 V versus SCE in pH 0 buffer containing: GNPs only (black line); DA-saturated GNPs (modified *via* sonication) and 10 mM DA (red line). (b) Variable potential study of single GNPs: GNPs in buffer only (black), GNPs (no pre-exposure) and 10 mM dopamine (blue). GNPs modified *via* pre-exposure (different exposures time) and sonication in 10 mM DA solutions were also measured at +0.55 V. The error bars are derived from SD/$(n)^{1/2}$, where SD is the standard deviation and n is the number of the spikes.

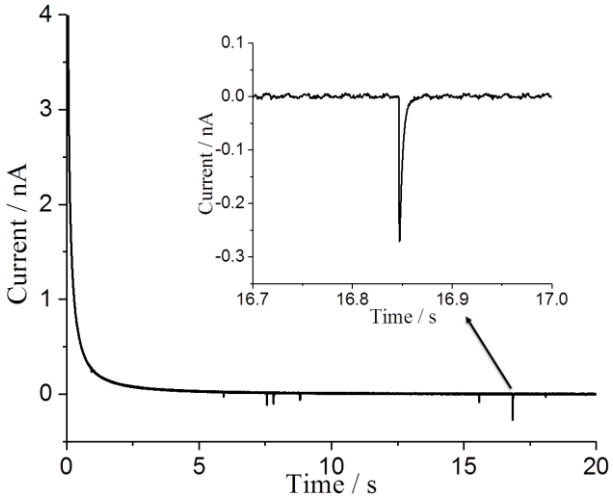


Figure 6.7. Representative chronoamperometric profiles of nano-impacts at +0.40 V versus SCE in pH 0 buffer containing GNPs only.

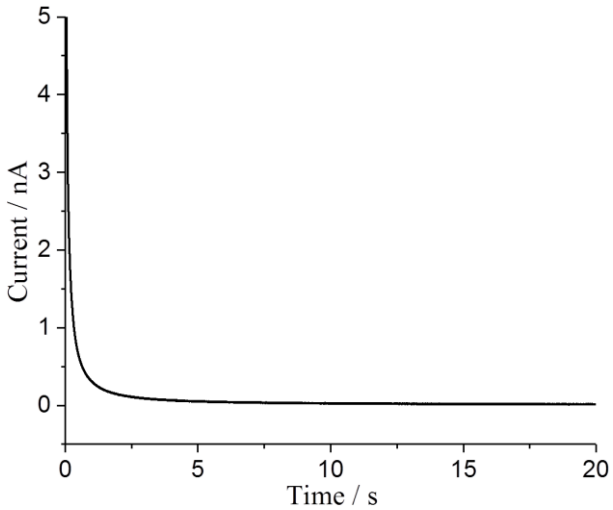


Figure 6.8. Representative chronoamperometric profiles of nano-impacts at +0.55 V versus SCE in pH 0 buffer without addition of GNPs suspensions.

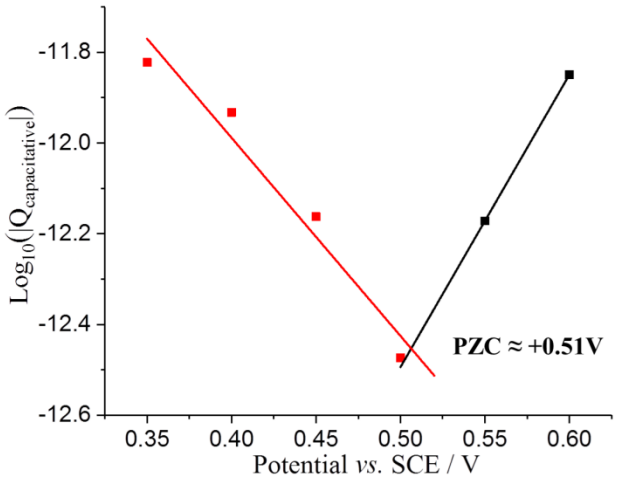


Figure 6.9. Capacitative impacts with absolute charge in logarithmic (log_{10}) scale plotted against applied potential (vs. SCE). Red squares: values with negative charge; black squares: values with positive charge. The intersection potential of the two lines is used to estimate the PZC value of GNPs, where PZC is determined to be +0.51 V (vs. SCE) under pH 0 conditions.

Analogous nano-impacts experiments of GNPs were conducted in buffer solution containing 10 mM DA. At lower potentials (negative of +0.40 V), the amplitudes of the spikes were similar to those seen without DA, whereas the amplitudes of the spikes increased significantly when the applied potential more positive than +0.45 V (Figure 6.6), suggesting that DA is involved in charge transfer and oxidised when a single GNP collides with the electrode at a sufficiently high potential. To further investigate the oxidation reaction of DA catalysed by GNPs, the average charge of individual spikes at a range of potentials was determined and then plotted as a function of potentials (Figure 6.6b, blue circles). Comparing this to the capacitative behaviour of single GNPs seen in the absence of DA (black squares), the average charge at each potential is significantly larger at potentials above +0.45 V, indicating that at sufficiently positive potentials the oxidation of DA accompanied the capacitative charge of single GNPs, contributing to the injection of the measured charge when individual GNPs collide with the electrode. Figure 6.10b compares the potential dependence of the impact charge with the voltammetry seen for 10 mM DA on the carbon *micro*disc electrode in the absence of GNPs. It is apparent that the GNPs likely catalyse the oxidation since appreciable currents flow at potential where DA is not electroactive on glassy carbon. The DA oxidation may likely result from adsorbed DA molecules on GNPs rather than free molecules in aqueous phase, which was further investigated by experiments conducted in 10 mM DA solution with GNPs modified with 10 mM DA solution by pre-exposure or sonication (Figure 6.6b). The impact charge of GNPs at +0.55 V increased with an increasing exposure time in the DA solution and saturated for 12 h or longer pre-exposure and sonication in the DA solution, confirming the oxidation of adsorbed DA on GNPs. Potential variation studies were then conducted with DA-saturated GNPs in 10 mM DA solution (Figure 6.10a, red dots). The spike shapes

were analysed statistically (Table 6.1), showing the majority has a sharp on-and-off shape corresponding to single GNP colliding with and leaving the electrode.

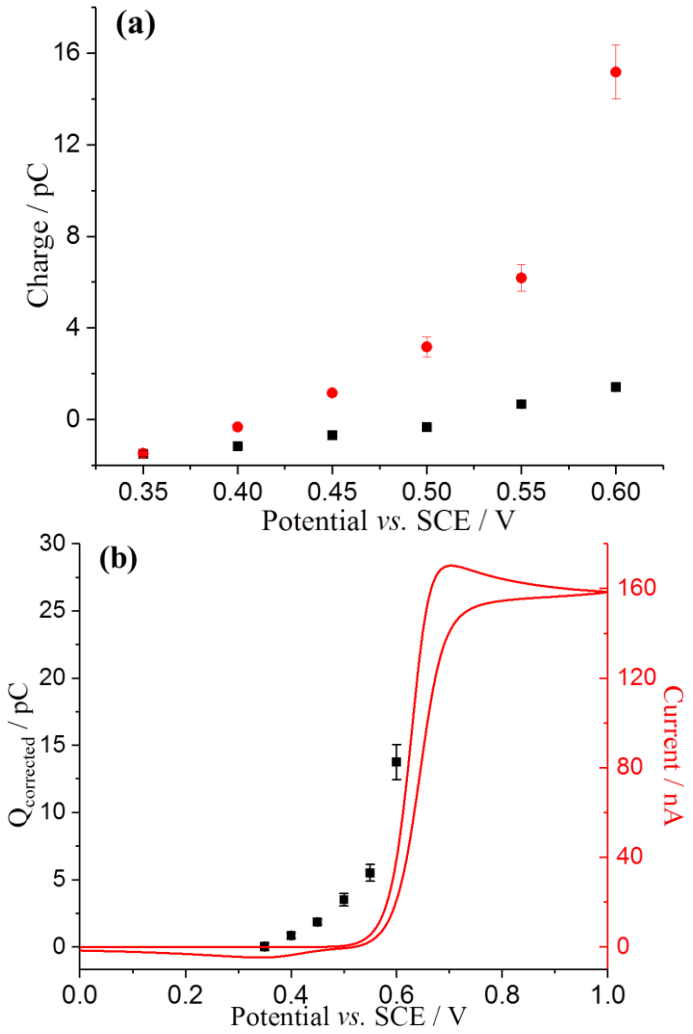


Figure 6.10. (a) Variable potential study of single GNPs: GNPs only (black), DA-saturated GNPs (modified *via* sonication) and 10 mM dopamine (red). The error bars are derived from SD/$(n)^{1/2}$, where SD is the standard deviation and n is the number of the spikes. (b)Voltammogram of a *micro*disc carbon electrode in pH 0 buffered solution containing 10mM dopamine at a scan rate of 25 mV s^{-1}. Overlayed squares are the average corrected charge transferred per individual impact spike ($Q_{correct} = Q_{total} - Q_{capacitative}$) of GNPs at a *micro*disc electrode.

Table 6.1. Statistics of spike shape of DA-saturated GNPs (modified via sonication) in 10mM of DA at different potentials.

Potentials	+0.35V	+0.40V	+0.45V	+0.50V	+0.55V	+0.60V
NOT Sharp	7	6	6	4	3	1
Total	248	146	170	213	193	112
% of Sharp	97%	96%	97%	98%	99%	99%

To further confirm the catalysis of DA oxidation by GNPs, the corrected charge transferred per individual impact spike (corresponding to the Faradaic charge) was calculated and compared with the voltammetric response of DA in solution phase at the same *micro*disc electrode. The switch on potential of DA oxidation decreases from ca. +0.55 V vs. SCE in the solution phase (Figure 6.10b, red line) to ca. +0.40 V in the adsorbed DA on GNPs (Figure 6.10b, black squares). The origin of this potential shift of ca. 120 mV likely reflects the fact that the product (dopamine-*o*-quinone) is more strongly adsorbed on GNPs than on the *micro*disc electrode, resulting in a more favoured oxidation of DA, since if both the GNP and *micro*disc signals were solution phase processes the greater mass transport rate to/from the GNPs would shift the potential to more positive potentials which is the opposite of what is observed.

Comparing the surface coverage of adsorbed DA on GNPs from UV-vis with the surface coverage of oxidised product on GNPs after impact (see Tables 6.2-3), a partial oxidation of adsorbed DA on GNPs occurs at low overpotentials. As shown in Figure 6.11a, the percentage of oxidation was determined and shown to increase progressively with the potential. Analogous nano-impacts experiments were conducted in different DA concentrations at +0.55 V to compare the percentage of oxidation of adsorbed DA on GNPs with variable surface coverage corresponding to DA solution concentration. Figure 6.11b shows that even at variable concentrations of dopamine (and therefore different surface coverages), a consistent 5.6 ± 0.5 % of the dopamine undergoes oxidation. The partial oxidation of DA suggests that the oxidation blocks further movement of electrons through the platelet, indicating that the electrons possibly transfer around the surface of instead of through the GNPs, as shown in Scheme 6.2 and that the adsorbed oxidised product prevents further charge transfer either across the GNP surface or from the electrode.

Table 6.2. Percentage of oxidation of the adsorbed dopamine during the impact at different potentials.

Potential (V)	Γ from UV-Vis of 10mM DA-GNPs (mol / mg of GNP)	Γ from Impact (mol / mg of GNP)	Percentage of oxidation (%)
+0.35	11.4×10^{-8}	$(3.30 \pm 1.60) \times 10^{-11}$	0.03 ± 0.01
+0.40	11.4×10^{-8}	$(9.17 \pm 0.27) \times 10^{-10}$	0.80 ± 0.02
+0.45	11.4×10^{-8}	$(2.02 \pm 0.11) \times 10^{-9}$	1.8 ± 0.1
+0.50	11.4×10^{-8}	$(3.82 \pm 0.46) \times 10^{-9}$	3.4 ± 0.4
+0.55	11.4×10^{-8}	$(5.99 \pm 0.56) \times 10^{-9}$	5.3 ± 0.5
+0.60	11.4×10^{-8}	$(1.50 \pm 0.12) \times 10^{-8}$	13.1 ± 1.0

Table 6.3. Percentage of oxidation of the adsorbed dopamine for different dopamine concentrations during the impact at +0.55 V.

DA Concentration (mM)	Γ from UV-Vis (mol / mg of GNP)	Γ from Impact at E = 0.55V (mol / mg of GNP)	Percentage of oxidation (%)
5	8.84×10^{-8}	$(4.96 \pm 0.56) \times 10^{-9}$	5.6 ± 0.6
10	11.4×10^{-8}	$(5.99 \pm 0.56) \times 10^{-9}$	5.3 ± 0.5
20	13.0×10^{-8}	$(7.73 \pm 0.65) \times 10^{-9}$	5.9 ± 0.5

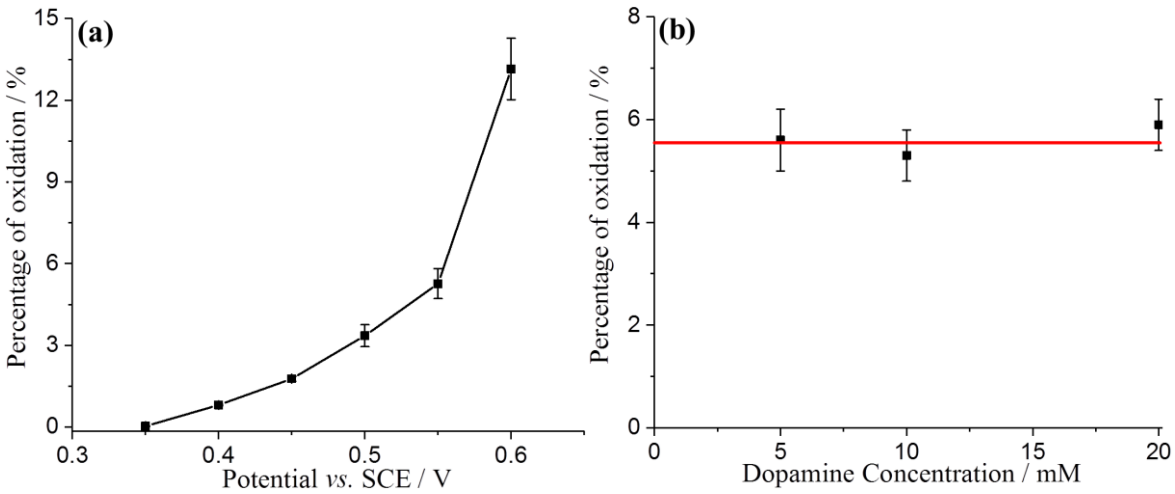
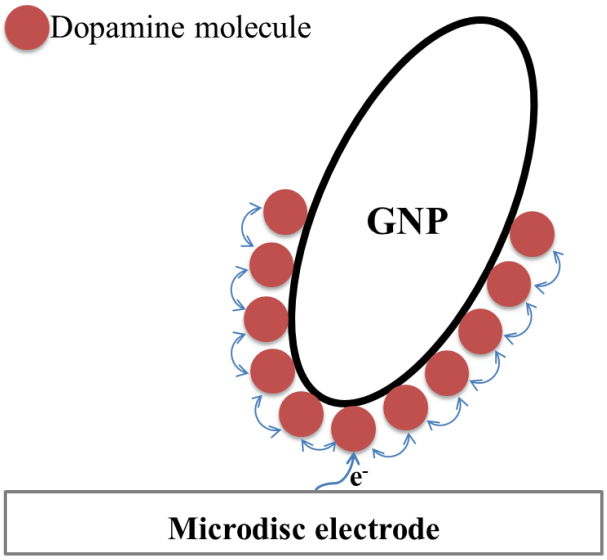


Figure 6.11. The percentage of adsorbed dopamine on GNPs oxidised during the impact between GNPs and electrode as a function of (a) applied potential; (b) dopamine concentration.

Scheme 6.2. Model of charge diffusion over the surface of GNPs.



Tafel analysis was then performed with the nano-impact data to derive the oxidative transfer coefficient (β) for the adsorbed DA oxidation. The impact current (I) can be estimated by $I = Q/t$, where Q is the average Faradaic charge and t is the average impact duration, as shown in Table 6.4. As shown in Figure 6.12, In I was plotted as a function of potential, resulting in a linear slope with a value of 13.70 ± 0.78 V^{-1}. The transfer coefficient, β, can hence be estimated as 0.35 ± 0.02, suggesting the oxidation of adsorbed species on GNP is not reversible and undergoes slow electron transfer kinetics. This further confirms the fact that the spikes in current occur as a result of adsorbed dopamine at a lower potential rather than the solution phase dopamine (as is seen on the *micro* and *macro* disc electrodes), allowing the GNPs to catalyse the dopamine oxidation.

Table 6.4. Summary of the average impact duration and corresponding error of mean (derived from SD/$(n)^{1/2}$, where SD is the standard deviation and n is the number of the spikes) at different potentials.

Potentials	+0.35V	+0.40V	+0.45V	+0.50V	+0.55V	+0.60V
Impact time (ms)	25.1	23.2	25.7	23.9	24.8	24.3
Error of mean (ms)	1.5	1.9	1.9	1.9	1.3	1.6

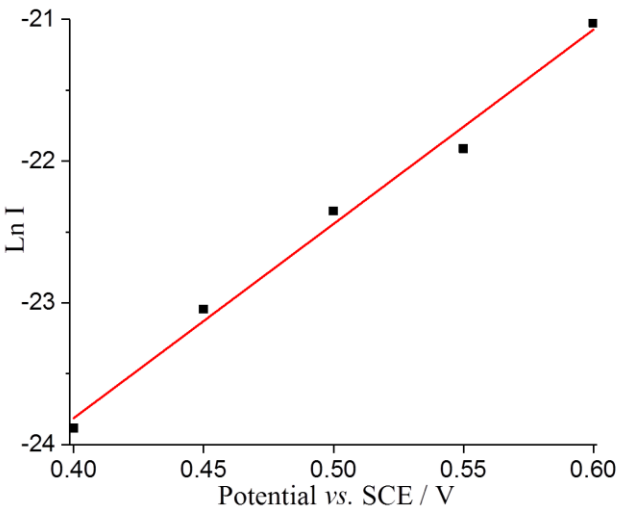


Figure 6.12. Tafel analysis from nanoimpacts comparing the current of the nanoimpact at different potentials.

6.4 Conclusions

Graphene nanoplatelets were modified with dopamine to allow the investigation of dopamine oxidation at a single GNP by nano-impacts. Compared with solution phase voltammetry on carbon *micro* and *macro* disc electrodes whereby the electron transfer is reversible, the irreversible oxidation of dopamine onset at ca. +0.40 V for adsorbed dopamine (vs ca. +0.55 V vs. SCE for solution phase dopamine). This catalysis is attributed to the increased affinity for the oxidative product, dopamine-*o*-quinone, for the nanoplatelet over the larger electrodes. A model was proposed to explain the incomplete oxidation of the adsorbed dopamine, whereby electron transfer is restricted to surface molecules.

Bibliography

(1) Chen, L.; Tanner, E. E. L.; Lin, C.; Compton, R. G. *Chemical Science* **2018**, *9*, 152-159.
(2) Kavan, L.; Yum, J.-H.; Grätzel, M. *Nano Lett* **2011**, *11*, 5501-5506.
(3) Kavan, L.; Yum, J.-H.; Nazeeruddin, M. K.; Grätzel, M. *ACS Nano* **2011**, *5*, 9171-9178.
(4) Ju, M. J.; Kim, J. C.; Choi, H.-J.; Choi, I. T.; Kim, S. G.; Lim, K.; Ko, J.; Lee, J.-J.; Jeon, I.-Y.; Baek, J.-B.; Kim, H. K. *ACS Nano* **2013**, *7*, 5243-5250.
(5) Ju, M. J.; Jeon, I.-Y.; Lim, K.; Kim, J. C.; Choi, H.-J.; Choi, I. T.; Eom, Y. K.; Kwon, Y. J.; Ko, J.; Lee, J.-J.; Baek, J.-B.; Kim, H. K. *Energy & Environmental Science* **2014**, *7*, 1044-1052.
(6) Poon, J.; Lin, Q.; Batchelor-McAuley, C.; Salter, C.; Johnston, C.; Compton, R. G. *Journal of Physical Chemistry C* **2015**, *119*, 13777-13784.
(7) Yang, Y.; Han, C.; Jiang, B.; Iocozzia, J.; He, C.; Shi, D.; Jiang, T.; Lin, Z. *Materials Science and Engineering: R: Reports* **2016**, *102*, 1-72.
(8) Ju, M. J.; Jeon, I.-Y.; Kim, H. M.; Choi, J. I.; Jung, S.-M.; Seo, J.-M.; Choi, I. T.; Kang, S. H.; Kim, H. S.; Noh, M. J.; Lee, J.-J.; Jeong, H. Y.; Kim, H. K.; Kim, Y.-H.; Baek, J.-B. *Science Advances* **2016**, *2*.
(9) Goh, M. S.; Pumera, M. *Analytical Chemistry* **2010**, *82*, 8367-8370.
(10) Hornykiewicz, O. *Pharmacological reviews* **1966**, *18*, 925-964.
(11) Nam, H. J.; Kim, B.; Ko, M. J.; Jin, M.; Kim, J. M.; Jung, D.-Y. *Chemistry – A European Journal* **2012**, *18*, 14000-14007.
(12) Cheng, W.; Compton, R. G. *TrAC Trends in Analytical Chemistry* **2014**, *58*, 79-89.
(13) Robbs, P. H.; Rees, N. V. *Physical Chemistry Chemical Physics* **2016**, *18*, 24812-24819.
(14) Sokolov, S. V.; Eloul, S.; Katelhon, E.; Batchelor-McAuley, C.; Compton, R. G. *Physical Chemistry Chemical Physics* **2017**, *19*, 28-43.
(15) Pumera, M. *ACS Nano* **2014**, *8*, 7555-7558.
(16) Li, X.; Batchelor-McAuley, C.; Shao, L.; Sokolov, S. V.; Young, N. P.; Compton, R. G. *Journal of Physical Chemistry Letters* **2017**, *8*, 507-511.
(17) Peljo, P.; Manzanares, J. A.; Girault, H. H. *Langmuir* **2016**, *32*, 5765-5775.
(18) Poon, J.; Batchelor-McAuley, C.; Tschulik, K.; Compton, R. G. *Chemical Science* **2015**, *6*, 2869-2876.
(19) Lin, Q.; Lin, C.; Wu, H.; Batchelor-McAuley, C.; Compton, R. G. *Journal of Physical Chemistry C* **2016**, *120*, 20216-20223.
(20) Carter, J. E.; Johnson, J. H.; Baaske, D. M. *Analytical Profiles of Drug Substances* **1982**, *11*, 257-272.
(21) Kätelhön, E.; Tanner, E. E. L.; Batchelor-McAuley, C.; Compton, R. G. *Electrochimica Acta* **2016**, *199*, 297-304.
(22) López, T.; Bata-García, J. L.; Esquivel, D.; Ortiz-Islas, E.; Gonzalez, R.; Ascencio, J.; Quintana, P.; Oskam, G.; Álvarez-Cervera, F. J.; Heredia-López, F. J.; Góngora-Alfaro, J. L. *International Journal of Nanomedicine* **2011**, *6*, 19-31.
(23) Chen, L.; Li, X.; Tanner, E. E.; Compton, R. G. *Chemical Science* **2017**, *8*, 4771-4778.
(24) Chen, L.; Tanner, E. E.; Compton, R. G. *Physical Chemistry Chemical Physics* **2017**, *19*, 17521-17525.
(25) Batsanov, S. S. *Inorganic Materials* **2001**, *37*, 871-885.
(26) Soriaga, M. P.; Hubbard, A. T. *Journal of the American Chemical Society* **1982**, *104*, 2735-2742.
(27) Soriaga, M. P.; Hubbard, A. T. *Journal of the American Chemical Society* **1982**, *104*, 3937-3945.
(28) Britto, P.; Santhanam, K.; Ajayan, P. *Bioelectrochemistry and Bioenergetics* **1996**, *41*, 121-125.
(29) Boggess, R. K.; Martin, R. B. *Journal of the American Chemical Society* **1975**, *97*, 3076-3081.
(30) Gerhardt, G.; Adams, R. N. *Analytical Chemistry* **1982**, *54*, 2618-2620.
(31) Britto, P. J.; Santhanam, K. S. V.; Ajayan, P. M. *Bioelectrochemistry and Bioenergetics* **1996**, *41*, 121-125.

(32) Guidelli, R.; Compton, R. G.; Feliu, J. M.; Gileadi, E.; Lipkowski, J.; Schmickler, W.; Trasatti, S. *Pure and Applied Chemistry* **2014**, *86*, 245-258.
(33) Guidelli, R.; Compton, R. G.; Feliu, J. M.; Gileadi, E.; Lipkowski, J.; Schmickler, W.; Trasatti, S. *Pure and Applied Chemistry* **2014**, *86*, 259-262.
(34) Compton, R. G.; Banks, C. E. *Understanding Voltammetry*, 2nd ed.; Imperial College Press: London, 2011.
(35) Li, D.; Lin, C.; Batchelor-McAuley, C.; Chen, L.; Compton, R. G. *Journal of Electroanalytical Chemistry* **2018**, *826*, 117-124.
(36) Albery, J. *Electrode Kinetics*, 1st ed.; Clarendon Press: Oxford, 1975.
(37) Lin, C.; Chen, L.; Tanner, E. E. L.; Compton, R. G. *Physical Chemistry Chemical Physics* **2018**, *20*, 148-157.
(38) Gileadi, E.; Argade, S.; Bockris, J. O. M. *Journal of Physical Chemistry* **1966**, *70*, 2044-2046.

Chapter 7

Surface Area Measurements of Graphene and Graphene Oxide *via* Dopamine Adsorption

Building on the previous Chapter, the possible use of dopamine, monitored spectroscopically, as a probe molecule for surface area measurements is next investigated. Using high surface area carbon materials, including both graphene and graphene oxide (GO), the method is established as a complement or alternative to methylene blue or conventional N_2 (BET) adsorption. The molecular reorientation (flat to vertical) of dopamine on the graphene and GO surface provides a direct indication of the monolayer coverage and the rapid adsorption (within 10 min to saturation) offers high convenience. The smaller dopamine molecule size and less self-repulsion compared to methylene blue may yield a more closely-packed surface coverage on the materials of interest. Especially for materials with complex morphologies and internal structures, the dopamine adsorption may lead to a more 'correct' measurement.

The work presented in this Chapter has been published in *Applied Materials Today*.[1] Dr. Bertold Rasche performed the XRD measurements and Dr. Colin Johnston carried out the BET measurements reported in this Chapter.

7.1 Introduction

Graphene and graphene oxide (GO) are the objects of intensive and worldwide studies with numerous applications identified, including batteries, supercapacitors, sensors, catalysts, transistors, photovoltaics, drug delivery, etc., based on their mechanical, electrical and/or catalytic activities.[2-10] Diverse and numerous approaches to their synthesis have been developed prompting an exceptional need for the reliable characterisation of the materials. Not least due to the use of graphene and GO as catalysts, electro-catalysts and catalyst supports, the characterisation of the surface area is desirable and widely undertaken.

Conventionally the measurement of the surface areas of solids in the form of powders, particles or platelets is carried out using gas adsorption isotherm measurements in which the uptake of a gas *via* adsorption onto the solid is measured as a function of pressure at a constant temperature. For the purpose of inferring surface areas the data is commonly obtained using nitrogen gas, occasionally CO_2, water or argon, and analysed using the BET isotherm dating from 1938.[11] The isotherm essentially allows for the extension of the simple Langmuir isotherm to embrace multi-layer adsorption and for different enthalpies of adsorption of the adsorbate either directly onto the solid (ΔH_1) or onto an already adsorbed molecule (ΔH_2) and takes the form

$$\frac{P}{N_s(P_0 - P)} = \frac{1}{NC} + \frac{C-1}{NC}\frac{P}{P_0} \tag{7.1}$$

where N_s is the number of molecules adsorbed, N is the total number of sites corresponding to a monolayer, P_0 is the saturation vapour pressure of the adsorbate and

$$C = \exp\left(\frac{\Delta H_1 - \Delta H_2}{RT}\right) \tag{7.2}$$

Noting that N or N_s is proportional to the corresponding masses or volumes of gas, plots of $P/N_s(P_0-P)$ against P/P_0, or their equivalent, allow the determination of C and N. The surface area is related to the latter *via* $S = N \times A$ where A is the estimated area of one molecule. In modern practice the measurement is automated and carried out routinely.[12] The BET approach is enshrined by the International Organisation for Standardisation (ISO 9277:2010) recommendation on the measurement of disperse solids such as nano-powders and porous solids. The directive stresses that the BET method is only applicable to isotherms of type 2 (disperse, nonporous or macroporous solids) and type 4 (mesoporous solids, pore diameter between 2 nm and 50 nm).[13-15]

The caveats associated with the BET isotherm and especially the fact that many applications of graphene and GO are solution rather than gas phase based, encourage the exploration of complementary solution phase based approaches to the characterisation of the surface area. Probably the best established method is that of the adsorption of the blue dye methylene blue (MB) from water, aqueous or ethanol based solutions onto suspensions of the solid of interest, typically monitored spectroscopically. The amount adsorbed at full uptake is again, in conjunction with an estimated MB molecular area, used to estimate the area of the solid in contact with the solution.

Both the BET and MB methods have been widely studied in the context of graphene and GO characterisation. Generally the surface areas determined by MB adsorption tend to be larger than that reported by BET measurements made on the same sample. Early work[16] contrasted values attained by BET of 600 m^2/g to those from MB adsorption of 1850 m^2/g attributing the discrepancy, at least in part, to the agglomeration of the graphene/GO sheets. Such discrepancies have been repeatedly identified along with various key observations all of which indicate the difficulty of the task. These observations include the recognition of MB dimer and trimer formation,[17] and the contrasting uptake of MB between graphene and

GO, which is attributed to functional groups on the latter. Furthermore, increased functionality on GO has been shown to increase the MB uptake,[18] while aggregation of GO has been emphasised as a further key parameter.[19] In a study[20] of GO yarns, a surface area of 4 to 6 times the BET values were measured via MB adsorption and thought to be more reliable partly due to the observation of a type 3 adsorption isotherm in the BET analysis. Comparison of the BET and MB methods in the cases of carbon nanotubes[21] and active carbons[22] is even more complex with porosity and pH effects having marked influences.

This Chapter explores the use of a possible alternative to MB for surface area measurements *via* adsorption onto different samples of high surface area carbon materials including both graphene and GO. In particular it is noted that Chapters 4-6 have shown that dopamine and related quinone type molecules adsorb strongly and quickly onto graphene nanoplatelets and that phase transitions due to molecular reorientation on the surface (flat to vertical) can be observed. The latter can, at least in principle, offer an indication of the realisation of monolayer coverage or otherwise. Moreover, as is shown below, dopamine adsorbs much more rapidly compared to MB offering an improvement in convenience. In the following, MB and dopamine adsorption alongside corresponding BET measurements are compared for five different high surface area carbon samples.

7.2 Experimental

7.2.1 Materials and Reagents

Five graphene and graphene oxide samples were acquired from different commercial sources: graphene nanoplatelets (GNP-Powder, 15 μm in width, 6-8 nm in thickness) with a known average area of 297 ± 152 μm^2 (from scanning electron microscopy[23], as described in Chapter 3) from Strem Chemicals, MA, USA; a liquid sample of graphene

nanoplatelets suspension (GNP-Liquid, 7% graphene content by mass) and an aerogel/paste of graphene nanoplatelets (GNP-Paste, 1.7% graphene content by mass) from Applied Graphene Materials, UK; a sample of exfoliated graphite in form of powder (Exfoliated Graphite) and a sample of graphene oxide powder (GO) from Global Graphene Group, USA. All samples were analysed as received without any other purification.

The pH 0 solution was freshly prepared from hydrochloric acid (37%) and its pH was confirmed using a Hannah pH231 pH meter (Hannah, Bedfordshire, UK). As discussed in Chapter 6, dopamine is reported to be more stable and water-soluble in the protonated form in acidic environments,[24] hence all dopamine solution was prepared with pH 0 solution. The latter was degassed thoroughly with pure nitrogen (BOC Gases, UK) for 20 min to prevent degradation of the solution by atmospheric oxygen prior to the addition of dopamine.

7.2.2 Characterisation of Graphene and Graphene Oxide Samples

The morphology and surface structure of graphene and graphene oxide samples were characterized using Scanning Electron Microscopy (SEM) and Transmission Electron Microscope (TEM, JEOL 3000F instrument, Japan). SEM was performed using a JSM-6500F instrument (JEOL Ltd., Japan) and operated with an accelerating voltage of 5 kV using a secondary electron imaging mode. A glassy carbon plate (MFCD00133992 GC plate, 3 mm thick, Lancashire, UK), cleaned in aqua regia, was used as an electron imaging substrate. The dilute suspensions of graphene and GO samples were prepared and drop-casted onto the substrate, followed by dying under a nitrogen atmosphere. TEM was performed using a JEOL 3000F instrument (JEOL Ltd., Japan) and operated at 300 kV. The samples were prepared by placing a drop of the dilute suspensions of samples onto carbon grids (Agar Scientific) and allowing the solvent to evaporate in a desiccator.

7.2.3 BET Measurements

The BET measurements reported in this Chapter were carried out by Dr. Colin Johnston of the Department of Materials.

Nitrogen adsorption/desorption isotherms at 77 K were measured volumetrically on a Micromeritics Gemini VII 2390t surface area analyser (Micromeritics Instrument Corp., Norcross, USA). The Liquid and Paste samples were dried using a Büchi rotary evaporator. Prior to measurement, all samples were degassed in N_2 atmosphere at 393 K for at least 12h. The specific surface areas were determined by applying the BET (Brunauer–Emmett–Teller) equation to the relative pressure range 0.05–0.25 for the adsorption branch of the isotherm. BET calculation was performed with the Gemini VII Version 3.04 software delivered with the analysis equipment.

7.2.4 Dopamine Adsorption Measurements

The adsorption of dopamine onto each graphene and graphene oxide samples are measured via UV-vis spectroscopy. Specifically, a known amount of carbonaceous materials was mixed with a defined unit volume (1.0 mL) of dopamine solutions at a wide range of concentrations. The amount of material used for dopamine solution at each concentration was estimated by calculation such that the carbonaceous materials used must adsorb at least 20% of dopamine in solution, assuming a full monolayer surface coverage on the adsorbent. The mixture of carbon materials and dopamine solution was then sonicated (FB15050, Fisher Scientific, 50/60 Hz, 80W, Germany) for 20 min to allow full adsorption, followed by centrifugation (Eppendorf Centrifuge 5430 R) for 10 min at 14000 rpm. The original dopamine solution prior to adsorption and the supernatant after adsorption were both diluted into the calibration region then examined by UV-vis spectroscopy. UV-vis spectroscopy was conducted using a Shimadzu spectrometer UV-1800 and quartz cells with a 10 mm optical path. In all cases, a baseline correction was conducted prior to any

measurement, and the absorbance was recorded from 400–220 nm. The surface area of each sample measured by dopamine adsorption can be then estimated with a known dopamine molecule area (6.5×10^{-15} cm^2 as described in Chapter 6).

7.2.5 Methylene Blue Adsorption Measurements

For methylene blue adsorption measurement, a wide range of concentrations of MB solution were prepared. A known amount of carbonaceous materials was added into 20 mL of different concentrations of MB solutions and subjected to sonication for 360 minutes to allow full adsorption uptake. The amount of material added in must reduce at least 20% of MB concentration (corresponding to UV-vis absorbance signal), assuming a full monolayer coverage. The suspensions were then subjected to centrifugation to obtain the supernatant. Both original MB solution and the supernatant were diluted into the calibration region then examined by UV-vis spectroscopy to determine the concentrations. In all cases, a baseline correction was conducted prior to any measurement, and the absorbance was recorded from 800–400 nm. The surface area of each sample measured by MB adsorption can be then estimated with a literature[16,20] molecule area (13.0×10^{-15} cm^2).

7.3 Results and Discussion

7.3.1 Characterisation of Graphene and Graphene Oxide Samples

Of the five high surface area carbons employed in this Chapter, three different graphene nanoplatelet samples were used, one in a powdered state and two dispersed in water. One aqueous based sample is in the form of a suspension of particles and the other is a paste. These three samples are designated as GNP-Powder, GNP-Liquid and GNP-Paste, respectively. GNP-Liquid and GNP-Paste (from Applied Graphene Materials, UK) were produced differently according to the supplier. The GNP-Paste production uses a carbonate

template while the GNP-Liquid is formed without a template. The GNP-Powder (STREM Chemicals, USA) is a more conventional graphene nanoplatelet sample and according to the producer is comprised of plates 6-8 nm in thickness and 15 µm in width. Additional to these samples, a sample of exfoliated graphite, which has a comparatively low surface area and finally a high surface area graphene oxide (Global Graphene Group, USA) were studied.

In terms of morphology and crystallinity these samples vary substantially. The scanning and transmission electron microscopy (SEM and TEM) images reveal flakes of varying sizes in case of the GNP-Powder, the exfoliated graphite and the graphene oxide, with the latter showing the thinnest and smallest flakes (Figures 7.1&2). The X-ray diffraction patterns of these materials show that the GNP-Powder and the exfoliated graphite are relatively crystalline as their diffraction patterns match the one of graphite (Figure 7.3). Particularly the stacking ((00*l*) diffraction peaks) is well established. Nevertheless, the broadening of the peaks illustrates that the flakes are small and the number of orderly stacked layers is ca. 25 to 30, as estimated from Rietveld fits. In contrast, the much smaller and thinner plates of the GO sample give only an amorphous signal, indicating the effective separation of all layers.

The morphology of the two dispersion samples is markedly different (Figures 7.1(c)&(d) and (e)&(f)). The sample produced with a carbonate template (GNP-Paste) results in a material that is formed of a fused array of graphene based sheets. In contrast, the sample without a template (GNP-Liquid) results in a carbon-black like product. Consistently, the XRD pattern of the GNP-Paste still shows peaks that can be indexed with graphite, although only the (00*l*) diffraction peaks are visible and even these are very broad. The corresponding Rietveld fit suggests a maximum number of orderly stacked layers between 2 and 7. The GNP-Liquid only yields an amorphous signal.

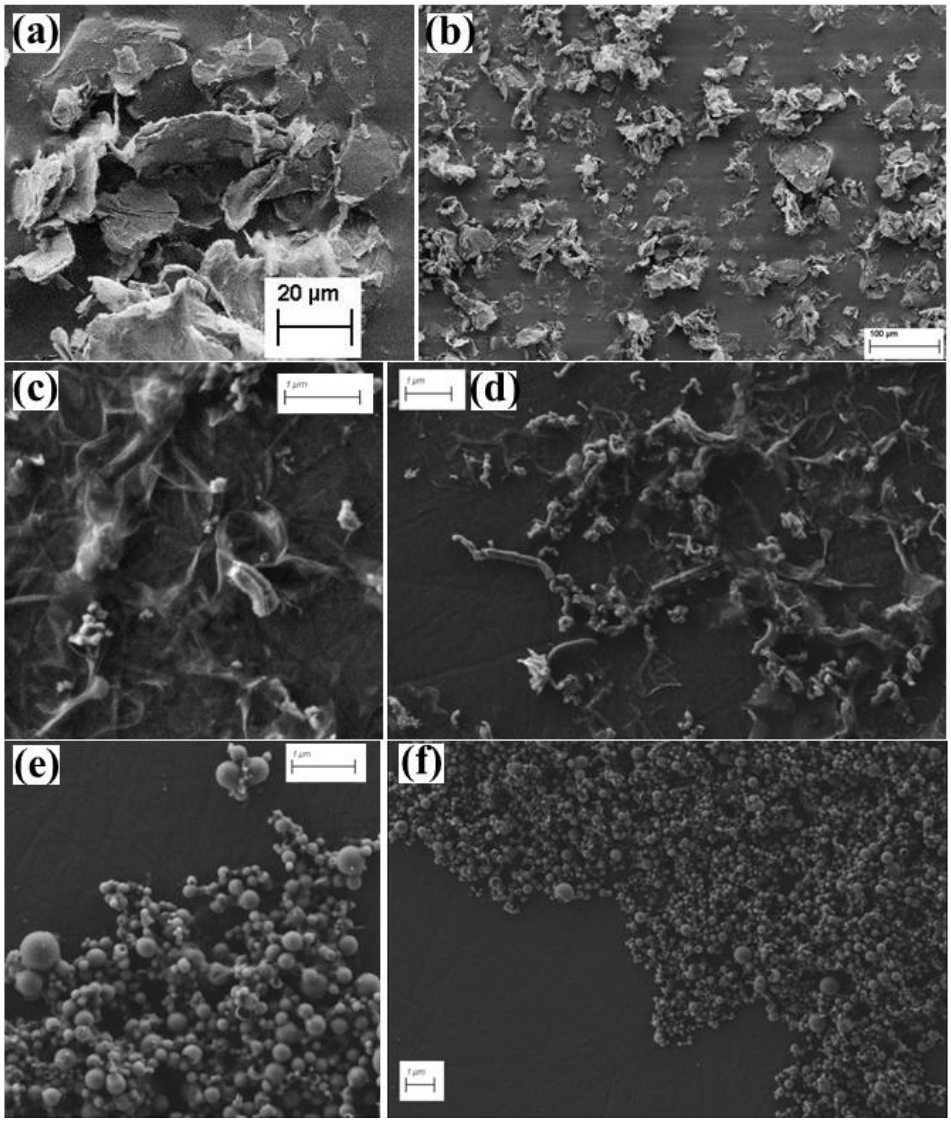


Figure 7.1. (a)&(b) SEM images of GNP-Powder sample, (c)&(d) SEM images of GNP-Paste sample, (e)&(f) SEM images of GNP-Liquid sample.

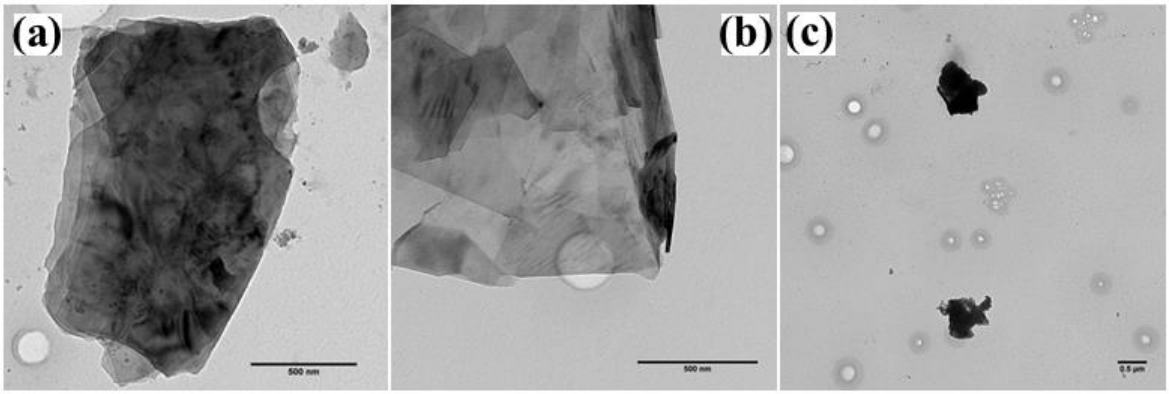


Figure 7.2. (a)&(b) TEM images of GO sample, (c) TEM image of Exfoliated Graphite sample.

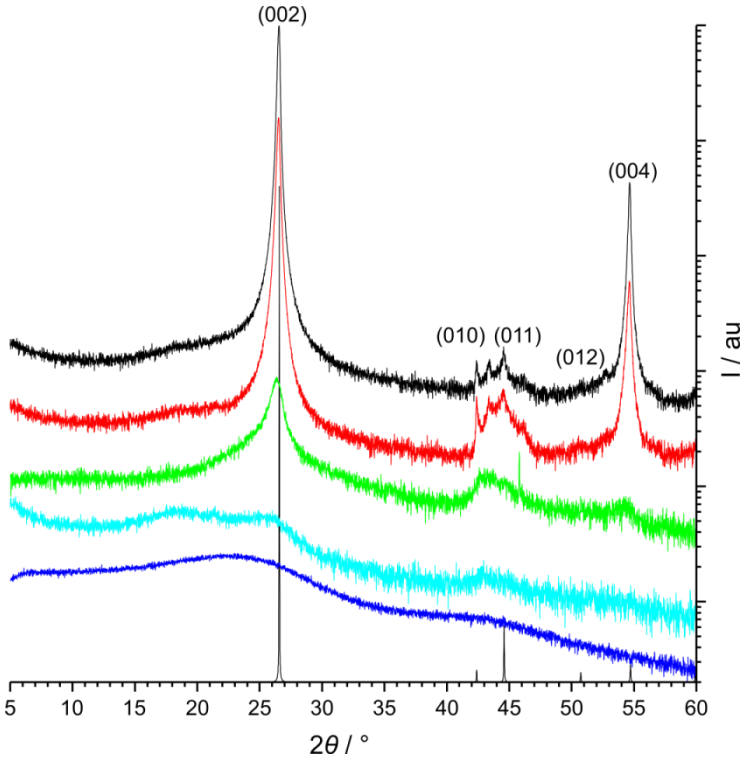


Figure 7.3. X-ray diffraction patterns of the different carbon based samples on a logarithmic scale: GNP-powder (black), exfoliated graphite (red), GNP-paste (green), GNP-liquid (blue) and graphene oxide (turquoise). As reference the theoretical diffraction pattern of graphite is given together with the corresponding Miller indices.

7.3.2 Adsorption of Dopamine and Methylene Blue on Graphene and GO

The measurement of the carbon surface areas using UV-vis spectroscopy is achieved through indirect assessment of the amount of probe molecules that is adsorbed onto the material from a solution of known concentration. Using UV-vis spectroscopy the remaining solution phase concentration of probe molecules (MB or Dopamine) is measured after it has been mixed with the high surface area carbon and the solid has been physically removed via centrifugation. 1 mL of 150 mM dopamine solution was mixed with GNP-Powder or GO and sonicated for different periods to determine the equilibrium time for the full adsorptive uptake. The absorbance of dopamine in aqueous solution reaches a maximum at 279 nm with the extinction coefficient (ε) of (0.25 ± 0.004) $M^{-1}\,m^{-1}$, as detailed described in Chapter 6. As shown in Figure 7.4, it is evident that the reduction in magnitude of absorbance peak is related to the adsorption onto

carbon materials. Figure 7.5 plots the amount of dopamine adsorbed by a unit amount (1 mg) of GNP-Powder or GO as a function of adsorption time. The adsorbed amount increases progressively on extending the adsorption time to ca. 10 min and reaches a plateau afterwards, suggesting a maximum uptake of dopamine by both GNP-Powder or GO at this concentration.

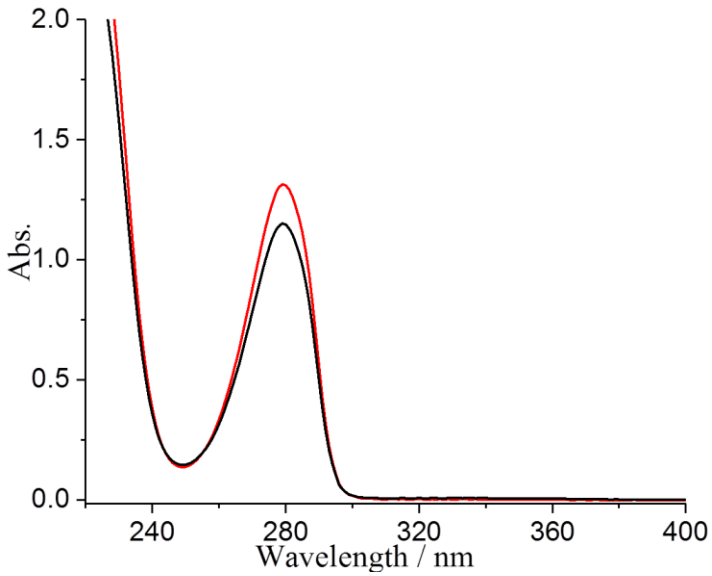


Figure 7.4. UV-vis absorption spectra of a pH 0 solution containing 150 mM dopamine before GNP-Powder adsorption (red line) and after adsorption (black line); dilution factor = 300.

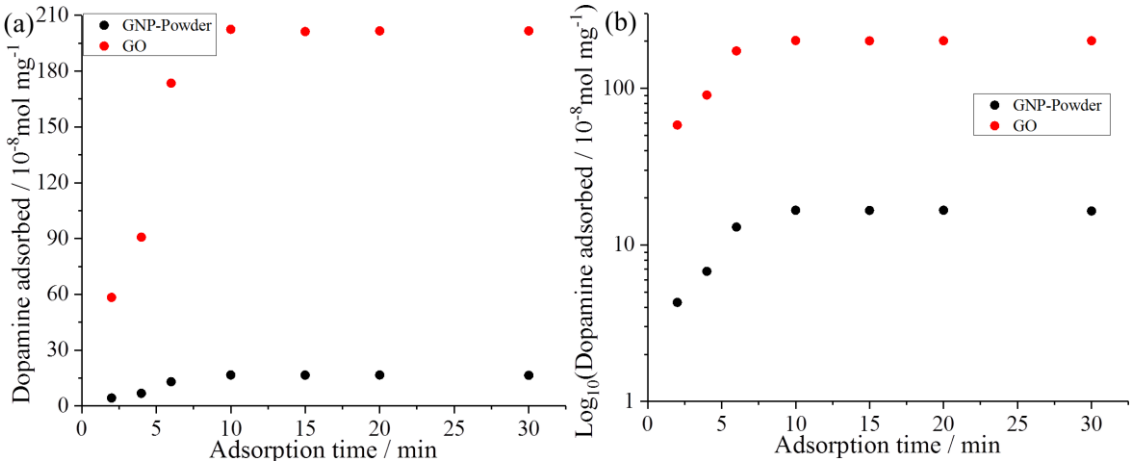


Figure 7.5. (a) The amount of adsorbed dopamine by GNP-Powder and GO as a function of adsorption time (b) The corresponding semi-logarithmic plot.

Analogous experiments were conducted for MB adsorption onto both GNP-Powder and GO. As shown in Figure 7.6, the absorbance peak of MB in aqueous solution is at 664 nm in good agreement with literature[19]. The extinction coefficient (ε) of MB is determined as (5.4 ± 0.097) M^{-1} m^{-1}, as the Beer–Lambert plot illustrated in Figure 7.7.

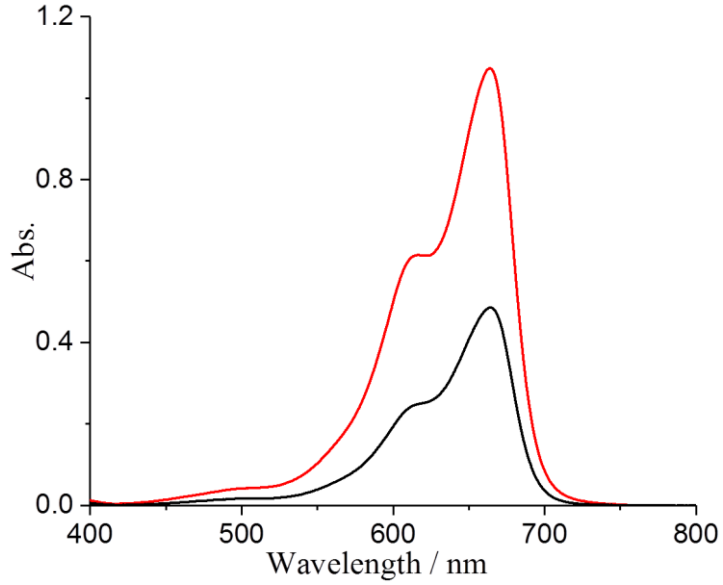


Figure 7.6. UV-vis absorption of 0.03 mM MB in water before GNP-powder adsorption (red line) and after adsorption (black line); dilution factor = 2.5.

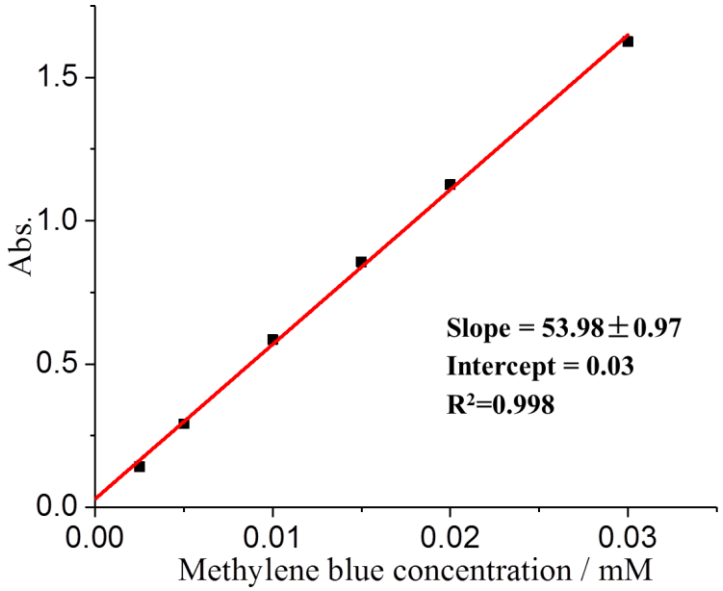


Figure 7.7. Beer–Lambert plot of methylene blue in aqueous solution.

The amount of MB adsorbed on GNP-Powder or GO was plotted against the adsorption time, as depicted in Figure 7.8. To reach the adsorption saturation, GNP-Powder and GO need to be sonicated in MB solution for at least ca. 300 min or 240 min, respectively. This is consistent with prior literature[17,25-27], where an overnight (at least 24 hr) stirring was applied to realise maximum adsorption. An additional experiment was conducted where the carbon materials were stirred in the MB solution continuously at 600 rpm without aid of sonication (see Figure 7.9) and GO requires at least ca. 16 hr adsorption time (18 hr for GNP-Powder) to reach the saturation. In both measurements with or without sonication, it is notable that the adsorbed amount of MB is consistent, suggesting the materials are rigid and their structure and surface areas are not altered by sonication. Moreover, the adsorption time required for saturation of GO is shorter than GNP-Powder suggesting faster adsorption kinetics. This affinity might be tentatively attributed to the abundant oxygen-containing function groups on the GO surface leading to a negatively charged GO surface[28-30] hence causing the enhanced adsorption *via* electrostatic interactions[17,18] with MB as a cationic dye. Comparing the adsorption of dopamine and MB onto graphene and GO materials, dopamine adsorbs *much* more rapidly (10 min to saturation vs. 300 min for MB) offering improved convenience.

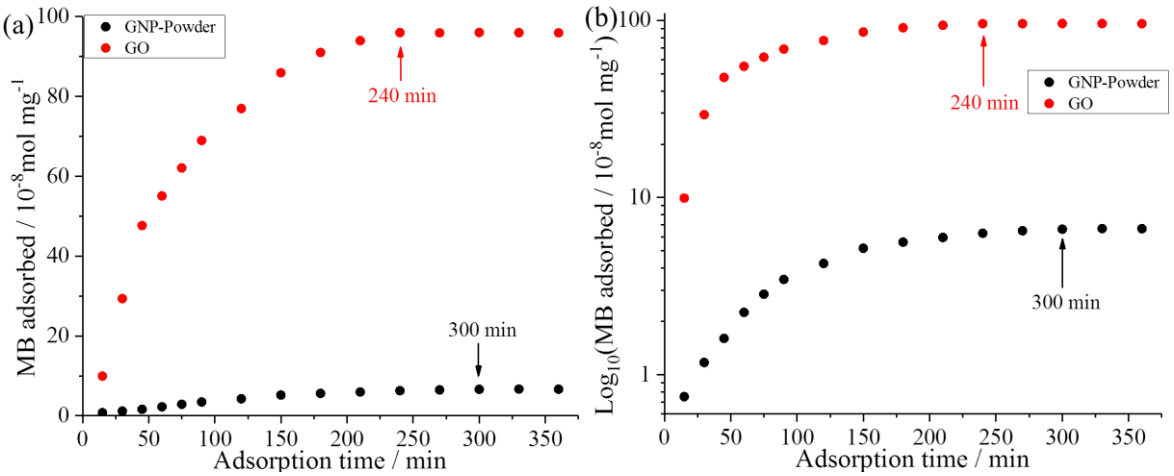


Figure 7.8. (a) The amount of adsorbed methylene blue by GNP-Powder and GO as a function of adsorption time (b) The corresponding semi-logarithmic plot.

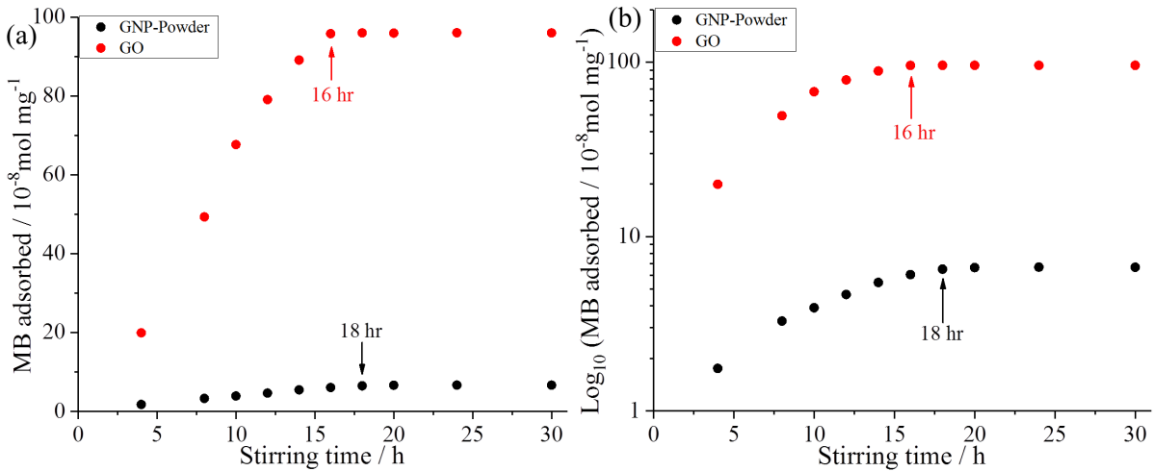


Figure 7.9. (a) The amount of adsorbed methylene blue by GNP-powder and GO as a function of adsorption (via strring at 600 rpm) time. (b) The corresponding semi-logarithmic plot.

Having studied the adsorption of dopamine and MB onto GNP-Powder and GO as a function of time, the experiments were then conducted over a wide range of adsorbate concentrations to obtain the corresponding adsorption isotherms. Figure 7.10 presents the dopamine adsorption isotherms for all five different graphene and GO samples in aqueous solutions. The presence of two expected[31] and distinct plateaux in all five isotherms suggest a flat to vertical concentration driven phase transition (as extensively discussed in Chapters 4-6) of dopamine molecules adsorbed on graphene and GO, corresponding to a flat molecular orientation on the adsorbent surface at low concentrations (≤ca.200 mM) and a vertical dopamine orientation at higher concentrations (≥ca.350 mM). This can be confirmed by comparing the ratio of the theoretical estimated dopamine molecule area in the flat orientation to the vertical orientation with the ratio of the dopamine adsorbed amount at the second plateau to the first plateau. The theoretical molecule areas of dopamine in the flat view and vertical view are estimated as 6.5×10^{-15} cm^2 and 3.6×10^{-15} cm^2, respectively, as described in Chapter 6. This results in a ratio of flat to vertical molecular areas of 1.80. In the dopamine isotherms, the adsorbed amount of dopamine per unit amount of carbonaceous material reaches the first plateau at adsorbate concentrations close to 200 mM and the second plateau at concentrations close to 400 mM. The ratios of these two limiting uptakes are calculated and tabulated in Table

7.1 with values ranging from 1.65 to 1.8, very close to the ratio of the molecular areas in the two different orientations. This suggests this concentration driven flat to vertical phase transition occurs on the surfaces of all five graphene/GO materials and provides an indication of the monolayer coverage at low concentrations (≤ca.200 mM). It is notable that the experimental ratios of the two plateaux are all slightly smaller than the ratio of the theoretical molecule areas, which might be tentatively attributed to the increased self-repulsion among dopamine molecules in the vertical orientation due to the protonated amine group (positively charged) leading to a less close packing on the surface of the adsorbent. Moreover, the GNP-Powder has a known width, thickness and average surface area (297 ± 152 μm^2), as provided by the supplier[32] and confirmed by the previous work[33-36] spectrophotometrically and electrochemically. The average surface area of each GNP-Powder attained from the dopamine adsorption at the first plateau is 308 ± 28 μm^2, confirming the applicability of dopamine as a probe to determine the surface area of graphene-based materials.

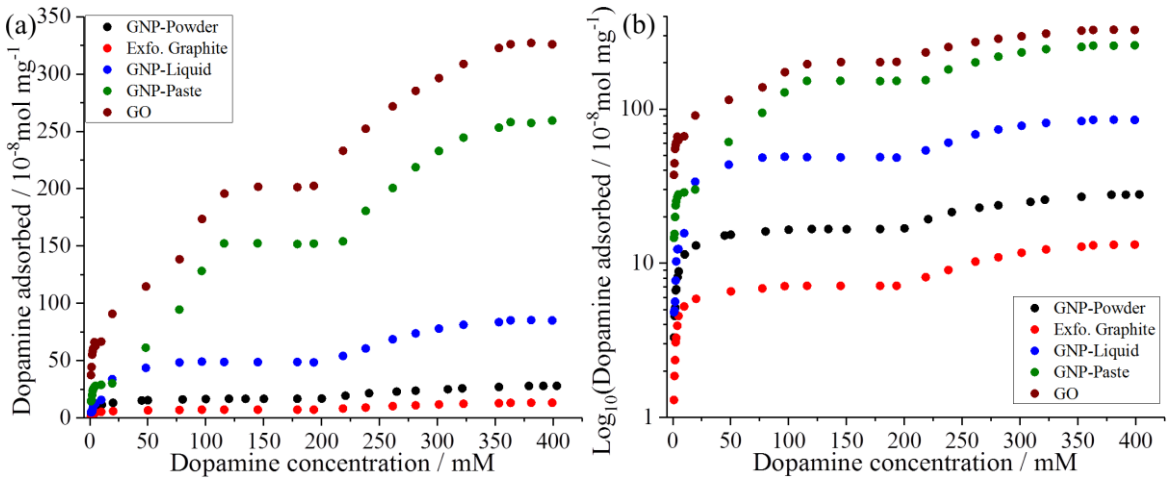


Figure 7.10. (a) Dopamine adsorption isotherms for five graphene and graphene oxide samples in pH 0 solution. (b) The corresponding semi-logarithmic plots to show the feature of isotherms for materials with low adsorption capacity .

Table 7.1 Ratios of the adsorbed dopamine amount at second plateau to the first plateau in Figure 7.10a.

	GNP-Powder	Exfo. Graphite	GNP-Liquid	GNP-Paste	GO
$n_{2nd\ plateau}$ / $n_{1st\ plateau}$	1.68	1.78	1.76	1.71	1.65

Analogous adsorption experiments with MB solutions over a wide range of concentrations were then conducted to construct the adsorption isotherms of MB for the five graphene and GO materials. As shown in Figure 7.11, the adsorbed amount of MB by four graphene-based materials (GNP-Powder, Exfoliated Graphite, GNP-Liquid and GNP-Paste) reaches a maximum at ca. 0.02 mM whereas for GO the uptake approaches the limiting level at ca. 0.01 mM MB concentration. This suggests the adsorption onto GO is thermodynamically favourable, attributed to the strong affinity between MB molecules and GO, as discussed previously.

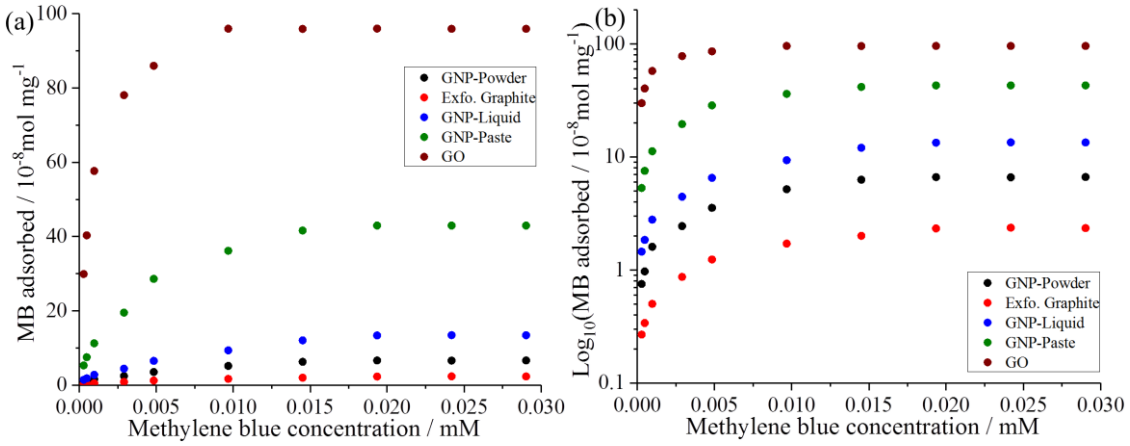


Figure 7.11. (a) Methylene blue adsorption isotherms for five graphene and graphene oxide samples in aqueous solution. (b) The corresponding semi-logarithmic plots to show the feature of isotherms for materials with low adsorption capacity.

To examine possible reorientation of MB molecules on the material surfaces, experiments were also conducted at higher concentrations (up to 3.8 mM), as shown in Figure 7.12. Note that this concentration corresponds to the maximum possible before a significant formation of dimers causes a distorted UV-vis spectrum and a possibly different adsorption manner onto the adsorbent.[19] There is no second plateau in Figure 7.12 suggesting that no phase transition occurs and that MB adopts a flat orientation on the adsorbent, consistent with literature.[16,37]

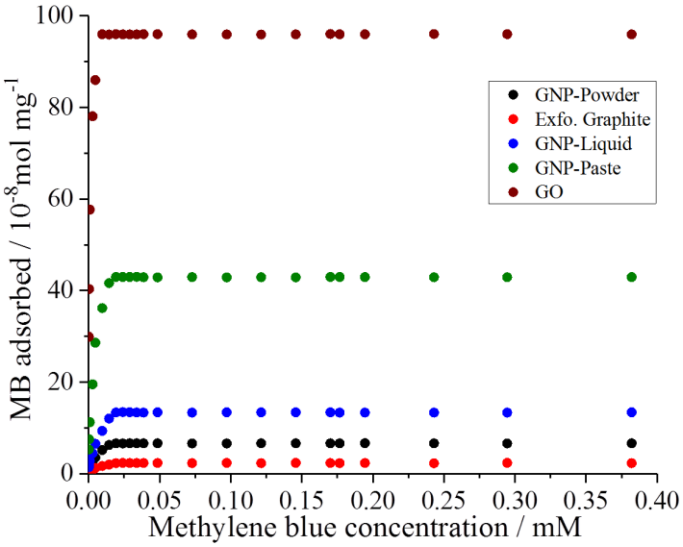


Figure 7.12. Full range of methylene blue adsorption isotherm for five graphene and GO samples in aqueous solution.

7.3.3 Comparison of BET, Dopamine and MB Absorption Techniques

Having studied adsorption isotherms of both dopamine and MB for all five graphene and GO samples, the surface area of each graphene and graphene oxide sample can be probed from the equilibrium uptake of both adsorbates, as given in Table 7.2, and compared with values obtained from the BET-N_2 technique. The dopamine measurement shows good agreement with BET for the two low surface area samples (GNP-Powder and Exfoliated Graphite). For the other three samples (GNP-Liquid, GNP-Paste and GO), the values obtained from dopamine adsorption are much larger compared to those from BET. The BET method is well-known in the community for its incapability of measuring carbonaceous materials with large surface areas, attributed to the agglomeration state of the dry samples during the measurement[16,38] and extremely weak adsorbate-adsorbent interaction.[20] The former is the main issue for the measurement of very thin GO sheets. Moreover, it is also very challenging for the BET technique to measure carbonaceous materials with complex internal structures.[20] In particular, this might explain the marked discrepancy of the surface area of the GNP-Paste sample measured from BET and

dopamine, as the latter has a complex fused sheet like morphology and internal structure (SEM: Figures 7.1(c)&(d)). Consequently, for the values of the GNP-Liquid, the GNP-Paste and the GO sample, the dopamine measurements can be considered to give a more 'correct' indication.

Table 7.2. Comparison of surface areas obtained by N_2 adsorption (BET), dopamine and MB absorption techniques.

	GNP-Powder	Exfo. Graphite	GNP-Liquid	GNP-Paste	GO
BET Surface Area (S_{BET} / m^2/g)	62	25	122	163	500
Dopamine Surface Area (S_{DA} / m^2/g)	64	27	190	596	783
MB Surface Area (S_{MB} / m^2/g)	54	19	109	349	780
S_{BET}/ S_{DA}	0.97	0.93	0.64	0.27	0.64
S_{MB}/ S_{DA}	0.83	0.70	0.57	0.59	1.00

Comparing the values obtained from dopamine and MB adsorption, the GO surface area determined from both methods is remarkably consistent. MB is a cationic dye, which has strong electrostatic interactions with GO attributed to the functional groups as discussed previously. Dopamine is also in cationic form under the experimental conditions employed (pH=0). This consistent behaviour suggests both methods can be used to accurately measure the surface area of GO-based materials, which have abundant functional groups attributing to an enhanced affinity. This result is also consistent with prior literature[16,19,20,38] where MB is used to measure high surface area GO or rGO based materials. To the best of knowledge, there is no literature reporting using MB as a probe molecule to determine the surface area of graphene-based (not GO) materials. The surface areas of other graphite/graphene samples (GNP-Powder, Exfoliated Graphite, GNP-Liquid and GNP-Paste) measured from dopamine are larger than those from MB. The dopamine

might give more ‘correct’ values for following reasons: First, the monolayer dopamine adsorption has been confirmed *via* phase transitions of molecular reorientation whereas the MB adsorption on carbonaceous materials is more complicated for reasons such as the concentration-driven MB dimer and trimer formation on the material surface;[17] Second, as discussed previously, the surface area of the GNP-Powder is known, as provided by the supplier[32] and further confirmed spectrophotometrically and electrochemically by the previous work.[33-36] The consistency between this known surface area and the values from BET (for low surface area carbon materials) and dopamine measurements suggests the values from dopamine adsorption are more reliable. Third, it would be more challenging for cationic MB to achieve fully closed packing on the adsorbent if the adsorptive interaction is not strong enough due to self-repulsion, whereas for dopamine, the positive-charged amine group is on the side chain possibly giving less self-repulsion among adsorbed dopamine molecules. The surface areas of the GNP-Liquid and the GNP-Paste samples measured from dopamine and MB adsorption have the largest discrepancy. This might be attributed to large molecular structure of MB causing difficulties in achieving a full surface coverage, especially for materials that have complex morphologies and internal structures.

7.4 Conclusions

In conclusion it is clear that unambiguous measurement of graphene and graphene oxide surface areas are elusive! However, the use of the dopamine adsorption method as a complement to the BET and MB adsorption measurements may be recommended on the basis that the flat to vertical transition allows confirmation of the attainment of a monolayer coverage. The fact that the measurements are faster than the MB equivalent and that the approach is simple to adopt are further benefits.

Bibliography

(1) Chen, L.; Batchelor-McAuley, C.; Rasche, B.; Johnston, C.; Hindle, N.; Compton, R. G. *Applied Materials Today* **2020**, *18*, 100506.
(2) Pumera, M. *Energy & Environmental Science* **2011**, *4*, 668-674.
(3) Pumera, M.; Ambrosi, A.; Bonanni, A.; Chng, E. L. K.; Poh, H. L. *TrAC Trends in Analytical Chemistry* **2010**, *29*, 954-965.
(4) Ambrosi, A.; Chua, C. K.; Bonanni, A.; Pumera, M. *Chemical Reviews* **2014**, *114*, 7150-7188.
(5) Pumera, M. *Materials Today* **2011**, *14*, 308-315.
(6) Schwierz, F. *Nature Nanotechnology* **2010**, *5*, 487.
(7) Raccichini, R.; Varzi, A.; Passerini, S.; Scrosati, B. *Nature Materials* **2014**, *14*, 271.
(8) Yu, X.; Cheng, H.; Zhang, M.; Zhao, Y.; Qu, L.; Shi, G. *Nature Reviews Materials* **2017**, *2*, 17046.
(9) El-Kady, M. F.; Shao, Y.; Kaner, R. B. *Nature Reviews Materials* **2016**, *1*, 16033.
(10) Choi, W.; Lahiri, I.; Seelaboyina, R.; Kang, Y. S. *Critical Reviews in Solid State and Materials Sciences* **2010**, *35*, 52-71.
(11) Brunauer, S.; Emmett, P. H.; Teller, E. *Journal of the American Chemical Society* **1938**, *60*, 309-319.
(12) Lowell, S.; Shields, J. E. *Powder Surface Area and Porosity*; Springer Science & Business Media, 2013; Vol. 2.
(13) Attard, G.; Barnes, C. *Surfaces*; Oxford University Press, 1998; Vol. 59, p 6-9.
(14) *International Organization for Standardization*; Determination of the Specific Surface Area of Solids by Gas Adsorption - BET Method, ISO 9277:2010, 2010.
(15) Leofanti, G.; Padovan, M.; Tozzola, G.; Venturelli, B. *Catalysis Today* **1998**, *41*, 207-219.
(16) McAllister, M. J.; Li, J.-L.; Adamson, D. H.; Schniepp, H. C.; Abdala, A. A.; Liu, J.; Herrera-Alonso, M.; Milius, D. L.; Car, R.; Prud'homme, R. K. *Chemistry of Materials* **2007**, *19*, 4396-4404.
(17) Haubner, K.; Murawski, J.; Olk, P.; Eng, L. M.; Ziegler, C.; Adolphi, B.; Jaehne, E. *ChemPhysChem* **2010**, *11*, 2131-2139.
(18) Yan, H.; Tao, X.; Yang, Z.; Li, K.; Yang, H.; Li, A.; Cheng, R. *Journal of Hazardous Materials* **2014**, *268*, 191-198.
(19) Montes-Navajas, P.; Asenjo, N. G.; Santamaría, R.; Menendez, R.; Corma, A.; García, H. *Langmuir* **2013**, *29*, 13443-13448.
(20) Aboutalebi, S. H.; Jalili, R.; Esrafilzadeh, D.; Salari, M.; Gholamvand, Z.; Aminorroaya Yamini, S.; Konstantinov, K.; Shepherd, R. L.; Chen, J.; Moulton, S. E. *ACS Nano* **2014**, *8*, 2456-2466.
(21) Li, Y.; Du, Q.; Liu, T.; Peng, X.; Wang, J.; Sun, J.; Wang, Y.; Wu, S.; Wang, Z.; Xia, Y. *Chemical Engineering Research and Design* **2013**, *91*, 361-368.
(22) Wang, S.; Zhu, Z. H.; Coomes, A.; Haghseresht, F.; Lu, G. Q. *J Colloid Interface Sci* **2005**, *284*, 440-446.
(23) Poon, J.; Batchelor-McAuley, C.; Tschulik, K.; Compton, R. G. *Chem. Sci.* **2015**, *6*, 2869-2876.
(24) Carter, J. E.; Johnson, J. H.; Baaske, D. M. *Analytical Profiles of Drug Substances* **1982**, *11*, 257-272.
(25) El-Kady, M. F.; Strong, V.; Dubin, S.; Kaner, R. B. *Science* **2012**, *335*, 1326.
(26) Rubino, R. S.; Takeuchi, E. S. *Journal of Power Sources* **1999**, *81*, 373-377.
(27) Choucair, M.; Thordarson, P.; Stride, J. A. *Nature Nanotechnology* **2009**, *4*, 30.
(28) Li, D.; Müller, M. B.; Gilje, S.; Kaner, R. B.; Wallace, G. G. *Nature Nanotechnology* **2008**, *3*, 101.
(29) Li, M. j.; Liu, C. m.; Xie, Y. b.; Cao, H. b.; Zhao, H.; Zhang, Y. *Carbon* **2014**, *66*, 302-311.
(30) Si, Y.; Samulski, E. T. *Nano Lett* **2008**, *8*, 1679-1682.
(31) Chen, L.; Tanner, E. E. L.; Lin, C.; Compton, R. G. *Chemical science* **2018**, *9*, 152-159.
(32) Inc, S. C. *Strem Product Catalog* **2012**.

(33) Poon, J.; Batchelor-McAuley, C.; Tschulik, K.; Compton, R. G. *Chemical Science* **2015**, *6*, 2869-2876.
(34) Chen, L.; Li, X.; Tanner, E. E. L.; Compton, R. G. *Chemical science* **2017**, *8*, 4771-4778.
(35) Chen, L.; Tanner, E. E. L.; Compton, R. G. *Physical Chemistry Chemical Physics* **2017**, *19*, 17521-17525.
(36) Wu, H.; Lin, Q.; Batchelor-McAuley, C.; Gonçalves, L. M.; Lima, C. F.; Compton, R. G. *Analyst* **2016**, *141*, 2696-2703.
(37) Zhang, D.; Fu, L.; Liao, L.; Liu, N.; Dai, B.; Zhang, C. *Nano Research* **2012**, *5*, 875-887.
(38) Schniepp, H. C.; Li, J.-L.; McAllister, M. J.; Sai, H.; Herrera-Alonso, M.; Adamson, D. H.; Prud'homme, R. K.; Car, R.; Saville, D. A.; Aksay, I. A. *Journal of Physical Chemistry B* **2006**, *110*, 8535-8539.

Chapter 8

Single Entity Electrocatalysis: Oxygen Reduction Mediated *via* Methyl Viologen Doped Nafion Nanoparticles

Chapters 4-7 explored the adsorption of various large organic molecules onto graphene nanoplatelets and the role of adsorption in electrocatalysis. From this Chapter to Chapter 11, this thesis will focus on the study of Nafion, a sulfonated tetrafluoroethylene based fluoropolymer-copolymer, in the forms of nanoparticles and films as supports for authentic electrocatalysts (Chapter 8), as well as for the study of 'fake' catalysis attributed to the retarded mass transport (Chapter 9). Ion transport in the film and particles is assessed (Chapter 10), which leads to their use as a novel improved reference electrode for real applications (Chapter 11).

In this Chapter, Nafion particles doped with methyl viologen are shown to be electrocatalytic towards oxygen reduction in aqueous solution when immobilised on a carbon electrode surface. In this way an efficient homogeneous electron transfer mediator, methyl viologen, can be confined to act heterogeneously with the benefits of that type of process without losing catalytic effectiveness. Kinetic and mechanistic parameters are deduced from cyclic voltammetry and from single entity nano-impact experiments, and the process is shown to occur *via* electron transfer to dioxygen at the Nafion particle-solution interface with the initial formation of superoxide.

The work presented in this Chapter has been published in *Physical Chemistry Chemical Physics*.[1] Dr. Chuhong Lin developed the theory and carried out all the simulations reported in this Chapter.

8.1 Introduction

In many valuable electrochemical applications catalysis of the process is desirable to ensure that the reaction occurs with a minimum of overpotential leading to improved selectivity and promoted cost efficiency. Such electrocatalysis[2-6] falls with two broad categories. In homogeneous catalysis a redox active mediator, M, is used to bring about electron transfer to a target species, T, at a lower overpotential than is required to drive direct electron transfer to or from the target:

$$M \pm e^{-} \rightleftharpoons N \tag{8.1}$$

$$N + T \rightarrow M + product \tag{8.2}$$

In this classical EC' mechanism,[7] the mediator is regenerated in the chemical step and hence available for further reaction at the electrode. Examples of this type of process include the use of the ferricyanide/ferrocyanide couples, $Fe(CN)_6^{3-/4-}$ to mediate the oxidation of cysteine[8] or hydrogen sulphide,[9] the ferrocene/ ferrocenium couple to catalyse the oxidation of glucose,[10] and the hydroquinone/quinone couple to mediate the oxidation of NADH.[11] The use of a mediator requires the addition of a reagent (M) to the solution in order to facilitate the catalysis. In contrast, in heterogeneous electrocatalysis, the electron transfer takes place at an electrode surface which is either intrinsically catalytic to the process of interest or else is modified so as to become so. The latter approach allows use of cheaper bulk electrode material such as carbon. Clearly this is preferable in the sense of being reagent free in respect of the bulk solution and hence facilitating the separation of reaction products if so required. Nevertheless, some homogeneous electron transfer mediators such as methyl viologen or ruthenium trisbipyridine are both effective and act on diverse substrates.[12,13] This Chapter provides a proof-of-concept for a generic approach

for the immobilization of cationic molecules allowing reagent free use and the easy recycling of the catalytic material.

In particular sub-micron sized Nafion particles doped with methyl viologen are prepared and utilised as recoverable and recyclable entities for modifying the surface of a glassy carbon electrode. The modified electrode is characterised and shown to behave in an analogous manner towards the reduction of dissolved oxygen in aqueous solution as does dissolved solution phase methyl viologen.[14] In this way a well-characterised and often employed homogeneous electron transfer mediator is used for heterogeneous electrocatalysis with all of the benefits of the latter. In the following, the kinetics and mechanism of the methyl viologen Nafion particle catalysed reduction of oxygen are determined and the reaction product is shown to be hydrogen peroxide.

8.2 Experimental

8.2.1 Synthesis of MV-Nafion Particles

The Nafion particles doped with MV^{2+} (MV-Nafion particles) were synthesized as described in Chapter 3. The obtained suspension of sub-micron sized MV-Nafion particles has been characterised previously giving an average radius of 0.43 ± 0.26 μm.[12] In this Chapter, five different concentrations of MV^{2+} aqueous solutions (300 mM, 150 mM, 75 mM, 37.5 mM and 18.75mM) were used to synthesize MV-Nafion particles at different doping level (noted as 100%, 50%, 25%, 12.5% and 6.25%, respectively, in the following sections).

8.2.2 Cyclic Voltammetry of Ensembles of MV-Nafion Particles

For the cyclic voltammetry (CV) measurements, a glassy carbon macroelectrode (GC, diameter 3.0 mm) was used as the working electrode. 10 μL of evenly dispersed MV-

Nafion particles suspension was drop-casted on the GC macroelectrode to modify the electrode and left to dry under a nitrogen environment. The number of Nafion particles immobilized on the electrode in this way is approximately 1.8×10^8 (see Appendix B1 for a detailed calculation). CV was conducted at selected scan rates of between 25 mVs^{-1} to 400 mVs^{-1} in degassed Phosphate buffered saline buffer (PBS, pH = 7.4, consisting of 137.0 mM NaCl, 2.7 mM KCl, 10.0 mM Na_2HPO_4, and 1.8 mM KH_2PO_4.). For the measurements with the presence of oxygen, the PBS buffer was placed in a water bath at 25°C to for 30 min to obtain air saturated condition. This experiment was repeated using equal amounts of MV-Nafion particles at different doping levels. Note that the voltammograms shown in this Chapter are the first scans unless specified otherwise.

8.2.3 Impact Electrochemistry of Single MV-Nafion Particles

For the electrochemical study of single MV-Nafion particles, chronoamperometry was performed with a home-fabricated carbon fibre wire microelectrode (diameter 7.0 μm, length ca. 1mm, fabrication procedure see Chapter 3). Note that the potentiostat used in this work accurately conserves the charge transferred arising from a particle-impact process despite possible alteration in the spike shape.[15,16] 4.5 mL of PBS buffer was degassed using N_2 for 15 min to remove dissolved electroactive oxygen and then 500 µL of MV-Nafion stock suspension was added. The cell was sealed and sonicated for 1 min to obtain a well dispersed suspension, followed by immediate chronoamperometric scans under an atmosphere of N_2 during the measurements. For the nano-impact experiments in the presence of air-level oxygen, the PBS buffer was placed in water bath at 25°C to for 30 min prior to the addition of MV-Nafion particles. For nano-impact experiments at oxygen saturated level, the buffer was gassed thoroughly with O_2, and an atmosphere of O_2 was maintained during the experiment.

8.3 Theory and Simulation

In this section, a theoretical model of the MV^{2+} mediated oxygen reduction reaction (ORR) is built and implemented both for macrosized electrodes modified by MV^{2+} doped Nafion particles and for single doped Nafion particles. The cyclic voltammetry of the system with different kinetic conditions is then explored computationally and the electrochemical features to characterise the kinetics of MV^{2+} mediated ORR as recorded in a subsequent section of this Chapter are predicted and quantified.

All the simulations reported in this section were developed and carried out by Dr. Chuhong Lin.

8.3.1 Theoretical Model

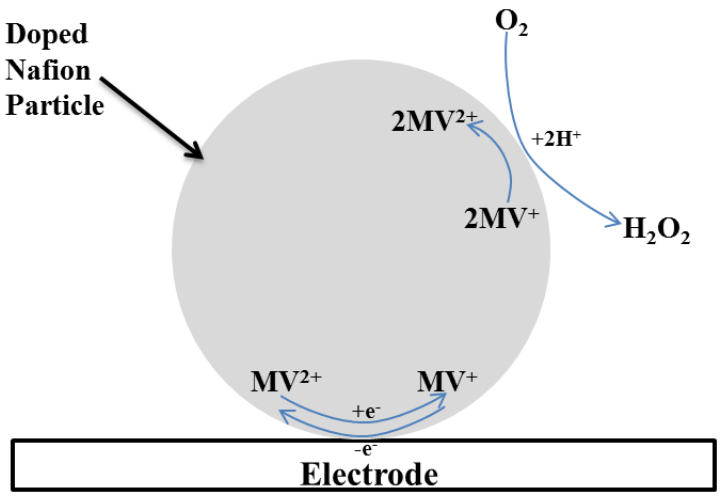
The reaction of oxygen reduction mediated by MV^{2+} doped Nafion particles is assumed to follow a heterogeneous EC' mechanism, as shown in Scheme 8.1 (E: electron transfer step; C': catalytic reaction step; heterogeneous: the catalyst is on the electrode surface). For the redox active film containing molecular redox active species,[17] the reaction mechanism is modelled as:

$$MV^{2+}(\text{particle}) + e^- \underset{}{\overset{k_{el_MV}}{\rightleftharpoons}} MV^{+}(\text{particle}),\ E_{f_MV} \tag{8.3}$$

$$2MV^{+}(\text{particle}) + O_2(\text{sol}) \xrightarrow{k_{MV_orr}} 2MV^{2+}(\text{particle}) + H_2O_2(\text{sol}) \tag{8.4}$$

In the electron transfer step, the MV^{2+} in the doped Nafion particles is partly reduced to MV^{+} with both species confined to the particles. E_{f_MV} is the formal potential of the redox reaction and k_{el_MV} is the electron transfer rate constant. The confined MV^{+} is oxidized by O_2 in solution, regenerating MV^{2+} with a catalytic reaction rate of k_{MV_orr}. The product of the mediated oxygen reduction reaction (Eqn.(8.4)) is H_2O_2.[18] The catalytic step is regarded as a chemically irreversible process in this Chapter and H_2O_2 is not re-oxidized

into O_2. Besides, it is assumed that H_2O_2 does not further react with MV^+ to generate water in the experimental conditions, which is evidenced by the experimental data, as discussed below.



Scheme 8.1. Graphical representation of the mechanism of the mediated oxygen reduction by MV^{2+} doped Nafion particles.

The catalyst $MV^{2+/+}$ is doped in the Nafion particles, on the surface of which the oxygen can be chemically reduced by MV^+. In addition, the electrochemical oxygen reduction reaction may occur simultaneously with the EC' reaction on the Nafion particles *via* direct reaction at the underlying electrode surface. The electrochemical ORR is described as:

$$O_2(sol) + 2e^- + 2H^+(sol) \xrightarrow{k_{el_orr}} H_2O_2(sol), \quad E_{f_orr} \tag{8.5}$$

where E_{f_orr} is the formal potential of oxygen reduction reaction on Nafion particles and k_{el_orr} is the corresponding standard electrochemical rate constant.

In the experiments reported below, both Nafion particle ensembles and single Nafion particles are used to mediate the electrochemical reduction of oxygen. The ensemble of Nafion particles is a layer of particles supported on a macrosized, planar substrate electrode. With the large coverage of Nafion particles on the substrate, the Nafion modified electrode can be simplified for modelling as a homogeneous, macrosized

electrode covered with a layer of Nafion-MV^{2+}. For individual Nafion particles, in the nano-impact experiment, the particle suspended in solution collides on the substrate electrode due to the Brownian motion of the particle. Simulating a micro-/nano-size spherical particle located on a flat substrate requires a relatively long simulation time. For the convenience of simulation, it is approximated that the electrochemical responses of the supported particle to that of an isolated particle with a correction factor in the flux of ln2 (details are discussed in Appendix B3). The geometries of the two electrodes and the simplified models used in the simulation are illustrated in Figure 8.1.

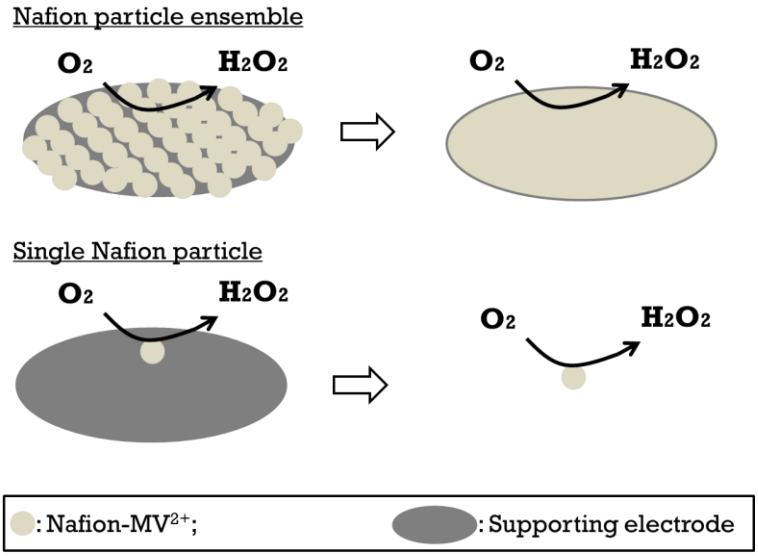


Figure 8.1. Illustration of the simplified geometry for the Nafion particle ensemble and the single Nafion particle electrodes.

8.3.1.1 Simulation of the Cyclic Voltammetry of Nafion Particle Modified Electrodes

If a monolayer of Nafion particles is immobilized on the macrosized, planar substrate electrode of radius r_{el}, the electrochemical response of the Nafion particle modified electrode can be treated as a normal macroelectrode of r_{el} radius covered with a uniform layer of Nafion-MV^{2+}. Therefore, the concentration on the electrode surface is identical at

any position and only the concentration distribution on the dimension x perpendicular to the electrode surface needs to be taken into consideration.

At the electrode surface, the reaction equations for the reactive species MV^{2+} and O_2 are written as:

$$\begin{aligned}\frac{\partial \Gamma_{MV^{2+}(ads)}}{\partial t} = &-k_{el_MV}\exp\left(-\frac{\alpha_{el_MV}F\left(E-E_{f_MV}\right)}{RT}\right)\Gamma_{MV^{2+}(ads)} \\ &+k_{el_MV}\exp\left(\frac{\left(1-\alpha_{el_MV}\right)F\left(E-E_{f_MV}\right)}{RT}\right)\left(\Gamma_{max}-\Gamma_{MV^{2+}(ads)}\right) \\ &+2k_{MV_orr}\left(\Gamma_{max}-\Gamma_{MV^{2+}(ads)}\right)c_{O_2(sol),\,x=0}\end{aligned} \tag{8.6}$$

$$-D_{O_2}\left.\frac{\partial c_{O_2(sol)}}{\partial z}\right|_{x=0} = -k_{MV_orr}\left(\Gamma_{max}-\Gamma_{MV^{2+}(ads)}\right)c_{O_2(sol),\,x=0} \tag{8.7}$$

where t is time, $\Gamma_{MV2+(ads)}$ and Γ_{max} are the real-time surface coverage (mol m^{-2}) of MV^{2+} and the initial surface coverage of MV^{2+} before the reaction, respectively. $c_{O2(sol),x=0}$ is the surface concentration of O_2 and x = 0 refers to the electrode surface. D_{O2} is the diffusion coefficient (m^2 s^{-1}) of dissolved oxygen, which equals 1.96 × 10^{-9} m^2 s^{-1} at 298 K in aqueous solution.[19] At t = 0, the surface concentration of O_2 equals the oxygen concentration in bulk solution $c_{O2(sol)}^{*}$ and $c_{O2(sol)}^{*}$ = 0.26 mM in an aqueous solution saturated by air and 1.24 mM in a solution saturated by pure oxygen gas at 298 K.[20] During the reaction, the surface coverage of MV^{+} equals $\Gamma_{max} - \Gamma_{MV2+(ads)}$. Note that an "effective" surface coverage Γ (mol m^{-2}) is used in the simulation as discussed above, to characterise the concentration of MV^{2+} doped in Nafion particles ρ_{MV2+} (mol m^{-3}). The conversion between the effective initial surface coverage of MV^{2+} Γ_{max} used in simulation and the MV^{2+} doping level ρ_{MV2+} in experiment is:

$$N_{NP}\rho_{MV^{2+}}\left(\frac{4}{3}\pi r_{NP}^{3}\right) = \Gamma_{max}\left(\pi r_{el}^{2}\right) \tag{8.8}$$

where N_{NP} is the number of Nafion particles modified on the electrode, r_{NP} is the radius of a Nafion particle, and r_{el} is the radius of the electrode approximated in the simulation as shown in Figure 8.1. N_{NP} can be estimated from the drop-casting experiment. In this work, the number of Nafion particles immobilized on the electrode is approximately 1.8×10^8 and the average radius of the Nafion particle is 0.43 μm.

The electron transfer kinetics of the redox reaction $MV^{2+/+}$ is described by the Butler-Volmer equation, where k_{el_MV} is the electron transfer rate constant (s^{-1}), α_{el_MV} is the transfer coefficient and the overpotential is calculated from $E-E_{f_MV}$ which is the difference between the applied electrode potential (V) E and the formal potential (V) of $MV^{2+/+}$ E_{f_MV}. F (96485 C mol^{-1}) is the Faraday constant, R (8.3145 J mol^{-1}) is the gas constant, T (298.15 K) is the room temperature. The catalytic reaction is assumed a second-order process and a catalytic reaction rate k_{orr} is defined with the unit of mM^{-1} s^{-1}. If the electrochemical oxygen reduction reaction occurs directly on the electrode surface, Eqn.(8.7) should be re-written as:

$$\begin{aligned} -D_{O_2}\left.\frac{\partial c_{O_2(sol)}}{\partial z}\right|_{x=0} &= -k_{MV_orr}\left(\Gamma_{max}-\Gamma_{MV^{2+}(ads)}\right)c_{O_2(sol),\,x=0} \\ &\quad -k_{el_orr}\exp\left(-\frac{\alpha_{el_orr}F\left(E-E_{f_orr}\right)}{RT}\right)c_{O_2(sol),\,x=0} \end{aligned} \tag{8.9}$$

The electron-transfer rate constant of the oxygen reduction reaction k_{el_orr} is defined with the unit of m s^{-1}, where the concentration of protons within the interfacial solution is treated as a constant and embraced within k_{el_orr}. α_{el_orr} is the transfer coefficient of the oxygen reduction reaction.

Assuming that sufficient supporting electrolyte is added to the solution[21] and the experiment time is short enough to not cause any apparent convection,[22] the mass transport of the reactive species is only due to the diffusion. The real-time concentration variation of O_2 in solution is governed via Fick's second law:

$$\frac{\partial c_{O_2(sol)}}{\partial t} = D_{O_2} \frac{\partial^2 c_{O_2(sol)}}{\partial x^2} \tag{8.10}$$

By solving Eqn.(8.10) with the boundary conditions Eqn.(8.6) and Eqn.(8.7), the concentration profile of O_2 in solution can be solved as a function of both the experiment time t and the distance from the electrode x. The current, as a function of potential, can be calculated from:

$$\begin{aligned} \frac{I}{\pi {r_{el}}^2 F} = & -k_{el_MV} \exp\left(-\frac{\alpha_{el_MV} F\left(E - E_{f_MV}\right)}{RT} \right) \Gamma_{MV^{2+}(ads)} \\ & + k_{el_MV} \exp\left(\frac{\left(1-\alpha_{el_MV}\right) F\left(E - E_{f_MV}\right)}{RT} \right) \left(\Gamma_{max} - \Gamma_{MV^{2+}(ads)} \right) \\ & - k_{el_orr} \exp\left(-\frac{\alpha_{el_orr} F\left(E - E_{f_orr}\right)}{RT} \right) c_{O_2(sol),\, x=0} \end{aligned} \tag{8.11}$$

and the cyclic voltammetry of MV^+ mediated oxygen reduction reaction can be simulated. The applied potential E used in the cyclic voltammetry varies linearly as a function of the reaction time t and the scan rate v (V s^{-1}), defined as:

$$E = \begin{cases} E_{ini} - vt, & t < \dfrac{\left|E_{ini} - E_{rev}\right|}{v} \\ E_{rev} + v\left(t - \dfrac{\left|E_{ini} - E_{rev}\right|}{v} \right), & t > \dfrac{\left|E_{ini} - E_{rev}\right|}{v} \end{cases} \tag{8.12}$$

where [E_{ini}, E_{rev}] is the potential window for the cyclic voltammetry of the MV^+ mediated ORR and $E_{ini} > E_{rev}$ in this case.

The mass transport eqn.(8.10), accompanied with the boundary conditions (8.6), (8.7) and (8.9), is numerically solved by the finite difference method[23] The simulation program is written in Matlab R2017a and run on an Intel(R) Xeon(R) 3.60G CPU. The convergence of the simulation was tested in light with the space dimension and the time dimension. On average one cyclic voltammogram took c.a. one minute to compute.

8.3.1.2 Simulation of the Potential-Dependent Current Signals of Single Nafion Particles

A doped Nafion particle attached to an electrode is treated as an isolated spherical electrode with the same radius of r_{NP} and a correction factor applied for the loss of flux caused by the shielding of the substrate surface.[24] For an unshielded spherical electrode, only the dimension along the radius r needs to be considered when calculating the concentration distribution at the electrode-electrolyte interface. The reaction rate equations at the sphere electrode surface, $r = r_{NP}$, are the same as used for Nafion particle ensembles. The diffusion toward a sphere is expressed as:

$$\frac{\partial c_{O_2(sol)}}{\partial t} = D_{O_2}\left(\frac{\partial^2 c_{O_2(sol)}}{\partial r^2} + \frac{2}{r}\frac{\partial c_{O_2(sol)}}{\partial r}\right) \tag{8.13}$$

Boundary conditions (8.6), (8.7)and (8.9) are applied at the sphere surface $r = r_{NP}$.

The current expression is similar to Eqn.(8.11) but the correcting coefficient of ln2 is added in the term of the oxygen reduction reaction:

$$\begin{aligned}\frac{I}{\ln 2\pi {r_{el}}^2 F} = &-k_{el_MV}\exp\left(-\frac{\alpha_{el_MV}F\left(E-E_{f_MV}\right)}{RT}\right)\Gamma_{MV^{2+}(ads)} \\ &+k_{el_MV}\exp\left(\frac{\left(1-\alpha_{el_MV}\right)F\left(E-E_{f_MV}\right)}{RT}\right)\left(\Gamma_{max}-\Gamma_{MV^{2+}(ads)}\right) \\ &-k_{el_orr}\exp\left(-\frac{\alpha_{el_orr}F\left(E-E_{f_orr}\right)}{RT}\right)c_{O_2(sol),\,x=0}\end{aligned} \tag{8.14}$$

The validity of the coefficient ln2 is discussed in Appendix B3.

The potential-dependence of the electrochemical response of the MV^+ mediated oxygen reduction reaction on single doped Nafion particles can be simulated. The combination of experiment and simulation reveals the kinetics of the given system, which be discussed in the following sections.

8.3.2 Theoretical Results

8.3.2.1 Macroelectrodes Modified by MV^{2+} doped Nafion Particle Ensembles

In the theoretical model of MV^{+} mediated ORR, there are three key kinetic factors: the electron transfer rate constant, the second-order catalytic rate constant and the amount of MV^{2+} immobilized on the electrode. Dimensionless parameters are applied to simplify the simulation. The dimensionless electron-transfer rate constant, the catalytic rate constant and the amount of immobilized MV^{2+} are defined as:

$$K_{\mathrm{el_MV}} = \frac{k_{\mathrm{el_MV}} r_{\mathrm{el}}^2}{D_{\mathrm{O_2}}} \tag{8.15}$$

$$K_{\mathrm{MV_orr}} = \frac{k_{\mathrm{MV_orr}} \Gamma_{\max} r_{\mathrm{el}}}{D_{\mathrm{O_2}}} \tag{8.16}$$

$$\gamma_{\max} = \frac{\Gamma_{\max}}{c_{\mathrm{O_2}}^{*} r_{\mathrm{el}}} \tag{8.17}$$

The dimensionless current I^{*} and the dimensionless electrode potential E^{*} are also applied in Figure 8.2 and Figure 8.3, expressed as:

$$I^{*} = \frac{I}{\pi F D_{\mathrm{O_2}} c_{\mathrm{O_2}}^{*} r_{\mathrm{el}}} \tag{8.18}$$

$$E^{*} = \frac{F\left(E - E_{\mathrm{f_MV}}\right)}{RT} \tag{8.19}$$

Various kinetic conditions lead to different responses on the cyclic voltammetry. The influences in respect with the electron-transfer step and the catalytic reaction are presented in Figure 8.2. Note that the oxygen reduction reaction on Nafion is excluded in Figure 8.2, where $k_{\mathrm{el_orr}} = 0$ is set, to initially exclusively explore the influence of the kinetics of MV^{+} mediated ORR.

Figure 8.2a shows the voltammograms with $K_{\mathrm{el_MV}}$ varying from 1 to 10^6, where $K_{\mathrm{MV_orr}}$ and $\gamma_{\max}$ are kept constant. When $K_{\mathrm{el_MV}} < 10^4$ (line 1-2 in Figure 8.2a), there is one peak in

the forward wave, of which the peak current is independent of K_{el_MV} but the position depends on the value of K_{el_MV}. As K_{el_MV} increases, the peak becomes broad and splits into two in the case of fast electron transfer rates (line 3-5), indicating that the split wave[25] is only observable in the case of a fast redox process. Figure 8.2b shows the voltammograms with K_{MV_orr} from 10^4 to 10^8 and constant K_{el_MV} and γ_{max}. As for the case of K_{el_MV}, a clear split wave is only available at large catalytic reaction rates (line 3-5). Figure 8.2c shows the voltammograms under different initial amounts of immobilized MV^{2+} γ_{max} where K_{el_MV} and K_{MV_orr} are constants. The split wave is observed with high MV^{2+} amounts (line 3-5). It is also found that in the presence of the split wave, the initial amount of MV^{2+} affects significantly the peak currents of the second peak (the peak at the relatively negative overpotential). Therefore, combining Figure 8.2a, 2b and 2c, the kinetics of the MV^{2+} mediated ORR can be determined via the cyclic voltammetry. In the presence of the split wave, the first peak (the one at the relatively positive overpotential) is related to the catalytic kinetics and the second peak corresponds to the surface redox process.

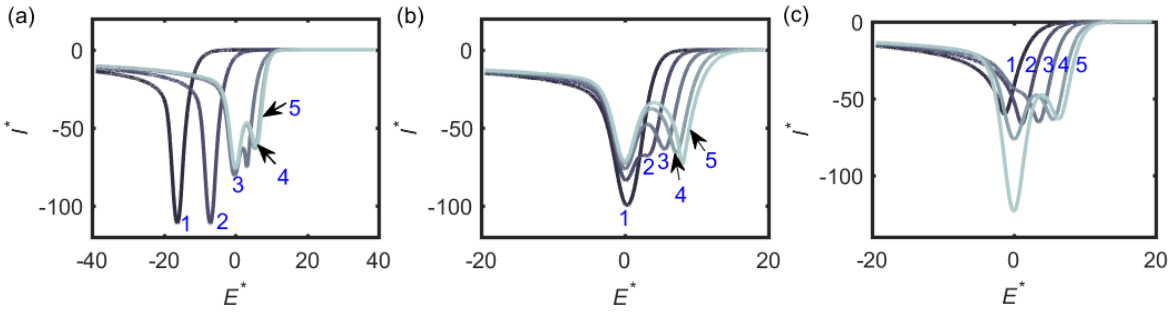


Figure 8.2. (a) Cyclic voltammetry of various K_{el_MV}. The values of K_{el_MV} from line 1 to line 5 are 1.0, 10^2, 10^4, 10^5, 10^6. K_{MV_orr} = 10^6 and γ_{max} = 10^{-2}. Line 4 and line 5 almost overlap. (b) Cyclic voltammetry of various K_{MV_orr}. The values of K_{MV_orr} from line 1 to line 5 are 10^4, 10^5, 10^6, 10^7, 10^8. K_{el_MV} = 10^5 and γ_{max} = 10^{-2}. (c) Cyclic voltammetry of various γ_{max}. The values of γ_{max} from line 1 to line 5 are 5×10^{-4}, 2×10^{-3}, 10^{-2}, 5×10^{-2}, 10^{-1}. K_{el_MV} = 10^5 and K_{MV_orr} = 10^6. The voltammograms are simulated under a dimensionless scan rate $\frac{Fvr_{el}^2}{RTD_{O_2}}$ of 4×10^3.

8.3.2.2 Single MV^{2+} doped Nafion Particles

The cyclic voltammograms on an isolated spherical particle acting as an electrode in different kinetic conditions are shown in Figure 8.3. In the absence of the catalytic reaction, the cyclic voltammogram presents the features of a surface redox process, a pair of waves on the forward and backward directions; the current at high overpotential tends to zero at high overpotentials. However, in the presence of the catalytic step, the surface redox species work as catalysts and keep cycling during the reaction; thus, a steady-state current can be observed at high overpotential in this case.[26]

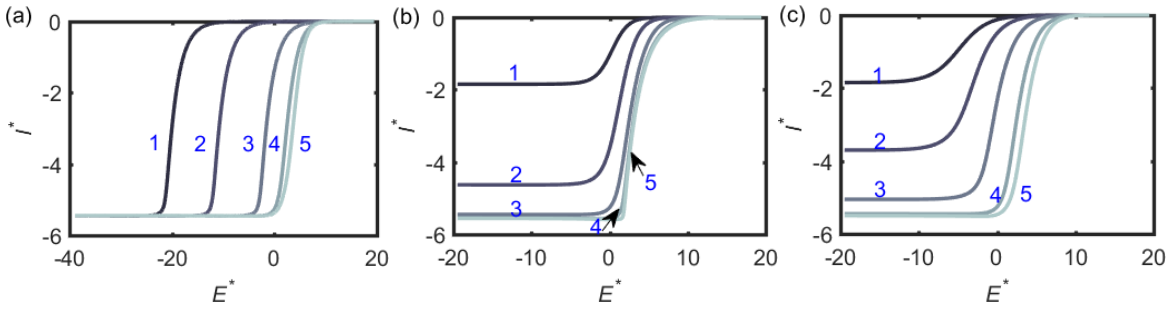


Figure 8.3. (a) Current-potential responses on the isolated particle of various K_{el_MV}. The values of K_{el_MV} from line 1 to line 5 are 10^{-6}, 10^{-4}, 10^{-2}, 10^{-1}, 1. K_{MV_orr} = 1 and γ_{max} = 50. Line 4 and line 5 almost overlap. (b) Current-potential responses on the isolated particle of various K_{MV_orr}. The values of K_{MV_orr} from line 1 to line 5 are 10^{-2}, 10^{-1}, 1, 10^{1}, 10^{2}. K_{el_MV} = 10^{-1} and γ_{max} = 50. (c) Current-potential responses on the isolated particle of various γ_{max}. The values of γ_{max} from line 1 to line 5 are 5×10^{-7}, 2×10^{-6}, 10^{-5}, 5×10^{-5}, 10^{-4}. K_{el_MV} = 10^{2} and K_{MV_orr} = 10^{3}.

The influence of the dimensionless parameters $K_{el_MV,}$ K_{MV_orr} and γ_{max} on the current-potential response of a supported single Nafion particle are tested in Figure 8.3. In Figure 8.3a, decreasing the electron-transfer rate constant leads to the voltammogram shifting toward the direction of more negative potentials. The steady-state current at high overpotentials ($E^* < -10$) depends on the values of K_{MV_orr} and γ_{max}, as shown in Figure 8.3b and 3c. Faster K_{MV_orr} and larger γ_{max} produce higher steady-state current, showing that the overall reaction rate at high overpotentials is determined by the catalytic process.

In the absence of the electrochemical ORR on Nafion, the limiting current at high overpotential of the MV^+ mediated ORR can be derived as:

$$I_{ss}^{*} = 4\ln 2 \frac{n_e K_{MV_orr} \gamma_{max}}{1 + K_{MV_orr} \gamma_{max}} \tag{8.20}$$

where n_e =2 is the stoichiometry number of MV^+ in Eqn.(8.4) and 4ln2 corresponds to the geometry of a spherical particle supported on the substrate. The derivation of Eqn.(8.20) is similar as reported in previous work.[26] Taking line 2 in Figure 8.3b as an example, the simulated current at high overpotentials I_{ss}^{*} is 4.6. The steady-state current calculated from Eqn.(8.20) with parameters K_{MV_orr} = 10^{-1} and γ_{max} = 50 is also 4.6, validating the simulation.

However, in the simulation of real experiment results, the electrochemical oxygen reduction reaction on Nafion particles has to be considered as there is ORR current observed on bare Nafion particles modified electrodes. The kinetics of the electrochemical oxygen reduction reaction on Nafion particles is assumed to be identical with that reported before on carbon electrodes, where k_{el_orr} = 5x10^{-6} m s^{-1}, α_{el_orr} = 0.3 and E_{f_orr} = −0.42 V (vs SCE).[27]

8.4 Results and Discussion

In this section, MV^{2+} doped Nafion particle mediated oxygen reduction reaction (ORR) is investigated *via* cyclic voltammetry and nano-impacts using both experiment and theory. To explore the kinetics of the complicated system, first cyclic voltammograms were recorded on the electrode drop-casted with an ensemble of Nafion particles and second the nano-impact methodology was applied to investigate the single Nafion particle behaviour. By the combination of experiment and theory, the voltammetric features corresponding to

various kinetic conditions are analysed and the kinetics of the MV^{2+} mediated ORR on MV^{2+} doped Nafion particles revealed.

8.4.1Experimental Results

8.4.1.1 Macroelectrodes Modified by MV^{2+} doped Nafion Particle Ensembles

Prior to investigating the oxygen reduction reaction (ORR) mediated by MV-Nafion particles, the electrochemical behaviour of the ensemble of MV-Nafion particles was studied in an oxygen-free buffer solution. First, a glassy carbon (GC) macroelectrode was modified with MV-Nafion particles *via* dropcasting and cyclic voltammograms were recorded. Figure 8.4 shows the first three scans of this modified electrode immersed in a degassed pH 7.4 PBS buffer at a scan rate of 100 mV s^{-1}. Two reduction peaks were observed at ca. −0.70 V and −1.22 V *vs.* SCE, likely corresponding to two one-electron transfers between MV^{2+} and MV^{+}, MV^{+} and MV respectively (as shown in Scheme 8.2).[28] The peak potentials are consistent with the reported values for reduction of MV^{2+} on a glassy carbon electrode coated with a Nafion film.[29,30]

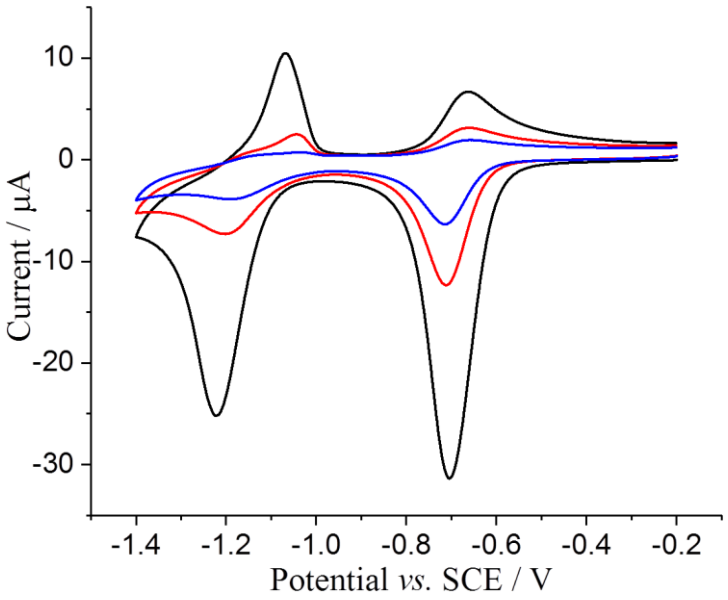
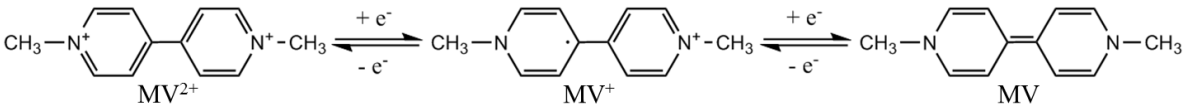


Figure 8.4. Cyclic voltammograms of a glassy carbon macroelectrode modified with MV-Nafion particles in a degassed PBS buffer (pH = 7.4) at a scan rate of 100 mV s^{-1} (black: first scan; red: second scan; blue: third scan).



Scheme 8.2. The structures and two-electron reduction of methyl viologen.

This was further confirmed by the cyclic voltammograms recorded for 1.0 mM of $MVCl_2$ dissolved in the buffer solution using the same glassy carbon electrode, as shown in Figure 8.5, where two similar reductive peaks position were also measured.

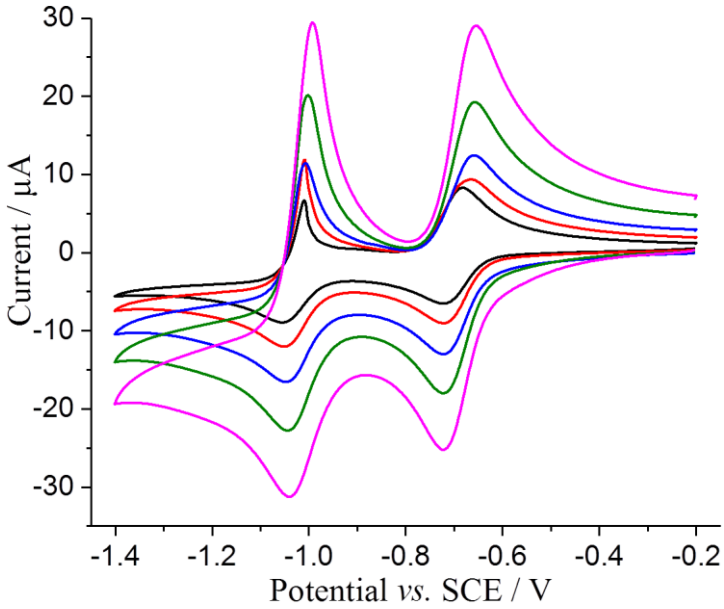


Figure 8.5. Cyclic voltammograms of a bare glassy carbon macroelectrode in a degassed PBS buffer (pH = 7.4) containing 1 mM $MVCl_2$ recorded as a function of scan rate (25 mV s^{-1}, black line; 50 mV s^{-1}, red line; 100 mV s^{-1}, blue line; 200 mV s^{-1}, green line; 400 mV s^{-1}, magenta line).

It is noticeable that the charge passed in both reduction and oxidation of the particle modified electrodes decays progressively with the number of scans, as shown in Figure 8.4, likely indicating loss of MV species from the particles. Analogous experiments were then conducted over narrower potential windows corresponding to the MV^{2+} and MV^{+}, MV^{+} and MV couples only. The resultant voltammograms, as depicted in Figure 8.6, suggest that the reduction of MV^{2+} to MV^{+} is reversible, consistent with literature,[31] and both

cationic forms of MV, namely MV^{2+} and MV^{+} are retained and stable in the Nafion particles after formation, while the neutral form is rapidly lost from the particles.

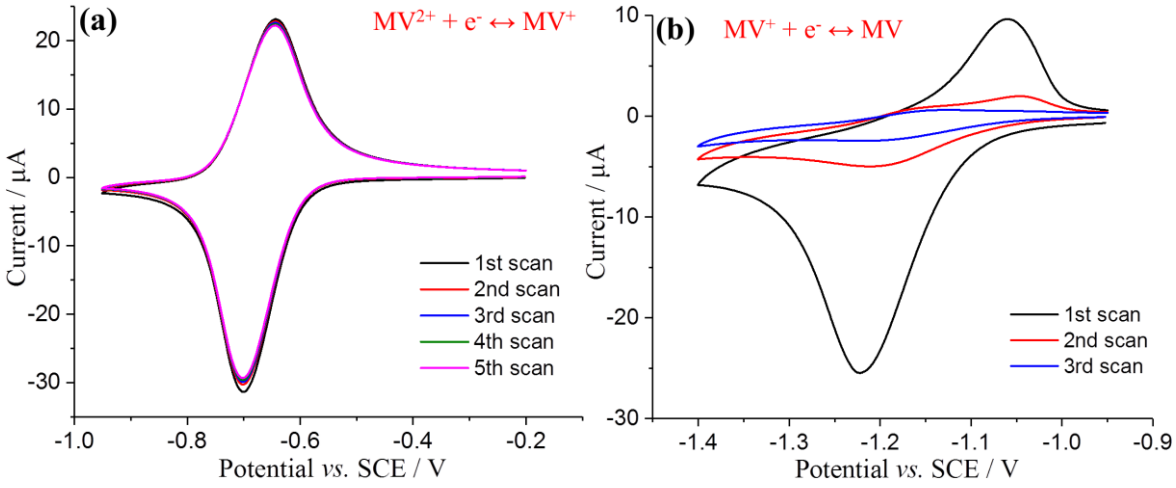


Figure 8.6. Cyclic voltammograms of a glassy carbon macroelectrode modified with MV-Nafion particles in a degassed PBS buffer (pH = 7.4) at a scan rate of 100 mV s^{-1}. (a) recorded from −0.2 to −0.95 V and reversed back to −0.2 V (a) recorded from −0.95 to −1.4 V and back to −0.95 V.

This was further confirmed by a 'stopped' voltammetric experiment as follows. Specifically the cyclic scan is interrupted by a 'stop at −0.2 V for 10s' meaning holding the potential at −0.2 V for 10 seconds during the cyclic voltammetry measurement. As shown in Figures 8.7-9, both of the reductive and oxidative peaks are identical over successive scans even when the potential was held at −0.2 V or −0.95 V for various times, further confirming that both MV^{2+} and MV^{+} are stable in the Nafion particle. As for the neutral form, MV, it is clearly observed that the oxidative (backward) peak markedly decays when increasing the 'stop' time at −1.4 V, as neutrally charged MV has more time to diffuse out of the particles. Note that the equilibrium time in the cyclic voltammetry experiments was set as 3 seconds to equilibrate the electrode at the start potential. Therefore, all the MV^{2+} species in the Nafion particles would be reduced into MV^{+} when the start potential being −0.95 V as shown in Figures 8.6b and 9.

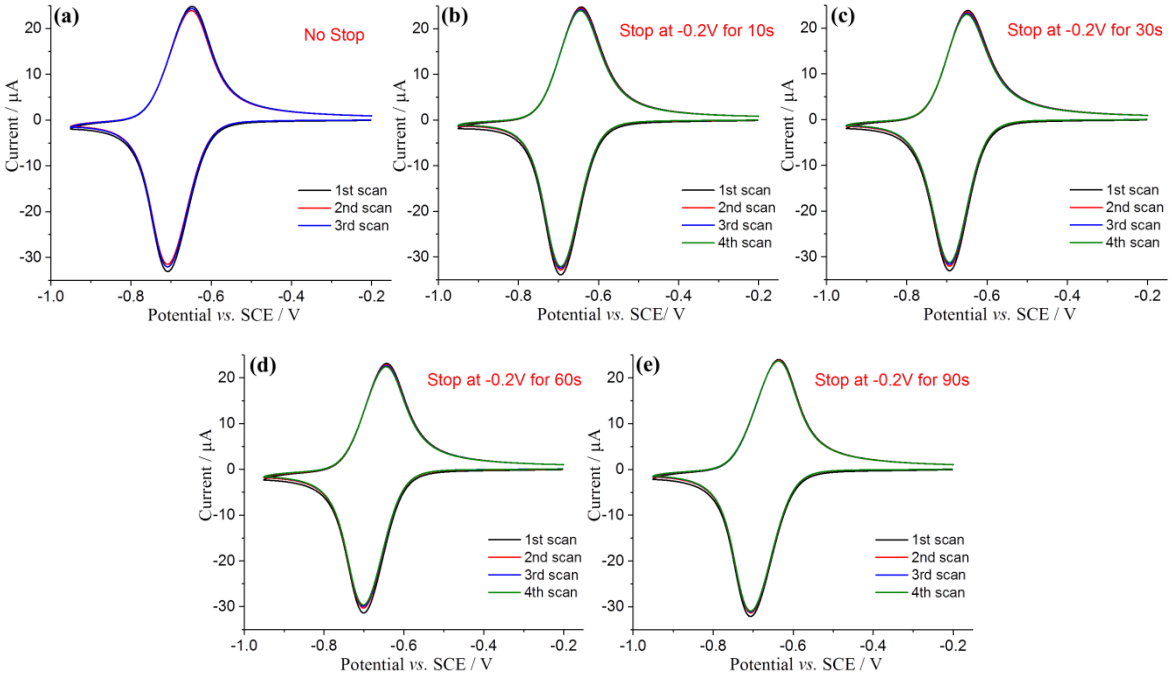


Figure 8.7. Cyclic voltammograms of a glassy carbon macroelectrode modified with MV-Nafion particles in a degassed PBS buffer (pH = 7.4) at a scan rate of 100 mV s^{-1}. The potential was held at −0.2 V for various time then recorded from −0.2 to −0.95 V and back to −0.2 V. (a) 0 s, (b) 10 s, (c) 30 s, (d) 60 s, (e) 90 s.

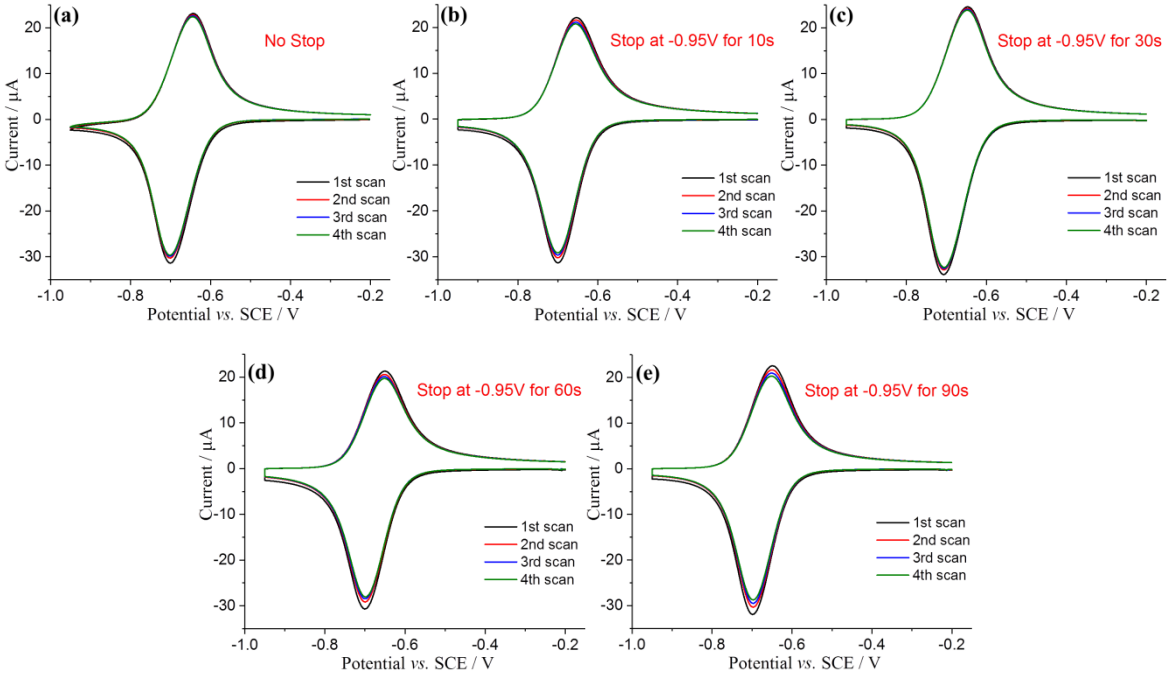


Figure 8.8. Cyclic voltammograms of a glassy carbon macroelectrode modified with MV-Nafion particles in a degassed PBS buffer (pH = 7.4) at a scan rate of 100 mV s^{-1}. The CVs were recorded from −0.2 to −0.95 V and held at −0.95 V for various time then reversed back to −0.2 V. (a) 0 s, (b) 10 s, (c) 30 s, (d) 60 s, (e) 90 s.

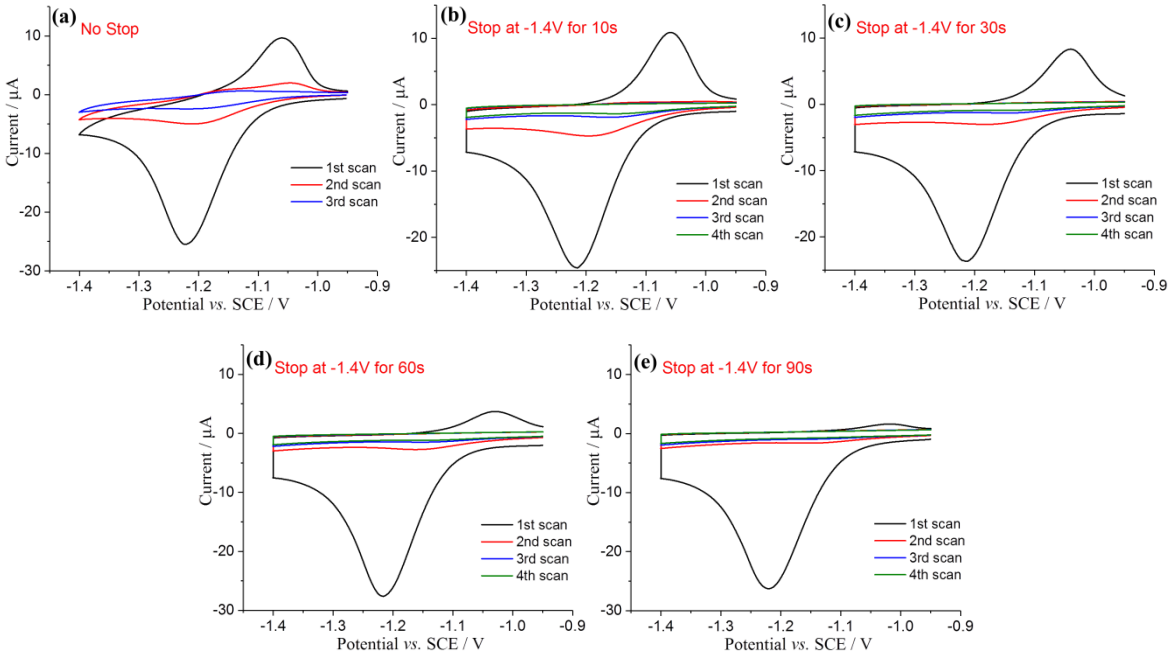


Figure 8.9. Cyclic voltammograms of a glassy carbon macroelectrode modified with MV-Nafion particles in a degassed PBS buffer (pH = 7.4) at a scan rate of 100 mV s^{-1}. The CVs were recorded from −0.95 to −1.4 V and held at −1.4 V for various time then reversed back to −0.95 V. (a) 0 s, (b) 10 s, (c) 30 s, (d) 60 s, (e) 90 s.

Voltammetric methods were further used to study the electrocatalytic behaviour of MV-Nafion particles in the presence of oxygen. When MV^{2+} is absent in air saturated pH 7.4 PBS buffer solution, the voltammogram shows an irreversible peak at ca. −0.71 V for the ORR, scanning on the glassy carbon electrode as shown in Figure 8.10a. The CVs of a MV-Nafion particle modified GC electrode were also conducted in the presence of saturated air showing a large pre-wave in the first electron transfer between MV^{2+} and MV^{+} at −0.53 V, which is attributed to the catalytic reduction of oxygen. Comparing the voltammograms without MV^{2+} (black line) or without oxygen (grey line) clearly demonstrates the mediating activity of MV-Nafion particles modified on the electrode for the reduction of oxygen. An excellent enhancement in the oxygen reduction reaction on GC electrode modified with undoped (pure) Nafion particles can be seen from the significant increase in peak current and anodic shift in overpotential about 180 mV.

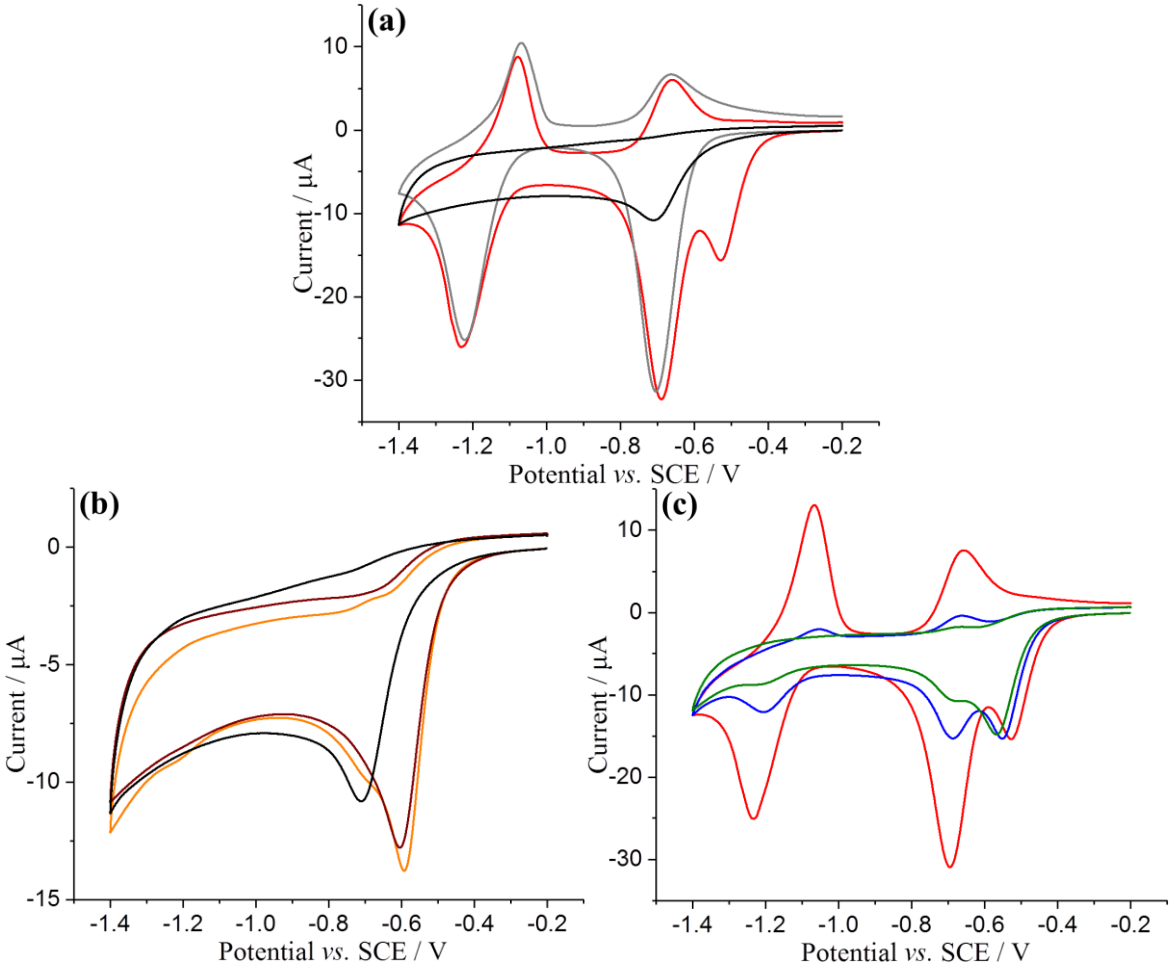


Figure 8.10. (a) Voltammograms of a glassy carbon macroelectrode modified with MV-Nafion particles in a degassed pH 7.4 PBS buffer (grey line) and in air saturated pH 7.4 PBS buffer (red line); Voltammograms of a glassy carbon macroelectrode modified with undoped Nafion particles in air saturated pH 7.4 PBS buffer (black line) at a scan rate of 100 mV s^{-1}. (b) Voltammograms of a glassy carbon macroelectrode modified with MV-Nafion particles at various doping levels of MV^{2+} (0% doping, black; 6.25% doping, brown; 12.5% doping, orange) in air saturated pH 7.4 PBS buffer at a scan rate of 100 mV s^{-1}. (c) MV-Nafion particles at higher doping levels of MV^{2+} (25% doping, green; 50% doping, blue; 100% doping, red).

To further investigate this catalytic reduction of oxygen, analogous voltammetric experiments were then conducted with the same GC macroelectrode modified with MV-Nafion particles at different doping levels (from 100% to 6.25%), as shown in Figure 8.10. At a low doping level (6.25%) only one irreversible catalytic peak is observed, in the form of an increased reductive wave accompanied by a loss of reversibility. The peak potential of the oxygen catalytic reduction shifts to more positive potentials with an increase in

MV^{2+} doping level, when the radical cation MV^{+} is formed electrochemically, the catalytic process is efficient and re-produces MV^{2+} on the voltammetric timescale. As the doping level reaches 25% and above, a gradual split[32,33] of the reductive wave was observed with the first peak continues to shift to a more positive potential whilst the second peak stays unperturbed. The latter peak corresponds to the MV^{2+}/MV^{+} couple where all the oxygen in the vicinity of the electrode is depleted so that the current of the second peak of the split wave, which corresponds to reduction of MV^{2+}, increases proportionally to the doping level of MV^{2+}. However the first peak current does not change much with the variation of MV^{2+} doping levels. This is because the height of the first reduction is controlled by the diffusion of O_2 to the surface as the very effective catalysis leads to a near-zero concentration of oxygen at the electrode surface.

The scan rate dependency of the voltammetric response at two different doping levels of MV^{2+} was further examined, as shown in Figure 8.11. The first peak current was found to be directly proportional the square root of scan rate (Figure 8.11 inset), suggesting that the electrochemical process of the first peak is diffusion controlled. The diffusion of molecular O_2 from bulk solution to the MV-Nafion particles interfacial surface is the rate limiting step of the first peak as discussed above. At this point, a "split" was observed in the 'total catalysis' process[34] where the peak current for the first peak is governed by the diffusion of oxygen. A comparison between the experimental I_p-$v^{1/2}$ relationship in Figure 8.11 and the multiple electron-transfer, reversible Randles–Sevcik equation[7] (Eqn.(8.21)) shows that the electron transfer number of the mediated ORR is approximately 2, indicating the product of the mediated ORR by MV-Nafion is H_2O_2 consistent with literature references.[18,35]

$$I_p = 0.446 n_e F A c^* \sqrt{\frac{n_e F D v}{RT}} \tag{8.21}$$

where A is the electrode geometry area, c^* is the bulk concentration of the reactant, D is the diffusion coefficient of the reactant and v is the scan rate, F (96485 C mol^{-1}) is the Faraday constant, R (8.3145 J mol^{-1}) is the gas constant, and T (298.15 K) is the room temperature.

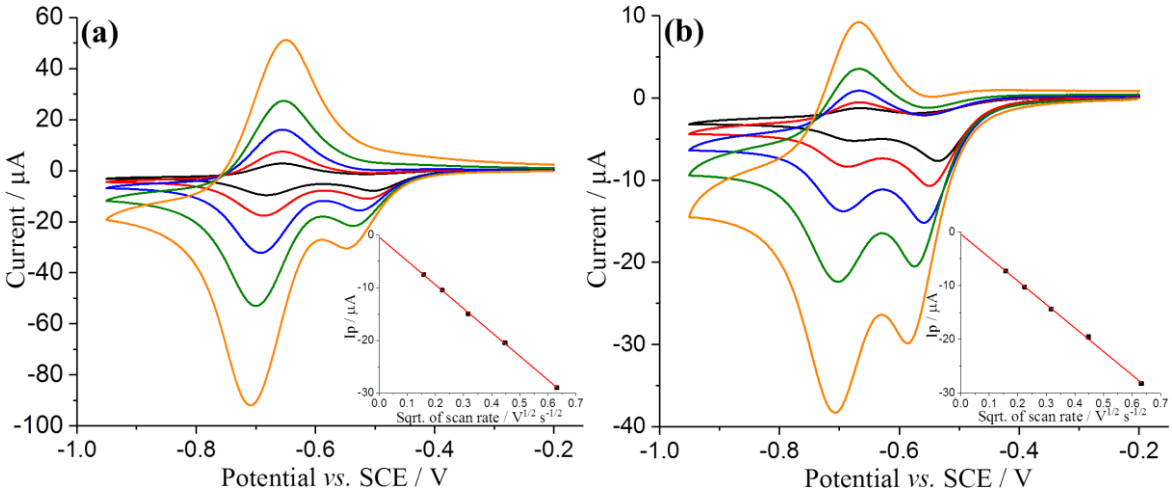


Figure 8.11. (a) Voltammograms of a glassy carbon macroelectrode modified with MV-Nafion particles at 100% doping level in an air saturated pH 7.4 PBS buffer recorded as a function of scan rate (25 mV s^{-1}, black line; 50 mV s^{-1}, red line; 100 mV s^{-1}, blue line; 200 mV s^{-1}, green line; 400 mV s^{-1}, orange line). Inset: the plot of peak current as a function of the square root of the scan rate from 25 mV s^{-1} to 400 mV s^{-1}. (b) Analogous voltammetric study conducted with MV-Nafion particles at 50% doping level.

8.4.1.2 Single MV^{2+} doped Nafion Particles

The nano-impact method was applied to investigate the catalytic reduction of oxygen at single MV-Nafion particles. First, a clean carbon wire microelectrode was immersed in a PBS buffer solution and a known amount of dispersed MV-Nafion particles was added. In the absence of oxygen, under potentiostatted conditions, clear reductive (Faradaic) current spikes were detected at −0.9 V *versus* SCE as shown in Figure 8.12. This potential is significantly more negative than −0.70 V, the first reductive peak potential of MV-Nafion, ensuring the complete reduction of MV^{2+} to MV^{+}. The onset of the current spikes was found to be dependent on the potential and no reductive spikes of MV-Nafion particles

were seen at the applied potential of −0.50 V or more positive, confirming the spikes correspond to faradaic reduction of MV^{2+}-containing particles. Another control experiment was conducted with no particles in the solution (Figure 8.13), and no spikes were detected, further confirming that the occurrence of spikes arises from random collisions of particles with the electrode.

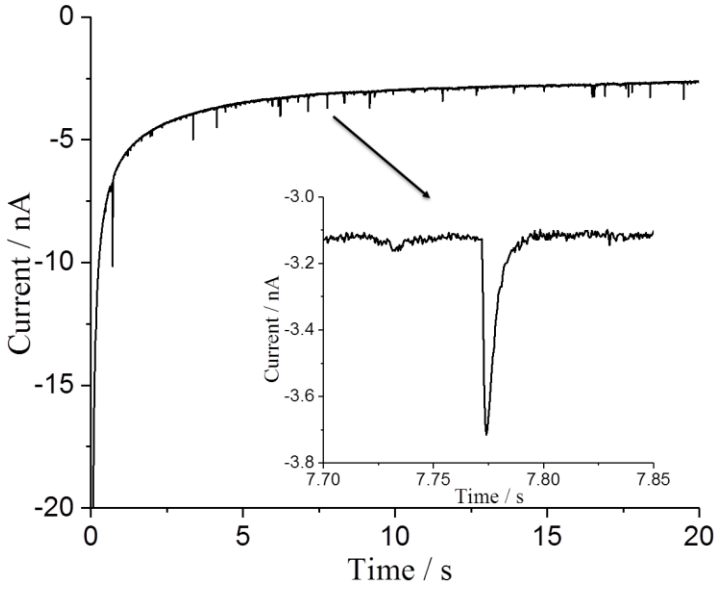


Figure 8.12. Representative chronoamperometric profiles of nano-impacts at +0.90 V versus SCE in a degassed pH 7.4 PBS buffer containing MV-Nafion particles only.

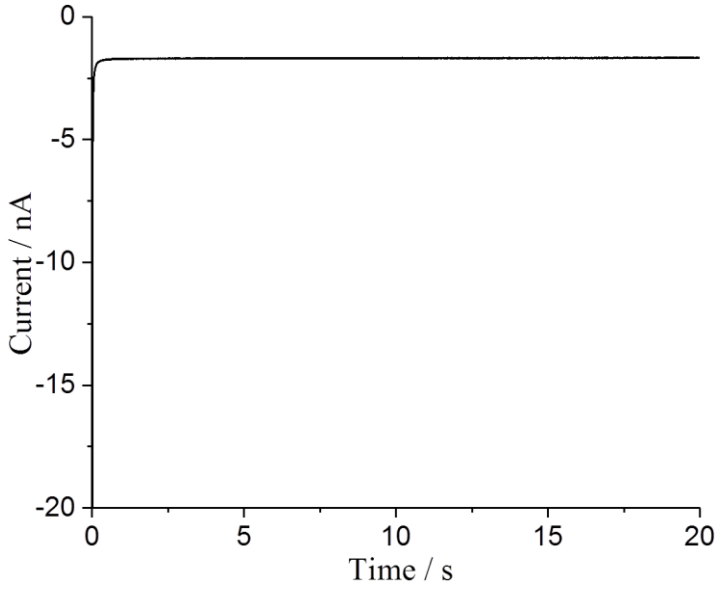


Figure 8.13. Representative chronoamperometric profiles of nano-impacts at +0.90 V versus SCE in a degassed pH 7.4 PBS buffer without addition of MV-Nafion particles suspensions.

A potential variation study was then conducted and chronoamperograms were recorded at different potentials, from −0.2 to −1.4 V. The average charge of individual impacts was calculated and plotted as a function of potential, as shown in Figure 8.14. The presence of two plateaux suggests the two steps of reduction of single MV-Nafion particles corresponding to the reduction of MV^{2+} to MV^{+}, and the subsequent reduction of MV^{+} to MV at more negative potentials. The average charge at the second plateau (5.29 ± 0.30 pC at −1.3 V) is almost twice that at the first plateau (2.74 ± 0.26 pC at −0.8 V), consistent with a second electron transfer occurring during a single particle impacting at higher potentials. The doping amount of MV^{2+} in single Nafion particles, ratio of MV^{2+}:SO_3^-, can also be determined as 1:20 by impact results at full doping level (see Appendix B2 for detailed calculation).

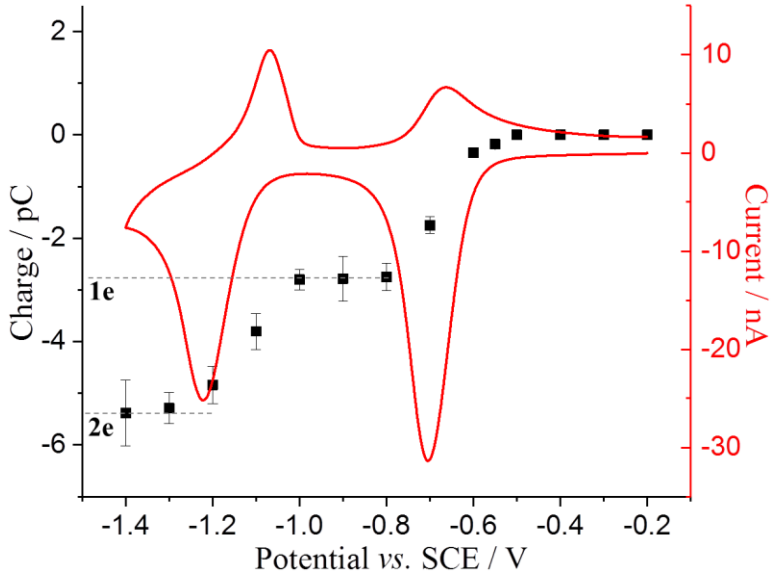


Figure 8.14. Potential variable study of single MV-Nafion particles in a degassed pH 7.4 PBS. The error bars are derived from SD/$(n)^{1/2}$, where SD is the standard deviation and n is the number of the spikes. Overlayed voltammogram was recorded at a glassy carbon macroelectrode modified with MV-Nafion particles in a degassed PBS buffer (pH = 7.4) at scan rate of 100 mV s^{-1}.

Analogous nano-impact experiments of MV-Nafion particles were conducted in air saturated PBS buffer. At potentials negative of −0.40 V, tiny but clear spikes were observed whilst no spikes were seen without oxygen. The amplitudes of the spikes

increased significantly when the applied potential was more negative than −0.55 V (Figure 8.15), indicating the mediated reduction of oxygen by MV^+ occurs when single MV-Nafion particles collide with electrode. To further investigate the reduction of oxygen mediated by MV-Nafion particles, the average charge of individual spikes was determined and plot as function of potential (Figure 8.15b, red circles). Comparing this to the direct reduction of single MV-Nafion particles (black squares), the average charge at each potential is significantly larger, suggesting that mediated reduction of oxygen accompanied the direct reduction of MV^{2+} doped in single particles, contributing to the injection of the measured charge when individual particles collide with the electrode. The onset of spikes decreases from *ca.* −0.5 V vs. SCE in N_2 saturated buffer to *ca.* −0.3 V in air saturated solution, suggesting that at lower potentials (from −0.5 to −0.3 V) only tiny conversion from MV^{2+} to MV^+, which is too small to be detected, but the mediated ORR is so effective resulting in an amplified spike signal even for very short duration impacts. This was further investigated by experiments conducted in air saturated solution with MV-Nafion particles at 50% doping level (green up triangles). The impact charge at −0.55 V is similar for both "full" and "half" doping level of MV^{2+} whereas the onset of spikes shifts to −0.4 V for half doping MV-Nafion particles, which also consistent with voltammetric responses. Moreover, analogous particle-impacts experiments for full doping MV-Nafion particles in oxygen saturated buffer were also conducted (blue down triangles), whose impact charge was found to be *ca.* four times larger than that of in air saturated solution consistent with oxygen level in solution. This further confirms that the catalytic process is efficient enough to re-produce MV^{2+} even at much higher concentrations of oxygen. However, although an "improved" ORR is found in the presence of MV^{2+}, in order to discern kinetic information of this system and the extent to which the mediator MV^{2+} is doped in the Nafion Particles simulation is required and is discussed next.

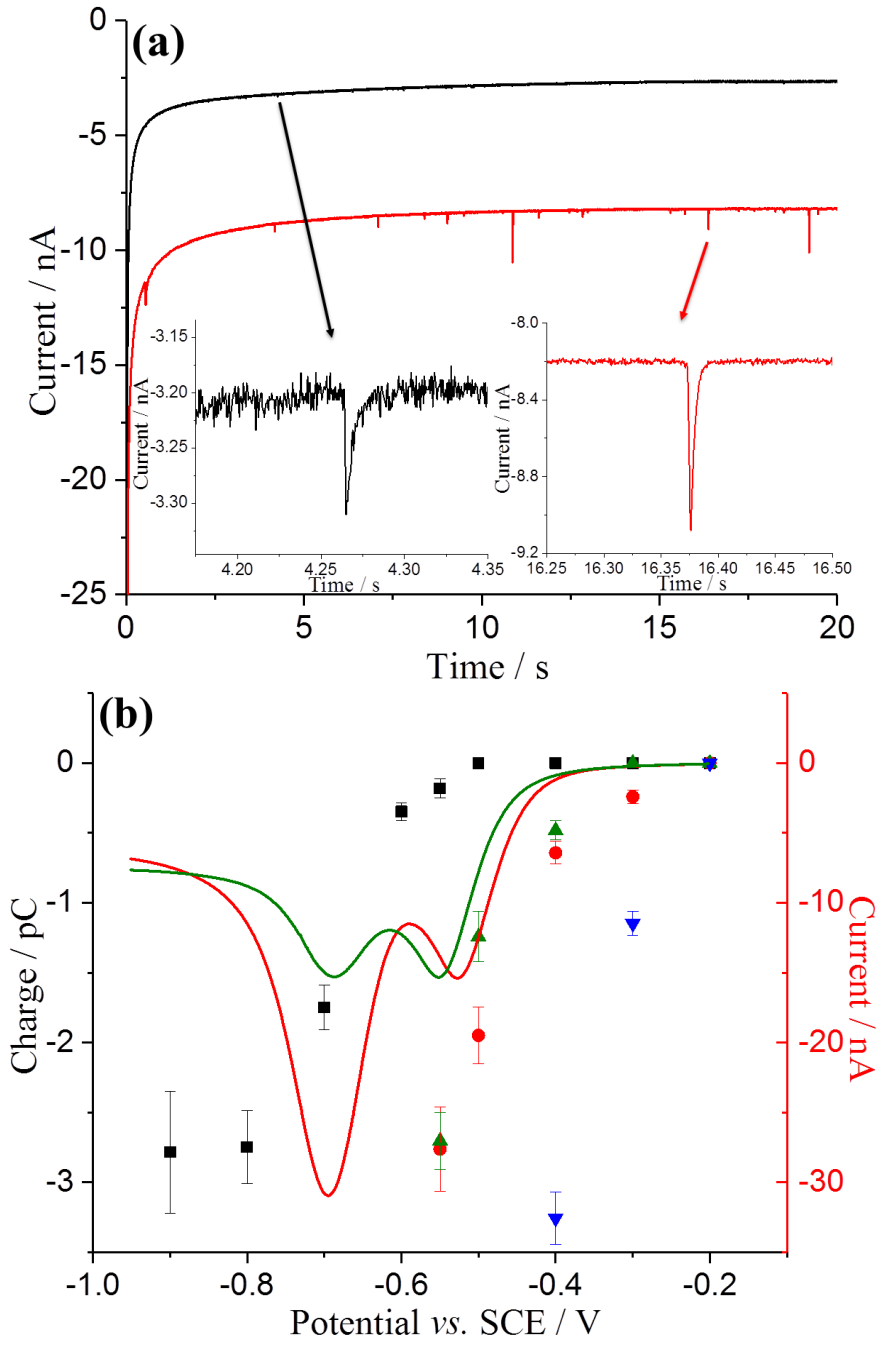


Figure 8.15. (a) Representative chronoamperometric profiles of the nano-impact of MV-Nafion particles at −0.55 V versus SCE in a degassed pH 7.4 PBS buffer (black line) and in an air saturated pH 7.4 PBS buffer (red line). (b) Variable potential study of single MV-Nafion particles: full doping particle in a degssed buffer (black squares); full doing particles in an air saturated buffer (red circles); half doping particles in an air saturated buffer (green up triangles) and full doing particles in an oxygen saturated buffer (blue down triangles). The error bars are derived from $SD/(n)^{1/2}$, where SD is the standard deviation and n is the number of the spikes. Overlayed voltammograms were recorded at a glassy carbon macroelectrode modified with MV-Nafion particles (full doping, red line; half doping, green line) in an air saturated PBS buffer (pH = 7.4) at scan rate of 100 mV s^{-1}.

8.4.2 Simulation of Experimental Results

All simulations reported below were carried out by Dr. Chuhong Lin.

8.4.2.1 Kinetic Study of MV^{2+} Doped Nafion Particle Ensembles

Experimentally a split wave is observed in the voltammogram of ensembles of doped nanoparticles. Based on the EC' mechanism, the split wave is only observable when the redox process is fast. As discussed above, the first peak of the split wave in Figure 8.10 corresponds to the catalytic process while the second one is the simple redox process MV^{2+}/MV^{+}. The peak heights of the split waves and the potential separation between the two peaks characterise the kinetics of the system, from which the values of k_{orr} and Γ_{max} (see Section 8.3.1.1) can be fitted. The cyclic voltammetry of MV^{+} mediated oxygen reduction reaction is simulated with the kinetic parameters matching the experimental results.

The comparison between the simulated (blue dash lines) and the experimental (black solid lines) CVs is shown in Figure 8.16. Figure 8.16a shows the cyclic voltammograms with various doping levels of MV^{2+} (100%, 50%, 25%, 12.5% and 6.25% from left to right), which is represented by the variation of Γ_{max} in the simulation. The key kinetic parameters are k_{el_MV} = 200 s^{-1} and k_{MV_orr} = 4×10^{3} mM^{-1} s^{-1}. The surface coverages used to simulate the five different doping levels are 3.5×10^{-5}, 1.75×10^{-5}, 8.5×10^{-6}, 4.25×10^{-6}, and 2.1×10^{-6}mol m^{-2}. The scan rate of the CVs in Figure 8.16a is 0.1 V s^{-1}, $D_{O2(sol)}$ = 1.96×10^{-9} m^2 s^{-1}, $c_{O2(sol)}{}^{*}$ = 0.26 mM, r_{el} = 1.5 mm, E_{f_MV} = −0.694 V (vs SCE). The kinetic parameters for the electrochemical oxygen reduction reaction are k_{el_orr} = 5×10^{-6} m s^{-1}, α_{el_orr} = 0.3 and E_{f_orr} = −0.42 V (vs SCE). The simulation to the first peak of the split wave fits well with the experiment; while for the second peak, minor uncertainty in the doping levels leads to slight differences from the experimental data notably at low doping

levels. However in general the fit is excellent. Figure 8.16b shows the cyclic voltammograms of various scan rates with 100% doping level of MV^{2+} (0.025, 0.05, 0.10, 0.20, 0.40 V s^{-1}, from top to bottom). With identical kinetic parameters, the simulation in Figure 8.16b fits the experiment well, confirming that the kinetics of MV^{2+} mediated ORR contains a reversible redox process $MV^{2+/+}$ (200 s^{-1}) and a fast catalytic process with the rate constant of 4×10^{3} mM^{-1} s^{-1}. The effective doping level of MV^{2+} on Nafion particles is also found to be 3.5×10^{-5} mol m^{-2} for 100% doped particles, which corresponds to 4.1 mM MV^{2+} absorbed throughout the individual 100% doped particles according to Eqn.(8.8). Note MV^{2+} is absorbed throughout the Nafion particles, not adsorbed on the surface. The effective doping level used in the simulation is because that with respect to the bulk solution, the redox species MV^{2+} which absorbs in Nafion particles are immobilized at the electrode surface. For the same reason, the electron transfer rate constant of MV^{2+}/MV^{+} is defined with a unit of s^{-1} rather than m s^{-1}.

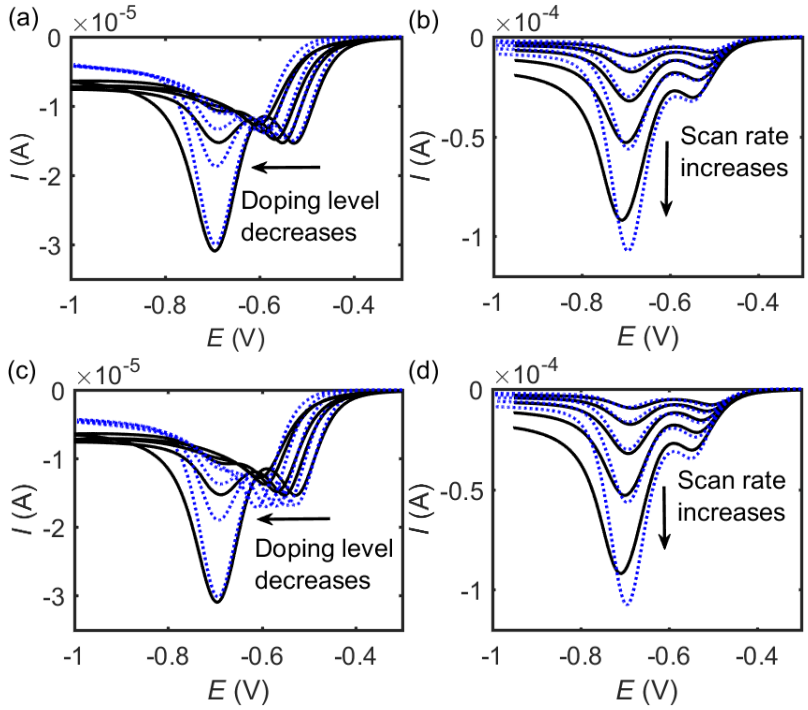


Figure 8.16. (a) CVs of various doping levels of MV^{2+}; (b) CVs of various scan rates. The simulations in (c) and (d) exclude the electrochemical oxygen reduction reaction on Nafion. The black solid line represents the experimental results and the blue dash line shows the simulation. The experiment conditions and the simulation parameters can be found in text.

The simulation in Figures 8.16c and 16d excludes the electrochemical ORR on Nafion. In this case, the difference between modelling the electrochemical ORR and ignoring the electrochemical ORR does not affect the waveshape much, although the first peak of the split wave fits better with appropriate consideration of the electrochemical ORR on Nafion. The oxygen reduction peak (at ca. −0.53 V vs SCE) mediated by the 100% MV doped Nafion particle is approximately −0.1 V from the formal potential of ORR (at ca. −0.42 V vs SCE). Comparing with the ORR peak (at ca. −0.71 V vs SCE) on the glassy carbon modified with pure Nafion particle as shown in Figure 8.10, the overpotential required for the mediated ORR decreases ca. 0.2 V, showing the improvement of the ORR catalysis after doping Nafion particles with MV.

8.4.2.2 Kinetic Study of Single MV^{2+} Doped Nafion Particles

To investigate single MV^{2+} doped Nafion particles, the average charge Q of nano-impact signals is employed to characterize the overall catalytic reaction on the single Nafion particle. The average charge is measured over a series of potentials in experiment. The current-potential dependence is simulated for a spherical electrode with the radius of 0.43 μm and a correction factor of ln2 applied as discussed in Appendix B3. To compare the simulated current-potential response and the nano-impact charges under different electrode potentials, both the current I and the charge Q are normalized by the corresponding values at the given highest overpotential (hop). Note that in experiments, the nano-impact signal cannot be measured at potentials more negative than −0.55 V, due to the interference of the increasing noise and the rapidly increasing background current.

Figure 8.17 shows the experimental charge (black open circles) and the simulated current (blue solid lines) under various electrode potentials. Based on the EC' mechanism, the kinetic parameters used in Figure 8.17 are the same as determined from Figure 8.16, where the electron transfer rate constant of $MV^{2+/+}$ k_{el_MV} = 200 s^{-1}, the catalytic rate

constant of the mediated ORR k_{MV_orr} = 4×10^{3} mM^{-1} s^{-1} and the doping concentration of MV^{2+}, $\rho_{MV2+,}$ is 4.1 mM in each potential (the doping concentration is constant for both ensemble and single Nafion particles and the effective surface coverage Γ_{max} on a 100% doped single Nafion particle is 2.6×10^{-6} mol m^{-2} according to Eqn.(8.8). The simulations in Figures 8.17a and 17b take into consideration both the MV^{2+} mediated ORR and the electrochemical ORR (k_{el_orr} = 5×10^{-6} m s^{-1}; α_{el_orr} = 0.3); while those of Figure 8.17c and 17d exclude the electrochemical ORR. It is found that the simulated potential dependence fits the experimental electrochemical response for both the air saturated system ($c_{O2(sol)}^{*}$ = 0.26 mM) and the oxygen saturated system ($c_{O2(sol)}^{*}$ = 1.24 mM), when involving the electrochemical ORR in the model. However, if excluding the electrochemical ORR, neither the air saturated nor the oxygen saturated condition can be simulated, showing that the electrochemical ORR needs to be modelled in order to precisely quantify the kinetics of the MV^{2+} mediated ORR system.

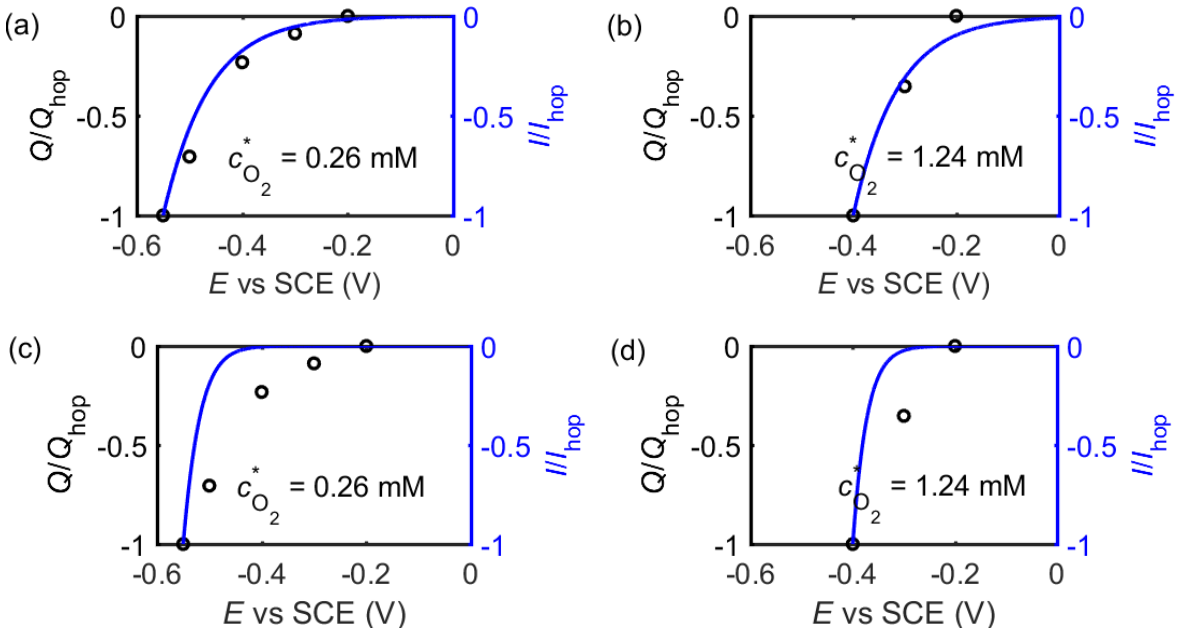


Figure 8.17. Potential dependence of the nano-impact charge and the simulated current-potential response. (a) Air saturated solution (c_{O2}^{*} = 0.26 mM); (b) Oxygen saturated solution. (c) and (d) are the simulation excluding the electrochemical oxygen reduction reaction. The simulation parameters are the same as used in Figure 8.15. r_{NP} = 0.43 μm.

Although the direct, electrochemical ORR current is improved on nanoparticles due to the increase of the diffusion efficiency, in real application, the aim is to use a monolayer or several layers of doped Nafion particles modified on a glassy carbon electrode, as a good substitute for a noble metal electrocatalyst for ORR. In the kinetic study of MV^{2+} doped Nafion particles modified macroelectrodes, the improvement of the oxygen reduction rate by the immobilized MV^{2+} is proved. With the investigation of single MV^{2+} doped Nafion particle, the kinetics of the immobilized MV^{2+} mediated ORR is confirmed, of which the mechanism includes a fast $MV^{2+/+}$ redox process of 200 s^{-1} and a fast catalytic ORR reaction of 4×10^{3} mM^{-1} s^{-1}.

8.5 Conclusions

Nafion particles were doped with methyl viologen to allow the employment of a homogeneous electron transfer mediator in heterogeneous electrocatalysis. By combination of experiment and simulation, the MV^{2+} mediated oxygen reduction reaction is analysed and quantified *via* the cyclic voltammetry measured from macroelectrodes modified by MV^{2+} doped Nafion particles and nano-impact signals measured from single MV^{2+} doped Nafion particles. This study proves that MV^{2+} doped Nafion particles are able to effectively enhance the oxygen reduction reaction current at relatively low overpotentials on carbon based materials, due to the fast redox cycling of MV^{2+}/MV^{+} and the catalytic ability of MV^{+} for oxygen reduction. The strategy is generic and can be applied to design a wide range of soft nanoparticles containing various redox molecules for diverse catalytic reactions and applications, as an alternative to precious metal nanomaterials heavily used in current energy technology such as full cells.

Bibliography

(1) Chen, L.; Lin, C.; Compton, R. G. *Physical Chemistry Chemical Physics* **2018**, *20*, 15795-15806.
(2) Kelly, T. G.; Chen, J. G. *Chemical Society Reviews* **2012**, *41*, 8021-8034.
(3) Hong, W. T.; Risch, M.; Stoerzinger, K. A.; Grimaud, A.; Suntivich, J.; Shao-Horn, Y. *Energy and Environmental Science* **2015**, *8*, 1404-1427.
(4) Watanabe, M.; Tryk, D. A.; Wakisaka, M.; Yano, H.; Uchida, H. *Electrochimica Acta* **2012**, *84*, 187-201.
(5) Koper, M. T. M. *Nanoscale* **2011**, *3*, 2054-2073.
(6) Hu, C.; Dai, L. *Angewandte Chemie - International Edition* **2016**, *55*, 11736-11758.
(7) Compton, R. G.; Banks, C. E. *Understanding Voltammetry*, 2nd ed.; Imperial College Press, 2011.
(8) Nekrassova, O.; Allen, G. D.; Lawrence, N. S.; Jiang, L.; Jones, T. G. J.; Compton, R. G. *Electroanalysis* **2002**, *14*, 1464-1469.
(9) Jeroschewski, P.; Steuckart, C.; Kühl, M. *Analytical Chemistry* **1996**, *68*, 4351-4357.
(10) Dong, S.; Wang, B.; Liu, B. *Biosensors and Bioelectronics* **1992**, *7*, 215-222.
(11) Carlson, B. W.; Miller, L. L. *Journal of the American Chemical Society* **1985**, *107*, 479-485.
(12) Yang, H.; Li, X.; Batchelor-McAuley, C.; Sokolov, S. V.; Compton, R. G. *Physical Chemistry Chemical Physics* **2018**, *20*, 682-689.
(13) Yang, H.; Li, X.; Batchelor-McAuley, C.; Sokolov, S. V.; Kätelhön, E.; Compton, R. G. *Chemistry – A European Journal* **2017**, *23*, 17605-17611.
(14) Lin, Q.; Li, Q.; Batchelor-McAuley, C.; Compton, R. G. *Physical Chemistry Chemical Physics* **2013**, *15*, 7760-7767.
(15) Kätelhön, E.; Tanner, E. E. L.; Batchelor-McAuley, C.; Compton, R. G. *Electrochimica Acta* **2016**, *199*, 297-304.
(16) Sokolov, S. V.; Eloul, S.; Katelhon, E.; Batchelor-McAuley, C.; Compton, R. G. *Physical Chemistry Chemical Physics* **2017**, *19*, 28-43.
(17) Limoges, B.; Savéant, J.-M.; Yazidi, D. *Journal of the American Chemical Society* **2003**, *125*, 9192-9203.
(18) Kong, C.; Qin, L.; Liu, J.; Zhong, X.; Zhu, L.; Long, Y.-T. *Analytical Methods* **2010**, *2*, 1056-1062.
(19) Akita, K. *Industrial & Engineering Chemistry Fundamentals* **1981**, *20*, 89-94.
(20) Davis, R. E.; Horvath, G. L.; Tobias, C. W. *Electrochimica Acta* **1967**, *12*, 287-297.
(21) Dickinson, E. J. F.; Limon-Petersen, J. G.; Rees, N. V.; Compton, R. G. *Journal of Physical Chemistry C* **2009**, *113*, 11157-11171.
(22) Ngamchuea, K.; Eloul, S.; Tschulik, K.; Compton, R. G. *Analytical Chemistry* **2015**, *87*, 7226-7234.
(23) Compton, R. G.; Laborda, E.; Ward, K. R. *Understanding Voltammetry: Simulation of Electrode Processes*; Imperial College Press, 2013.
(24) Streeter, I.; Compton, R. G. *Journal of Physical Chemistry C* **2007**, *111*, 18049-18054.
(25) Savéant, J.-M. *Chemical Reviews* **2008**, *108*, 2348-2378.
(26) Lin, Q.; Lin, C.; Wu, H.; Batchelor-McAuley, C.; Compton, R. G. *The Journal of Physical Chemistry C* **2016**, *120*, 20216-20223.
(27) Zhang, H.; Lin, C.; Sepunaru, L.; Batchelor-McAuley, C.; Compton, R. G. *Journal of Electroanalytical Chemistry* **2017**, *799*, 53-60.
(28) Bird, C.; Kuhn, A. *Chemical Society Reviews* **1981**, *10*, 49-82.
(29) Lu, T.-H.; Sun, I. W. *Talanta* **2000**, *53*, 443-451.
(30) Oliveira, U. M. F. d.; Lichtig, J.; Masini, J. C. *Journal of the Brazilian Chemical Society* **2004**, *15*, 735-741.
(31) Maalouf, R.; Chebib, H.; Saïkali, Y.; Vittori, O.; Sigaud, M.; Jaffrezic-Renault, N. *Biosensors and Bioelectronics* **2007**, *22*, 2682-2688.
(32) Song, P.; Fisher, A. C.; Wadhawan, J. D.; Cooper, J. J.; Ward, H. J.; Lawrence, N. S. *RSC Advances* **2016**, *6*, 70237-70242.

(33) Ward, K. R.; Lawrence, N. S.; Hartshorne, R. S.; Compton, R. G. *Journal of Physical Chemistry C* **2011**, *115*, 11204-11215.
(34) Savéant, J.-M. *Elements of molecular and biomolecular electrochemistry: an electrochemical approach to electron transfer chemistry*; John Wiley & Sons, 2006; Vol. 13.
(35) Sun, W.; Xue, J.; Chen, J.; Mao, L.; Jin, L.; Yamamoto, K.; Tao, S.; Jin, J. *Talanta* **1999**, *49*, 345-356.

Chapter 9

Unscrambling Illusory Inhibition and Catalysis in Nanoparticle Electrochemistry

During the investigation of work in Chapter 8, a 'fake' catalytic behaviour of *undoped* Nafion particles toward oxygen reduction (a lower overpotential and a higher peak current) was surprisingly seen. To fully understand this, a comprehensive investigation synergising experiment and simulation was conducted and reported in this Chapter.

Voltammetry is ubiquitously used in the characterisation of new materials for electrocatalysis. It often sets at least the starting point of any analysis aiming to explore whether electrodes decorated with nano- or other particles feature advanced catalytic behaviour over their bare equivalents. Such analysis bears a substantial and entirely unexpected level of complexity as the mass transport inside the porous layer formed by the particles has a dramatic impact on the measurement. Using the well-studied oxidation of ferrocenemethanol at glassy carbon, experiments in the presence of non-conducting electrochemically-inert microspheres on an electrode surface reproduce trends in the theoretical predictions and illustrates how experimental results may mislead. In addition, the reduction of oxygen at glassy carbon electrodes modified with Nafion particles demonstrates that unless compared with theoretical work, an electrocatalytic activity of Nafion may falsely be inferred. Moreover, the role of electrostatics is explored in three further reactions where the voltammetry is startlingly altered by electrostatic effects.

The work presented in this Chapter includes a series of (three) publications in *Applied Materials Today*.[1-3] Dr. Enno Kätelhön developed the theory and carried out all the simulations reported in this Chapter.

9.1 Introduction

Recent years have seen great advances in research on nanostructured electrodes.[4-10] Surfaces are often modified with nanoparticles and dramatic changes in the voltammetry may be observed since at individual[11-13] or ensembles[5,11] of nanoparticles, reaction kinetics, analyte mass transport, and adsorption can differ significantly from what is seen at bare electrodes. Observations give rise to high hopes, expectations, and great opportunities setting electrocatalysis at the heart of recent research in material science. Much attention has been attracted by topics including carbon materials,[14-16] titanates and TiO_2,[17] nanorods and nanowires,[18,19] and functionalised nanomaterials for bio-sensing.[20]

Voltammetry is certainly the most commonly used technique in electrochemistry and for decades has been the starting point of almost every electrochemical investigation. This includes studies of electrocatalysis[21-24] at new surface materials which aim to determine whether a modification alters the speed at which an electrochemical reaction progresses. To this end, at an electrode modified with nanoparticles, one may conduct a simple voltammetric analysis. The electrode is set in contact with a solution comprising the reactant of interest, and, while the electrode current is monitored, the electrode potential is varied linearly with time from a potential at which no reaction occurs to a potential at which the reaction fully driven by the electrode and only limited by the mass transport of the reactant towards it. Intuitively one may then infer that an "earlier" (lower overpotential) occurrence of a current peak signifies an accelerated reaction and a "later" peak indicates an irreversible reaction. Equally, one may interpret varied peak-to-peak separations in cyclic voltammetry, where the electrode potential is subsequently swept back to its initial value, as changes in the reaction speed: Greater separations suggest slower reaction kinetics as both the forward- and the backward peak occur "later" while smaller separations may be interpreted to result from a more reversible reaction. This work

however proves that such experiments feature a considerably greater complexity and a far more rigorous analysis is needed.

This Chapter first theoretically investigated a reversible electrochemical reaction at a macroelectrode modified with a single layer or layers of inactive spherical nanoparticles which simply serve to 'block'[25] the electrode. The results show that depending on the voltage scan rate both seemingly accelerated and seemingly retarded reactions are observed! Whilst the former has been previously noted[26-29] for other porous materials, the latter is a new voltammetric insight and results from locally enhanced diffusive fluxes. Using the well-characterised one-electron oxidation of ferrocenemethanol in aqueous solution at glassy carbon, the voltammetric peak-to-peak separations and peak currents are experimentally shown to follow theoretically-predicted trends if electrodes are modified with polystyrene microspheres which are non-conducting, non-reactive, and non-absorbing under the set experimental conditions. In addition, the complexity of such analysis at the example of an often-studied reaction, the reduction of oxygen is illustrated: A glassy carbon electrode decorated with a layer or layers of Nafion particles shows elevated voltammetric peak currents and peak potentials which, in the absence of any catalytic reaction, may falsely suggest electrocatalytic activity. Finally, three other reactions (hexaammineruthenium (III) reduction, ferrocenemethanol oxidation, and ferrocyanide oxidation) in that there is an electrostatic interaction between the species involved in the reaction and the surface of the deposited particles are experimentally investigated to explore the role of electrostatics. A startlingly wide range of voltammograms is seen. The presented results are counter-intuitive and yet essential for *all* voltammetric analysis of catalysis at nanostructured interfaces and at porous electrode materials.

9.2 Experimental

9.2.1 Materials and Reagent

Polybead Carboxylate Microspheres (carboxylated polystyrene, aqueous suspension, 2.5% solid content) of three different sizes (0.5 ± 0.004 μm; 4.5 ± 0.18 μm; 20.0 ± 2.27 μm) were purchased from Polysciences (Germany). Phosphate buffered saline buffer solution (PBS, pH = 7.4) was composed of 137 mM NaCl, 2.7 mM KCl, 10 mM Na_2HPO_4 and 1.8 mM KH_2PO_4. The Nafion particles with an average radius of 0.43 ± 0.26 μm were synthesized as described in Chapter 3.

9.2.2 Electrochemical Measurements

A glassy carbon macroelectrode (GC, 3 mm diameter) was used as the working electrode. Varying amounts of the microsphere suspensions were drop-casted on the GC macroelectrode to modify the electrode and left to dry under a nitrogen atmosphere. Cyclic voltammetry was conducted at selected scan rates of between 25 mV s^{-1} to 800 mV s^{-1} in 1.0 mM ferrocenemethanol supported with 0.1 M KCl. For the study of Nafion particles, 10 μL of varying concentrations of fresh prepared Nafion particles suspension was drop-cast on the GC macroelectrode and left to dry under a nitrogen environment. The PBS buffer was placed in water bath at 25°C to for 1 h to obtain air saturated condition before measurements. Cyclic voltammetry was then conducted at selected scan rates of between 25 mV s^{-1} to 400 mV s^{-1} in an air-saturated PBS buffer. For the study of electrostatics, cyclic voltammetry was conducted at selected scan rates of between 25 mV mV s^{-1} to 800 mV s^{-1} in 1.0 mM hexaammineruthenium(III) chloride supported with 0.1 M KCl, ferrocenemethanol supported with 0.1 M KCl, and 1.0 mM potassium ferrocyanide supported with 0.1 M KCl.

9.3 Theoretical Model

All simulations reported below were developed and carried out by Dr. Enno Kätelhön.

The computational analysis investigates an electrochemically reversible reaction of the two species A and B,

$$A + e^- \rightleftarrows B \tag{9.1}$$

at a macroelectrode modified with varying numbers of equally sized inactive, i.e. non-conductive, non-adsorbing, and non-electroactive, spheres packed in complete layers (Figure 9.1a), similar to models previously described in literature,[30,31] on diffusion in porous materials. The solution initially comprises only one of the two species and mass transport solely occurs by virtue of diffusion as the experiment is assumed to be conducted in presence of a sufficient amount of electrolyte screening all electric fields in solution. For modelling purposes, this geometry is simplified along the lines of a diffusion domain approximation[32-34] (Figure 9.1b), and evaluated in cylindrical coordinates (Figure 9.1c). The experiment is conducted at a sufficiently high electrolyte concentration to screen the electric field in solution and to suppress migration. Mass transport is hence solely due to diffusion and can be modelled by diffusion equation:

$$\frac{\partial c_i(\vec{r},t)}{\partial t} = D\frac{\partial^2 c_i(\vec{r},t)}{\partial \vec{r}^{\,2}} \tag{9.2}$$

where c_i is the concentration of species i, $\vec{r}$ is the spatial coordinate $r\vec{e}_r + z\vec{e}_z$ in cylindrical coordinates and D_i is the diffusion coefficient of species i. The assumption of equal diffusion coefficients for the oxidised and the reduced species, $D_A = D_B$, further yields:

$$c_B(\vec{r},t) = c_A(\vec{r},t=0) + c_B(\vec{r},t=0) - c_A(\vec{r},t) = c_A^* + c_B^* - c_A(\vec{r},t) \tag{9.3}$$

where c_A^* and c_B^* are the initial homogeneous concentrations of *A* and *B*, respectively. The above equation enables to solve the entire theoretical model by only evaluating diffusion equation for one of the two species. The electrochemical reaction at the electrode is described by the Nernst equation:[32,35]

$$exp\left(\frac{F}{RT}\left(E-E_f^0\right)\right)=\frac{c_A\left(\vec{r},t\right)}{c_B\left(\vec{r},t\right)} \text{ for } r\in\left[0,r_{max}\right],z=0 \tag{9.4}$$

where E_f^0 is the formal potential and *F*, *R*, and *T* feature their usual significance. All other boundary conditions are set as indicated in Figure 9.1.

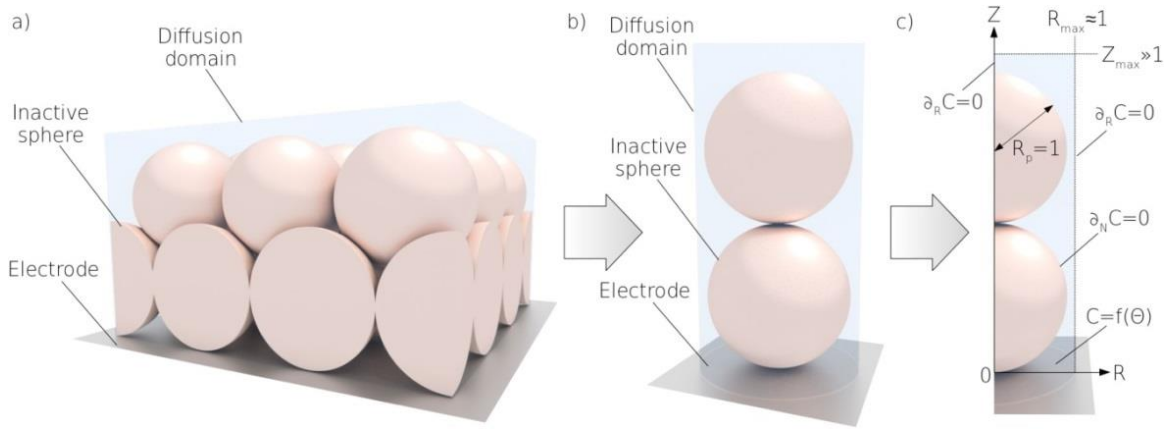


Figure 9.1. Illustration of the geometry considered. (a) The electrode surface is decorated with inactive nanoparticles arranged in a hexagonal packing pattern. (b) The structure depicted in (a) is approximated as a stack of spheres located centrally in a cylindrical diffusion domain. (c) The rotational symmetry of the diffusion domain is exploited to transform the three-dimensional structure into a two-dimensional geometry over which diffusion equation is solved subject to the boundary conditions shown. *R* and *Z* signify dimensionless cylindrical coordinates, *C* is the dimensionless concentration of the reactant, R_p is the particle radius, θ is the dimensionless electrode potential, and $f(\theta)$ represents a Nerstian Dirichlet-type boundary condition. The radius of the simulated space, R_{max}, is set to 1.05 in all calculations while Z_{max} is chosen sufficiently large value to not perturb the simulation results (see Appendix C for further details and derivations).

The theoretical model is solved by means of the Finite Difference apporach and the Alternating Direction Implicit method. For the purpose of this study, custom software was

developed by Dr. Enno Kätelhön. The simulation code is written in *C++* and utilises the *OpenMP* application programming interface for parallel computing. All further data processing and -visualisation is done in *Python* via the packages *NumPy* and *matplotlib*. Software testing[36] is of paramount importance in the development of electrochemical simulations and have conducted a broad range of tests including an analysis of the conservation of mass, comparisons with theoretical peak currents and peak-to-peak separations where feasible, and convergence studies.

To facilitate the comparison of theoretical findings with experimental data, theoretical results are wherever possible reported in the dimensionless coordinates defined in Table 9.1.

Table 9.1. Definition of the dimensionless coordinates used throughout the study. r_p is the particle radius, D is the diffusion coefficient of both species, E^0_f is formal potential of the reaction, c^* is the bulk concentration of the initially present species, S is the dimensionless surface of the electrode, and dA is a dimensionless surface element.

Parameter	Symbol (dimensioned)	Symbol (dimensionless) and transformation
Radial coordinate	r	$R=r/r_p$
Axial coordinate	z	$Z=z/z_p$
Time	t	$T=tD/r^2$
Potential	E	$\theta = F(E-E^0_f)/(RT)$
Scan rate	v	$\delta = Fvr_p^2/(RTD)$
Concentration	c	$C = c/c^*$
Flux	j	$J = \int_s dA\left(-\frac{\partial C}{\partial Z}\right)$

9.4 Results and Discussion

The following results and discussion section first presents the theoretical findings that are obtained from the numerical simulations. Next theory and experiment are compared using the paradigm of the relatively simple fully reversible ferrocenemethanol oxidation. Then the experimental demonstration of the more complex but often-studied reaction, reduction of oxygen, is addressed. Finally, the effect of electrostatic interactions between species involved in the reaction and the particles is experimentally investigated.

All simulations reported below were developed and carried out by Dr. Enno Kätelhön.

9.4.1 Simulation Results

Figure 9.2 presents cyclic voltammograms simulated for different electrode modifications and illustrates that, as one might anticipate, the voltammetry changes with the modification while voltammetric features of significance to the characterisation of catalytic materials—and many other electroanalytical applications—vary. The following provides an analysis of how these features, namely peak positions, peak-to-peak separations, and peak heights, are affected by the electrode modification.

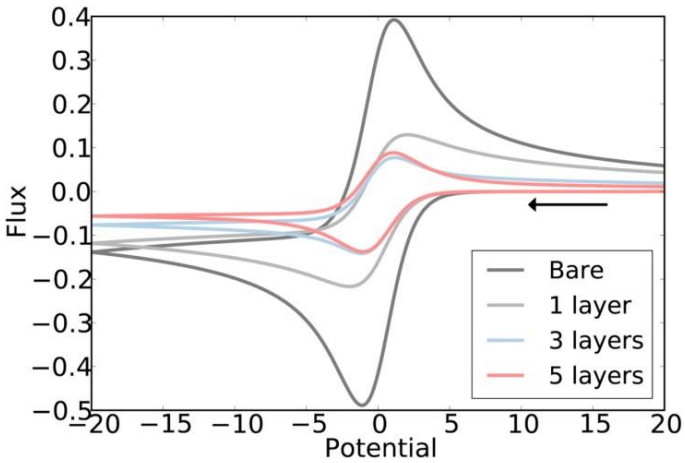


Figure 9.2. Voltammograms of different electrode geometries calculated for a dimensionless scan rate of 0.1. The theoretical model is evaluated for a bare macro electrode and compared with models of electrodes decorated with one, three, and five layers of inactive spheres.

The theoretical study commences with an investigation of the peak positions and the resulting peak-to-peak separations, i.e. the absolute difference between the potentials at which the peaks are observed. To this end, the voltammograms for different electrode modifications as a function of the dimensionless scan rate are evaluated, as shown in Figure 9.3. Note that the definition of the dimensionless scan rate (see Table 9.1) indicates the sphere radius and hence implicating the coverage of spheres. The figure reveals remarkable changes in the positions of the peaks: While at low and high scan rates peak positions approach the positions observed at bare electrodes, there are substantial variations in the intermediate region. At a scan rate of about five, the peak positions for all modified electrodes shift towards the thermodynamic formal potential which in the dimensionless coordinates employed equals zero, and the peak-to-peak separation falls to only less than half of the value observed at a bare electrode at the same scan rate. In stark contrast and possibly counter-intuitively, at a dimensionless scan rate of 0.1, a single layer of spheres results in peaks shifted in the opposite direction *away* from the formal potential while the peak-to-peak separation approximately doubles. Electrodes modified with more than one layer exhibit a similar voltammetry with even more pronounced shifts appearing at lower scan rates. The implications of this result for experimental work are tremendous: If the subtleties of an electrochemical system are not sufficiently recognised, any cyclovoltammetric analysis of an electrode modification may hence, and almost necessarily will, falsely suggest either accelerated or decelerated reaction kinetics independent of the actual kinetics. The factors in Figures 9.2 and 9.3 will be present in any particle modified electrode in the absence of any ‘active’ effects of the spheres. To further emphasise the significance of this finding, the peak-to-peak separations in dimensional coordinates for common experimental set-ups are replotted in Figure 9.4 where a dramatic impact can be seen for realistic parameters.

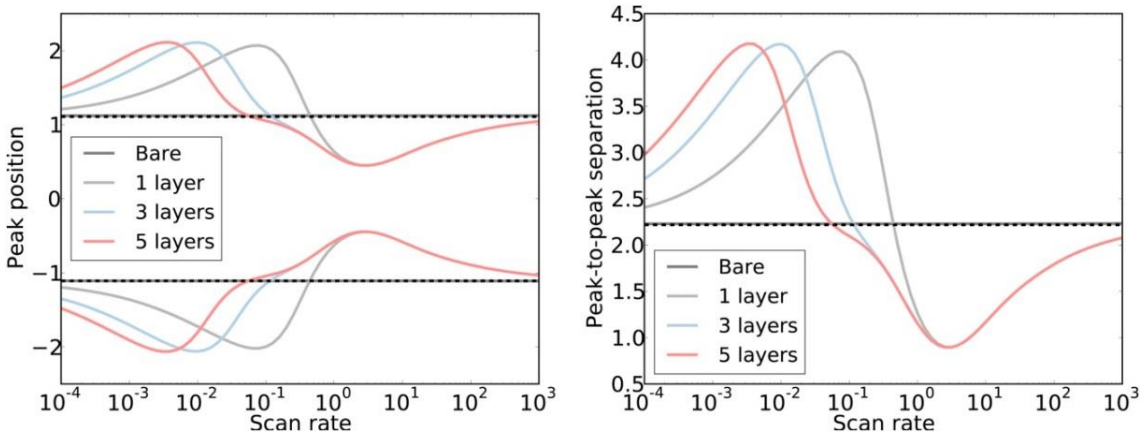


Figure 9.3. Peak positions and peak-to-peak separations as a function of the scan rate. Dashed black lines indicate the theoretical results for a bare electrode. The voltammetric scan covers a potential range of 20.

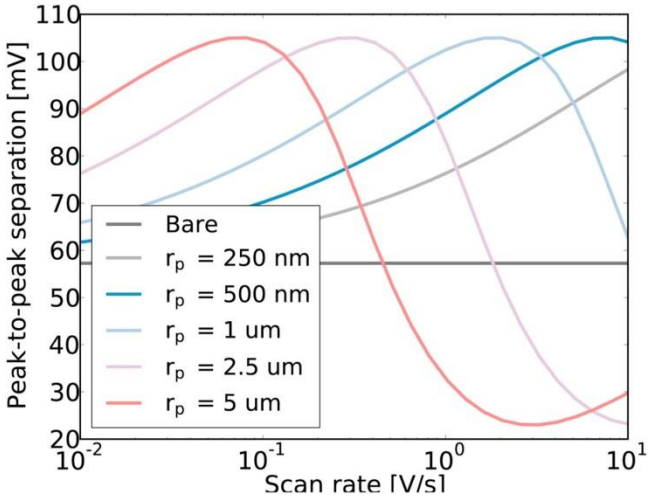


Figure 9.4. Replotted peak-to-peak separations in dimensional coordinates. Results are shown for mono- layers of identical spheres featuring sizes between 250 nm and 5 μm, an analyte diffusion coefficient of 10^{-9} m^2 s^{-1} and a temperature of 298 K.

To identify the underlying physical principles that lead to the remarkable dependency of the peak position on the scan rate, the concentration profiles of species *A* throughout the modelled time interval are analysed. Figure 9.5 depicts the concentration as a function of time and evaluated along a line parallel to the *Z*-axis and perpendicular to the electrode surface. This line cuts through one layer of spheres deposited on the electrode as illustrated in Figure 9.5a.

The analysis first focuses on the concentration profiles in Figure 9.5b which correspond to a dimensionless scan rate of 5 at which the peak shifts towards the formal potential. The concentration profile illustrates that mass transport in the two volumes formed by the sphere, the volume confined by the electrode and the sphere (I) and the volume above the sphere (II), are almost entirely decoupled in terms of diffusion. Concentration changes in (I) near the electrode have only little impact on the concentration in (II) above the sphere. In addition, it is noticed there is hardly any concentration gradient in (I) though the value of the absolute concentration changes with time. The solution in (I) hence remains close to the thermal equilibrium at any time, the concentration not only at the surface but throughout the entire volume approaches Nernst equation, and the voltammetry begins to approach a classical thin layer behaviour,[32,35] with peak positions and a peak-to-peak separation of zero rather than a one-dimensional diffusional voltammogram featuring a peak-to-peak separation of 2.218, which amounts to approximately 57 mV at room temperature.

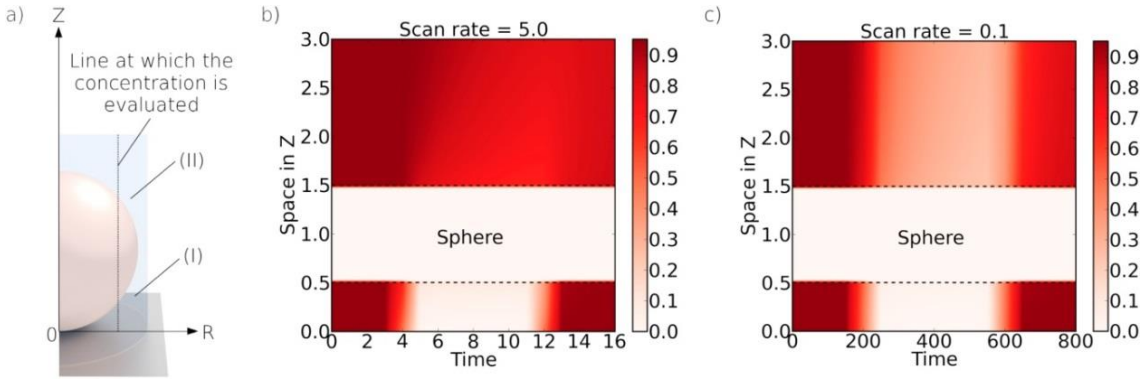


Figure 9.5. Concentration profiles as a function of *Z* and time evaluated for two different dimensionless scan rates and one layer of spheres. (a) Schematic depiction of the line at which the concentration profile is calculated. (b) and (c) Concentration profiles calculated for scan rates of 5 and 0.1, respectively. Please note that for the clarity of presentation voltammograms are modelled within a dimensionless potential range of ±10 rather than ±20 in all other simulations.

Second and much on the contrary, in Figure 9.5c, a completely different mass transport region at the slower scan rate of 0.1 is found. On this time scale, the volumes (I) and (II)

are weakly coupled in terms of diffusion and the concentration near the sphere in (II) follows the concentration in (I). It is noted that a slight delay in response as a result of the much narrowed space available to diffusion where the distance between the sphere and the outer boundary in *R* is the smallest. The observed voltammetry is hence a superposition of the thin-layer voltammetric signal seen in the previous case and the 'delayed' voltammetric signal that arises from material initially located in (II). Due to the limited diffusive coupling between (I) and (II), the latter material in (II) requires more time to reach the electrode surface and therefore only reacts when the electrode potential has already progressed to a greater absolute over- or underpotential. Consequentially, the forward- and backward peaks occur at potential shifts further away from the formal potential. In between the scan rates of 0.1 and 5 there is a point where both effects, the thin-layer effect and the delayed mass transport from (II), balance out and no potential shift is observed compared to the bare electrode.

Third, the peak positions at high and low scan rates, where the voltammetry approaches the behaviour of a bare electrode, can be readily understood with 'classic' voltammetric theory: At fast scan rates the diffusion field does not spread notably into the porous material formed by the spheres and the mass transport does hence not differ qualitatively from the mass transport to a bare electrode. At slow scan rates, the space near the electrode reaches the thermal equilibrium, which, due to the long time scale, embraces the entire surface modification and equally resembles the diffusion field of a bare electrode.

Next the peak heights of the first peaks as a function of the electrode modification are investigated. Figure 9.6 depicts a different analysis of the *same* simulated data already analysed with respect to the peak positions in Figures 9.3 and 9.4. The figure reveals reduced peak heights for all modifications and at all scan rates. The greater the amount of inactive material deposited on the electrode, the more pronounced is the reduction in peak

current and the more it spreads over a greater range of scan rates. This result is much in line with likely expectations as the modification with the inactive material retards the mass transport to the electrode. In addition, for small and large scan rates, peak heights again approach the ones modelled for a bare electrode for the reasons outlined in the previous paragraph: At long times scales, the space near the electrode reaches the steady state which is a thermal equilibrium similar to that at a bare electrode while, at short time scales, the diffusion field does not reach out far enough into the solution to be effected by the electrode modification.

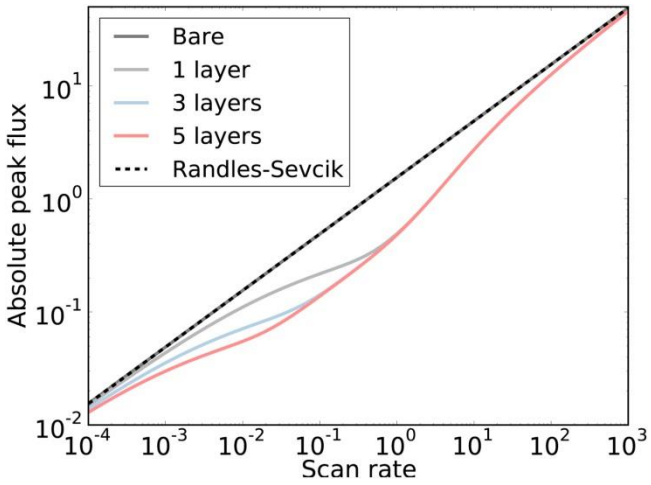


Figure 9.6. Oxidative peak heights as a function of the scan rate. The case of a bare macro electrode is additionally compared with Randles–Ševčík equation illustrating that both graphs overlap. The voltammetric scan again covers a dimensionless potential range of ±20.

9.4.2 Experimental Results

9.4.2.1 Validation of the Theoretical Results

To validate the theoretical findings, the experimental analysis commences with an investigation of the well-characterised electrochemically reversible one electron oxidation reaction of ferrocenemethanol, $FcCH_2OH$, at particle-modified glassy carbon electrodes. To this end, inactive carboxylated polystyrene microspheres of equal sizes (r_p = 250 nm, 2.25 μm, and 10 μm) were dropcasted onto the electrode surface to form dense layers in a

homogeneous hexagonal packing pattern as evident from the optical microscopic images of the 10 μm spheres shown in Figure 9.7.

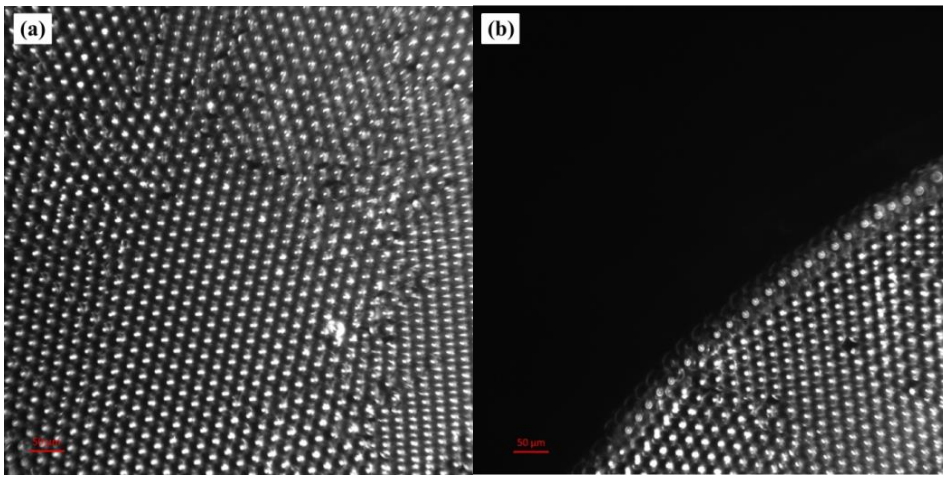


Figure 9.7. Optical microscopic images of a glassy carbon macroelectrode dropcasted with one layer of microspheres featuring a radius of 10 μm (a) middle view of the electrode (b) edge view.

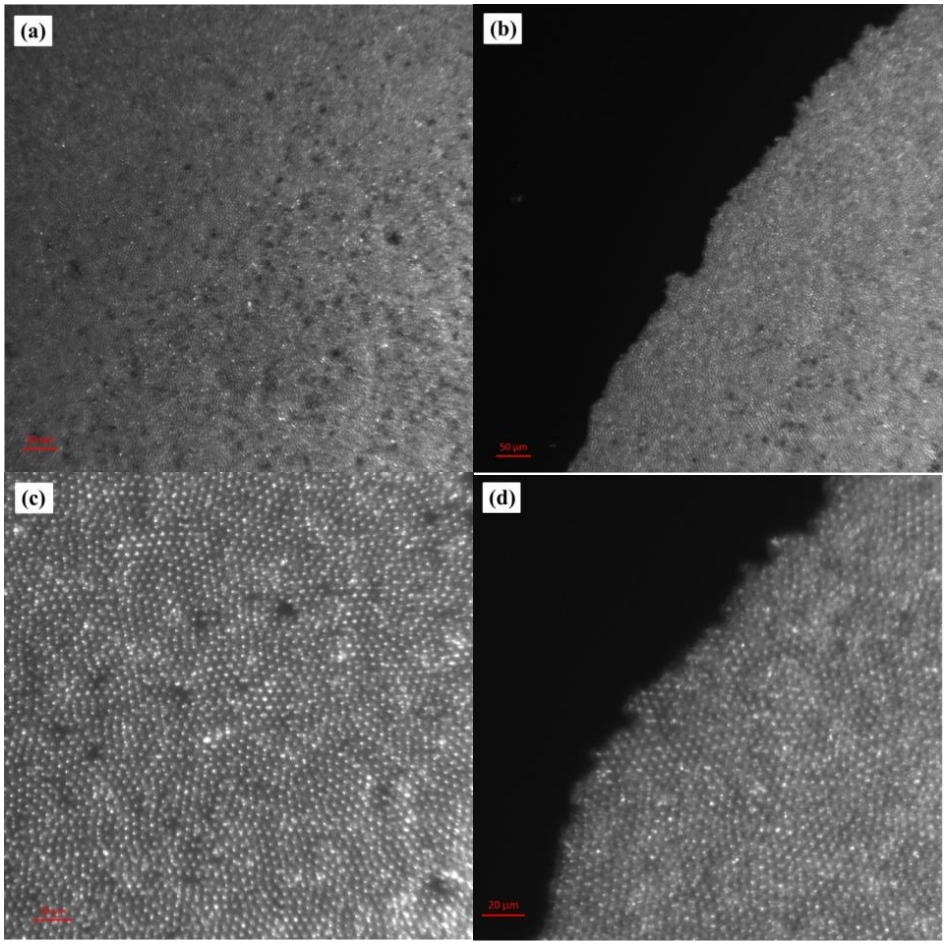


Figure 9.8. Optical microscopic images of a glassy carbon macroelectrode dropcasted with one layer of microspheres featuring a radius of 2.25 μm (a) middle view of the electrode (b) edge view (c) Zoon-in of the middle view (d) Zoom-in of the edge view.

Corresponding microscopic images for an electrode modified with smaller spheres featuring a radius of 2.25 μm, as depicted in Figure 9.8, reveal that these arrange in a less symmetrical fashion. A single-layer of spheres in a dense hexagonal packing is also seen though locally a few holes exist which feature sizes ranging from 5 μm to 15 μm and indicate that small areas of electrode surface have remained uncovered. It can be further noticed that the edge view of electrode surface shows rough outline in comparison with the larger (10 μm) microspheres. Nonetheless, a comparison with Figure 9.1a reveals that the electrode geometry for both particle sizes closely resembles the theoretical model.

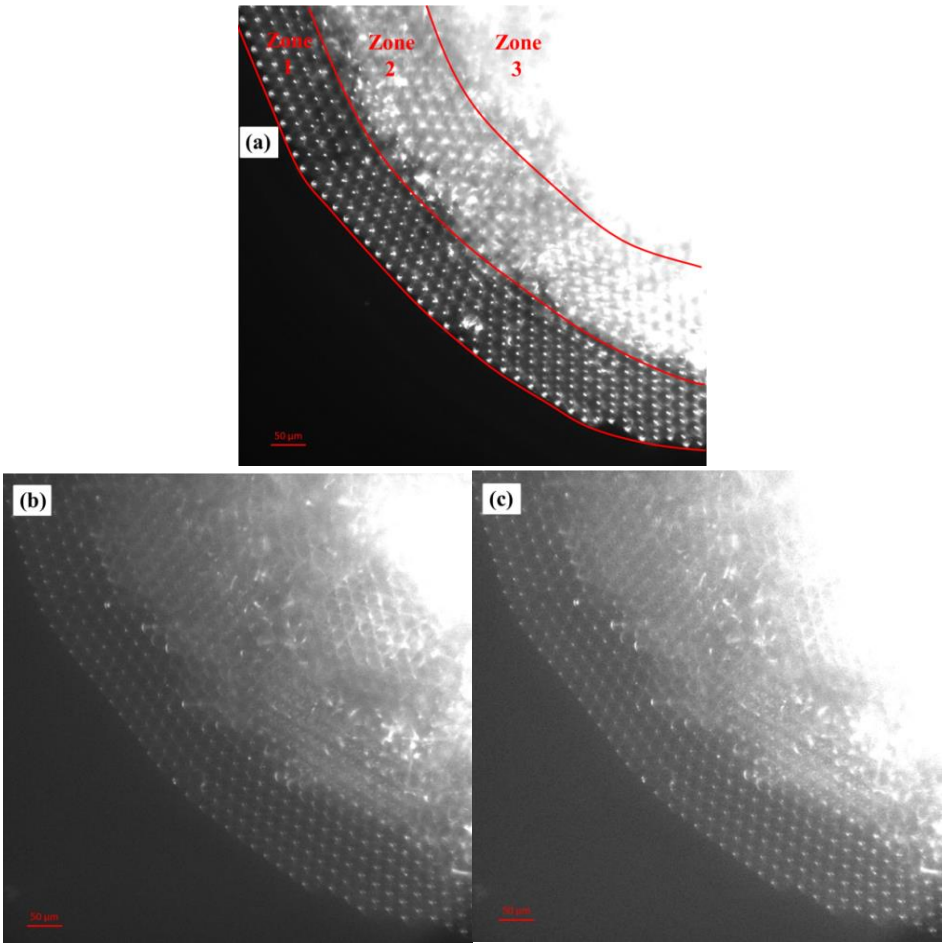


Figure 9.9. Optical microscopic images of a glassy carbon macroelectrode modified with one layer (Zone 1), two layers (Zone 2) and multiple layers (Zone 3) of polystyrene microspheres with 10 µm radius (a) original microspheres after drying on the electrode surface (b) after immersion in solution containing 1 mM ferrocenemethanol and 0.1 M KCl for 20 min (c) after a cyclic voltammetry from −0.2V *vs.* SCE to +0.6 V and back to −0.2V at the scan rate of 25 mV s^{-1}.

Prior to the investigation, the stability and electrochemical inactivity of the polystyrene microspheres in terms of possible swelling and shrinking under the utilised experimental conditions was first investigated. To this end layers of polystyrene microspheres were subsequently dropcasted centrally onto the electrode while the areas covered by each step decrease, hence forming three zones as seen in Figure 9.9a. A solution containing 1 mM ferrocenemethanol and 0.1 M KCl was slowly injected into the support cell and the electrode surface was immersed. Microscopic images were taken after 20 min, which is the time scale for the following electrochemical experiments, and no change of the microspheres was observed as shown in Figure 9.9b. Furthermore, cyclic voltammetry was performed from −0.2 V vs. SCE to 0.6 V and back to −0.2 V at a scan rate of 25 mV s^{-1} and a third microscopic image was taken, see Figure 9.9c. Microspheres again remain visibly unaltered suggesting stability and inactivity of the deposited layers throughout electrochemical experiments.

Next cyclic voltammograms were recorded at different scan rates at a bare electrode and at the electrodes modified with polystyrene microspheres in a degassed solution containing 1.0 mM ferrocenemethanol and 0.10 M KCl. The peak current of ferrocenemethanol oxidation on the bare electrode is directly proportional to the square root of scan rates, as shown in Figure 9.10, suggesting that it is a diffusion-controlled electrochemical process. On the basis of one-electron-transfer revisable Randles-Ševčík equation[32] (Eqn.(9.5)), the diffusion coefficient is determined to 7.6×10^{-10} m^2 s^{-1} which matches the value of $(7.6 \pm 0.4) \times 10^{-10}$ m^2 s^{-1}priorly reported.[37] The formal potential is found to be 0.19 V vs SCE via determination of the mid-point potential.

$$I_p = 2.69 \times 10^5 A D^{0.5} C v^{0.5} \text{ at } 298\text{K} \quad (9.5)$$

where A is the geometrical surface area of working electrode, D is the diffusion coefficient, C is the concentration in the bulk solution, and v is scan rate.

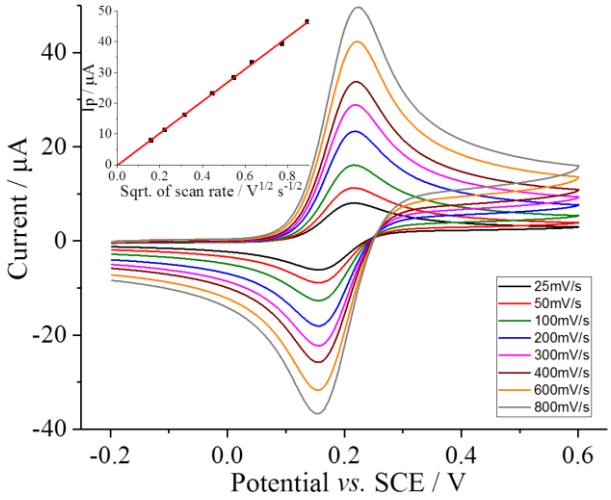


Figure 9.10. Voltammograms of a bare glassy carbon macroelectrode in solution containing 1mM ferrocenemethanol and 0.1m KCl recorded as a function of scan rate. Inset: the plot of peak current as a function of the square root of the scan rate from 25 mV s^{-1} to 800 mV s^{-1}.

The voltammetry of the bare electrodes is subsequently compared the theoretically predicted peak-to-peak separation of $2.218RT/F$[32] and peak currents which both apply for a reversible one-electron reaction. Good agreement is seen between experiment and theory as shown in Figure 9.11 and the theoretical model is hence confirmed.

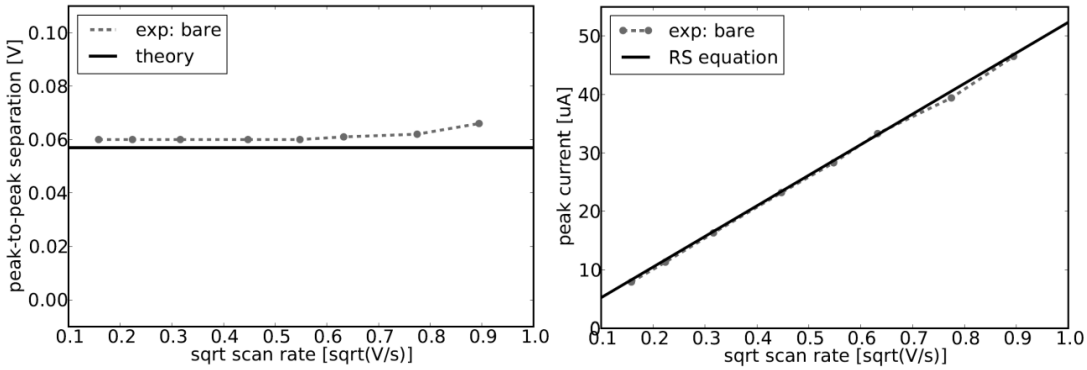


Figure 9.11. (a) Comparison of measured and theoretical peak-to-peak separations as a function of scan rate (b) Comparison of measured and theoretical peak currents as a function of scan rate. Theoretical peak heights are calculated via the Randles-Ševčík equation equation.

Moving on to considering modified electrodes, Figure 9.12a presents aggregated data of large number of voltammograms recorded for an average surface coverage of one layer of microspheres: The measured peak-to-peak separations (dashed lines) are plotted as a function of scan rate for comparison with simulated data (solid lines). Following the

theoretical prediction, significant variations in peak-to-peak separations for all sphere radii are found. Most notably and depending on the sphere radius, separations may increase *or* decrease with increasing scan rates which may falsely suggest negative *or* positive catalysis, respectively. Simulated trends are reproduced and, for the smallest spheres, an almost an ideal match between experiment and theory is seen. Differences may relate to the assumptions made in the theoretical model - particularly the diffusion domain approximation and the assumption of perfect hexagonal packing – and imperfections in the experiment inducing the imperfections in the deposited layers of spheres, and a potentially limited electrolytic support within nano-scaled features inside the porous layer. Similar results are obtained for two and three layers of spheres as shown in Figures 9.12b&c.

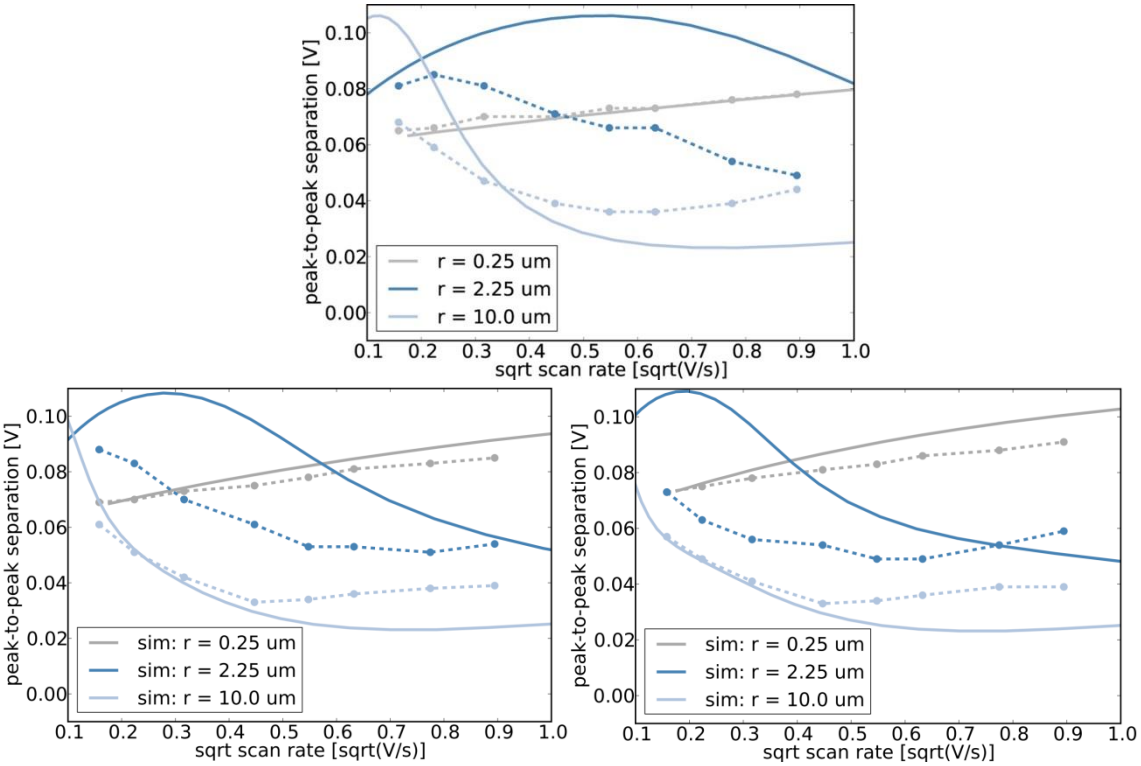


Figure 9.12. (a) Comparison of measured (dashed lines) and simulated (solid lines) peak-to-peak separations as a function of scan rate for three different sizes of microspheres and an average surface coverage of one layer of spheres. All simulations here and in the following use a diffusion coefficient of 7.61×10^{-10} m^2 s^{-1}. Experimental data was recorded in a solution comprising 1 mM ferrocenemethanol and 100 mM potassium chloride. (b) Two layers of spheres (c) Three layers of spheres.

Having shown the applicability of the theoretical model in terms of peak-to-peak separations, the analysis turns towards measured peak currents. Figure 9.13a plots the peak currents as a function of the scan rate for an average surface coverage of one layer of spheres (dashed lines). In agreement with theoretical predictions and in stark contrast to the expected square-root dependency of the peak current on the scan rate at a bare electrode, significant variations are seen with the scan rate *and* the particle size. The same figure compares experimental data with simulations (solid lines) which reproduce trends in experimental data and support the validity of the theoretical model. Similar results are obtained for averages of two and three layers are shown in Figures 9.13b&c

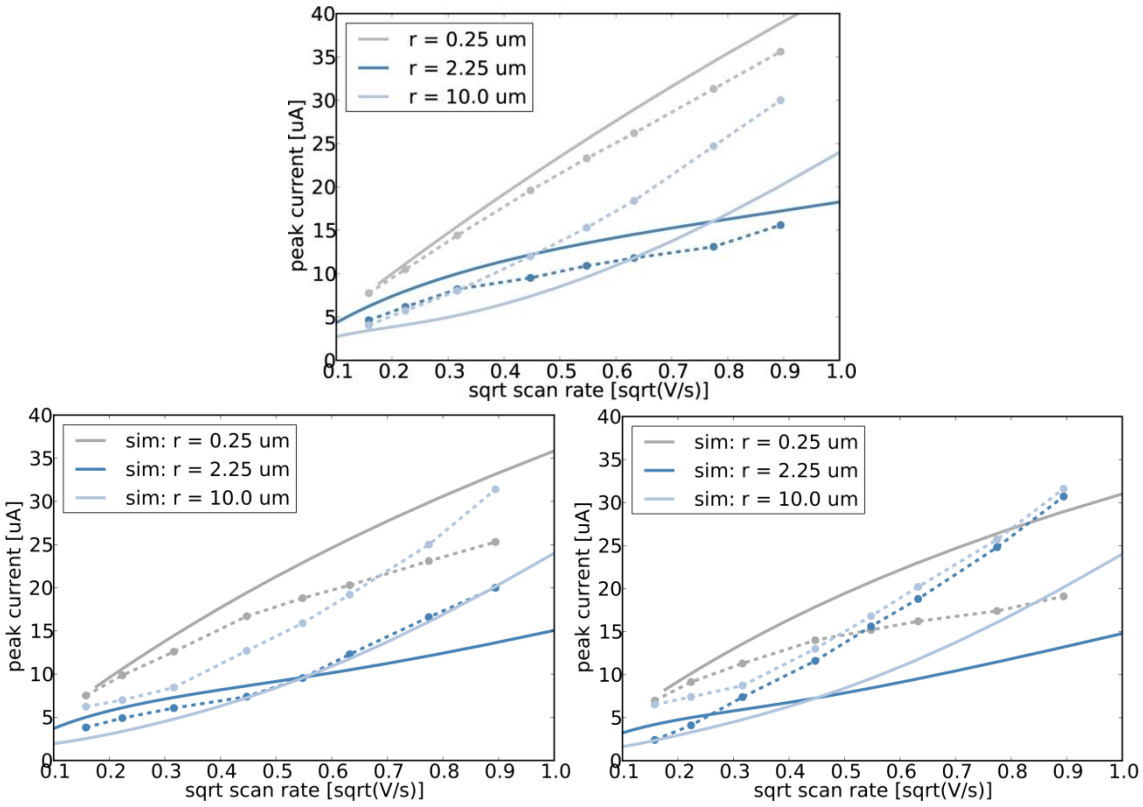


Figure 9.13. (a) Comparison of measured (dashed lines) and simulated (solid lines) peak currents as a function of scan rate for three different sizes of microspheres and an average surface coverage of one layer of spheres. Experimental data was collected from the same voltammograms as analysed in Figure 9.12 (b) Two layers of spheres (c) Three layers of spheres.

9.4.2.2 A More Complex System: Oxygen Reduction

The above experimental data has confirmed the theoretically-predicted complexity of any voltammetric analysis at nano-structured surfaces. Using the relatively simple and well-studied reaction of ferrocenemethanol at glassy carbon, it has been demonstrated that a sole voltammetric analysis of particle-modified electrode cannot provide insight into the catalytic properties of the material deposited unless accompanied by suitable theoretical models or data obtained from other experimental techniques. To further emphasise this fact, the following presents data of a reaction that is much more in the focus of current research, namely the reduction of oxygen.[38] In comparison to ferrocenemethanol, this is a much more complex process as it involves multiple electron-transfers, reaction intermediates, and species that may adsorb at some electrode surfaces:

$$O_2 + 2H^+ + 2e^- \rightarrow H_2O_2 \tag{9.6}$$

or:

$$O_2 + 4H^+ + 4e^- \rightarrow 2H_2O \tag{9.7}$$

While the above theoretical model of a reversible one-electron transfer is hence not applicable, experimental data of the oxygen reduction nonetheless strikingly illustrates the complexity of the mass transport in porous layers and points out the risk of misinterpretation of experimental results.

The following investigates the voltammetry of a glassy carbon electrode modified with layers of Nafion particles featuring an average radius of 430 nm, as used in Chapter 8. To this end, the electrochemical activity of the Nafion particles was first measured: Voltammograms were recorded at a bare- and a modified electrode in Argon-saturated phosphate buffered saline solution at pH 7.4 where no changes are seen except for an expected[39] small increase in the electrode capacitive current, as shown in Figure 9.14, suggesting the particles are inactive in the buffer solution.

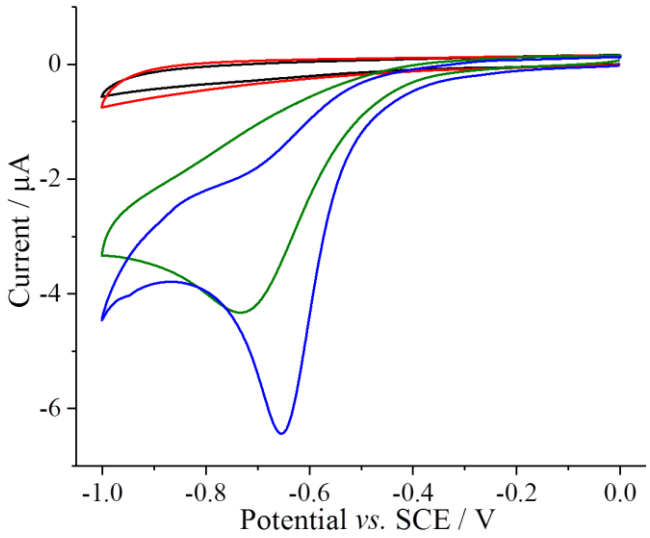


Figure 9.14. Voltammograms of a bare (black) and modified (with 15 layer of Nafion particles; red) glassy carbon macroelectrode in Argon-degassed pH 7.4 PBS buffer solution and voltammograms of a bare (green) and modified (with 15 layer of Nafion particles; blue) glassy carbon macroelectrode in air-saturated pH 7.4 PBS buffer solution; scan rate = 25 mV s^{-1}.

The bare glassy carbon electrode is subsequently characterised in air-saturated phosphate buffered saline solution at pH 7.4 featuring an oxygen concentration of 0.26 mM,[40] which is known to be the two-electron process[41] shown in Eqn.(9.6). Via a Tafel analysis (Figure 9.15b),[42] the electrochemical transfer coefficient, α,[43,44] is determined to 0.25 and by comparison with the multiple-electron-transfer irreversible Randles-Ševčík[32] (Eqn. (9.8)) the diffusion coefficient is found to be 2.00×10^{-9} m^2 s^{-1}. Both values are in excellent agreement with prior literature values of (0.24 ± 0.06)[45] and (1.95×10^{-9} m^2 s^{-1})[46], respectively.

$$I_p = -0.496\sqrt{n' + \alpha}nFAc\sqrt{\frac{FvD}{RT}} \qquad (9.8)$$

where n is the number of electrons transferred in an overall electrochemical process (n = 2), n' is the number of electrons involved before the rate determining step (n' = 0),[45] C is the oxygen concertation in solution (C = 0.26 mM), F is the Faraday constant, R is the gas constant and T is temperature.

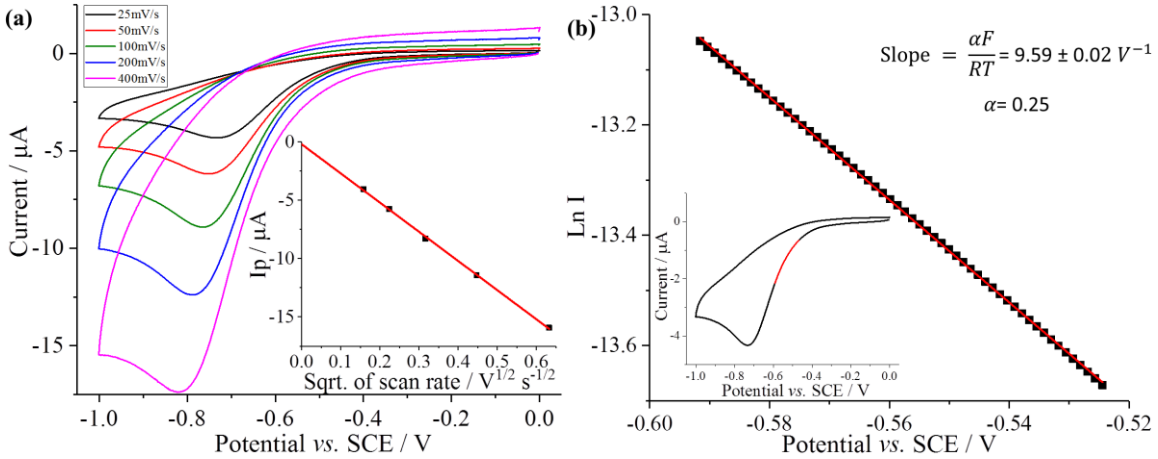


Figure 9.15. (a) Voltammograms of a bare glassy carbon macroelectrode in an air-saturated pH 7.4 PBS buffer solution recorded as a function of scan rate. Inset: the plot of peak current as a function of the square root of the scan rate. (b) Tafel analysis for voltammogram of a bare glassy carbon macroelectrode in air-saturated pH 7.4 PBS buffer at a scan rate of 25 mV s^{-1}. The highlighted red region in inset voltammogram was selected as the Tafel analysis region, where the diffusion plays a near negligible role.[42]

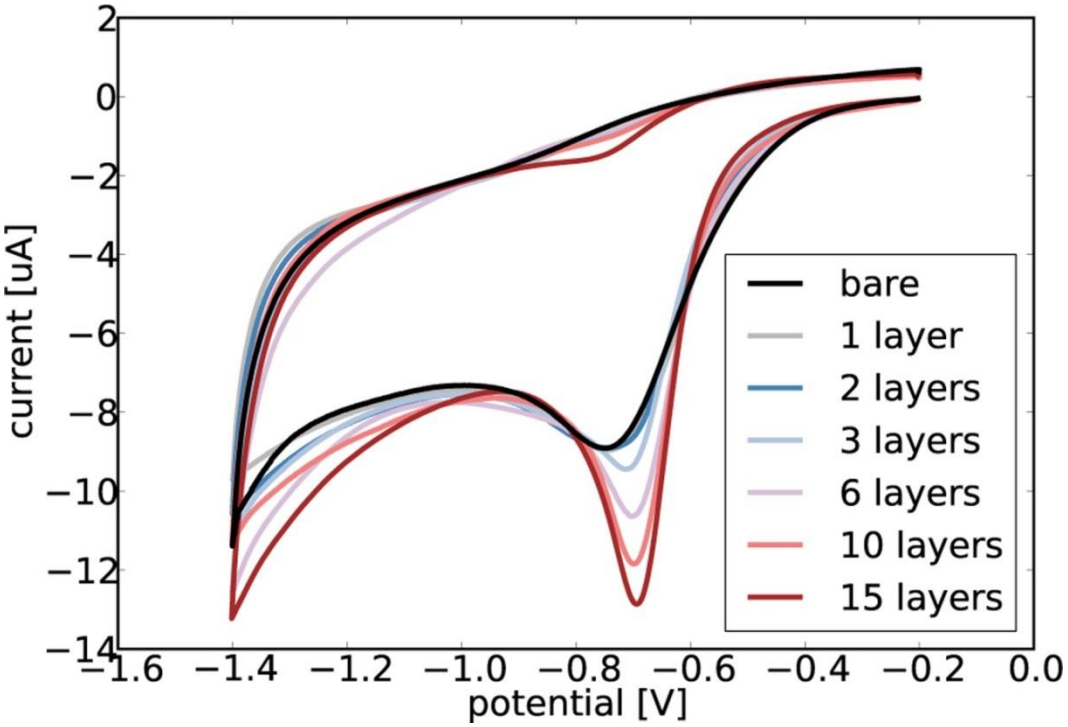


Figure 9.16. Voltammograms of air-saturated pH 7.4 phosphate-buffered saline solution at a glassy carbon electrode modified with Nafion particles. Particles feature a radius of 430 nm and have been dropcasted onto the electrode. Voltammograms are recorded at a scan rate of 100 mV s^{-1}.

Figure 9.16 compares the voltammetry of a bare glassy carbon electrode and particle-modified electrodes. The latter are modified with the above Nafion particles while various average numbers of particle layers are deposited on the electrode surface. As one would anticipate from the analysis of the voltammetry of ferrocene methanol at similar electrodes, the figure reveals a strong dependency of the voltammograms on the amount of Nafion deposited. Most notably, there is a shift of about 60 mV in the position of the oxygen peak towards lower overpotentials and a dramatic increase of more than 40% in the peak current. The Tafel analysis further yields an α value of 0.39 rather than 0.25 at a bare glassy carbon electrode, as shown in Figure 9.17. All three findings might intuitively be attributed to a false and electrochemically implausible electrocatalytic activity of Nafion particles, though the above theoretical analysis suggests they are likely purely diffusional effects.

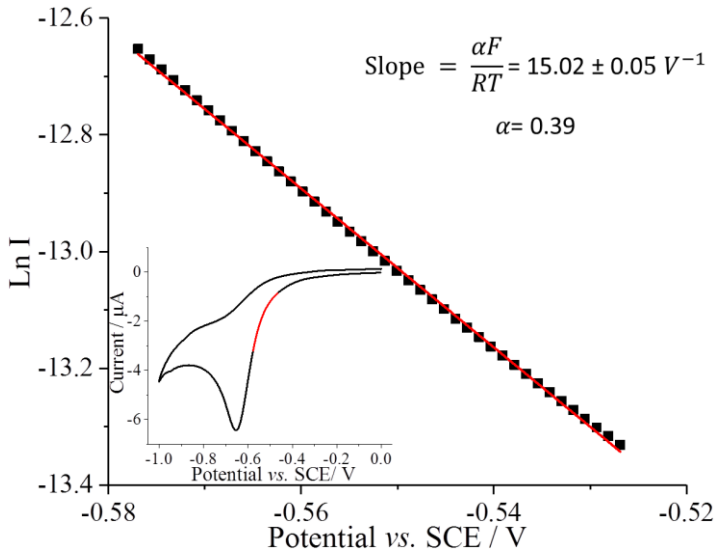


Figure 9.17. Tafel analysis for voltammogram of a glassy carbon macroelectrode modified with 15 layers of Nafion particles in an air-saturated pH 7.4 PBS buffer at a scan rate of 25 mV s^{-1}. The highlighted red region in inset voltammogram was selected as the Tafel analysis region.

9.4.2.3 Electrostatic Interactions

In the following, three different reactions are discussed, all of which are more complex as reactants or products adsorb onto the surfaces of the spheres or the reactant electrostatically interacts with the spheres.

9.4.2.3.1 Hexaammineruthenium (III) Reduction

The following presents a more complex system that features electrostatic interactions. Nafion particles are negatively charged due to the SO_3^- groups of Nafion.[47,48] Hexaammineruthenium (III) is positively charged and hence likely affected by an attractive electrostatic interaction with the Nafion particles. The formerly well-characterised[49] reversible one-electron reduction of $[Ru(NH_3)_6]^{3+}$ is studied at a bare glassy carbon electrode in an argon-saturated 0.1 M KCl solution containing 1.0 mM $[Ru(NH_3)_6]Cl_3$, see Figure 9.18. reversible Randles-Ševčík equation, diffusion coefficient is found to be 8.34×10^{-10} m^2 s^{-1} which matches the priorly reported value[50] of $(8.43 \pm 0.03) \times 10^{-10}$ m^2 s^{-1}. The formal potential is estimated to be −0.176 V vs SCE via the determination of the mid-point potential.

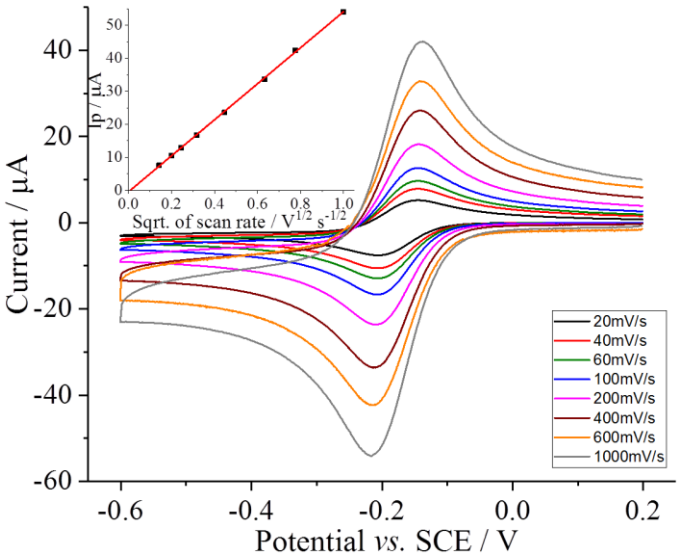


Figure 9.18. Voltammograms of a bare glassy carbon macroelectrode in solution containing 1mM $[Ru(NH_3)_6]Cl_3$ and 0.1 M KCl recorded as a function of scan rates. Inset: Plot of peak current as a function of the square root of the scan rate.

Figure 9.19 compares the voltammetry of a bare glassy carbon electrode with that of modified electrodes with one layer and three layers of Nafion particles. As one would anticipate from the analysis above, a strong dependency of the voltammograms on the amount of Nafion particles deposited and scan rate is observed. Most notably, there is shift

in the position of forward peak towards higher overpotentials and a dramatic increase in the peak current. This is likely due to the attractive interaction between $[Ru(NH_3)_6]^{3+}$ molecules and Nafion particles leading to the adsorption of $[Ru(NH_3)_6]^{3+}$ onto the Nafion particle surface and probably also absorption into the bulk of the particles.[51] Therefore, as the amount of Nafion particles deposited on electrode surface increases, the number of adsorbed reactant molecules increases which results in the peak appearing at higher overpotentials and larger peak currents. The higher overpotentials are herein likely due to the retarded mass transport inside the porous layer and the slow release of the adsorbed reactant while the elevated peak current may result from the net preconcentration of the reactant inside the porous layer.

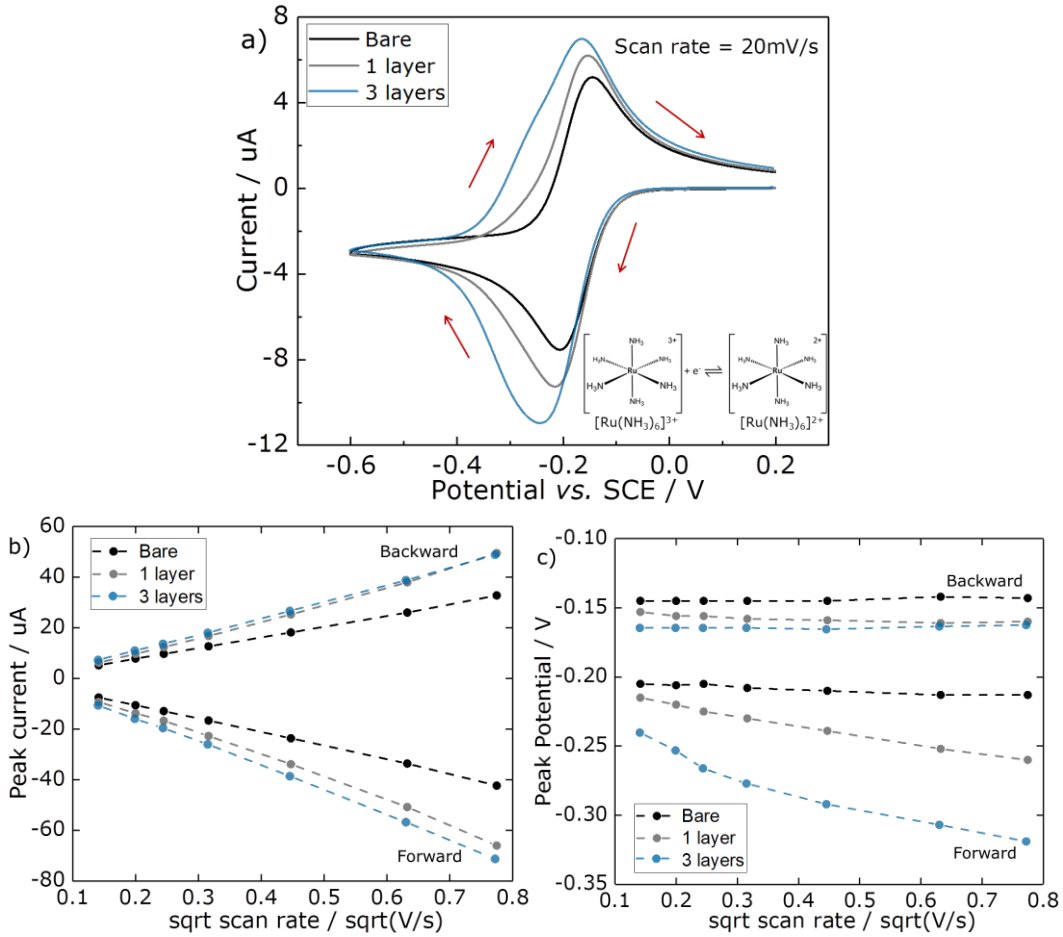


Figure 9.19. (a) Representative voltammograms at a bare glassy carbon macroelectrode and Nafion particles-modified electrodes in 0.1 M KCl containing 1 mM $[Ru(NH_3)_6]Cl_3$ recorded at 20 mVs^{-1}. (b) Measured peak currents as a function of scan rate for an average surface coverage of one and three layers of Nafion particles deposited on the electrode. (c) Measured peak potentials.

In terms of the reverse scan the peak potential shifts to lower overpotentials whilst a higher peak current is seen. The increase in the peak current likely relates to the increased amount of $[Ru(NH_3)_6]^{2+}$ formed on the forward scan. During the reverse scan, the $[Ru(NH_3)_6]^{2+}$ undergoes an oxidation to form the more positive-charged $[Ru(NH_3)_6]^{3+}$ which is affected by a stronger attractive interaction with Nafion particles. This may lead to this process being apparently more favoured—primarily thermodynamically due to the Ru (II/III) couple interacting with the SO_3^- and causing the lower overpotentials observed.

9.4.2.3.2 Ferrocenemethanol Oxidation

The oxidation of ferrocenemethanol at glassy carbon electrodes modified with Nafion particles is next studied. In this system, the reactant is charge neutral while the product is positively charged and hence features an attractive interaction with the Nafion particles.

Voltammograms are recorded at different scan rates at electrodes modified with one, two, and three layers of Nafion particles. The measured peak currents and peak potentials are plotted as a function of the scan rate and compared with the bare electrode data as depicted in Figure 9.20.

Here, a different dependency of the voltammograms on the amount of Nafion particles deposited is observed: there is a shift in the position of forward peak towards lower overpotentials and a decrease in the peak current. As the reactant is not charged and does not interact electrostatically with the Nafion spheres, the reduced peak currents are attributed to the retarded mass transport of the analyte towards the electrode in analogy with the polystyrene microspheres results. The oxidation product $FcCH_2OH^+$ is positively charged and affected by attractive electrostatic interactions with the Nafion spheres. This results in the oxidation process which is electrochemically reversible being more favoured and hence the peak potentials being reduced. Moreover, this attractive interaction between the oxidation product and the spheres leads to the adsorption and accumulation of the

$FcCH_2OH^+$ onto the Nafion surface and/or bulk. In the reverse scans, the complex dependency of the peak currents and peak potential on the amount of Nafion sphere deposited can therefore be understood in analogy with the reduction of $[Ru(NH_3)_6]^{3+}$.

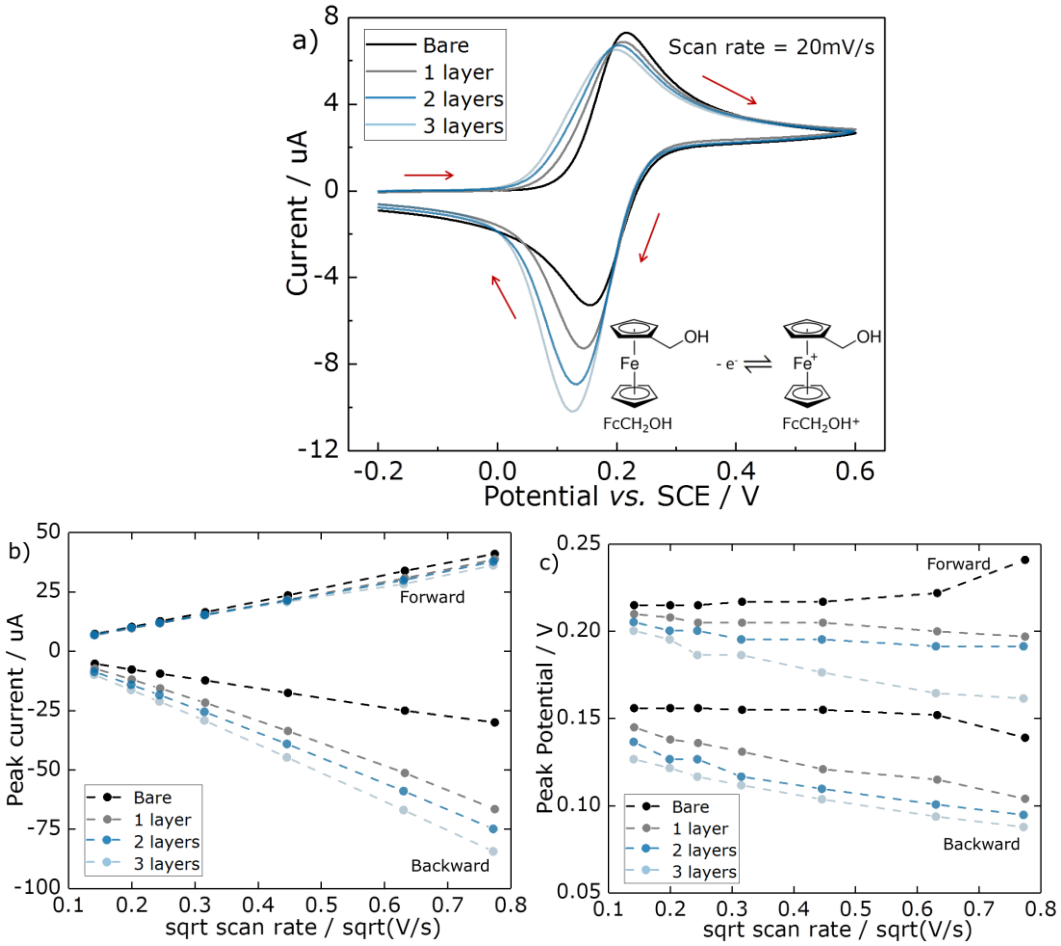


Figure 9.20. (a) Representative voltammograms at a bare glassy carbon macroelectrode and Nafion particles-modified electrodes in 0.1 M KCl containing 1 mM ferrocenemethanol recorded at 20 mVs^{-1}. (b) Measured peak currents as a function of scan rate for an average surface coverage of one, two and three layers of Nafion particles deposited on the electrode. (c) Peak potentials.

9.4.2.3.3 Ferrocyanide Oxidation

Having shown the complexity of an attractive interaction between the reactant or the product and the spheres, the following investigates the reaction of ferrocyanide where there are repulsive electrostatic forces between the reactant and the spheres. To this end, the oxidation of ferrocyanide $Fe[(CN)_6]^{4-}$ at a bare glassy carbon electrode as shown in the Figure 9.21. The diffusion coefficient is found to be 6.3×10^{-10} m^2 s^{-1} which is in good

agreement with the literature value[52] of (6.6 ± 0.3) × 10^{-10} m^2 s^{-1} while the formal potential is found to be 0.182 V vs SCE.

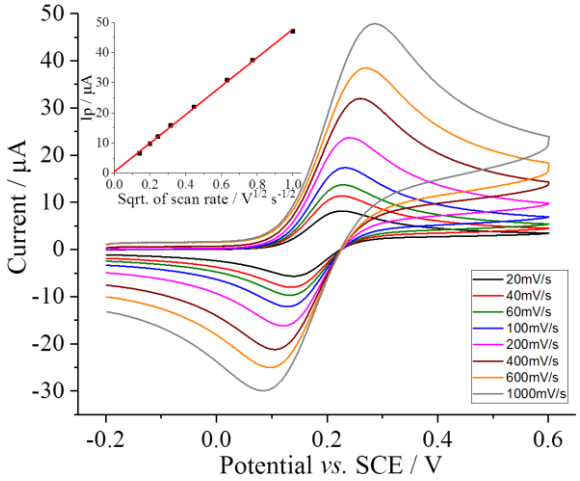


Figure 9.21. (a) Voltammograms of a bare glassy carbon macroelectrode in solution containing 1 mM $K_4[Fe(CN)_6]$ and 0.1 M KCl recorded as a function of scan rates. Inset: Plot of peak current as a function of the square root of the scan rate.

Figure 9.22 compares the voltammetry of the ferrocyanide oxidation at a bare electrode and at an electrode modified with three layers of Nafion particles. The latter shows a dramatic reduction in current and no clear peak can be seen, which is attributed to powerful electrostatic repulsion between the charged reactant and the Nafion leading to the reaction being almost fully blocked.

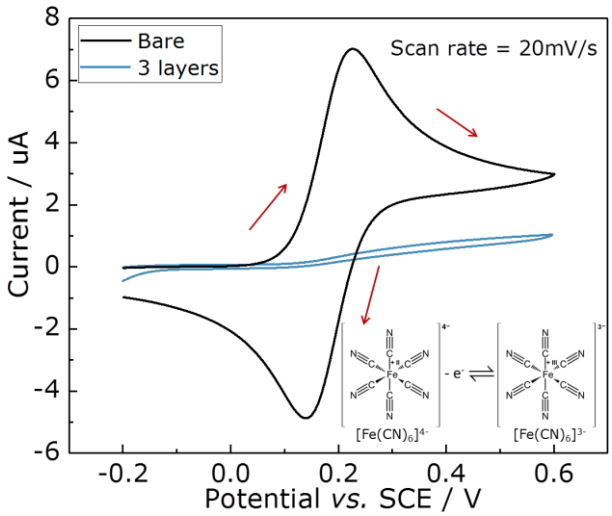


Figure 9.22. Representative voltammograms at a bare glassy carbon macroelectrode and the electrodes modified with three layers of Nafion particles in 0.1 M KCl containing 1 mM ferrocyanide recorded at 20 mVs^{-1}.

9.5 Conclusions

In conclusion, this work has demonstrated the paramount importance of theoretical modelling in all electrocatalytic analysis of nanoparticles on an electrode surface. The experimental system bears a remarkable and quite unexpected level of complexity which arises from the altered mass transport inside the porous layer formed by the deposited particles. Classical thin-layer behaviour or a retarded mass transport within the porous layer may dominate the voltammetry at certain scan rates. If these subtleties were to be ignored, false impressions of electrocatalysis – positive or negative – would be measured and, under many circumstances, a catalytic activity of the modifying nanoparticles would falsely be inferred. Using ferrocenemethanol oxidation at glassy carbon electrodes as a model system, good agreement of theoretically predicted trends and measured data are found. In addition, the complexity of the analysis of more complex reactions such as the reduction of oxygen is demonstrated experimentally and risks of misinterpreting experimental results are pointed out.

Furthermore, the impact of electrostatic effects on the voltammetry of three reversible systems is experimentally demonstrated: If reactants or products and the particle surfaces are charged, entirely different voltammetric features are observed which again shows the profound influence on the voltammetry exerted by modifying particles and signalling care is needed in any interpretation.

Bibliography

(1) Kätelhön, E.; Chen, L.; Compton, R. G. *Applied Materials Today* **2019**, *15*, 139-144.
(2) Chen, L.; Kätelhön, E.; Compton, R. G. *Applied Materials Today* **2019**, *16*, 141-145.
(3) Chen, L.; Kätelhön, E.; Compton, R. G. *Applied Materials Today* **2019**, 100480.
(4) Compton, R. G.; Wildgoose, G. G.; Rees, N. V.; Streeter, I.; Baron, R. *Chemical Physics Letters* **2008**, *459*, 1-17.
(5) Murray, R. W. *Chemical Reviews* **2008**, *108*, 2688-2720.

(6) Lu, Q.; Chen, J. G.; Xiao, J. Q. *Angewandte Chemie International Edition* **2013**, *52*, 1882-1889.
(7) Batchelor-McAuley, C.; Kätelhön, E.; Barnes, E. O.; Compton, R. G.; Laborda, E.; Molina, A. *ChemistryOpen* **2015**, *4*, 224-260.
(8) Wang, F.; Wu, X.; Li, C.; Zhu, Y.; Fu, L.; Wu, Y.; Liu, X. *Energy & Environmental Science* **2016**, *9*, 3570-3611.
(9) Aoki, K. J. *Journal of Electroanalytical Chemistry* **2016**, *779*, 7-17.
(10) Zhang, L.; Zhao, Z. J.; Gong, J. *Angewandte Chemie International Edition* **2017**, *56*, 11326-11353.
(11) Kleijn, S. E. F.; Lai, S. C. S.; Koper, M. T. M.; Unwin, P. R. *Angewandte Chemie International Edition* **2014**, *53*, 3558-3586.
(12) Mirkin, M. V.; Sun, T.; Yu, Y.; Zhou, M. *Accounts of Chemical Research* **2016**, *49*, 2328-2335.
(13) Sokolov, S. V.; Eloul, S.; Kätelhön, E.; Batchelor-McAuley, C.; Compton, R. G. *Physical Chemistry Chemical Physics* **2017**, *19*, 28-43.
(14) Banks, C. E.; Davies, T. J.; Wildgoose, G. G.; Compton, R. G. *Chemical Communications* **2005**, 829-841.
(15) Wang, L.; Pumera, M. *Applied Materials Today* **2016**, *5*, 134-141.
(16) Hassan, M.; Gomes, V. G. *Applied Materials Today* **2018**, *12*, 342-358.
(17) Bavykin, D. V.; Friedrich, J. M.; Walsh, F. C. *Advanced Materials* **2006**, *18*, 2807-2824.
(18) Zhu, Y. P.; Liu, Y. P.; Ren, T. Z.; Yuan, Z. Y. *Advanced Functional Materials* **2015**, *25*, 7337-7347.
(19) Serra, A.; Valles, E. *Applied Materials Today* **2018**, *12*, 207-234.
(20) Ju, H. *Applied Materials Today* **2018**, *10*, 51-71.
(21) McCreery, R. L. *Chemical Reviews* **2008**, *108*, 2646-2687.
(22) Chen, D.; Tang, L.; Li, J. *Chemical Society Reviews* **2010**, *39*, 3157-3180.
(23) Rountree, E. S.; McCarthy, B. D.; Eisenhart, T. T.; Dempsey, J. L.; ACS Publications, 2014.
(24) Suen, N.-T.; Hung, S.-F.; Quan, Q.; Zhang, N.; Xu, Y.-J.; Chen, H. M. *Chemical Society Reviews* **2017**, *46*, 337-365.
(25) Brookes, B. A.; Davies, T. J.; Fisher, A. C.; Evans, R. G.; Wilkins, S. J.; Yunus, K.; Wadhawan, J. D.; Compton, R. G. *Journal of Physical Chemistry B* **2003**, *107*, 1616-1627.
(26) Henstridge, M. C.; Dickinson, E. J. F.; Aslanoglu, M.; Batchelor-McAuley, C.; Compton, R. G. *Sensors and Actuators B: Chemical* **2010**, *145*, 417-427.
(27) Henstridge, M. C.; Dickinson, E. J. F.; Compton, R. G. *Russian Journal of Electrochemistry* **2012**, *48*, 629-635.
(28) Barnes, E. O.; Chen, X.; Li, P.; Compton, R. G. *Journal of Electroanalytical Chemistry* **2014**, *720*, 92-100.
(29) Chan, H. T. H.; Kätelhön, E.; Compton, R. G. *Journal of Electroanalytical Chemistry* **2017**, *799*, 126-133.
(30) Newton, M. R.; Morey, K. A.; Zhang, Y.; Snow, R. J.; Diwekar, M.; Shi, J.; White, H. S. *Nano Lett* **2004**, *4*, 875-880.
(31) Volgin, V. M.; Davydov, A. D.; Kabanova, T. B. *Russian Journal of Electrochemistry* **2012**, *48*, 817-834.
(32) Compton, R. G.; Banks, C. E. *Understanding Voltammetry*, 2nd ed.; Imperial College Press: London, 2011.
(33) Reller, H.; Kirowa-Eisner, F.; Gileadi, E. *Journal of Electroanalytical Chemistry and Interfacial Electrochemistry* **1982**, *138*, 65-77.
(34) Amatore, C.; Saveant, J. M.; Tessier, D. *Journal of Electroanalytical Chemistry and Interfacial Electrochemistry* **1983**, *147*, 39-51.
(35) Bard, A. J.; Faulkner, L. R. *Electrochemical Methods: Fundamentals and Applications*; Wiley, 2000.
(36) Kätelhön, E.; Compton, R. G. *Analyst* **2015**, *140*, 2592-2598.
(37) Amatore, C.; Da Mota, N.; Sella, C.; Thouin, L. *Analytical Chemistry* **2007**, *79*, 8502-8510.
(38) Shao, M.; Chang, Q.; Dodelet, J.-P.; Chenitz, R. *Chemical Reviews* **2016**, *116*, 3594-3657.
(39) Lufrano, F.; Staiti, P.; Minutoli, M. *Journal of the Electrochemical Society* **2004**, *151*, A64-A68.

(40) Davis, R. E.; Horvath, G. L.; Tobias, C. W. *Electrochimica Acta* **1967**, *12*, 287-297.
(41) Sundberg, K. M.; Smyrl, W. H.; Atanasoska, L.; Atanasoski, R. *Journal of the Electrochemical Society* **1989**, *136*, 434-439.
(42) Li, D.; Lin, C.; Batchelor-McAuley, C.; Chen, L.; Compton, R. G. *Journal of Electroanalytical Chemistry* **2018**, *826*, 117-124.
(43) Guidelli, R.; Compton, R. G.; Feliu, J. M.; Gileadi, E.; Lipkowski, J.; Schmickler, W.; Trasatti, S. *Pure and Applied Chemistry* **2014**, *86*, 245-258.
(44) Guidelli, R.; Compton, R. G.; Feliu, J. M.; Gileadi, E.; Lipkowski, J.; Schmickler, W.; Trasatti, S. *Pure and Applied Chemistry* **2014**, *86*, 259-262.
(45) Nissim, R.; Compton, R. G. *ChemElectroChem* **2014**, *1*, 763-771.
(46) Ju, L.-K.; Ho, C. S. *Biotechnology and Bioengineering* **1985**, *27*, 1495-1499.
(47) Kusoglu, A.; Weber, A. Z. *Chemical Reviews* **2017**, *117*, 987-1104.
(48) Mauritz, K. A.; Moore, R. B. *Chemical Reviews* **2004**, *104*, 4535-4586.
(49) Chen, L.; Compton, R. G. *ACS Sensors* **2019**, *4*, 1716-1723.
(50) Wang, Y.; Limon-Petersen, J. G.; Compton, R. G. *Journal of Electroanalytical Chemistry* **2011**, *652*, 13-17.
(51) Chen, L.; Lin, C.; Compton, R. G. *Physical Chemistry Chemical Physics* **2019**, *21*, 607-616.
(52) Konopka, S. J.; McDuffie, B. *Analytical Chemistry* **1970**, *42*, 1741-1746.

Chapter 10

Electrochemical Characterisation and Comparison of Transport in Nafion Films and Particles

The dynamics of the charge transfer processes *within* the Nafion films and particles is assessed in this Chapter, as the fundamental investigation for their use as a novel improved reference electrode for practical applications (Chapter 11). The diffusional transport of the dication and monocation of methyl viologen, MV^{2+} and MV^{+}, in hydrated Nafion films and particles is studied electrochemically. Methodology is established for characterising the relative rates of transport and for evaluating the diffusion coefficient of the two ions. The transport in the particles is shown to be significantly faster than in films of similar thickness whilst the diffusion of MV^{2+} is confirmed to be faster than that of MV^{+}.

The work presented in this Chapter has been published in *Physical Chemistry Chemical Physics*.[1] Dr. Chuhong Lin developed the theory and carried out all the simulations reported in this Chapter.

10.1 Introduction

As a well-known perfluorosulfonated, cation exchange polymer, Nafion has been widely applied in the field of energy and catalysis, including fuel cells, solar cells, electrocatalysts and electrochemical sensors.[2-6] In Chapter 8 and previous work, Nafion particles doped with different redox active species were synthesised and their electrochemical responses were characterised and studied with an aim of developing new electrocatalysts.[7,8] The focus of these previous studies was on the reaction kinetics of the electrochemically activated doped Nafion particles with reactants present in solution such as oxygen. In this Chapter, the dynamics of the charge transfer processes *within* the particles is addressed. The behaviour of Nafion materials is known to strongly depend on the preparation procedures. As reported in the literature, the morphology and properties of bulk Nafion materials are quite different from thin films even when similarly prepared.[9,10] It is inferred that when Nafion films are immersed into water, phase separation takes place with each phase domain of the size of a few nanometres, depending on the hydration degree.[11] In comparison to Nafion particles, Nafion films are more commonly investigated and used in practical applications.[12,13] Comparative studies of the electrochemical behaviour of Nafion films and the ion transport properties of Nafion materials in general including Nafion particles are of potential value.[9] This interest is driven by both practical and fundamental needs: one is to understand the ion transport behaviour of Nafion in the electrode system and to explore the origin of any differences related to the structure of the material; the other is to develop an electrochemical characterisation approach which helps to understand the structure-functionality of Nafion (or related ionomers).

In this Chapter, the electrochemical signals of the one-electron-transfer reaction of methyl viologen (MV) ions $MV^{2+} + e^{-} = MV^{+}$ in both Nafion thin films and sub-micron sized particles are measured and analysed. Two simulation models are used to describe the

two geometries: first for a film and second for a single particle to allow the investigation of the ion transport properties of the Nafion materials in the two different forms. Combining experiment with simulation, it is found that the ion transport of MV^{2+} and MV^{+} is much faster in Nafion particles than in Nafion films, showing that the preparation of the material has a non-negligible influence on transport and by implication the material structure.

10.2 Experimental

10.2.1 Preparation and Electrochemical Characterisation of MV-Nafion Films on Electrodes

A MV-Nafion stock solution containing MV^{2+} with a MV^{2+}:SO_3^- ratio of 1:20 was prepared by directly dissolving 0.7 mg of $MVCl_2$ into 1.30 mL of 5 wt% Nafion perfluorinated resin solution. The mixture was shaken on a vortex (Whirlmixer, Loughborough, UK) for 3 min.

MV-Nafion thin films were obtained by evenly drop-casting 0.1 μL of MV-Nafion stock solution on a GC electrode and left to dry under a N_2 atmosphere. The dry thickness of the thin films was determined to be 0.35 μm (see Appendix D1). Note that the Nafion film prepared is uniform and its estimated thickness is accurate, as verified by AFM imaging.[14] Before measurements in Phosphate buffered saline buffer (PBS, pH = 7.4, consisting of 137.0 mM NaCl, 2.7 mM KCl, 10.0 mM Na_2HPO_4, and 1.8 mM KH_2PO_4.), the latter was vigorously bubbled with argon to remove dissolved O_2 and an atmosphere of argon was maintained during the experiment. Cyclic voltammetry was then conducted with a glassy carbon (GC) macroelectrode (diameter 3.0 mm) as working electrode at selected scan rates of between 25 mV s^{-1} to 800 mV s^{-1}. Similar experiments were conducted with 0.5 μL and 1.5 μL MV-Nafion film, corresponding to 1.75 μm and 5.26 μm film thicknesses.

10.2.2 Preparation and Electrochemical Characterisation of single MV-Nafion Particles

The Nafion particles doped with MV^{2+} (MV-Nafion particles) were synthesized as described in Chapter 3. In this Chapter, two different concentrations of MV^{2+} aqueous solutions (300 mM, 150 mM) were used to synthesize MV-Nafion particles at a different doping ratio (ratio of MV^{2+}:SO_3^-) of 1:20 and 1:40, respectively (noted as "fully-doped" and "half-doped" in the following sections)

For the single MV-Nafion particles study, chronoamperometry was performed with a home-fabricated carbon microcylinder electrode (diameter 7.0 μm, length ca. 1mm, fabrication procedure see Chapter 3) as the working electrode. Note that the potentiostat used in this work accurately conserves the charge transferred arising from a particle-impact process.[15] 500 μL of MV-Nafion stock suspension was added into 4.5 mL of degassed PBS buffer. The cell was sealed and sonicated for 1 min to obtain a well dispersed suspension, followed by immediate chronoamperometric scans under an atmosphere of argon during the measurements.

10.2.3 Preparation and Electrochemical Characterisation of Layers of MV-Nafion Particles on Electrodes

For the study of ensembles of MV-Nafion particles, 10 μL of above MV-Nafion stock suspension was drop-casted on the GC electrode left to dry. 15 layers of Nafion particles were determined on the surface of GC electrode (see Appendix D2). Cyclic voltammetry was recorded at selected scan rates of between 25 mVs^{-1} to 800 mVs^{-1} in a degassed PBS buffer. Similar experiments were also performed for 3 layers and 5 layers of MV-Nafion particles by drop-casting diluted stock suspension.

10.3 Theory and Simulation

To study the electrochemical behaviour of the redox species doped in the Nafion thin-films and the Nafion particles, two simulation models were developed: one is a one-dimensional thin-film model for simulating cyclic voltammetry on a Nafion film coated electrode; the other is a two-dimensional particle model for simulating the current-time and cyclic voltammetric response corresponding to one Nafion particle when instantaneously subjected to a reducing potential sufficient to reduce the MV^{2+} under the potential. The simulation procedure is introduced and key parameters in understanding the ion transport in Nafion materials are derived.

All simulations reported in this section were carried out by Dr. Chuhong Lin.

10.3.1 Nafion thin-film simulation

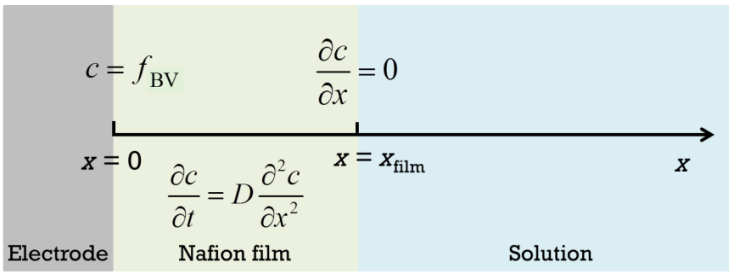


Figure 10.1. Illustration of the Nafion thin-film simulation in a single dimension *x*. Simulation equations and boundary conditions are listed. x_{film} is the thickness of the Nafion film. f_{BV} refers to the Butler-Volmer equation. *c* is concentration, *D* is the diffusion coefficient, *x* is the dimension perpendicular to the electrode surface, *t* is the reaction time, x_{film} is the film thickness.

Figure 10.1 illustrates the simulation model of the Nafion thin-film coated electrode. The thin-film model is well established in the study of mass transport inside a coating layer,[16] in which the electroactive species are confined in the film. It is assumed that the reactant diffuses in Nafion and the electron transfer only takes place at the electrode surface which is $x = 0$ in Figure 10.1. The mass transport of the reactant MV^{2+} and the product MV^{+} in the Nafion thin-film is described by the diffusion equation:

$$\frac{\partial c}{\partial t} = D\nabla^2 c = D\frac{\partial^2 c}{\partial x^2} \tag{10.1}$$

where c is the concentration, t is the reaction time, D is the diffusion coefficient and x is the distance from the electrode surface. For the reactant and the product, the diffusion coefficients are typically not the same in Nafion.[2] The redox reaction studied in this work is a one-electron-transfer reaction $MV^{2+} + e^- = MV^+$ and MV^{2+} is the species initially doped in Nafion. On the electrode surface, the electron-transfer kinetics is described by the Butler-Volmer equation and the surface concentrations of the redox species follows:[17,18]

$$-D_{MV^{2+}}\left.\frac{\partial c_{MV^{2+}}}{\partial x}\right|_{x=0} = -k_0 \exp\left(-\frac{\alpha F\left(E-E_f\right)}{R_{gas}T_r}\right)\left.c_{MV^{2+}}\right|_{x=0} + k_0 \exp\left(\frac{\beta F\left(E-E_f\right)}{R_{gas}T_r}\right)\left.c_{MV^{+}}\right|_{x=0} \tag{10.2}$$

$$-D_{MV^{+}}\left.\frac{\partial c_{MV^{+}}}{\partial x}\right|_{x=0} = k_0 \exp\left(-\frac{\alpha F\left(E-E_f\right)}{R_{gas}T_r}\right)\left.c_{MV^{2+}}\right|_{x=0} - k_0 \exp\left(\frac{\beta F\left(E-E_f\right)}{R_{gas}T_r}\right)\left.c_{MV^{+}}\right|_{x=0} \tag{10.3}$$

where F is the Faraday constant, R_{gas} is the gas constant, T_r is the room temperature, E is the applied electrode potential and E_f is the formal potential of the MV^{2+}/MV^+ redox reaction within the film, k_0 is the standard electron-transfer rate constant. As the electron transfer is fast in this redox reaction, k_0 is assigned a large value and both the cathodic and anodic transfer coefficients, α and β, are treated as 0.5. The initial concentration of the reactant MV^{2+} is c^* and there is no product MV^+ in the Nafion film before the redox reaction. By solving the diffusion equation with given boundary conditions, the current can be calculated by:

$$I = F\pi r_{el}^{\,2}\left(D_{MV^{2+}}\left.\frac{\partial c_{MV^{2+}}}{\partial x}\right|_{x=0}\right) \tag{10.4}$$

r_{el} is the radius of the substrate electrode on which the Nafion film is coated. The electrode potential used in the cyclic voltammetry is a function of the reaction time and the scan rate v, described as:

$$E = \begin{cases} E_{\text{ini}} - vt, & t < \dfrac{|E_{\text{ini}} - E_{\text{rev}}|}{v} \\ E_{\text{rev}} + v\left(t - \dfrac{|E_{\text{ini}} - E_{\text{rev}}|}{v}\right), & t > \dfrac{|E_{\text{ini}} - E_{\text{rev}}|}{v} \end{cases} \tag{10.5}$$

where $[E_{\text{ini}}, E_{\text{rev}}]$ is the potential window.

10.3.2 Single Nafion Particle Simulation

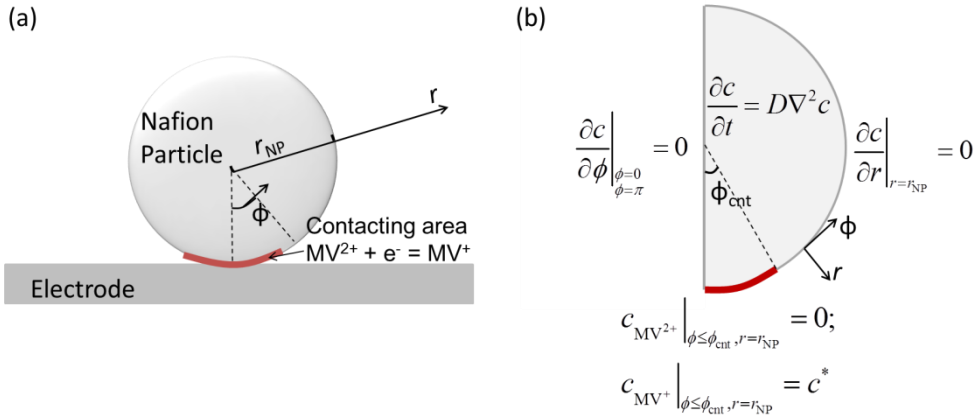


Figure 10.2. (a) Illustration of the single Nafion particle model in the two-dimension (r, ϕ) coordinates. The contacting area where electron transfer in assumed to take place is marked by red. (b) Simulation model, where ϕ_{cnt} is the angle corresponding to the edge of the contacting area.

Next the current signal after a Nafion particle is suddenly subjected to a potential for example by hitting an electrode after diffusion to it within a solution is simulated. The model is illustrated in Figure 10.2a, where the Nafion particle is treated as a sphere. In the experiments reported below, the dry radius of the particles was characterised *via* SEM as 0.46 ± 0.40 μm.[7] Upon the impact the soft particles are presumed to partially distort and it is assumed that there is a certain well-defined contacting area between the electrode and the Nafion particle where the redox reaction of MV^{2+} takes place, shown by the red area marked in Figure 10.2a. The diffusion of MV^{2+} inside the Nafion particle is modelled in spherical coordinates (r, ϕ, φ), where r is the radial distance, ϕ is the polar angle and φ is the zenith angle, as shown in Figure 10.2b. Due to the symmetry, the diffusion equation inside a spherical particle is written as:

$$\frac{\partial c}{\partial t} = D\nabla^2 c = D\left(\frac{\partial^2 c}{\partial r^2} + \frac{2}{r}\frac{\partial c}{\partial r} + \frac{1}{r^2}\frac{\partial^2 c}{\partial \phi^2} + \frac{1}{r^2 \tan\phi}\frac{\partial c}{\partial \phi}\right) \tag{10.6}$$

The equation is solved in the range of $r \in [0\ r_{NP}]$ and $\phi \in [0\ \pi]$. At the contacting area, under the high overpotentials assumed applied, the reactant is fully consumed $c_{MV2+}(r_{NP}, 0<\phi<\phi_{cnt}]) = 0$ and $c_{MV+}(r_{NP}, 0<\phi<\phi_{cnt}]) = c^*$ (c^*: bulk concentration), where ϕ_{cnt} is the polar angle corresponding to the end of the contacting area. The current measured from the electrode *via* the electron transfer at the contacting area can be calculated by the time derivative of the amount of reactant:

$$I = F\frac{\partial}{\partial t}\left(2\pi \int c \cdot r \sin\phi \mathrm{d}r\mathrm{d}\phi\right) \tag{10.7}$$

The single-particle model in Figure 10.2 can be used to simulate both the current-time response of single particles (chronoamperometry) and the current-potential response of layers of particles (cyclic voltammetry, see below). The boundary condition at the contacting area also follows the Butler-Volmer equation as in Eqn.(10.2) and Eqn.(10.3). For comparison with the experiments reported below, the simulated current-time response was further filtered by a simple first-order low pass filter with a cutoff frequency f_{cutoff} of 50 Hz and resampled according to the sampling frequency $f_{sampling}$ applied in the experiment (2 kHz). Note for practical applications the filtering of the signal in the potentiostat needs to be characterised *via* fitting the current pulse signal output by the potentiostat. By fitting to a simple first-order low-pass filter, f_{cutoff} = 50 Hz is measured for the experimental potentiostat. The details of the filter characterisation have been reported in the literature.[15,19]

In the simulation, the diffusion equation Eqn.(10.6) was solved by the finite difference method in Matlab 2018a. The alternating direction implicit method was applied to solve the two-dimensional problem, of which the details can be found in the literature.[20] The

validation and the convergence of the simulation conditions were tested before fitting to the experimental data.

10.3.3 Dimensional and Dimensionless Simulation

By solving the diffusion equation with the boundary conditions shown in Figure 10.1 and Figure 10.2, the current response can be calculated. To avoid selecting the exact experimental conditions for the simulation, dimensionless parameters were first applied when building up the two models. The transformation between the dimensional and dimensionless parameters used in both the thin-layer and the single particle models are shown in Table 10.1. In the thin-layer model, the dimensionless current flux J is calculated from solving the equations listed in Table 10.2. J is a function of the dimensionless scan rate δ, overpotential θ and the diffusion coefficient $d_{\mathrm{MV+}}$:

$$J = f\left(\delta, \theta, d_{\mathrm{MV+}}\right) \tag{10.8}$$

Similarly, the current-potential response of a single particle can be written as (the equations list in Table 10.3):

$$J = f\left(\delta, \theta, d_{\mathrm{MV+}}, \phi_{\mathrm{cnt}}\right) \tag{10.9}$$

where one more parameter, the contacting angle ϕ_{cnt}, needs to be considered. The current-time response of a single particle is a function of the dimensionless T and the contacting angle ϕ_{cnt}:

$$J = f\left(T, \phi_{\mathrm{cnt}}\right) \tag{10.10}$$

Note that the current-time response of particle impacts cannot reflect the changed diffusion coefficients between the reactant and the product. Thus $d_{\mathrm{MV+}}$ is not involved in Eqn.(10.10).

When fitting to the real experimental data, the current expressions can be written as:

$$I = M \cdot \frac{D_{MV^{2+}}}{x_{film}^2} \cdot f\left(\frac{F\nu}{R_{gas}T_r} \cdot \frac{x_{film}^2}{D_{MV^{2+}}}, \frac{F\eta}{R_{gas}T_r}, \frac{D_{MV^{+}}}{D_{MV^{2+}}} \right) \tag{10.11}$$

$$I = \frac{3Q}{4\pi} \cdot \frac{D_{MV^{2+}}}{r_{NP}^2} \cdot f\left(\frac{F\nu}{R_{gas}T_r} \cdot \frac{r_{NP}^2}{D_{MV^{2+}}}, \frac{F\eta}{R_{gas}T_r}, \frac{D_{MV^{+}}}{D_{MV^{2+}}}, \phi_{cnt} \right) \tag{10.12}$$

$$I = \frac{3Q}{4\pi} \cdot \frac{D_{MV^{2+}}}{r_{NP}^2} \cdot f\left(t \cdot \frac{r_{NP}^2}{D_{MV^{2+}}}, \phi_{cnt} \right) \tag{10.13}$$

$M = F\pi r_{el}^2 x_{film} c^*$ is the charge associated with the full one-electron-transfer reaction of all the MV^{2+} in the Nafion film and the value of M can be measured from the current response at a low scan rate. $Q = 4/3\pi F r_{NP}^3 c^*$ is the charge associated with the full one-electron-transfer of all the MV^{2+} doped in one Nafion particle and Q can be measured from the current response in single Nafion particle experiment. From Eqn.(10.11), Eqn.(10.12) and Eqn.(10.13), it can be seen that the combined parameter x_{film}^2/D_{MV2+} (or r_{NP}^2/D_{MV2+} for the Nafion particle) is the key parameter with units of time (s) to understand ion transport in Nafion materials. Physically it gives the order of magnitude of the time response of the film or the particle to potential induced concentration perturbations.

It is possible to calculate a diffusion coefficient according to the dry thickness or the average particle radius measured from SEM images. However, as the Nafion material uptakes water the real volume will vary after immersing into water.[21,22] Accordingly the combined parameter x_{film}^2/D_{MV2+} can better describe the ion transport. The ion transport time (unit: s) is defined as $\tau_{it} = x_{film}^2/D_{MV2+}$ (r_{NP}^2/D_{MV2+} for the Nafion particle) in this Chapter. In the following text, the value of τ_{it} will be measured *via* fitting the experiment data by simulation, where the electrochemical response from a series of electrodes modified by Nafion films or particles; and the physical insights revealed by the combined parameter will be discussed.

Table 10.1. Dimensionless transformations.

Variable	Dimensionless Variable	Variable	Dimensionless Variable
x (film) r (SNP)	$X = x/x_{film}$ (film) $R = r/r_{NP}$ (SNP)	t	$T = tD_{MV2+}/x_{film}^2$ (film) $T = tD_{MV2+}/r_{NP}^2$ (SNP)
c	$C = c/c^*$	I	$J = Ix_{film}/(F\pi r_{el}^2 D_{MV2+}c^*)$ (film) $J = I/(Fr_{NP}D_{MV2+}c^*)$ (SNP)
D	$d = D/D_{MV2+}$	E	$\theta = F(E-E_f)/(R_{gas}T_r)$
v	$\delta = Fvx_{film}^2/(R_{gas}T_rD_{MV2+})$	k_0	$K_0 = k_0x_{film}/D_{MV2+}$ (film) $K_0 = k_0r_{NP}/D_{MV2+}$ (SNP)

SNP= Single Nafion Particle

Table 10.2. Equations and boundary conditions in dimensionless form for the Nafion film modelling.

Conditions	Equations
$X > 0$	$\frac{\partial C_{MV^{2+}}}{\partial T} = \nabla^2 C_{MV^{2+}}$; $\frac{\partial C_{MV^{+}}}{\partial T} = d_{MV^{+}} \nabla^2 C_{MV^{+}}$
$X = 0$	$\frac{\partial C_{MV^{2+}}}{\partial X} = -d_{MV^{+}} \frac{\partial C_{MV^{+}}}{\partial X} = K_0 \exp(-0.5\theta) C_{MV^{2+}} - K_0 \exp(0.5\theta) C_{MV^{+}}$
$X \rightarrow \infty$	$C_{MV^{2+}} = 1$; $C_{MV^{+}} = 0$

Table 10.3. Equations and boundary conditions in dimensionless format for the single Nafion particle modelling.

Conditions	Equations
$0 < R < 1$ and $0 < \phi_{cnt} < \pi$	$\frac{\partial C_{MV^{2+}}}{\partial T} = \nabla^2 C_{MV^{2+}}$; $\frac{\partial C_{MV^{+}}}{\partial T} = d_{MV^{+}} \nabla^2 C_{MV^{+}}$
$R = 1$ and $\phi \le \phi_{cnt}$	$\frac{\partial C_{MV^{2+}}}{\partial R} = -d_{MV^{+}} \frac{\partial C_{MV^{+}}}{\partial R} = K_0 \exp(-0.5\theta) C_{MV^{2+}} - K_0 \exp(0.5\theta) C_{MV^{+}}$
$R = 1$ and $\phi_{cnt} < \phi < \pi$	$\partial C/\partial R = 0$
$0 < R < 1$ and $\phi = 0$	$\partial C/\partial \phi = 0$
$0 < R < 1$ and $\phi = \pi$	$\partial C/\partial \phi = 0$

10.4 Results

The electrochemical responses of doped Nafion thin-film and Nafion particles are reported in this section. Cyclic voltammetry on Nafion thin-film coated electrodes was measured for Nafion films of 0.35 μm, 1.75 μm and 5.26 μm dry thicknesses. The electroactive species MV^{2+} is confined in the Nafion film and the one electron transfer reaction $MV^{2+} + e^- = MV^+$ takes place at the electrode surface. To explore the contrasting electrochemical behaviour of the MV^{2+} doped Nafion particles, the current responses of individual Nafion particles were recorded and the cyclic voltammetry of multi-layer Nafion particle modified electrodes was measured and analysed.

All simulations reported below were carried out by Dr. Chuhong Lin.

10.4.1 Ion Transport in Nafion Thin-film Coated Electrodes

In Chapter 8, the cyclic voltammetry (CV) of $MV^{2+} + e^- = MV^+$ was reported for both free MV^{2+} in aqueous solution and MV^{2+} doped Nafion particles. The formal potential of $MV^{2+/+}$ in both cases was found to be −0.69 V vs SCE. For comparison with the simulation models introduced above, the overpotential $E-E_f$ is reported where the formal potential E_f = −0.690 V. Note that MV^+ can be further reduced to MV^0 at more negative potentials, but in this work only the redox reaction between MV^{2+} and MV^+ is considered since initial experiments, as described in Chapter 8, showed that neutral MV^0 is rapidly lost from the Nafion to the solution phase, consistent with the electrostatic binding of MV^+ and MV^{2+}.

Figure 10.3 shows the cyclic voltammogram of the MV^{2+}-doped Nafion film coated on a GC substrate electrode. The film was made from 0.1 μL Nafion suspension drop-casted on the substrate electrode. The experiment (shown by solid lines in Figure 10.3) and simulation (dashed lines) are combined to analyse the ion transport conditions in the

Nafion film and the value of the ion transport time τ_{it} is measured by fitting to voltammograms measured at different scan rates. The influence of the doping concentration of the electroactive species is also explored. Two different MV^{2+} doping concentrations are considered, one is the "fully-doped" case (MV^{2+}: SO_3^- = 1:20) shown in Figures 10.3 a-c and the other is "half-doped" (MV^{2+}: SO_3^- = 1:40) as shown in Figure 10.3d.

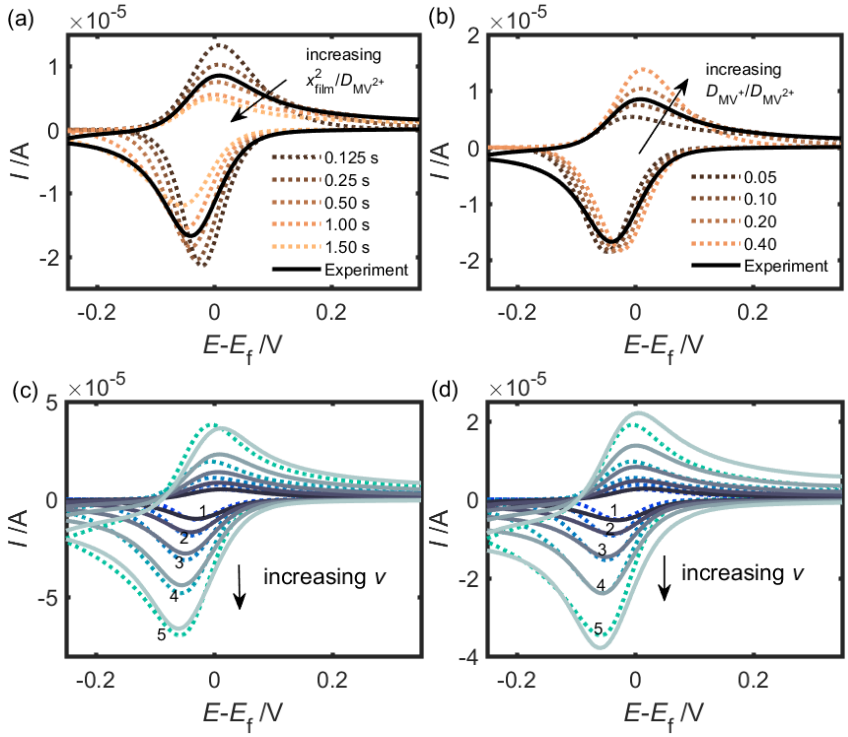


Figure 10.3. (a) Experimental voltammogram (black line) of a fully-doped Nafion thin-film coated electrode recorded at a scan rate of 0.1 V s^{-1} with simulated voltammograms (dashed lines) of various x_{film}^2/D_{MV2+} (0.125, 0.25, 0.50, 1.0, 1.50 s) and a fixed D_{MV+}/D_{MV2+} = 0.1. (b) same experiment data with simulation voltammograms of various D_{MV+}/D_{MV2+} (0.05, 0.1, 0.2, 0.4) and a fixed x_{film}^2/D_{MV2+} = 0.50 s. (c) Experimental voltammograms (solid lines) of the fully-doped Nafion film at various scan rates (v = 0.05, 0.10, 0.20, 0.40, 0.80 V s^{-1}), simulated by x_{film}^2/D_{MV2+} = 0.50 s and D_{MV+}/D_{MV2+} = 0.1 (dashed lines); (d) Experiment (solid lines) and simulation (dashed lines) voltammograms of the half-doped Nafion film. For the fully-doped film used in (a), (b) and (c), M = 2.0×10^{-5} C; for the half-doped film used in (d), M = 1.0×10^{-5} C.

The experimental voltammogram was simulated by the 1D thin-layer model. To infer suitable values for the key fitting parameters τ_{it} (x_{film}^2/D_{MV2+}) and D_{MV+}/D_{MV2+}, Figure 10.3a compares the experimental voltammogram of the fully-doped Nafion film at 0.1 V

s^{-1} scan rate with several simulation results of different τ_{it}; Figure 10.3b compares the same experimental data with simulated results of different D_{MV+}/D_{MV2+}. In Figures 10.3a and 3b, the parameters used in the thin-film CV were determined as τ_{it} = 0.5 ± 0.05 s and D_{MV+}/D_{MV2+} = 0.1 ± 0.05. To obtain the values of M (M, the total amount of chemicals doped in the thin film) for the Nafion films used in Figure 10.3, the forward peak of the fully-doped CV at the slowest scan rate of 0.025 V s^{-1} is integrated and the charge is approximately 2.0×10^{-5} C. Similarly, for the half-doped CV, $M = 1.0\times10^{-5}$ C is measured. Figure 10.3c shows the experiment (solid line) and simulation (dashed line) CVs of the fully-doped film under different scan rates, where the simulation is implemented with the fitting parameters mentioned above. Figure 10.3d shows the CVs of the half-doped film. The key modelling parameter τ_{it} used in the simulation for the fully-doped Nafion film and the half-doped film has the same value of 0.5 ± 0.05 s, indicating that the ion transport is independent of the doping concentration in the cases studied.

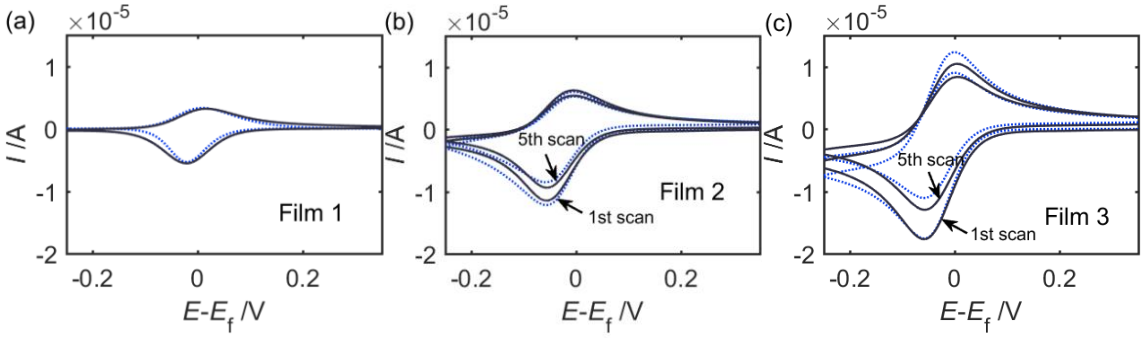


Figure 10.4. Multiple-scan CVs for (a) film 1, of which the dry thickness is 0.35 μm, τ_{it} = 0.5 s, D_{MV+}/D_{MV2+} = 0.1; (b) film 2, of which the dry thickness is 1.75 μm, τ_{it} = 12.5 s, D_{MV+}/D_{MV2+} = 0.1; (c) film 3, of which the dry thickness is 5.26 μm, τ_{it} = 60.0 s, D_{MV+}/D_{MV2+} = 0.1. The 1st scan and the 5th scan are presented in the figure and the voltammograms of the two scans overlap in Figure 10.4a. Black solid lines are the experiment results and blue dashed lines are from the simulation fitting. τ_{it} and D_{MV+}/D_{MV2+} = 0.1 are determined by fitting the experimental data.

Figure 10.4 shows the multi-scan cyclic voltammograms of three "fully-doped" Nafion films with different thicknesses. The dry thickness of the three films can be calculated from the Nafion density and was approximately 0.35 μm for film 1, 1.75 μm for film 2,

5.26 μm for film 3. It is noted that the dry thickness reflects the amount of Nafion doped on the electrode surface but not the "true" thickness of the coating film, as the Nafion is known to swell after immersion into aqueous solution.[23,24]

Applying multiple scans in the voltammetry allows the examination of the redox species, confirming that both the reactant and the product, are fully confined inside the Nafion film during the experiment and that no leaching of either takes place. Figure 10.4a shows the multiple-scan voltammograms of the film 1. For both the experiment (black line) and the simulation (blue dashed line), the voltammograms are identical after multiple scans, suggesting that the redox species MV^{2+}/MV^{+} can be fully cycled in the thin film 1. Integrating the forward and backward peaks gives the same charge for both the reductive and the oxidative processes, further confirming that there is no depletion of the redox species in film 1 during the reaction. However, Figures 10.4b and 4c show the multi-scan voltammograms of film 2 and film 3, where the current decreases after the 1st scan. It is also observed that after a few cycles, the current stops decreasing (see Figure 10.5), showing that the current decrease is not caused by the redox ions depletion during the reaction. As revealed by the simulation, the current decrease is attributed to the slow mass transport speed of the product MV^{+}, which however can be easily misunderstood as the chemical depleting from the thin-film. Comparing the τ_{it} values obtained from the three Nafion films with different thickness, it is found that:

$$\frac{\tau_{\text{it, film 1}}}{0.35^2} = \frac{\tau_{\text{it, film 2}}}{1.75^2} > \frac{\tau_{\text{it, film 3}}}{5.26^2} \tag{10.14}$$

As τ_{it} is proportional to the true film thickness in the reaction, Eqn.(10.14) indicates that the variation of the film thickness and the reactant diffusion speed is identical for the thinner films 1 and 2 but different from the thickest film 3. Taking the water-sorption of the Nafion films into consideration, it is possible that the two thinner films (1 and 2) can quickly adsorb solvent and the film reaches a stable state or a quasi-steady state scan after

immersing into water solution; in contrast the thickest film (film 3) may not fully equilibrate in the same solution. Note that film 3 gives essentially unchanged electrochemical responses even after immersion into the buffer solution for up to 60 minutes, as shown in Figure 10.6.

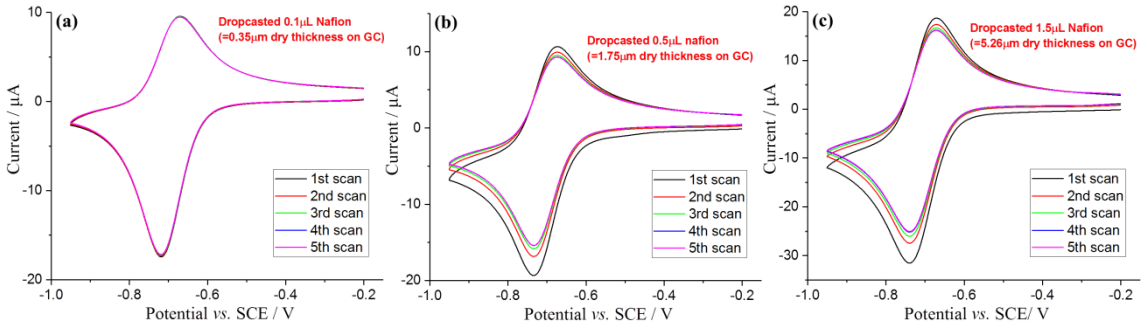


Figure 10.5. Multiple-scan experimental CVs for (a) film 1, of which the dry thickness is 0.35 μm (b) film 2, of which the dry thickness is 1.75 μm (c) film 3, of which the dry thickness is 5.26 μm; scan rate = 0.1 V s^{-1}.

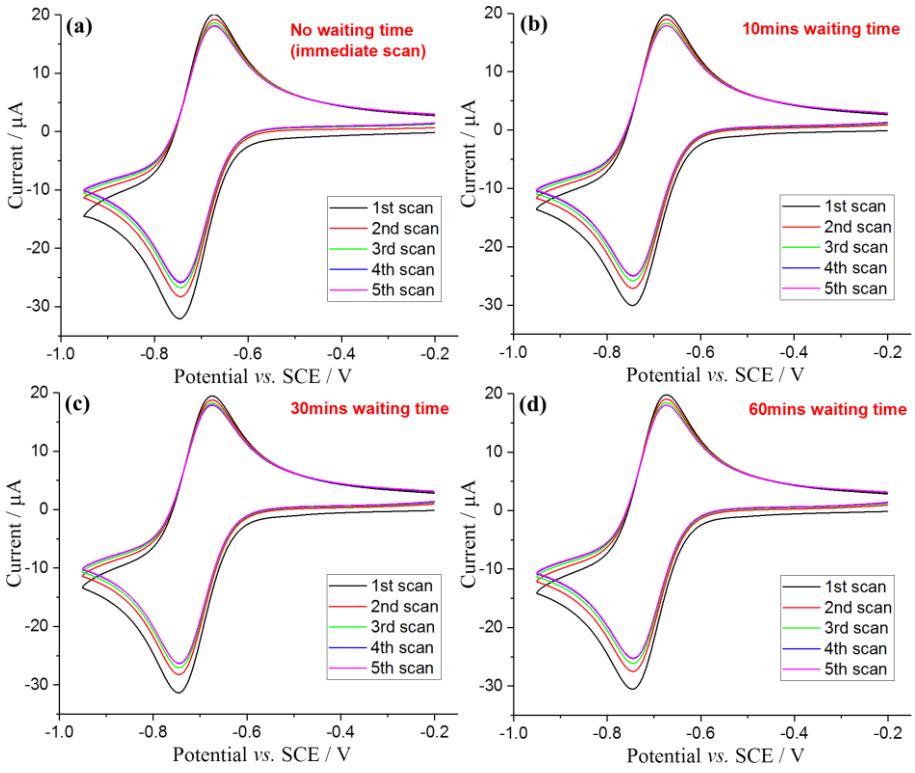


Figure 10.6. Multiple-scan experimental CVs of film 3(with dry thickness 5.26 μm) for different waiting time after immersing the films into the buffer solution (a) no waiting time (b) 10mins waiting time (c) 30mins waiting time (d) 60mins waiting time; scan rate = 0.1 V s^{-1}

The similar ion transport properties measured in film 1 and film 2 shows that in these cases the diffusion of the reactant is independent of the film thickness. The ion transport time τ_{it} is also proved to be independent of the doping concentration in Figure 10.3, indicating that the charge transport mechanism in these Nafion films is likely to be ion self-diffusion rather than electron hopping.[25] Figure 10.3 and Figure 10.4 both show that the diffusion of the product MV^+ is much slower than the reactant MV^{2+} (D_{MV+}/D_{MV2+} = 0.1), despite the lower ion charge. The interaction between the redox species and Nafion is both ionic and hydrophobic for methyl viologens.[26] In comparison to MV^{2+}, MV^+ is more hydrophobic and this is a possible reason explaining why MV^+ moves slower in the water-saturated Nafion film.[27]

10.4.2 Ion Transport in Single Nafion Particles

The one-electron-transfer reaction $MV^{2+} + e^- = MV^+$ in a single MV^{2+}-doped Nafion particle was next investigated *via* the nano-impact technique. The dry radius of the Nafion particles used was on average 0.46 μm. The chronoamperometry measured at the substrate electrode immersed in the Nafion particle suspension was recorded at a high overpotential where E = −1.0 V vs SCE and the overpotential $E - E_f$ is −0.3 V. Note that MV^{2+} can be only reduced to MV^+ at this overpotential.[8] The current responses ("spikes") of single particles observed in experiment is analysed by the single particle simulation model to infer the ion transport conditions in sub-micron Nafion particles.

Figure 10.7a shows some examples of the single particle signals measured. Figure 10.7b shows four individual spikes each of which corresponds to reduction of an individual Nafion particle, where the black line refers to the experimental data and the dashed lines are from simulations. In the single-particle simulation model, it is assumed that there is a "contacting" area between the particle and the electrode, where the electron transfer occurs on the surface of the contacting area. In contrast to the thin-film model, the two unknown

parameters in the single-particle model are τ_{it} and the contacting area which is characterised by the contacting angle ϕ_{cnt}, which both contribute to the signal current. Therefore, any spike signal can be simulated by either a short τ_{it} (faster ion transport) combined with a small ϕ_{cnt} (smaller electron-transfer area) or a long τ_{it} (slower ion transport) with a large ϕ_{cnt} (larger electron-transfer area). However, while the exact value of τ_{it} cannot be unambiguously measured, the ion transport speed can be still estimated relative to that in the film.

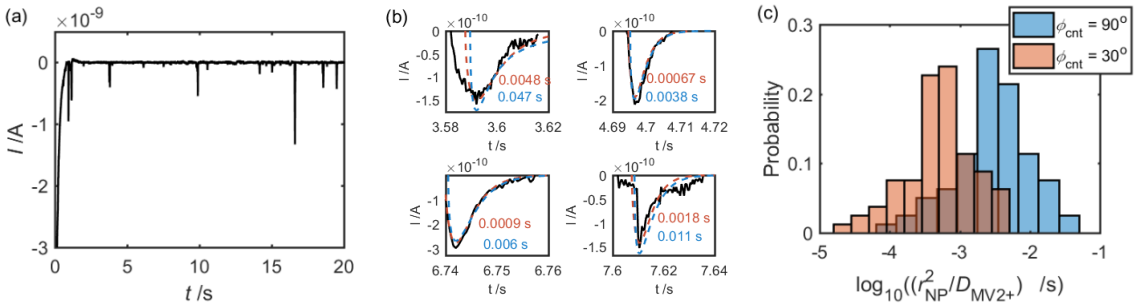


Figure 10.7. (a) Chronoamperometry measured in Nafion particle suspension; (b) Four individual Nafion particle experiment signals (black) with simulations of 30° (red) and 90° (blue) contacting angles; (c) Distribution of the measured τ_{it} in the simulations of 30° (red) and 90° (blue) contacting angles. In the simulation, the charge Q of each particle is calculated from their experimental current spikes.

To explore the possible ion transport speed in single particles, τ_{it} is calculated with different ϕ_{cnt}. Figure 10.7b shows two simulation conditions which are both able to fit the experimental spikes well. The red line is the simulation result of ϕ_{cnt} = 30° where the particle relatively minimally distorted on impact and the blue one is the extreme case where ϕ_{cnt} = 90° corresponding to the particle flattening to a hemisphere upon impacting with the electrode. When the contacting area is fixed, the value of τ_{it} can be calculated *via* fitting the spike, as explained in Eqn.(10.13). Figure 10.7c shows the distribution of τ_{it} measured for 70 independent, individual Nafion particles under the assumptions of ϕ_{cnt} = 30° (red) and ϕ_{cnt} = 90° (blue). As each individual particle is not identical, a distribution of τ_{it} can be recorded under a fixed ϕ_{cnt}. For ϕ_{cnt} = 30°, τ_{it} is from 10^{-5} s to 10^{-2} s; for ϕ_{cnt} = 90°,

τ_{it} is from 10^{-4} s to 10^{-1} s. Although the contacting area is not clear, it is apparent that the ion transport time τ_{it} (most of which are much smaller than 0.1 s) in Nafion particles is much faster than measured from Nafion thin layers (0.5 s).

10.4.3 Ion transport in Nafion particle modified electrodes

To further appreciate the difference observed between the Nafion thin film and the Nafion particles, the cyclic voltammetry of the Nafion particles modified electrode was recorded experimentally and analysed with the aid of simulation. Three Nafion particle modified electrodes were made by drop-casting different amounts of Nafion particles, which correspond to approximately 3, 5 and 15 layers of particles on the glassy carbon substrate electrode. The estimation of the number of layers of particles loaded on the electrode is approximated from the dry radius of the Nafion particle hence may not fully reflect the number of particles contributing to the electron transfer on the electrode. The reactant MV^{2+} is doped in the particles and the doping concentration is MV^{2+}:SO_3^- = 1:20 ("fully-doped"). The one-electron-transfer reaction $MV^{2+} + e^- = MV^+$ was studied on these Nafion particle modified electrodes and the single Nafion particle model was applied to the analysis of the experimental cyclic voltammetry on these particles. The analysis is developed by first assuming that the electrochemical response of each particle is independent and the redox species are all confined in the particles during the reaction so as to get an initial point of comparison with experiment. To understand the ion transport property in Nafion particles, the cyclic voltammetry of immobilized particles with different drop-casting amounts are measured and the current-potential response of the immobilized Nafion particles is compared with a Nafion film, in which the ion transport speed has been determined.

Figure 10.8a shows the cyclic voltammetry of MV^{2+}-doped Nafion particle modified electrodes with 3, 5 and 15 layers respectively at a scan rate of 0.1 V/s. Figure 10.8b

compares the voltammetric waveshape between a Nafion thin film (film 1) and a particle-modified electrode (15 layers). Figure 10.8c is the normalized current response of Figure 10.6b. If the ion transport speed in the two materials were similar, the same diffusion-controlled feature would be observed on the particles modified electrode, which is contradictory to experiment.

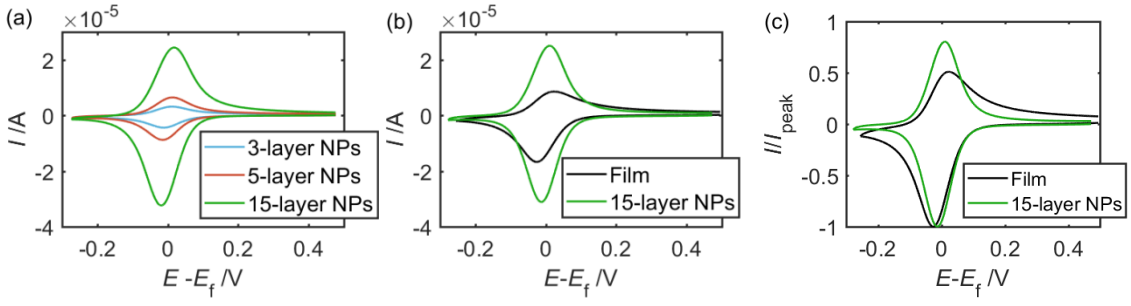


Figure 10.8. (a) Cyclic voltammetry recorded on three Nafion particles modified electrodes at a scan rate of 0.1 V s^{-1}. Blue line: 3 layers of Nafion particles are drop-casted on the glassy carbon macroelectrode; Red line: 5 layers; Green line: 15 layers. (b) Cyclic voltammetry of MV^{+}/MV^{2+} redox reaction in MV^{2+} doped Nafion film and Nafion particles (15 layers) modified electrode at 0.1 V s^{-1} scan rate. (c) Normalized current-potential responses in Nafion film and particles. For comparison, the current I in (c) is normalized by the forward peak current I_{peak}.

The single particle model was applied to simulate the data from the three electrodes on which *ca.* 3, 5 and 15 layers of Nafion particles are modified. Figure 10.9 shows the experiment and simulation peak currents of the three electrodes. The fitting of the simulation model to the experiment data can be found in the Appendix D3. The simulations of the 3, 5 and 15 layers of modifying particles employ the same τ_{it} (0.025 s) and D_{MV+}/D_{MV2+} (0.5) but different contacting area ϕ_{cnt}. The identical τ_{it} found for the three electrodes suggests that there is probably only one layer of Nafion particles contributing to the electron transfer on the electrode as the particle-particle contact seemingly play little role in districting the response. The fitting parameter of the contacting angle ϕ_{cnt} decreases when fewer amounts of particles are drop-casted on the electrode, hinting that more particles are stacked on the electrode, the less area of the particles can contact with the

electrode. The similarity of τ_{it} among the three electrodes confirms that there is only the first layer of particles triggering the redox reaction while the difference in ϕ_{cnt} may explain why the number of the particles involved in the reaction is different for the three electrodes.

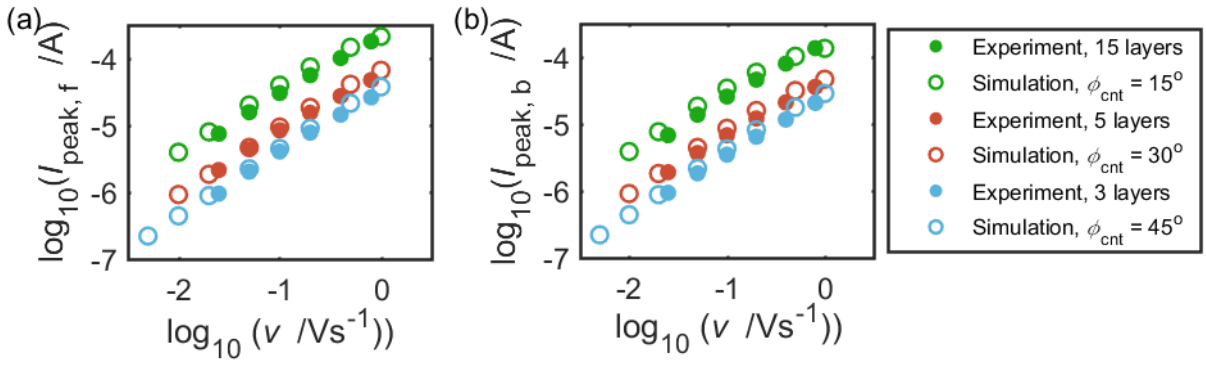


Figure 10.9. Experimental (solid circles) and simulated (open circles) peak currents under various scan rates. (a) Forward peak current, $I_{peak,\ f}$; (b) backward peak current, $I_{peak,\ b}$. Blue: 3 layers of Nafion particles modified electrode under the simulation of τ_{it} = 0.025, ϕ_{cnt} = 45° and D_{MV+}/D_{MV2+} = 0.5; Red: 5 layers modification under τ_{it} = 0.025, ϕ_{cnt} = 30° and D_{MV+}/D_{MV2+} = 0.5; Green: 15 layers modification under τ_{it} = 0.025, ϕ_{cnt} = 18° and D_{MV+}/D_{MV2+} = 0.5.

Figure 10.8 highlights the difference in the ion transport speed between the Nafion thin layer and the Nafion particles, where diffusion-controlled features are found in the thin-film voltammetry (from intra-film diffusion) but thin-layer features are found in the particle voltammetry. Via simulation, the parameters τ_{it} are also found to be different for the two Nafion materials, τ_{it} = 0.5 s for the film with dry thickness of 0.35 μm and τ_{it} = 0.025 s for the particles with dry radius of 0.46 μm, reflecting different hydration of particles and of films. Another interesting change is the difference of D_{MV+}/D_{MV2+} between Nafion films and particles. In Nafion particles, the ion transport speed of MV^+ is still slower than MV^{2+} (D_{MV+}/D_{MV2+} = 0.5) but not as much as in the film (D_{MV+}/D_{MV2+} = 0.1). Combining with single Nafion particle signals shown in Figure 10.8, it can be concluded that the ion transport of MV^{2+} and MV^+ is faster in Nafion particles than in Nafion thin films.

10.5 Discussion and Perspectives

The ion transport speed in two types of Nafion materials was measured and used to characterise the structure-functionality of Nafion materials. The ion transport speed, marked by τ_{it}, and the relative speed of MV^{+} and MV^{2+}, marked by $D_{product}/D_{reactant}$, was derived via fitting the experiment data with the theoretical models of Eqn.(10.11), (10.12) and (10.13). It was seen that the ion transport speed for the redox species MV^{2+} in Nafion particles is much faster than in the thin film of similar thicknesses. As discussed above, a possible explanation for this is the water-sorption influence on the ion transport property in Nafion materials. For the hydrophilic ions such as Na^{+} and Cl^{-}, higher water content leads to faster ion diffusion speeds;[28] while for hydrophobic ions such as MV^{2+} and MV^{+}, higher water content is suggested to lead to slower ion diffusion speeds.[27] The faster ion transport speed in Nafion particles may indicate that the water-sorption in the particles is much less than that in the films, showing that material preparation and processing have significant influence in the material structure and properties. A larger D_{MV+}/D_{MV2+} ratio measured in Nafion particles also suggests a structure difference between the particles and the films.

The combined voltammetry/impact approach offers applications beyond the present work. On the one hand, the ion transport properties of Nafion or other ionomer materials can be quantified and investigated directly in electrode systems. These can be influenced by many factors, such as the charges of the redox ions, the sizes of the redox ions, the doping concentration, the film thickness, the structure and component of the ionomer, and the supporting substrate.[2,9] In real applications, varying redox species or materials may lead to other charge transport mechanisms, such as electronic hopping, of which differ from the ion transport of MV^{2+}/MV^{+}. However, only little modification to the current simulation model is needed to include more complex situations, such as the permeability of the ions

or the conductivity of the materials. Moreover the key modelling parameter τ_{it} generally describes ion transport speed in the ionomer materials.

10.6 Conclusions

Contrasting transport in Nafion films and particles has been demonstrated and quantified. The observation of faster diffusion of MV^{2+} as compared to MV^{+} has been confirmed with the relative rates sensitive to the physical form of Nafion. The work highlights the existence of diverse transport behaviour from Nafion processed in different ways.

Bibliography

(1) Chen, L.; Lin, C.; Compton, R. G. *Physical Chemistry Chemical Physics* **2019**, *21*, 607-616.
(2) Mauritz, K. A.; Moore, R. B. *Chemical Reviews* **2004**, *104*, 4535-4586.
(3) Xuejiang, W.; Dzyadevych, S. V.; Chovelon, J.-M.; Renault, N. J.; Ling, C.; Siqing, X.; Jianfu, Z. *Talanta* **2006**, *69*, 450-455.
(4) Wang, T.; Zhao, D.; Guo, X.; Correa, J.; Riehl, B. L.; Heineman, W. R. *Analytical Chemistry* **2014**, *86*, 4354-4361.
(5) Holdcroft, S. *Chemistry of Materials* **2014**, *26*, 381-393.
(6) Desimoni, E.; Brunetti, B. *Electroanalysis* **2012**, *24*, 1481-1500.
(7) Yang, H.; Li, X.; Batchelor-McAuley, C.; Sokolov, S. V.; Kätelhön, E.; Compton, R. G. *Chemistry – A European Journal* **2017**, *23*, 17605-17611.
(8) Chen, L.; Lin, C.; Compton, R. G. *Physical Chemistry Chemical Physics* **2018**, *20*, 15795-15806.
(9) Kusoglu, A.; Weber, A. Z. *Chemical Reviews* **2017**, *117*, 987-1104.
(10) DeCaluwe, S. C.; Baker, A. M.; Bhargava, P.; Fischer, J. E.; Dura, J. A. *Nano Energy* **2018**, *46*, 91-100.
(11) Galperin, D.; Khalatur, P. G.; Khokhlov, A. R. In *Topics in Applied Physics*, 2009, pp 453-482.
(12) Hensley, J. E.; Way, J. D.; Dec, S. F.; Abney, K. D. *Journal of Membrane Science* **2007**, *298*, 190-201.
(13) Maldonado, L.; Perrin, J.-C.; Dillet, J.; Lottin, O. *Journal of Membrane Science* **2012**, *389*, 43-56.
(14) Krtil, P.; Trojánek, A.; Samec, Z. *Journal of Physical Chemistry B* **2001**, *105*, 7979-7983.
(15) Kätelhön, E.; Tanner, E. E. L.; Batchelor-McAuley, C.; Compton, R. G. *Electrochimica Acta* **2016**, *199*, 297-304.
(16) Peerce, P. J.; Bard, A. J. *Journal of Electroanalytical Chemistry and Interfacial Electrochemistry* **1980**, *114*, 89-115.
(17) Guidelli, R.; Compton, R. G.; Feliu, J. M.; Gileadi, E.; Lipkowski, J.; Schmickler, W.; Trasatti, S. *Pure and Applied Chemistry* **2014**, *86*, 259-262.
(18) Guidelli, R.; Compton, R. G.; Feliu, J. M.; Gileadi, E.; Lipkowski, J.; Schmickler, W.; Trasatti, S. *Pure and Applied Chemistry* **2014**, *86*, 245-258.

(19) Kätelhön, E.; Feng, A.; Cheng, W.; Eloul, S.; Batchelor-McAuley, C.; Compton, R. G. *Journal of Physical Chemistry C* **2016**, *120*, 17029-17034.
(20) Compton, R. G.; Laborda, E.; Ward, K. R. *Understanding Voltammetry: Simulation of Electrode Processes*; Imperial College Press, 2013.
(21) Hickner, M. A. *Journal of Polymer Science Part B: Polymer Physics* **2012**, *50*, 9-20.
(22) Satterfield, M. B.; Majsztrik, P. W.; Ota, H.; Benziger, J. B.; Bocarsly, A. B. *Journal of Polymer Science Part B: Polymer Physics* **2006**, *44*, 2327-2345.
(23) Eikerling, M. H.; Berg, P. *Soft Matter* **2011**, *7*, 5976-5990.
(24) Gebel, G.; Aldebert, P.; Pineri, M. *Polymer* **1993**, *34*, 333-339.
(25) White, H. S.; Leddy, J.; Bard, A. J. *Journal of the American Chemical Society* **1982**, *104*, 4811-4817.
(26) Safranj, A.; Gershuni, S.; Rabani, J. *Langmuir* **1993**, *9*, 3676-3681.
(27) Martin, C. R.; Dollard, K. A. *Journal of Electroanalytical Chemistry and Interfacial Electrochemistry* **1983**, *159*, 127-135.
(28) Goswami, A.; Acharya, A.; Pandey, A. K. *Journal of Physical Chemistry B* **2001**, *105*, 9196-9201.

Chapter 11

Reference Electrodes for Electrochemical Sensors Based on Redox Couples Immobilized within Nafion Films

Building on Chapter 8 and 10, a novel improved reference electrode for sensor and other applications is proposed in this Chapter. Specifically, the immobilization of both components of a redox couple within films of the sulfonated tetrafluoroethylene polymer, Nafion, on the surface of carbon electrodes is reported. In particular, cationic and/or water-insoluble species are used to develop stable and robust reference electrodes by adjustment and optimization of both the film thickness and the level of doping of the film, as an alternative to using standard commercial reference electrodes. Different redox couples were evaluated: methyl viologen dication/cation (MV^{2+}/MV^{+}), tris(2,2'-bipyridyl)-ruthenium(II)/ruthenium(III) ($Ru(bpy)_3^{2+}/Ru(bpy)_3^{3+}$), ferrocene/ferrocenium (Fc/Fc^{+}) and poly(viny-lferrocene)/poly(vinylferrocenium) ($PVFc/PVFc^{+}$). These reference electrodes demonstrate a good stability over 10 days and 1000 successive scans; in particular Nafion confined $Fc/Fc^{+}PF_6^{-}$ was shown to display the best performance. This type of reference electrode, as a solid-state electrolyte-free reference electrode, has several advantages, including full retention of the redox species within the films together with ease of both fabrication and miniaturization.

The work presented in this Chapter has been published in *ACS Sensors*[1] and a patent has been filed (GB1907791.6).

11.1 Introduction

The reference electrode is an essential component of both potentiometric and amperometric experiments and the many chemical sensors—such as for pH, for gases, for glucose, etc.—which depend on these types of measurements. The stability and robustness of the reference electrode often ultimately dictates the sensitivity and longevity of the sensor and hence its usefulness and range of applicability. Probably the most frequently made electrochemical sensing measurement is that of pH, where since the pioneering work of Beckman in the 1920s,[2,3] as in many other electrochemical sensors, the preferred reference electrode has been the silver/silver chloride electrode based on the half-cell reaction,

$$\mathrm{AgCl(s)} + e^- \rightleftarrows \mathrm{Ag(s)} + \mathrm{Cl^-(aq)} \tag{11.1}$$

for which the Nernst equation is

$$E = E^0 - \frac{RT}{F} \ln a_{\mathrm{Cl^-}} \tag{11.2}$$

where E and E^0 are the electrode potential and standard electrode potential (measured against a common reference electrode, conventionally a standard hydrogen electrode), R is the gas constant, T is the absolute temperature, and F is the Faraday constant. The term $a_{\mathrm{Cl^-}}$ is the activity of the chloride ion,

$$a_{\mathrm{Cl^-}} = \gamma[\mathrm{Cl^-}] \tag{11.3}$$

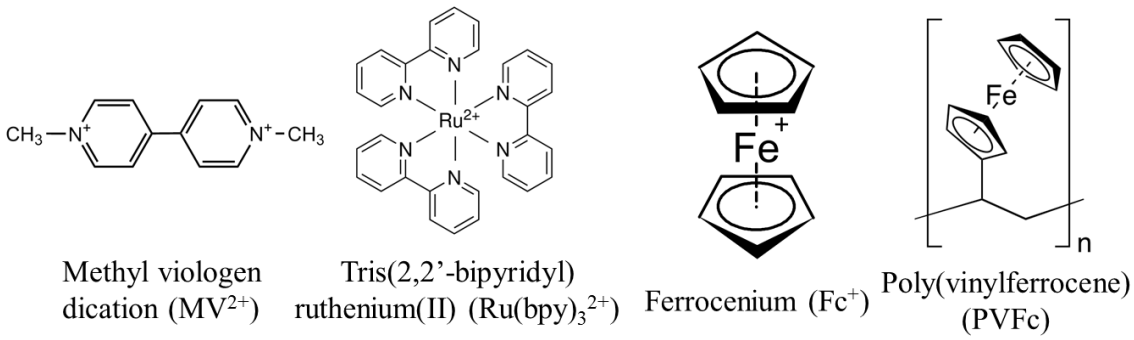
where γ is the corresponding activity coefficient.

Equations (11.1)–(11.3) emphasize that a fixed chloride concentration is mandatory if a reproducible and stable electrode potential is to be established on the reference electrode. This is usually realized by bathing a Ag/AgCl wire or foil in a solution of potassium chloride of a fixed molality, sometimes controlled by having solid KCl present to saturate the solution. At the same time it is essential to maintain some solid silver chloride at the

surface of the silver electrode so as to sustain equilibrium (11.1). These two requirements can prove problematic in some applications, particularly if the reference electrode is required to be miniaturized, such as for small-volume measurements, e.g. for use in scanning electrochemical microscopy (SECM) and scanning probe microscopy (SPM), or to be used in a flowing solution since maintaining the presence of a zone of aqueous chloride solution close to the electrode adds to the size while exposure of the bare Ag/AgCl electrode to chloride-containing solution can result in the loss of AgCl from the surface, for example, in the form of $AgCl_n^{(n-1)-}$ complexes of which $AgCl_2^-$ is well-characterized.[4,5] Thus the deployment of the $Ag/AgCl/Cl^-$ electrode or equally the closely related calomel electrode, $Hg/Hg_2Cl_2/Cl^-$ is often challenging. This observation encourages the search for easier-to-use reference electrode systems which do not suffer from rapid deterioration of the response from loss of key chemical components in the potential-determining equilibrium (11.1).

In the following an approach to the fabrication of reference electrode in which both components of a redox couple, $Ox. + e^- \rightleftarrows Red.$, are immobilized within an ion exchange polymer is considered. To do this, and building on the experience of ourselves[6-8] (as described in Chapters 8 and 10) and others[9-12] with the immobilization of cationic species within films and nanoparticles of Nafion, the well-known and widely applied sulfonated tetrafluoroethylene polymer, this Chapter specifically evaluates the redox couples methyl viologen dication/cation (MV^{2+}/MV^+), tris(2,2'-bipyridyl)ruthenium(II)/ruthenium(III) ($Ru(bpy)_3^{2+}/Ru(bpy)_3^{3+}$), ferrocene/ferrocenium (Fc/Fc^+), and poly(vinylferrocene)/poly-(vinylferrocenium) ($PVFc/PVFc^+$) within Nafion films (chemical structures see Scheme 11.1). Note that in all the cases studied, *both* components (*Ox.* and *Red.*) of a redox couple are present—hence can be interconverted electrochemically, as exploited in the synthetic approach taken below—and are capable of establishing the $Ox. + e^- \rightleftarrows Red.$ equilibrium at

the Nafion/electrode interface, thus pinning the potential of the latter. The work is thus distinct from the use of a pair of redox reagents which are not complementary as a redox pair and hence cannot be interconverted electrochemically; the latter approach has been recently exploited in some all-solid-state ion-selective electrodes.[13,14]



Scheme 11.1. Chemical structures of the redox couples used in this Chapter.

Nafion is selected as the host polymer since past work has demonstrated[15] that Nafion acts as a Donnan ion-exchange membrane in the presence of simple cations such as Li^+, Na^+, K^+, Ca^{2+}, and Mg^{2+}, such that stable, rapidly formed (<5 s) potentials are established at the polymer/electrolyte solution interface. Reference electrodes, as employed in voltammetric sensors, are typically bathed by high ionic strength electrolyte ("background" or "supporting" electrolyte), which will thus provide a fixed potential at the polymer/solution interface and, in combination with the fixed potential at the polymer/metal electrode, will give a stable half-cell electrode signal.

11.2 Experimental

11.2.1 Chemical Reagents

All chemicals were used as received without further purification, as described in Chapter 3. All solutions were prepared using ultrapure water (Millipore) with a resistivity of 18.2 MΩ cm at 298 K and degassed with Argon before use. Phosphate-buffered saline (PBS, pH =

7.4) buffer solution was composed of 137.0 mM NaCl, 2.7 mM KCl, 10.0 mM Na_2HPO_4, and 1.8 mM KH_2PO_4.

11.2.2 Electrochemical Measurements

All measurements were conducted using standard three-electrode setups employing different reference electrodes: saturated calomel electrode (SCE; BASi, Japan) or fabricated Nafion film reference electrodes. A glassy carbon (GC) macroelectrode and a graphite rod were used as working and counter electrodes, respectively.

11.2.3 Fabrication of the Nafion Film Reference Electrodes

Four different reference electrodes were fabricated and studied in this work. These were based on the following redox couples, MV^{2+}/MV^{+}, $Ru(bpy)_3^{2+}/Ru(bpy)_3^{3+}$, Fc/Fc^{+}, and $PVFc/PVFc^{+}$, immobilized in Nafion films. The fabrication of the Fc/Fc^{+} Nafion film reference electrode—the most successful electrode—is described in detail below and all other reference electrodes were fabricated in a similar way. The reference electrodes were optimized by adjusting the doping ratio (of redox couple to Nafion), the film thickness, and the film morphology.

11.2.3.1 Fabrication of the Fc/Fc^{+} Nafion film reference electrode

Preparation of the optimized Fc/Fc^{+} Nafion film reference electrode was carried out electrochemically. The Fc^{+}/Nafion stock samples (with the doping ratio of $Fc^{+}:SO_3^{-} = 1:30$) were prepared by directly dissolving 0.6 mg of $Fc^{+}PF_6^{-}$ into 1.30 mL Nafion perfluorinated resin solution. The mixture was shaken on a vortex (Whirlmixer, Loughborough, UK) for 5 min. Fc^{+}/Nafion films were obtained by drop-casting 10 μL of Fc^{+}-Nafion solution on a bare GC macroelectrode and dried in a nitrogen environment at room temperature. Prior to use, the GC surface was cleaned by successively polishing with three grades of alumina (1.0, 0.3 and 0.05 μm, Buehler, UK) in a decreasing particle size

order, followed by sonication in water and drying with nitrogen. The Fc/Fc^+ Nafion film reference electrode was then obtained electrochemically by sweeping the potential first cathodically from 0.5 V to −0.5 V *vs.* SCE then reversing back to 0.5V at 0.1 V/s for 20 repetitive scans in a degassed pH 7.4 PBS buffer, in the final scan stopping the potential at −0.005 V, as shown in Figure 11.1. At this point, the Fc^+ was partially reduced, and a Nafion film of $Fc/Fc^+PF_6^-$ was produced. Note that the decrease in peak current after the 1st scan in Figure 11.1a is likely attributed to the slow mass transport of the electro-generated product within the thick Nafion film, which might be easily misunderstood as the chemical depleting from the Nafion film, as investigated in detail in Chapter 10. The peak current stops decreasing after a few scans (magenta, brown and orange lines in Figure 11.1a) confirming that current decrease is not caused by the redox depletion during the reaction. The initial cycling is needed to stabilize the coating; the final partial scan injects a net charge so that both Fc and Fc^+ are present in the film. The relative amount of Fc and Fc^+ in Nafion films after the final scan is estimated to be 1:550 (See details in Appendix E4), and the dry thickness of this film was estimated to be 35 μm (See Appendix D1). The Nafion film prepared is uniform and homogeneous, and its estimated thickness verified by atomic force microscopy (AFM).[16]

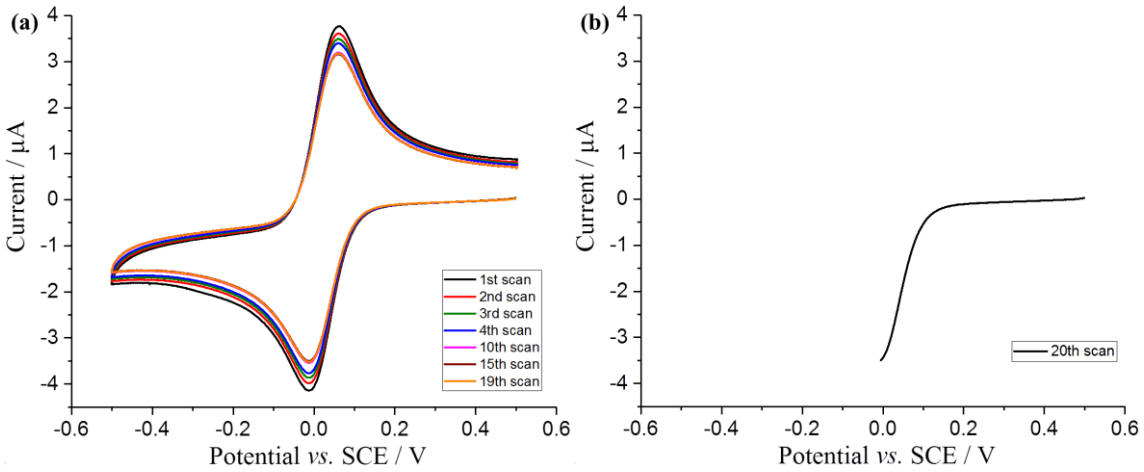


Figure 11.1. Voltammograms of a Fc^+-Nafion film (with a doping ratio of $Fc^+:SO_3^-$ = 1:30 and thickness of 35 μm) drop-casted glassy carbon electrode in pH 7.4 PBS buffer at a scan rate of 0.1 V s^{-1} for 20 successive scans. (a) 1st scan to 19th scan (b) the 20th scan.

11.2.3.2 Fabrication of the MV^{2+}/MV^{+} Nafion film reference electrodes

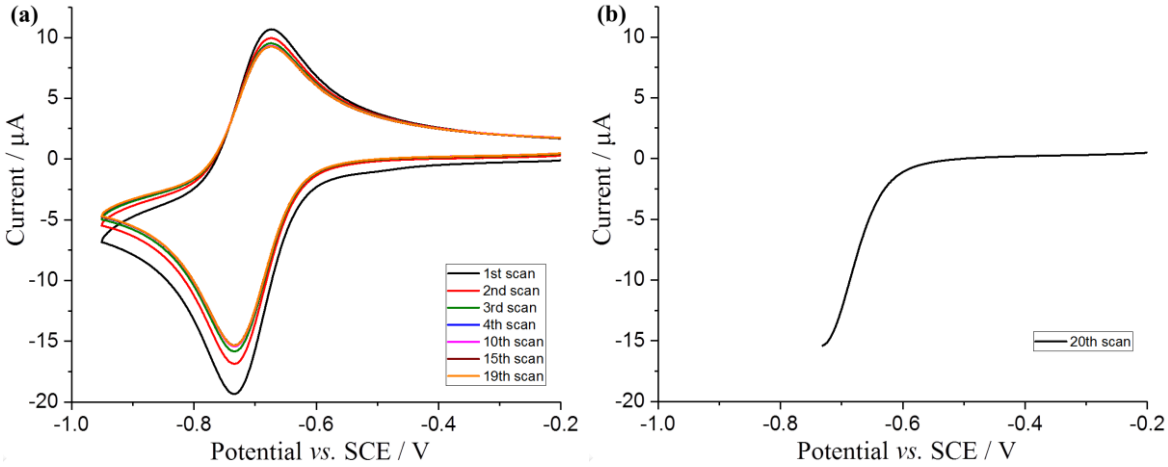


Figure 11.2. Voltammograms of a MV^{2+}-Nafion film (with the doping ratio of MV^{2+}:SO_3^- = 1:30 and thickness of 35 μm) drop-casted glassy carbon electrode in pH 7.4 PBS buffer at a scan rate of 0.1 V s^{-1} for 20 successive scans. (a) 1st scan to 19th scan (b) the 20th scan.

Similar to above, the MV^{2+}/Nafion stock samples (with the doping ratio of MV^{2+}:SO_3^- = 1:30) were prepared by directly dissolving 0.5 mg of $MVCl_2$ into 1.40 mL Nafion perfluorinated resin solution. The mixture was shaken on a vortex for 5 min. MV^{2+}/Nafion films with film thickness of 35 μm were obtained by drop-casting 10 μL of MV^{2+}-Nafion solution on a bare GC macroelectrode and dried in a nitrogen environment at room temperature. The MV^{2+}/MV^{+} Nafion film reference electrode was then obtained electrochemically by sweeping the potential first cathodically from −0.20 V to −0.95 V *vs.* SCE then reversing back to −0.20 V at 0.1 V/s for 20 repetitive scans in a degassed pH 7.4 PBS buffer and in the final scan, the potential stopping at −0.73 V, as shown in Figure 11.2. At this point, the MV^{2+} was partially reduced and a Nafion film of $MV^{2+}/MV^{+}Cl_2$ was produced. The relative amount of MV^{+} and MV^{2+} in Nafion films after fabrication is estimated to be 1:130 (see Appendix E4).

Note that for the doping ratio of MV^{2+}:SO_3^- = 1:4, 1:50, 1:100 and 1:200 , 0.5 mg of $MVCl_2$ were directly dissolved into 0.19 mL, 2.32mL, 4.64 mL, 9.29 mL of Nafion perfluorinated resin solution, respectively.

Note that for Nafion films with film thicknesses of 0.35 μm, 1.75 μm, 7.0 μm and 17.5 μm were obtained by drop-casting 0.1 μL, 0.5 μL, 2 μL and 5 μL of MV^{2+}-Nafion solution on the GC electrode, respectively.

11.2.3.3 Fabrication of the $Ru(bpy)_3^{2+}/Ru(bpy)_3^{3+}$ Nafion film reference electrodes

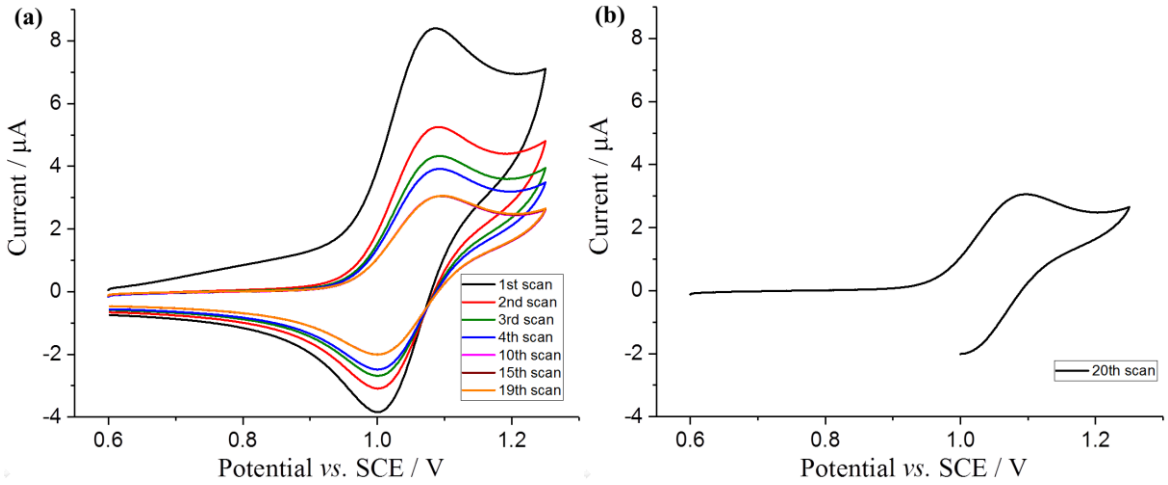


Figure 11.3. Voltammograms of a $Ru(bpy)_3^{2+}$-Nafion film (with the doping ratio of $Ru(bpy)_3^{2+}:SO_3^-$ = 1:30 and thickness of 35 μm) drop-casted glassy carbon electrode in a pH 7.4 PBS buffer at a scan rate of 0.1 V s^{-1} for 20 successive scans. (a) 1st scan to 19th scan (b) the 20th scan.

The $Ru(bpy)_3^{2+}$/Nafion stock samples (with the doping ratio of $Ru(bpy)_3^{2+}:SO_3^-$ = 1:30) were prepared by directly dissolving 1.4 mg of $Ru(bpy)_3Cl_2 \cdot 6H_2O$ into 1.34 mL Nafion perfluorinated resin solution. The mixture was then shaken on a vortex for 5 min. $Ru(bpy)_3^{2+}$/Nafion films with film thickness of 35 μm were obtained by drop-casting 10 μL of $Ru(bpy)_3^{2+}$/Nafion solution on a bare GC macroelectrode and dried in a nitrogen environment at room temperature. The $Ru(bpy)_3^{2+}/Ru(bpy)_3^{3+}$ Nafion film reference electrode was then obtained electrochemically by sweeping the potential first anodically from 0.60 V to 1.25 V *vs.* SCE then reversing back to 0.60 V at 0.1 V/s for 20 repetitive scans in a degassed pH 7.4 PBS buffer and in the final scan, the potential stopping at 1.0 V, as shown in Figure 11.3. At this point, the $Ru(bpy)_3^{2+}$ was partially oxidised and a Nafion

film of $Ru(bpy)_3^{3+}/Ru(bpy)_3^{2+}Cl_2$ was produced. The relative amount of $Ru(bpy)_3^{3+}$ and $Ru(bpy)_3^{2+}$ in Nafion films after fabrication is estimated to be 1:170 (see Appendix E4).

11.2.3.4 Fabrication of the PVFc/PVFc$^+$ Nafion film reference electrodes

The PVFc/Nafion stock samples (with the doping ratio of VFc moiety:SO_3^- = 1:30) were prepared by directly dissolving 0.8 mg of PVFc into 2.70 mL Nafion perfluorinated resin solution. The mixture was then shaken on a vortex for 5 min. PVFc/Nafion films with film thickness of 35 μm were obtained by drop-casting 10 μL of PVFc/Nafion solution on a bare GC macroelectrode and dried in a nitrogen environment at room temperature. The PVFc/PVFc$^+$ Nafion film reference electrode was then obtained electrochemically by sweeping the potential first anodically from −0.20 V to 0.80 V *vs.* SCE then reversing back to −0.20 V at 0.1 V/s for 20 repetitive scans in a degassed pH 7.4 PBS buffer and in the final scan, the potential stopping at 0.51 V, as shown in Figure 11.4. At this point, the PVFc was partially oxidised and a Nafion film of PVFc/PVFc$^+$ was produced. The relative amount of PVFc$^+$ and PVFc in Nafion films after fabrication is estimated to be 1:900 (see Appendix E4).

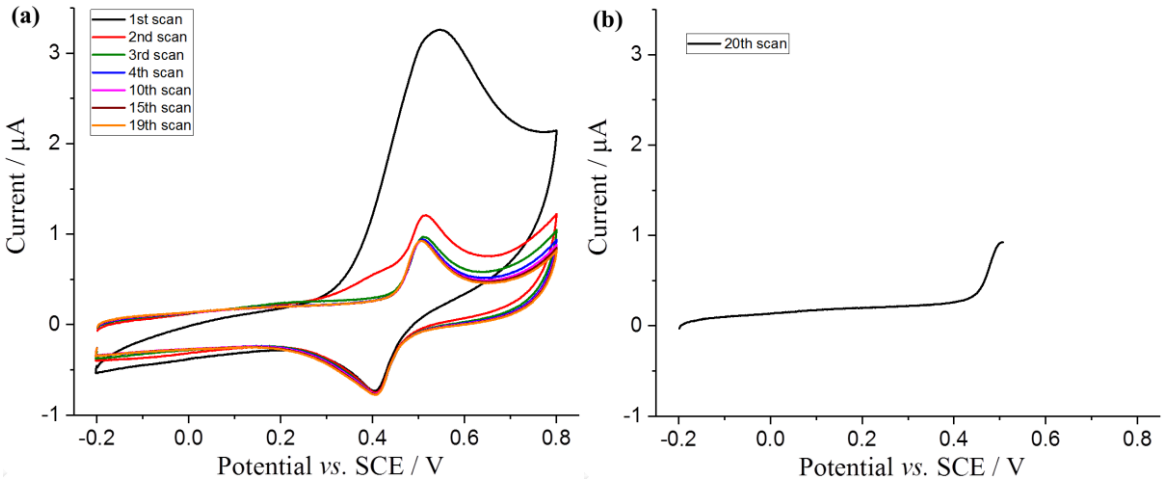


Figure 11.4. Voltammograms of a PVFc-Nafion film (with the doping ratio of VFc moiety:SO_3^- = 1:30 and thickness of 35 μm) drop-casted glassy carbon electrode in pH 7.4 PBS buffer at a scan rate of 0.1 V s^{-1} for 20 successive scans. (a) 1st scan to 19th scan (b) the 20th scan.

11.2.4 Fabrication of the Doped Nafion Particle Reference Electrodes

Nafion particles doped with MV^{2+} (300 mM) were synthesized by the re-precipitation method, as described in Chapter 3&8. 30 μL of obtained MV^{2+}/Nafion particles suspension was drop-cast on the GC electrode and dried in a nitrogen environment at room temperature. 45 layers of MV^{2+}/Nafion particles were drop-casted on the surface of GC electrode giving an approximate 38.7 μm total thickness. The MV^{2+}/MV^{+} Nafion particle based reference electrode was then obtained electrochemically, similarly to the MV^{2+}/ MV^{+} Nafion film, by sweeping the potential first cathodically from −0.20 V to −0.95 V *vs.* SCE then reversing back to −0.20 V at 0.1 V/s for 20 repetitive scans in a degassed pH 7.4 PBS buffer and in the final scan, the potential stopping at −0.73 V.

11.2.5 Characterisation and Stability Study of Nafion Film Reference Electrodes

The stability of the Nafion film reference electrodes was assessed voltammetrically in aqueous solutions with $[Ru(NH_3)_6]Cl_3$ as a redox indicator using cyclic voltammetry. $[Ru(NH_3)_6]^{3+}/[Ru(NH_3)_6]^{2+}$ was chosen as the redox couple because the reduction of $Ru(NH_3)_6^{3+}$ is fully reversible and well-characterized.[17] Cyclic voltammetry of 1.0 mM $[Ru(NH_3)_6]Cl_3$ in the presence of 0.1 M KCl supporting electrolyte was performed at a GC macroelectrode as working electrode with the fabricated reference electrode and a graphite counter electrode at 0.1 V s^{-1}, and the peak potentials of the voltammograms were monitored to give an indication of any drift or instability of the reference electrodes. Note that the presence of the fixed concentration of 0.1 M KCl ensures that there is a stable, constant potential at the polymer/electrolyte "interface" arising from the Nafion acting as a Donnan exclusion membrane, as discussed in Introduction.[15]

11.3 Results and Discussion

Three main parameters of the films, namely doping ratio, film thickness, and morphology, were investigated to optimise the performance and stability for all four Nafion film reference electrodes. The stability and robustness of the Fc/Fc^+ Nafion film reference electrodes fabricated under optimized conditions are shown to be optimal among the different systems investigated.

11.3.1 Electrode Performance Optimisation

Studies on a series of redox couples doped in Nafion film reference electrodes are reported below. In particular, the electrochemistry of MV^{2+}/MV^+ and $Ru(bpy)_3^{2+}/Ru(bpy)_3^{3+}$ doped in Nafion was first studied, as described in Chapter 8, and both cations of the couples are reported to have strong affinity for the SO_3^- group of Nafion.[6,7] The ion transport behaviour in Nafion film was investigated experimentally and theoretically in Chapter 10, and both cations were proved to fully be confined within both thin and thick Nafion films. Consequently, at least in principle, they can be applied as reference electrodes with a good stability. The fabrication procedure of MV^{2+}/MV^+ and $Ru(bpy)_3^{2+}/Ru(bpy)_3^{3+}$ Nafion film reference electrodes was described above. In the following, the reversible one-electron-transfer redox couple of $[Ru(NH_3)_6]^{3+}/[Ru(NH_3)_6]^{2+}$ is used to determine the potential of Nafion film reference electrodes and their stability. In essence, a cyclic voltammogram of $[Ru(NH_3)_6]^{3+}$ in fully supported aqueous media at a carbon working electrode is recorded using the candidate reference electrodes as the reference electrode in a conventional three-electrode voltammetric measurement. Any change in the potential of the Ru(III)/Ru(II) couple is used to infer changes of potential in the reference electrode. Two important parameters of the film, namely doping ratio (initial doped species:SO_3^-) and thickness of

the film, were initially investigated to optimize the performance and stability of the reference electrodes.

11.3.2 Effect of Doping Ratio

Five MV^{2+}/MV^{+} Nafion films with the same thickness (0.35 μm) but different initial doping ratios (the ratio of MV^{2+}:SO_3^-) were fabricated. Note that the relative amount of MV^{+} and MV^{2+} within Nafion film after fabrication is estimated as 1:133 (See Appendix E4 for details). Figure 11.5 shows a typical cyclic voltammogram of hexaammine-ruthenium(III) chloride recorded on a GC electrode with a freshly fabricated MV^{2+}/MV^{+} Nafion film reference electrode (with the initial doping ratio of MV^{2+}:SO_3^- = 1:30) and graphite counter electrode in a solution containing 1 mM $[Ru(NH_3)_6]Cl_3$ supported with 0.1M KCl. The midpoint potential (E_{mid}; taken as the average of the cathodic and anodic peak potentials) of the mediator was −0.165 V *vs.* MV^{2+}/MV^{+} Nafion film.

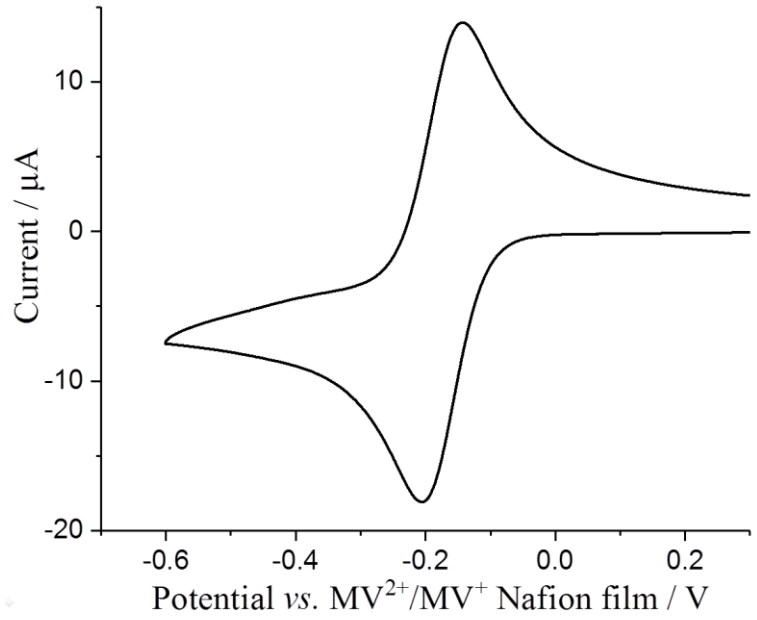


Figure 11.5. Voltammograms of a glassy carbon working electrode with a freshly prepared MV^{2+}/MV^{+} Nafion film reference electrode in 0.1 M KCl aqueous solution containing 1 mM $[Ru(NH_3)_6]Cl_3$ at a scan rate of 0.1 V s^{-1}.

The CVs of $[Ru(NH_3)_6]^{3+}$ were recorded over 3 h after the electrode was immersed in the solution, and the E_{mid} was determined and plotted as a function of time, as shown in Figure 11.6. At a very high initial doping ratio (MV^{2+}:SO_3^- = 1:4), the potential of the MV^{2+}/MV^+ Nafion films drifts (ca. 51 mV from the stabilized potential) in the first 10 min before it stabilizes. This might reflect the depletion of doped redox species in the film when the doping ratio is too high and the level of SO_3^- in Nafion is insufficient to retain the excess dopant chemicals. For doping ratios ranging from 1:30 to 1:100, a very stable potential with a deviation less than 0.5 mV of the thin Nafion film electrodes over 2 h was obtained. This is consistent with the previous study in Chapter 8, where excess MV^{2+} was used to dope Nafion and the final product after washing gave a stable doping ratio of 1:20, suggesting this is the maximum stable uptake limit. For the films with a doping ratio of 1:200, a fluctuating E_{mid} potential (±4 mV) was observed. This might result from an inhomogeneous distribution of the redox species, MV^{2+} and MV^+, within the Nafion film at extremely low doping ratios. A doping ratio (initial doped species:SO_3^-) of 1:30 was chosen for the subsequent study in this work.

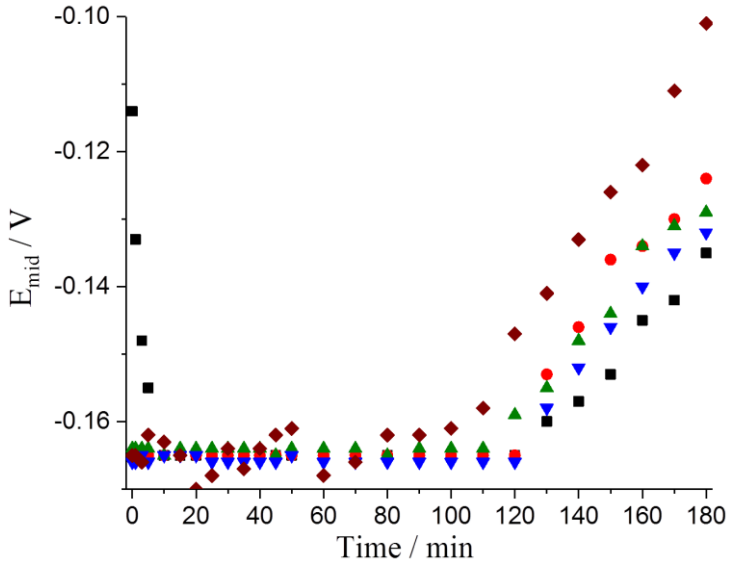


Figure 11.6. Midpoint potential, E_{mid}, of $[Ru(NH_3)_6]^{3+}$ reduction *vs.* MV^{2+}/MV^+ Nafion film (with the film thickness of 0.35 μm) reference electrodes with different doping ratios recorded over 3 h (doping ratio = 1:4, black points; 1:30, red points; 1:50, blue points; 1:100, green points; 1 : 200, brown points).

Another important observation was that, for all five different Nafion film reference electrodes of thickness 0.35 μm, the potential started to drift after ca. 120 min in the solution (35 ± 3 mV/h). This suggests that the Nafion films at this thickness (0.35 μm) have ca. 2 h lifetime in aqueous solution before degradation. Nafion film reference electrodes with different thickness were then investigated to achieve a longer lifetime and better stability.

11.3.3 Effect of Film Thickness

In a similar way, the stability of Nafion film reference electrodes with different film thicknesses was investigated by examining, *via* CV, the peak potential for the $[Ru(NH_3)_6]^{3+}$ reduction in aqueous solution. As depicted in Figure 11.7a, the E_{mid} potential of the Ru(III)/Ru(II) couple using five MV^{2+}/MV^{+} Nafion film reference electrodes at a same initial doping ratio (MV^{2+}:SO_3^- = 1:30) but with different film thickness was recorded over 6 h. The E_{mid} potential of the couple measured against the films with 0.35 μm and 1.75 μm thickness is stable (fluctuating within 1 mV) for 2 and 4.5 h, respectively, before it starts to drift (30 ± 3 mV/h), while the potential of the three thicker films does not drift at all within 6 h, suggesting an enhanced stability of the Nafion film reference electrodes in aqueous solution with a thicker film thickness. The drift in potential of the Nafion films with film thickness of 0.35 and 1.75 μm after 2 to 5 h was most likely due to a relatively fast chemical or mechanical degradation or aging of the very thin Nafion films.[18,19] The Nafion films/membranes prepared by drop-casting with thicknesses ranging from 25 to 50 μm have been reported to be thin enough to withstand the aggressive chemical and environmental conditions while meeting the durability targets for commercialisation, and they have been extensively investigated over the past decade.[20-22] Reinforced Nafion films can approach 5 μm in thickness without significantly compromising the stability.[23] This consistent with our observation, as the three thicker

films have little potential fluctuation (±0.5 mV) in the whole 6 h measurement time and good stability.

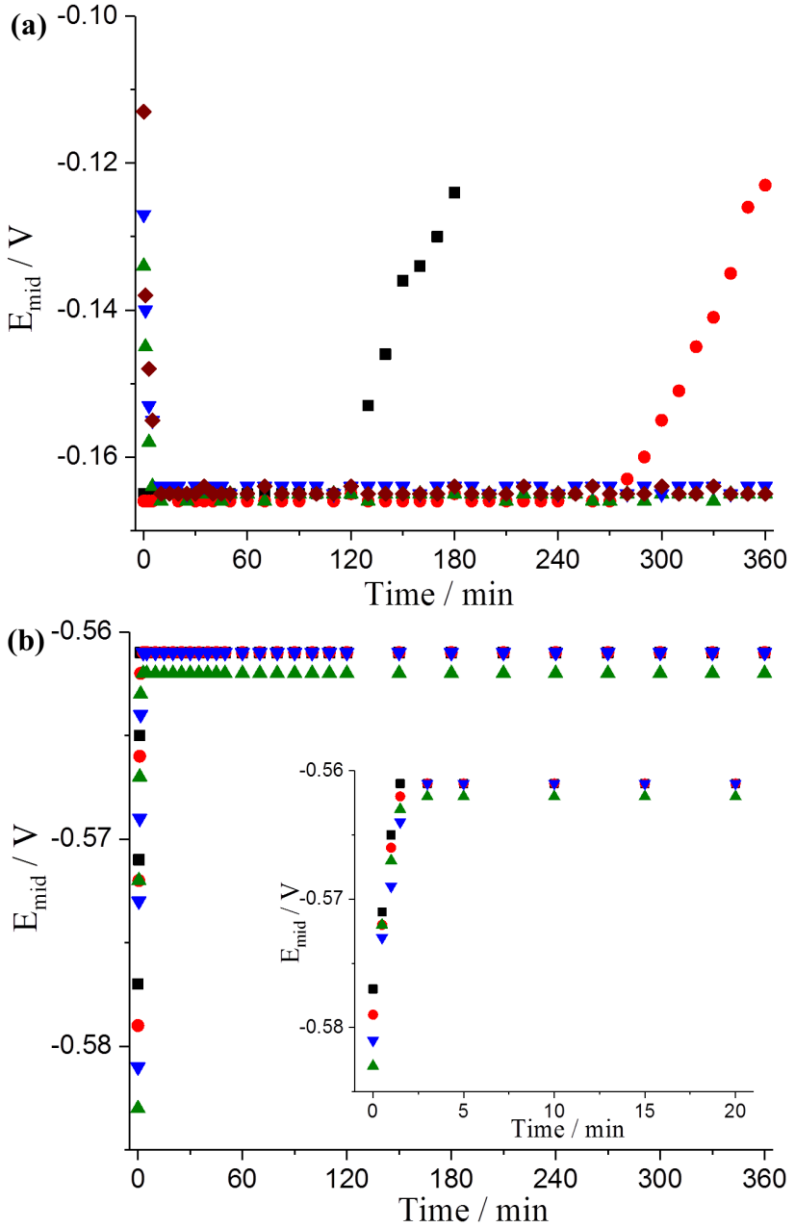
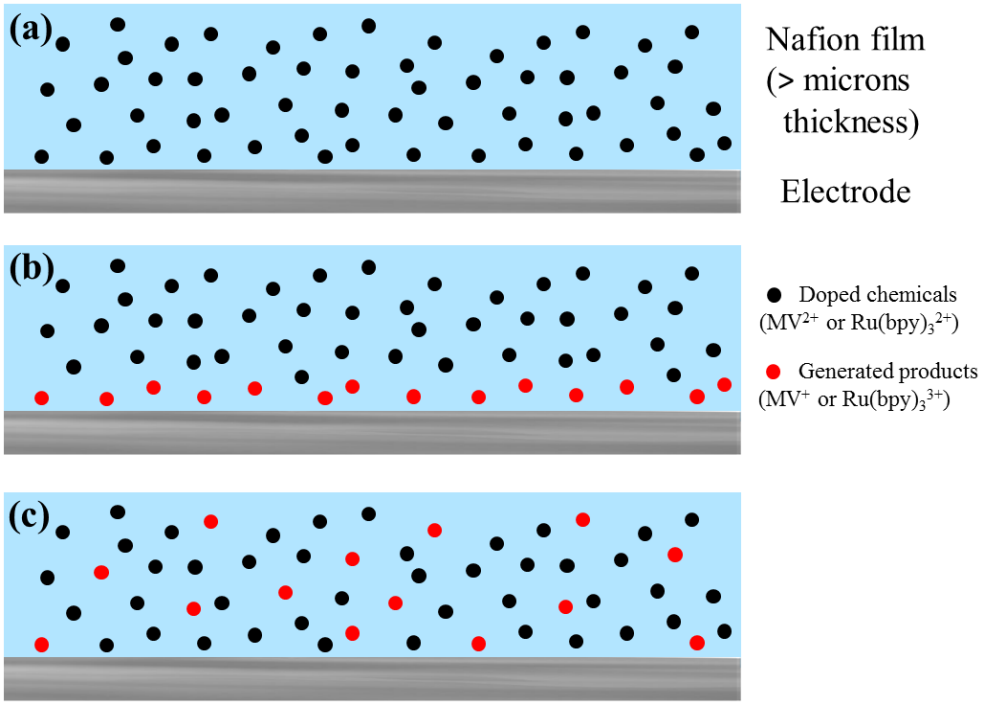


Figure 11.7. (a) Midpoint potential, E_{mid}, of $[Ru(NH_3)_6]^{3+}$ reduction *vs.* MV^{2+}/MV^{+} Nafion film (with a doping ratio of 1:30) reference electrodes with different film thickness recorded over 6 h (film thickness = 0.35 μm, black points; 1.75 μm, red points; 7.0 μm, blue points; 17.5 μm, green points; 35 μm, brown points). (b) E_{mid} of $[Ru(NH_3)_6]^{3+}$ reduction *vs.* $Ru(bpy)_3^{2+}/Ru(bpy)_3^{3+}$ Nafion film (with a doping ratio of 1:30) reference electrodes with different film thickness recorded over 6 h (film thickness = 7.0 μm, black points; 17.5 μm, red points; 35 μm, blue points; 52.6 μm, green points). Inset is a zoom-in of first 20 min.

Four $Ru(bpy)_3^{2+}$/$Ru(bpy)_3^{3+}$ Nafion film reference electrodes with a doping ratio of 1:30 and a thick film thickness (from 7.0 to 52.6 μm) were fabricated and examined. The relative amount of $Ru(bpy)_3^{2+}$ and $Ru(bpy)_3^{3+}$ in Nafion films is estimated to be 1:174 (Appendix E4). As shown in Figure 11.7b, all four Nafion film electrodes exhibit a good stability over 6 h, consistent with the observation of MV^{2+}/MV^{+} Nafion films, indicating that Nafion films thicker than 7 μm have at least 6 h lifetime and good stability in aqueous solution.

It is notable that there was an initial potential drift within the first a few minutes after fabrication for the three thicker MV^{2+}/MV^{+} Nafion film (7.0−35 μm) and all the four $Ru(bpy)_3^{2+}$/$Ru(bpy)_3^{3+}$ Nafion film (7.0−52.6 μm) reference electrodes before the potential became stable for at least the next 6 h. A larger initial potential drift and a longer drift time were also observed for the thickest film (ca. 52 mV initial potential drift within 5 min for 35 μm MV^{2+}/MV^{+} film, versus a 31 mV drift within 1.5 min for 7 μm film, as can be seen in Figure 11.7a). The previous section has discussed that both cations are fully confined inside Nafion at this doping ratio; hence, this potential drift does not result from depletion of doped redox species. It is inferred that this initial potential deviation is most likely due to the redistribution of the redox couples *via* diffusion within the Nafion films during/after fabrication process. This may be driven by concentration gradients or/and charge gradients within the thicker Nafion films (several micrometres or above), as MV^{+} or $Ru(bpy)_3^{3+}$ is only generated in the film near the electrode surface during the electrochemical oxidation/reduction of the film during its preparation, leading to the concentration and charge gradients across the films, and consequently the diffusion of both redox species inside the films, as illustrated in Scheme 11.2. This is also consistent with the fact that a thicker film requires a longer initial potential drift time to obtain a homogenous distribution within the film and hence a stable potential.

Scheme 11.2. Illustration of initial potential drift of the Nafion films: (a) Fresh prepared *via* drop-casting: the doped chemicals (MV^{2+} or $Ru(bpy)_3^{2+}$) are homogeneous within the film, (b) During electrochemically fabrication: generated products (MV^{+} or $Ru(bpy)_3^{3+}$) are formed in the film near the electrode surface side leading to concentration and charge gradients within the film, consequently causing the initial potential drift, (c) After a few minutes: the redox couples have become homogeneous within the films *via* diffusion, and the potential of the film is stabilised.



Chapter 10 has systematically investigated and compared the diffusional transport of MV^{2+} and MV^{+} in Nafion films and particles, and found that the transport in the particles was significantly faster than in films of similar thickness.[8] This observation suggests an experiment conducted using MV-doped Nafion particles to fabricate MV^{2+}/MV^{+} Nafion particle-based reference electrodes (fabrication details see 11.2.4). As depicted in Figure 11.8, the initial potential stabilization of MV^{2+}/MV^{+} Nafion particles reference electrode was completed much faster than that of Nafion films of similar thickness (ca. 45 mV drift within 1.5 min for 38.7 μm particle layers vs. 52 mV drift within 5 min for 35.1 μm film), consistent with the faster diffusional transport of both cations inside the particles consequently a short stabilization time for a homogeneous distribution in Nafion.

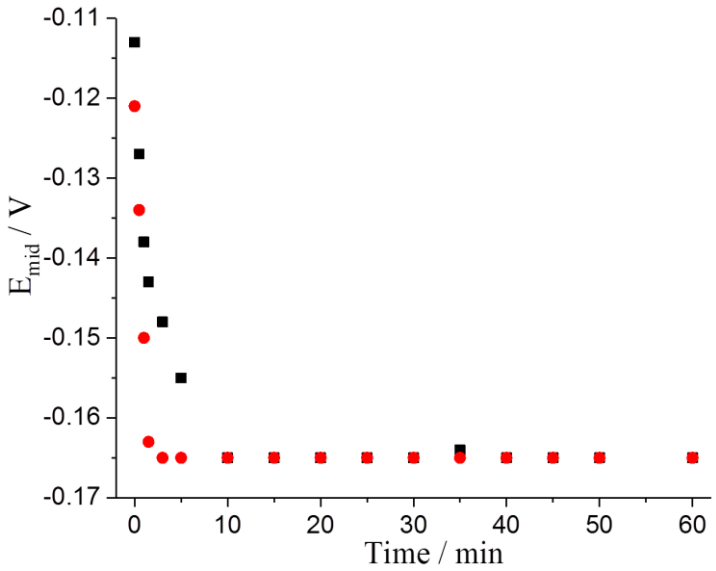


Figure 11.8. Midpoint potential, E_{mid}, of $[Ru(NH_3)_6]^{3+}$ reduction *vs.* MV^{2+}/MV^{+} Nafion (with a doping ratio of 1:30) reference electrodes. Black points: Nafion film with film thickness of 35.1 μm; red points: Nafion particles with 38.7 μm particle layers thickness.

Another important question arises, namely which part, the generated product during fabrication or the initial doped reactant, predominantly causes this initial potential drift. It is speculated that the product more likely has a significant effect, as it is only generated in the film near the electrode surface side and needs to diffuse cross the whole film to reach a homogeneous state, while the doped reactant is more like 'bulk' species within the entire film. The diffusion coefficient of MV^{2+} and MV^{+} within a Nafion film of several micrometres thickness has been reported previously as 3×10^{-9} cm^2 s^{-1} and 3×10^{-10} cm^2 s^{-1}, while the diffusion coefficients of $Ru(bpy)_3^{3+}$ and $Ru(bpy)_3^{2+}$ in Nafion film are 1.2×10^{-9} cm^2 s^{-1} and 2.7×10^{-9} cm^2 s^{-1}, respectively.[8,9,24] The $Ru(bpy)_3^{2+}/Ru(bpy)_3^{3+}$ Nafion films exhibit a faster initial potential stabilization compared with MV^{2+}/MV^{+} Nafion films at a same doping ratio and film thickness (see Figure 11.7), suggesting the inhomogeneous distribution of generated product ($Ru(bpy)_3^{3+}$ and MV^{+}) during the fabrication for a thick film is the cause of the observed initial potential drift, as $Ru(bpy)_3^{3+}$ diffuses faster than MV^{+} in Nafion film, whereas $Ru(bpy)_3^{2+}$ diffuses slower than MV^{2+}. This hypothesis is further investigated in the next section.

In subsequent studies, a film thickness of 35 μm was chosen, as films of this thickness demonstrated a good stability without significantly compromising their performance once the initial potential drift was stabilized within ca. 5 min. The influence of morphology of the film on this process was then investigated.

11.3.4 Effect of Film Morphology

The morphology of a Nafion film itself is an extremely complicated topic, as has been reviewed.[25-27] This Chapter qualitatively investigated how morphology might affect the performance and stability of the film. The Nafion films prepared via drop-casting have been proved to be uniform and homogeneous, and the estimated thicknesses are accurate, as verified by AFM.[16] In order to obtain a film with higher roughness but similar thickness, the same amount of Nafion stock mixture was drop-casted on electrode surface not once but casting five times the overall amount of material. In this way, a film with an obvious surface roughness as judged microscopically was obtained, as shown in Figure 11.9.

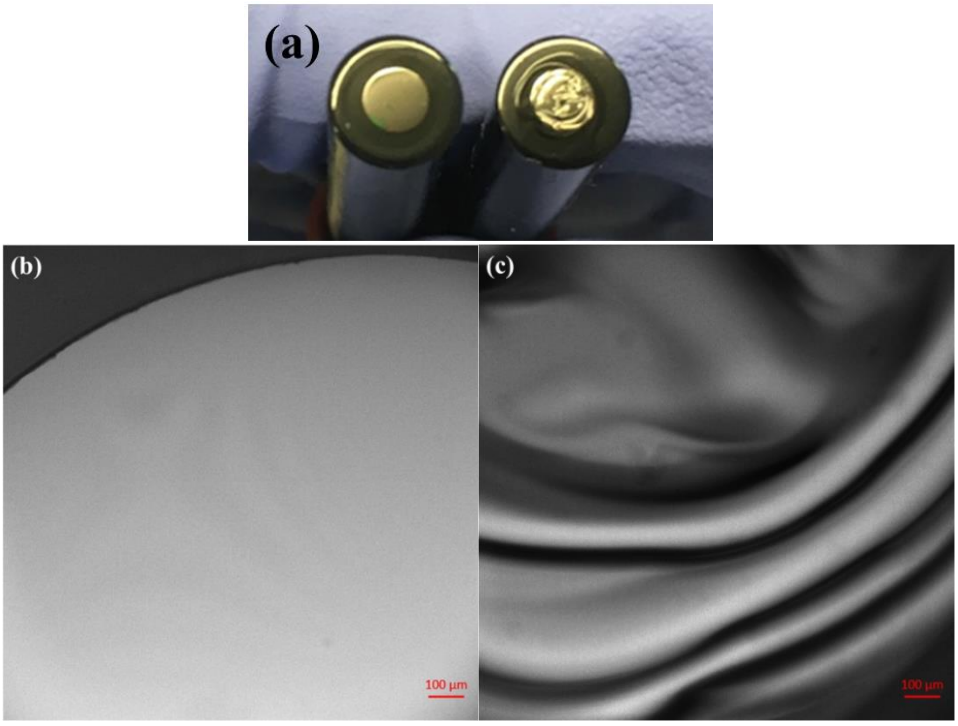


Figure 11.9. (a) Photo of a uniform Nafion film prepared by drop-casting (left) and a film with an obvious surface roughness as judged visually (right); (b) Optical microscope images of a uniform Nafion film; (c) Optical microscope images of a film with an obvious surface roughness.

Both MV^{2+}/MV^{+} and $Ru(bpy)_3^{2+}/Ru(bpy)_3^{3+}$ Nafion film reference electrodes with high film surface roughness were fabricated and examined. The E_{mid} potential was recorded and compared with that of more uniform films, as shown in Figure 11.10. A large initial potential deviation from the ultimate stable reading and a much longer stabilisation time for rough films were observed in both cases. This is consistent with the insight that the homogenization of generated MV^{+} or $Ru(bpy)_3^{3+}$ within an non-uniform film is probably diffusionally more difficult and requires a longer time, and consequently a stable potential is achieved more slowly. The potentials of both uniform and rough films were then tested over 3 days after their stabilization with the same film electrode after washing with water and being kept in air without any protection, as depicted in Figure 11.11. There was no significant difference. These results suggest that the morphology of Nafion films has a significant effect on initial performance (an initial potential drift) of the reference electrode but plays a negligible role in terms of stability.

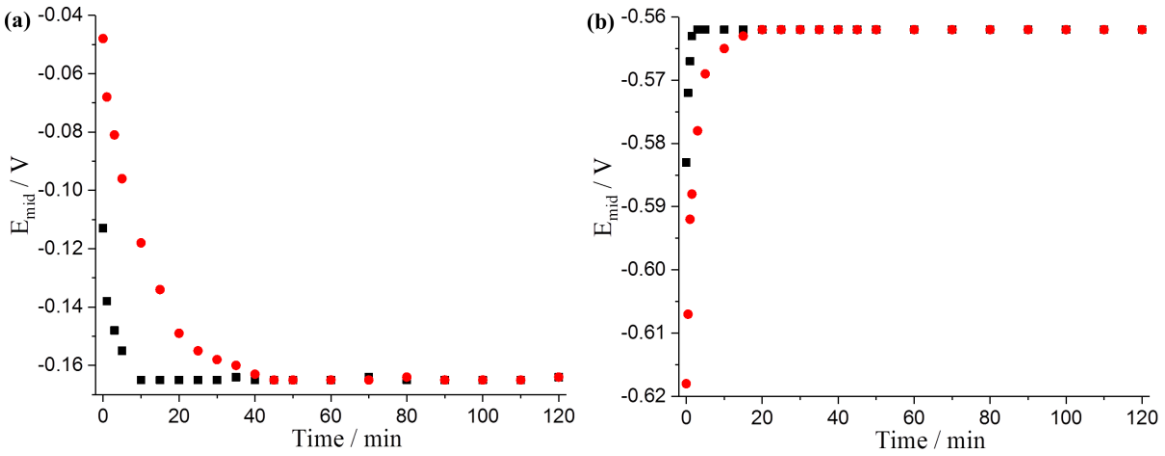


Figure 11.10. (a) Midpoint potential, E_{mid}, of $[Ru(NH_3)_6]^{3+}$ reduction *vs.* MV^{2+}/MV^{+} Nafion film (with a doping ratio of 1:30 and film thickness of 35.1 μm) reference electrodes recorded over 2 h (uniform film surface, black points; rough film surface, red points). (b) E_{mid} of $[Ru(NH_3)_6]^{3+}$ reduction *vs.* $Ru(bpy)_3^{2+}/Ru(bpy)_3^{3+}$ Nafion film (with a doping ratio of 1:30 and film thickness of 35.1 μm) reference electrodes recorded over 2 h (uniform film surface, black points; rough film surface, red points).

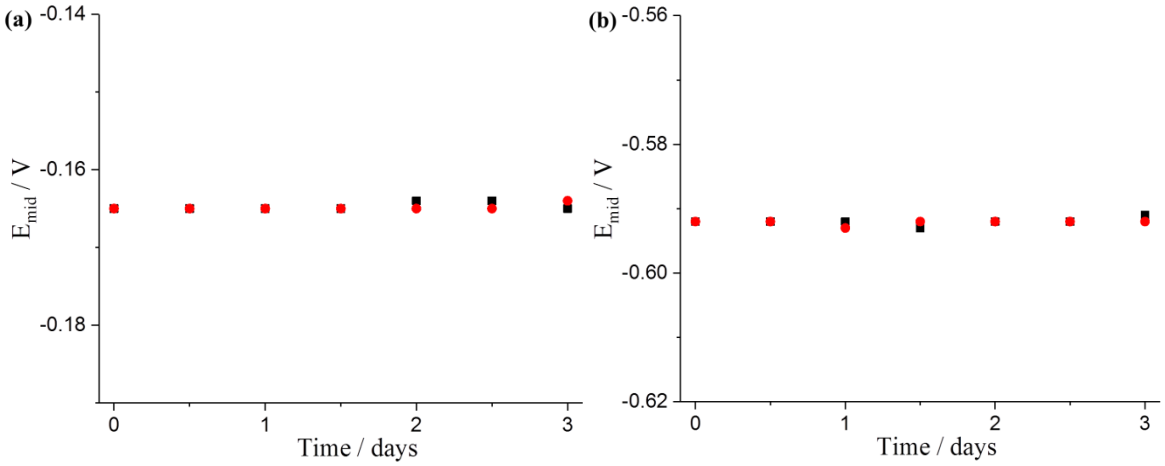


Figure 11.11. (a) Midpoint potential, E_{mid}, of $[Ru(NH_3)_6]^{3+}$ reduction *vs.* MV^{2+}/MV^{+} Nafion film (with a doping ratio of 1:30 and film thickness of 35 μm) reference electrodes recorded after the electrodes being fabricated and left in in air without any protection (uniform film surface, black points; rough film surface, red points). (b) E_{mid} of $[Ru(NH_3)_6]^{3+}$ reduction *vs.* $Ru(bpy)_3^{2+}/Ru(bpy)_3^{3+}$ Nafion film (with a doping ratio of 1:30 and film thickness of 35 μm) reference electrodes recorded after the electrodes being fabricated and left in in air without any protection (uniform film surface, black points; rough film surface, red points).

The following work next focused on whether the initial potential drift of fresh fabricated films could be mitigated or fully eliminated. In the previous section, it is inferred this drift is attributed to an inhomogeneous distribution of generated product within the films during the fabrication process. To examine this hypothesis, two more types of Nafion film reference electrodes, Fc/Fc^{+} and $PVFc/PVFc^{+}$, were fabricated and examined. These two couples were chosen because both Fc and PVFc are insoluble in water.

To prepare Fc/Fc^{+} Nafion film reference electrodes (initial doping ratio of $Fc^{+}:SO_3^{-}$ = 1:30 and thickness of 35 μm), the soluble salt, $Fc^{+}PF_6^{-}$, was initially doped into Nafion, and insoluble Fc was generated *via* partial electro-reduction of the film as described above. The Fc/Fc^{+} Nafion film reference electrodes demonstrated a superior stability without any initial drift, as shown in Figure 11.12 (black points) and discussed in detail in next section. The initial potential drift was successfully and fully eliminated, suggesting the above

hypothesis may be correct, namely that an inhomogeneous distribution of the generated product within the film plays a predominant role to cause an initial potential drift and this drift could be fully eliminated if the product is water-insoluble. Another Fc/Fc^+ Nafion film reference electrode with a high surface roughness was fabricated and examined. As shown in Figure 11.12 (red points), the film exhibited same stability without any initial potential drift showing insensitivity to morphology further confirming the hypothesis.

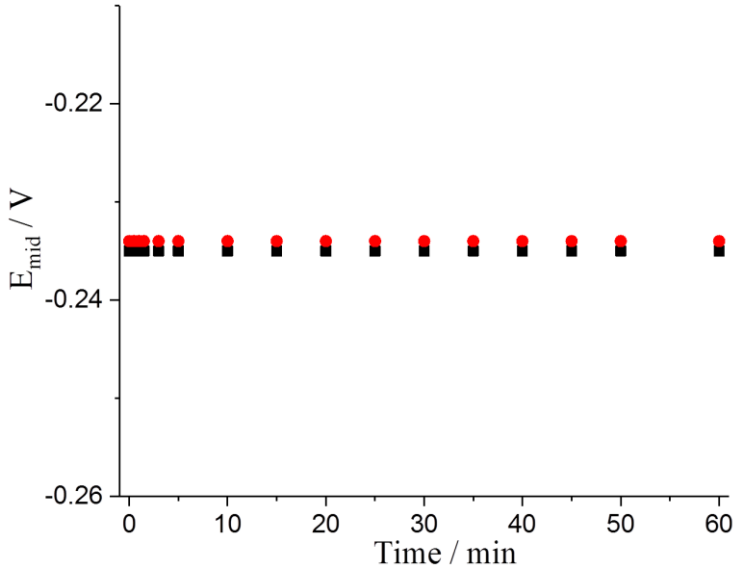


Figure 11.12. Midpoint potential, E_{mid}, of $[Ru(NH_3)_6]^{3+}$ reduction *vs.* Fc/Fc^+ Nafion film (with a doping ratio of 1:30 and film thickness of 35 μm) reference electrodes recorded over 1 h (uniform film surface, black points; rough film surface, red points).

$PVFc/PVFc^+$ Nafion film reference electrodes (initial doping ratio of VFc moiety:SO_3^- = 1:30, thickness of 35 μm, and the relative amount of $PVFc^+$ and PVFc in Nafion films is 1:903) were fabricated in a contrasting way relative to the Fc/Fc^+ Nafion film, where the insoluble PVFc was initially doped into Nafion but water-soluble $PVFc^+$ was electrochemically generated. The film reference electrodes were examined as a function of time, as depicted Figure 11.13, showing a good stability but with an initial potential drift (ca. 15 mV) for the first 15 min, suggesting the homogenization of the freshly generated $PVFc^+$ within the film. This observation is consistent with those of MV^{2+}/MV^+ and $Ru(bpy)_3^{2+}/Ru(bpy)_3^{3+}$, confirming again the hypothesis.

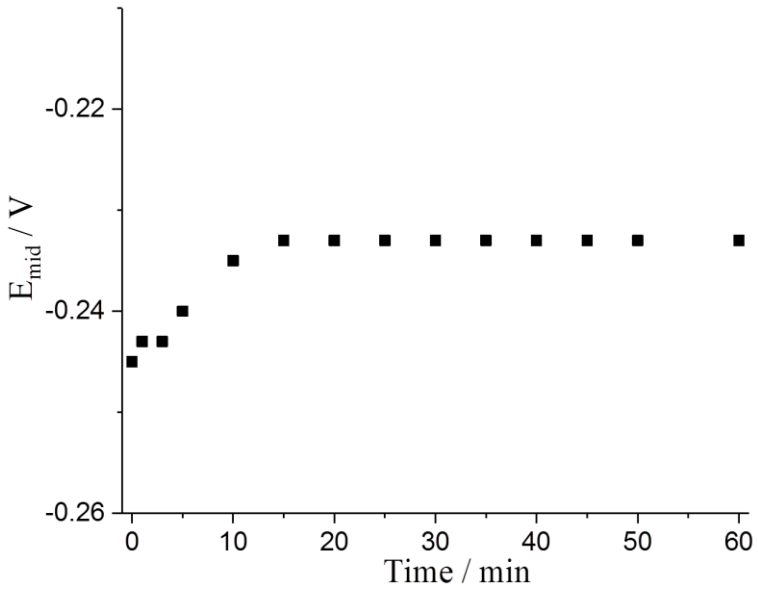


Figure 11.13. Midpoint potential, E_{mid}, of $[Ru(NH_3)_6]^{3+}$ reduction *vs.* PVFc/PVFc$^+$ Nafion film (with a doping ratio of 1:30, film thickness of 35.1 μm and uniform surface) reference electrodes recorded over 1 h.

All four types of Nafion film reference electrode under optimized conditions (doping ratio of 1:30, film thickness of 35 μm, and uniform film surface) were examined. The performance of the Fc/Fc$^+$ Nafion film reference electrode system is demonstrated in detail below; others are described in the Appendix E1-3.

11.3.5 Stability of the Fc/Fc$^+$ Nafion Film Reference Electrodes

The potential of optimized Fc/Fc$^+$ Nafion film reference electrodes and their stability were also assessed voltammetrically. In Figure 11.14a, the black line shows a CV of reduction of $[Ru(NH_3)_6]^{3+}$ against a freshly fabricated Fc/Fc$^+$ Nafion film reference electrode. The midpoint potential, E_{mid}, of the mediator was −0.235 V *vs.* Fc/Fc$^+$ Nafion film. The E_{mid} of reduction of $[Ru(NH_3)_6]^{3+}$ *vs.* SCE is −0.176 V, as shown in Figure 11.15. Therefore, the potential of fabricated Fc/Fc$^+$ Nafion film reference electrode in aqueous solution was determined as −0.059 V *vs.* SCE or +0.182 V *vs.* NHE, as illustrated in Scheme 11.3.

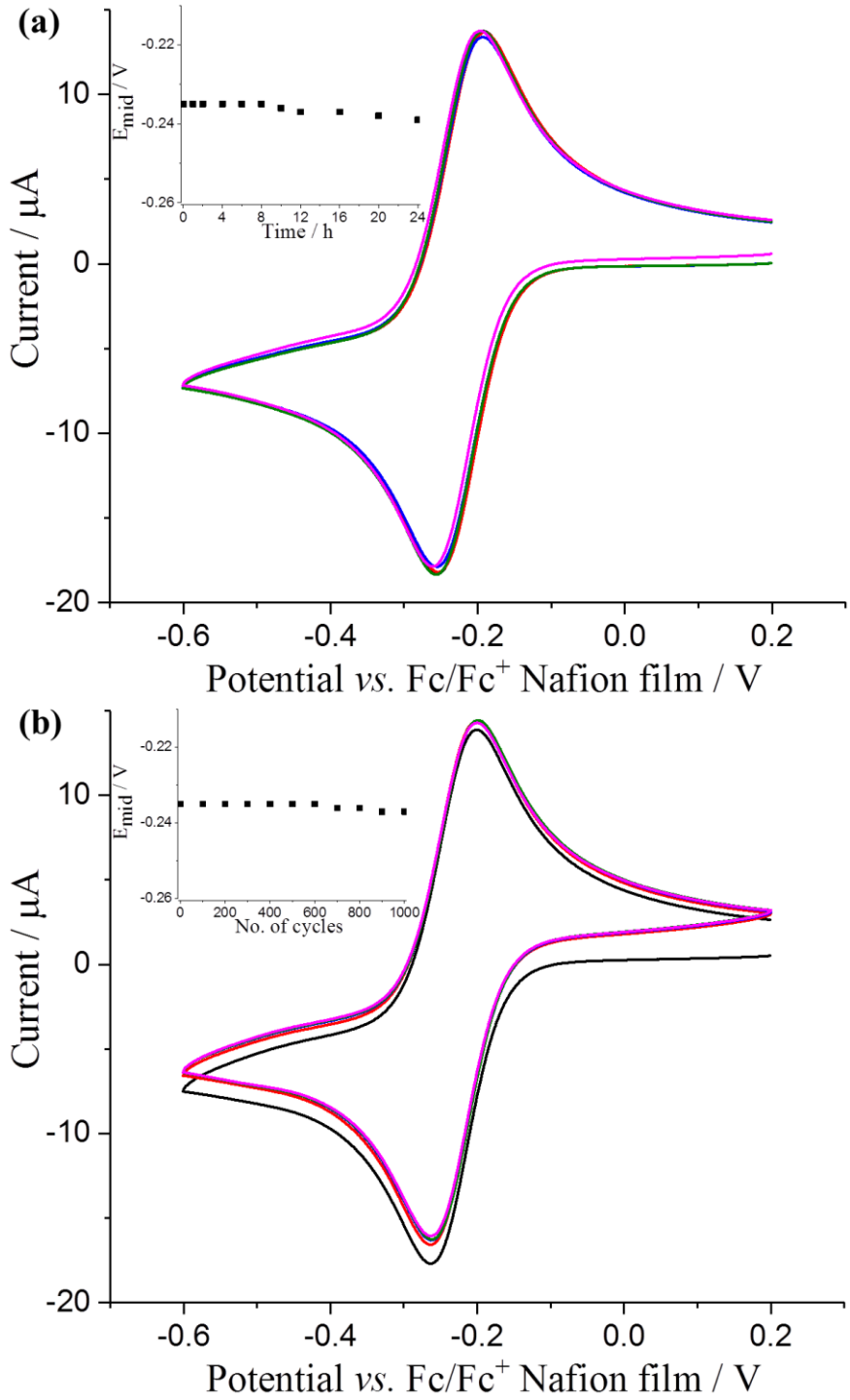


Figure 11.14. (a) Voltammograms of a glassy carbon working electrode with a Fc/Fc^+ Nafion film reference electrode in 0.1 M KCl aqueous solution containing 1 mM $[Ru(NH_3)_6]Cl_3$ at a scan rate of 0.1 V s^{-1}, recorded after the electrodes were immersed in solution (fresh, black line; 2 h, red line; 6 h, blue; 12 h, green line; 24 h, magenta line). Inset shows the midpoint potential, E_{mid}, over the time. (b) Voltammograms recorded over 1000 successive scans (1st scan, black line; 100th scan, red line; 200th scan, blue; 600th scan, green line; 1000th scan, magenta line). Inset shows the midpoint potential, E_{mid}, over the number of scans. Raw data of the insets are tabulated in Table 11.1 and 11.2.

Table 11.1. Raw data for the inset of Figure 11.14a - the midpoint potential, E_{mid}, of a freshly fabricated Fc/Fc^+ Nafion films over 24h immersing in solution.

Time / h	E_{mid} **potential / V**
0	−0.233
1	−0.233
2	−0.233
4	−0.233
6	−0.233
8	−0.234
10	−0.234
12	−0.235
16	−0.236
20	−0.237
24	−0.238

Table 11.2. Raw data for the inset of Figure 11.14b - the midpoint potential, E_{mid}, of a freshly fabricated Fc/Fc^+ Nafion films over 1000 successive scans.

No. of cycles	E_{mid} **potential / V**
1	−0.233
100	−0.233
200	−0.233
300	−0.233
400	−0.233
500	−0.233
600	−0.233
700	−0.234
800	−0.234
900	−0.235
1000	−0.236

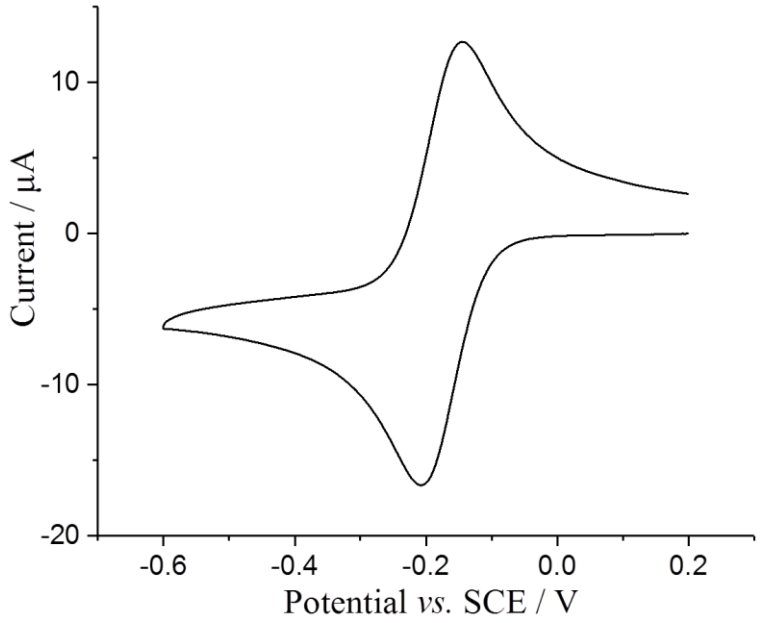


Figure 11.15. Voltammograms of a glassy carbon working electrode with a SCE reference electrode in 0.1 M KCl aqueous solution containing 1 mM $[Ru(NH_3)_6]Cl_3$ at a scan rate of 0.1 V s^{-1}. The midpoint potential, E_{mid}, of reduction of $[Ru(NH_3)_6]^{3+}$ *vs.* SCE is -0.176 ± 0.001 V.

Scheme 11.3. Potential of Fc/Fc^+ Nafion Film Reference Electrode in Aqueous Solution



As shown in Figure 11.14a, the CVs of $[Ru(NH_3)_6]^{3+}$ were recorded over a 24 h period after the electrodes had remained in the cell under the same conditions to check the stability of the Fc/Fc^+ Nafion film reference electrode. The peak potentials were very stable, with no deviation for the first 6 h after the Fc/Fc^+ Nafion film was immersed in the solution. The variation of E_{mid} with experimental time was within an average deviation of 2 mV over 12 h and less than 5 mV after 24 h in solution. Moreover, additional voltammograms were recorded every 1 or 2 days over a period of 10 days, with the same Fc/Fc^+ Nafion film electrode after washing with water and kept in air without any protection, as shown in Figure 11.16. This shows again a good stability of the Fc/Fc^+ film

with no significant drift of the E_{mid} within 10 mV over 10 days and no deviation in the first 4 days. Moreover, there was no visible degradation of the film over 10 days. There results clearly demonstrate the high stability and strong robustness of Fc/Fc^+ Nafion film used as reference electrode in aqueous solution.

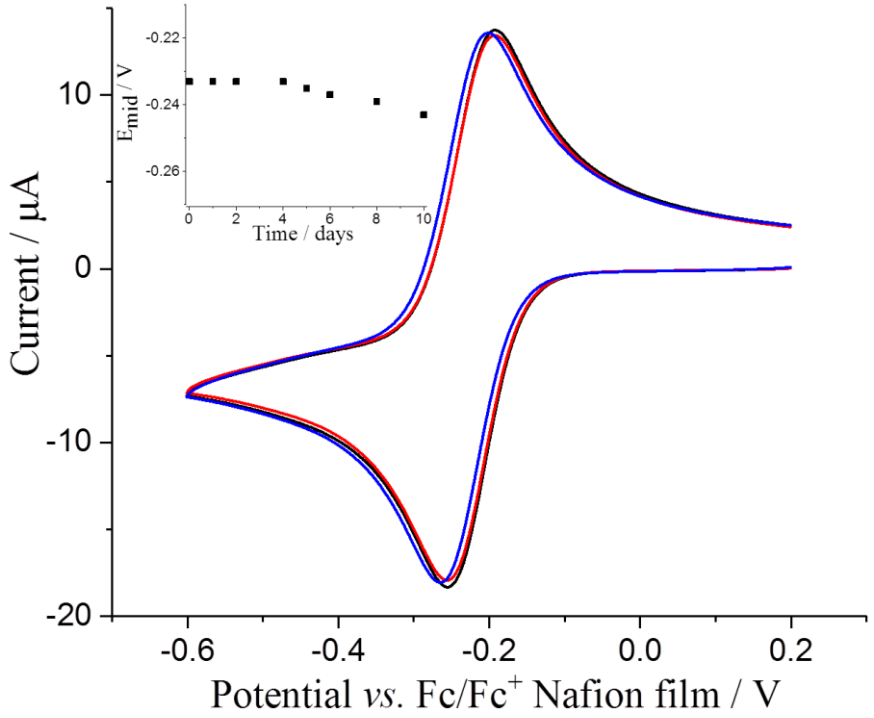


Figure 11.16. Voltammograms of a glassy carbon working electrode with the same Fc/Fc^+ Nafion film reference electrode in 0.1 M KCl aqueous solution containing 1 mM $[Ru(NH_3)_6]Cl_3$ at a scan rate of 0.1 V s^{-1} recorded after the electrodes being fabricated and left in in air without any protection (fresh, black line; 4 days kept in air, red line; 10 days kept in air, blue line). Inset shows the midpoint potential, E_{mid}, over the time.

To test the stability of the Fc/Fc^+ Nafion film after a series of measurements, the cyclic voltammetry was conducted over 1000 successive scans in the same conditions with a fresh fabricated Fc/Fc^+ Nafion film reference electrode. As shown in Figure 11.14b, there was no drift of the peak potential or E_{mid} between the first and 600th cycles and only 2 mV drift after 1000 cycles, demonstrating a superior stability of the Fc/Fc^+ Nafion films.

11.3.6 Reproducibility of the Fc/Fc$^+$ Nafion Films

The above results reveal a highly stable Fc/Fc$^+$ Nafion film reference electrode. An important question arises as to the reproducibility of this film electrode. Three Fc$^+$/Nafion stock samples were prepared and drop-casted on three different glassy carbon electrodes. Cyclic voltammetry using 1.0 mM $[Ru(NH_3)_6]^{3+}$ (in 0.1 M KCl) at a scan rate of 0.1 mV s^{-1} was recorded to examined each film reference electrodes. The midpoint potential, E_{mid}, remained at −0.235 ± 0.002 V vs. Fc/Fc$^+$ Nafion film in all cases, showing excellent reproducibility of the electrodes; see Table 11.3 and 11.4 for raw data.

Table 11.3. Summary of the midpoint potential, E_{mid}, of 3 freshly fabricated Fc/Fc$^+$ Nafion films

	Fc$^+$/Nafion 1	**Fc$^+$/Nafion 2**	**Fc$^+$/Nafion 3**
GC substrate 1	−0.235 V	−0.233 V	−0.236 V
GC substrate 2	−0.236 V	−0.234 V	−0.235 V
GC substrate 3	−0.235 V	−0.235 V	−0.237 V

Table 11.4. E_{mid} potential drift between 1st scan and the 1000th scan of the Fc/Fc$^+$ Nafion films listed in Table 11.3 after 1000 successive scans

	Fc$^+$/Nafion 1	**Fc$^+$/Nafion 2**	**Fc$^+$/Nafion 3**
GC substrate 1	2 mV	4 mV	−1 mV
GC substrate 2	3 mV	−2 mV	1 mV
GC substrate 3	−1 mV	2 mV	3 mV

Now four different Nafion film references electrodes with good stability over 10 days and performed over at least 1000 successive scans have been fabricated. That said, the performance and the durability of this type of Nafion film reference electrodes might be further improved in several ways, such as improving film chemistry,[28,29] incorporating additives and/or reinforcements,[30,31] and preforming thermal pre-treatment,[32-34] which could be expanded in further work.

11.4 Conclusions

The fabricated Nafion films have been developed into reference electrodes for use in aqueous solutions. Four redox couples, namely MV^{2+}/MV^{+}, $Ru(bpy)_3^{2+}/Ru(bpy)_3^{3+}$, Fc/Fc^{+}, and $PVFc/PVFc^{+}$ Nafion film reference electrodes, were fabricated and optimised, and they exhibited good stability over 10 days; in particular, the Fc/Fc^{+} Nafion films demonstrated the best performance. This is attributed in part to the strong binding of the cationic species within the Nafion films and the water insolubility of Fc and PVFc. MV^{2+}/MV^{+}, $Ru(bpy)_3^{2+}/Ru(bpy)_3^{3+}$, and $PVFc/PVFc^{+}$ Nafion films have a small initial potential drift (<30mV) after the first a few minutes of fabrication before the potential is fully stabilized. This drift likely results from the inhomogeneous distribution of generated product within the film during the fabrication process and can be fully eliminated by careful selection of the dopant couple. Comparing with conventional reference electrodes such as the Ag/AgCl electrode or SCE, the proposed Nafion film reference electrode has several advantages: The film electrode is a solid-state liquid-free reference electrode, and there is no contamination of the test solution. The type of electrode is easy and simple to fabricate, and the film can be drop-casted on different substrates, such as cheap graphite rods. The substrate can be very small; hence, the electrode could be miniaturized for application in analytical devices at nanoscales, such as SECM and SPM.

Bibliography

(1) Chen, L.; Compton, R. G. *ACS Sensors* **2019**, *4*, 1716-1723.
(2) Thackray, A.; Myers, M. *Arnold O. Beckman: One hundred years of excellence*; Chemical Heritage Foundation, 2000; Vol. 3.
(3) Beckman, A. O.; Fracker, H. E. *U.S. Patent 2058761* **1936**.
(4) Jonte, J. H.; Martin Jr, D. S. *Journal of the American Chemical Society* **1952**, *74*, 2052-2054.
(5) Seward, T. M. *Geochimica et Cosmochimica Acta* **1976**, *40*, 1329-1341.
(6) Yang, H.; Li, X.; Batchelor-McAuley, C.; Sokolov, S. V.; Kätelhön, E.; Compton, R. G. *Chemistry–A European Journal* **2017**, *23*, 17605-17611.

(7) Chen, L.; Lin, C.; Compton, R. G. *Physical Chemistry Chemical Physics* **2018**, *20*, 15795-15806.
(8) Chen, L.; Lin, C.; Compton, R. G. *Physical Chemistry Chemical Physics* **2019**, *21*, 607-616.
(9) Rubinstein, I.; Bard, A. J. *Journal of the American Chemical Society* **1980**, *102*, 6641-6642.
(10) Buttry, D. A.; Anson, F. C. *Journal of the American Chemical Society* **1983**, *105*, 685-689.
(11) Sheppard, S.-A.; A. Campbell, S.; R. Smith, J.; W. Lloyd, G.; C. Walsh, F.; R. Ralph, T. *Analyst* **1998**, *123*, 1923-1929.
(12) Momma, T.; Kakuda, S.; Yarimizu, H.; Osaka, T. *Journal of the Electrochemical Society* **1995**, *142*, 1766-1769.
(13) Jaworska, E.; Naitana, M. L.; Stelmach, E.; Pomarico, G.; Wojciechowski, M.; Bulska, E.; Maksymiuk, K.; Paolesse, R.; Michalska, A. *Analytical Chemistry* **2017**, *89*, 7107-7114.
(14) Zhen, X. V.; Rousseau, C. R.; Bühlmann, P. *Analytical Chemistry* **2018**, *90*, 11000-11007.
(15) Grygolowicz-Pawlak, E.; Crespo, G. A.; Ghahraman Afshar, M.; Mistlberger, G.; Bakker, E. *Analytical Chemistry* **2013**, *85*, 6208-6212.
(16) Krtil, P.; Trojánek, A.; Samec, Z. *Journal of Physical Chemistry B* **2001**, *105*, 7979-7983.
(17) Wang, Y.; Limon-Petersen, J. G.; Compton, R. G. *Journal of Electroanalytical Chemistry* **2011**, *652*, 13-17.
(18) Borup, R.; Meyers, J.; Pivovar, B.; Kim, Y. S.; Mukundan, R.; Garland, N.; Myers, D.; Wilson, M.; Garzon, F.; Wood, D.; Zelenay, P.; More, K.; Stroh, K.; Zawodzinski, T.; Boncella, J.; McGrath, J. E.; Inaba, M.; Miyatake, K.; Hori, M.; Ota, K., et al. *Chemical Reviews* **2007**, *107*, 3904-3951.
(19) Rodgers, M. P.; Bonville, L. J.; Kunz, H. R.; Slattery, D. K.; Fenton, J. M. *Chemical Reviews* **2012**, *112*, 6075-6103.
(20) Mauritz, K. A.; Moore, R. B. *Chemical Reviews* **2004**, *104*, 4535-4586.
(21) Kim, Y. S.; Lee, K.-S. *Polymer Reviews* **2015**, *55*, 330-370.
(22) Kusoglu, A.; Weber, A. Z. *Chemical Reviews* **2017**, *117*, 987-1104.
(23) Liu, W.; Suzuki, T.; Mao, H.; Schmiedel, T. *ECS Transactions* **2013**, *50*, 51-64.
(24) Rubinstein, I.; Bard, A. J. *Journal of the American Chemical Society* **1981**, *103*, 5007-5013.
(25) Gebel, G.; Diat, O. *Fuel Cells* **2005**, *5*, 261-276.
(26) Hickner, M. A.; Pivovar, B. S. *Fuel Cells* **2005**, *5*, 213-229.
(27) Duncan, A. J.; Leo, D. J.; Long, T. E. *Macromolecules* **2008**, *41*, 7765-7775.
(28) Kim, Y. S.; Welch, C. F.; Hjelm, R. P.; Mack, N. H.; Labouriau, A.; Orler, E. B. *Macromolecules* **2015**, *48*, 2161-2172.
(29) Moore, R. B.; Martin, C. R. *Macromolecules* **1988**, *21*, 1334-1339.
(30) D'Urso, C.; Oldani, C.; Baglio, V.; Merlo, L.; Aricò, A. S. *Journal of Power Sources* **2014**, *272*, 753-758.
(31) Laberty-Robert, C.; Vallé, K.; Pereira, F.; Sanchez, C. *Chemical Society Reviews* **2011**, *40*, 961-1005.
(32) Gebel, G.; Aldebert, P.; Pineri, M. *Macromolecules* **1987**, *20*, 1425-1428.
(33) Alberti, G.; Narducci, R. *Fuel Cells* **2009**, *9*, 410-420.
(34) Collette, F. M.; Lorentz, C.; Gebel, G.; Thominette, F. *Journal of Membrane Science* **2009**, *330*, 21-29.

Chapter 12

Overall Conclusions

Nanoparticles play a significant role in modern technologies and applications due to their different chemical and physical properties related to the nanoscale dimension. This thesis has investigated the electrochemistry of graphene and Nafion polymer nanoparticles, focussing particularly on electrocatalysis.

First, the surface adsorption of large organic molecules on the surface of graphene, widely applied in advanced catalysts and ultra-sensitive sensors, was investigated and quantified. The adsorption of catechol on single graphene nanoplatelets (GNPs) was first demonstrated electrochemically and spectroscopically, where this adsorption process was found to be Langmuirian and undergoes a flat to vertical concentration driven phase transition at high concentrations. Impact electrochemistry was successfully applied to monitor the *in-situ* surface coverage of catechol on *single* GNPs, giving the hitherto inaccessible desorption kinetics.

Furthermore, to seek new insights into such adsorption processes, the adsorbed phenyl hydroquinone on GNPs was proved to undergo a flat to edgewise then an edgewise to endwise phase transition on the graphene surface with the increase of adsorbate concentrations.

The electrocatalysis of GNPs towards dopamine oxidation via adsorption was then demonstrated. Nano-impacts was utilised so as to allow the observation of the electrochemistry of dopamine *exclusively* at single GNPs, showing a lower overpotential of adsorbed dopamine oxidation than solution phase dopamine. This catalysis was confirmed to result from the increased affinity for the oxidative product, dopamine-*o*-quinone, for the nanoplatelets over glassy carbon electrodes.

The developed methodology was then applied to, using dopamine as the probe molecule, accurate surface area measurements of high surface area carbon materials, including both graphene and graphene oxide (GO). The results from dopamine adsorption were compared with values from traditional probe molecules notably N_2 (BET) and methylene blue uptake, showing the dopamine adsorption probably gives a more 'correct' measurement. The molecular reorientation (flat to vertical) of dopamine on the graphene and GO surface provides a confirmation of the attainment of a monolayer coverage and the rapid adsorption (within 10 min to saturation) offers high convenience.

As with graphene based materials, the electrocatalytic behaviour of Nafion nanoparticles, has potential applications in the field of energy and catalysis, and was also investigated in this thesis. In particular, oxygen reduction catalysed by *single* Nafion particles doped with methyl viologen (MV) was investigated using impact electrochemistry. The MV-Nafion particles demonstrated a strong electrocatalytic ability with a fast redox cycling of MV^{2+}/MV^{+}. A generic approach was proposed to deploy an efficient *homogeneous* electron transfer mediator as a *heterogeneous* electrocatalyst with the benefits of the latter.

The *undoped* Nafion particles also demonstrated a 'fake' catalytic behaviour toward oxygen reduction. The origin of this observation was investigated using the well-characterised ferrocenemethanol oxidation in the presence of non-conducting electrochemically-inert polystyrene microspheres. It was found that the 'classic' voltammetry for electrocatalysis with a particle modified electrode bears a remarkable and quite unexpected level of complexity. Either accelerated or retarded mass transport can occur locally attributed to the porous layer formed by the nanoparticles, resulting in shifts in peak positions in any direction - anodic or cathodic - and peak currents varying in a complex fashion.

Finally, this thesis has proposed, developed and validated a novel improved reference electrodes for *real* applications based on redox couples immobilised within Nafion films. In particular, the dynamics of the charge transfer and diffusional ion transport processes *within* the Nafion films and particles were first assessed using voltammetry and nano-impacts. The contrasting behaviour was highlighted and elucidated experimentally and computationally, with the MV^{2+}/MV^{+} redox couple as a model system. The transport in the particles was shown to be significantly faster than in films of similar thickness while the diffusion of MV^{2+} was confirmed to be faster than that of MV^{+}.

Four different Nafion film reference electrodes based on different redox couples of cationic and/or water-insoluble species were fabricated and evaluated. Reference electrodes with a good stability over 10 days and 1000 successive voltammetric measurements were successfully realised by adjustment and optimisation of the film thickness, the level of doping of the film, film morphology, and careful selection of dopant couples. The proposed reference electrodes demonstrate several advantages, including full retention of the redox species within the films together with ease of both fabrication and miniaturization.

In summary, this thesis has presented methods developed for investigation of graphene and polymer nanoparticle electrocatalysis. In particular, generic methodologies have been developed for the surface adsorption study on GNPs where a molecular phase transition is seen and the role of adsorption in electrocatalysis classified. This has been further successfully applied for a new approach to the accurate surface area determination for the carbon materials with complex internal structures and high surface areas. Furthermore, Nafion in the forms of nanoparticles and films has shown authentic electrocatalysis but also a ‘fake’ catalysis attributed to the retarded mass transport. Overall the need to complement traditional voltammetry approaches based on drop-casted ensembles with individual particle measurement is clear.

Appendix A

Calculation of adsorbed molecule surface coverage on GNPs for the determination of molecule orientation in Chapter 4-7

For single GNP particle, average surface area of GNP is 297 ± 152 μm^2 and the thickness is 7.1 ± 2 nm (estimated from scanning electron microscopy[1]). Hence the volume (V) of a single GNP can be estimated as (2.11 ± 1.08) × 10^{-18} m^3. The bulk density of the GNPs is 1 × 10^5 g m^{-3} reported by the supplier.[2] For loose powders, the density of a single GNP is assumed to be the same as graphite, 2.26 × 10^6 g m^{-3}.[3] Therefore, the mass for single GNP can be estimated as (4.77 ± 2.44) × 10^{-9} mg.

The amount of catechol (n) adsorbed onto 1 mg of GNPs reaches the first plateau at n_{max} = 1.6 × 10^{-7} mol mg^{-1}. For 1 mg of GNP, the total surface area is:

$$\frac{1}{(4.77\pm2.44)\times10^{-9}mg}\times(2.97\pm1.52)\times10^{-6}cm^2=(6.23\pm3.19)\times10^2cm^2mg^{-1}$$

Therefore, the maximum surface coverage (Γ_{max}) at the first plateau can be determined as:

$$\Gamma_{max}=\frac{1.6\times10^{-7}mol\cdot mg^{-1}}{(6.23\pm3.19)\times10^2cm^2mg^{-1}}=(2.5\pm0.8)\times10^{-10}mol\cdot cm^{-2}$$

The average area occupied by each individual molecule ($S_{R\text{-}Ct}$) can be then determined as:

$$S_{R-Ct}=\frac{1}{N_A\Gamma_{max}}=\frac{1}{6.022\times10^{23}mol^{-1}\times(2.5\pm0.8)\times10^{-10}mol\cdot cm^{-2}}=(6.7\pm1.7)\times10^{-15}cm^2$$

A similar calculation is conducted to obtain $S'_{R\text{-}Ct}$ at the second plateau, so as for the phenyl hydroquinone (Chapter 5) and dopamine (Chapter 6).

Bibliography

(1) Poon, J.; Batchelor-McAuley, C.; Tschulik, K.; Compton, R. G. *Chemical Science* **2015**, *6*, 2869-2876.
(2) Nam, H. J.; Kim, B.; Ko, M. J.; Jin, M.; Kim, J. M.; Jung, D.-Y. *Chemistry – A European Journal* **2012**, *18*, 14000-14007.
(3) Kawaguchi, M. *Advanced Materials* **1997**, *9*, 615-625.

Appendix B

Appendix B1: Amounts of Nafion Particles in Drop-casting and Nano-impact Experiments

For the single MV-Nafion particle, the average radius has been estimated from SEM[1] as 0.43 ± 0.26 μm and the density of Nafion in water ρ_{Nafion} is 1.858 g cm^{-3}.[2]

Hence the mass of one single particle is

$$m_{Nafion} = \frac{4}{3}\pi r^3 \rho_{Nafion} = 6.36\times10^{-13} g$$

The total mass of Nafion used to synthesize Nafion particles is

$$m_{total} = V\rho_{bulk} \times wt\% = 50\mu L \times 0.921 g/cm^3 \times 12.5\% = 5.76\times10^{-3} g$$

where ρ_{bulk} is the density of Nafion perfluorinated resin solution, of which value obtained from the supplier Sigma-Aldrich.

The number of Nafion particle synthesized is

$$N = \frac{m_{total}}{m_{Nafion}} = \frac{5.76\times10^{-3} g}{6.36\times10^{-13} g} = 9.05\times10^{9}$$

The volume of final Nafion particle suspension is 0.5 mL, as described in Chapter 3.

Therefore the concentration of Nafion particle suspension is

$$C = \frac{N}{V} = \frac{9.05\times10^{9}}{0.5mL} = 1.81\times10^{10} particles/mL$$

For drop-casting experiments, 10 μL of evenly dispersed stock MV-Nafion particles suspension was drop-casted on the GC macroelectrode, as described in Chapter 8, hence the number of Nafion particle drop-casted on the GC electrode is

$$N_{GC} = C\times V_{GC} = 1.81\times10^{10} particles/mL \times 10\mu L = 1.81\times10^{8} particles$$

For nano-impact experiments, 0.5 mL of stock Nafion particle suspension is diluted to 5 mL suspension. Hence the concentration of Nafion particles for nano-impact experiments can also be determined as

$$C_{Im\,pact} = \frac{1.81\times10^{10}\ particles/mL}{N_A} \times \frac{0.5mL}{5mL} = 3.0\times10^{-12}\ mol/L$$

Appendix B2: Doping Amount of MV^{2+} in Individual Nafion Particles (ratio of MV^{2+}:SO_3^-)

The mass for single particles is as described above:

$$m_{Nafion} = \frac{4}{3}\pi r^3 \rho_{Nafion} = 6.36\times10^{-13}\ g$$

Equivalent weight (EW) of Nafion is defined as the number of grams of dry Nafion per mole of sulfonic acid groups when the material is in the acid form.[3] Nafion used in this work is 1100 EW.

The amount of SO_3^- can be then determined as

$$n_{SO_3^-} = \frac{6.36\times10^{-13}\ g}{1100\ g/mol} = 5.78\times10^{-16}\ mol$$

The average charge of individual impacts at first plateau, Q, is 2.74 ± 0.26 pC.

Hence the amount of MV^{2+} in one single Nafion particle is

$$n_{MV^{2+}} = \frac{Q}{neN_A} = 2.84\times10^{-17}\ mol$$

The doping amount of MV^{2+} in individual Nafion Particles (ratio of MV^{2+}:SO^{3-}) is

$$\frac{n_{MV^{2+}}}{n_{SO_3^-}} = \frac{2.84\times10^{-17}\ mol}{5.78\times10^{-16}\ mol} = \frac{1}{20}$$

Therefore, the doping amount of MV^{2+} in Nafion Particles is 1:20, 1:40, 1:80, 1:160, and 1:320 corresponding to doping level 100%, 50%, 25%, 12.5% and 6.25%, respectively.

Appendix B3: Supported Spherical Electrode Model vs Isolated Spherical Electrode Model

A spherical electrode located on a flat substrate which partly shields the particle from diffusion is simulated in the cylindrical coordinates as illustrated in Figure B1a, where *r* and *z* are the two dimensions parallel and perpendicular to the supporting electrode surface. For an isolated spherical electrode, in the absence of the flat surface only the concentration distribution at the dimension *r* needs to be solved. Comparing the two geometries in Figure B1a solving a partial differential equation in the isolated sphere model is much easier than the attached sphere model. As the steady-state currents of the two models have analogous expressions when the electrode size is small, the overall cyclic voltammetric wave of the shielded sphere model can be approximated by the isolated sphere model for a simple one-electron-transfer reaction. The steady-state expressions of the two models are:[4,5]

$$I_{\text{attached}} = 4\pi \ln 2 FDr_{\text{el}}c^{*} \tag{B1}$$

$$I_{\text{isolated}} = 4\pi FDr_{\text{el}}c^{*} \tag{B2}$$

I_{attached} equals I_{isolated} times a coefficient of ln2.

Figure B1 shows the cyclic voltammogram of a simple one-electron-transfer reaction at spherical electrodes of 1 um. The black solid line is the simulation with the model of a spherical electrode attached on the substrate; while the blue dashed line is from the model of an isolated spherical electrode with a correction coefficient of ln2. The two voltammetric waves fully overlap with each other in the same simulation conditions and different approaches to calculate the electrode current. For both models, the initial concentration of the reactant is taken as 1 mM; the diffusion coefficient is 10^{-9} m^2 s^{-1}; and the electron transfer rate constant is 1 m s^{-1}. The concentration distribution at the

electrode-electrolyte interface can be calculated from solving the diffusion equation. In the simulation of the attached spherical electrode, the current is calculated by:

$$I = 2\pi r_{el} FD \int_0^{\pi} \left(r_{el} \sin(\theta) \frac{\partial c}{\partial \vec{n}}\bigg|_{r=r_{el}} \right) \mathrm{d}\theta \tag{B3}$$

where θ is the angle of a point at the electrode surface deviating from the z axis. The current expression in the simulation of the isolated spherical electrode with the correcting coefficient ln2 is written as:

$$I = 4\pi r_{el}^{\ 2} FD \frac{\partial c}{\partial \vec{n}}\bigg|_{r=r_{el}} \tag{B4}$$

From Figure B1b, it is found that the simulation results based on the two models fully overlap in the case of 1 μm radius spherical electrodes, proving the possibility of replacing the simulation of a one-electron-transfer reaction on a microsize attached spherical electrode by the isolated sphere model. In this work, as the radius of the Nafion sphere is about 0.43 μm and the electrochemical oxygen reduction reaction on Nafion is treated as a simple two-electron-transfer process, it is possible to use the corrected isolated sphere model in the simulation.

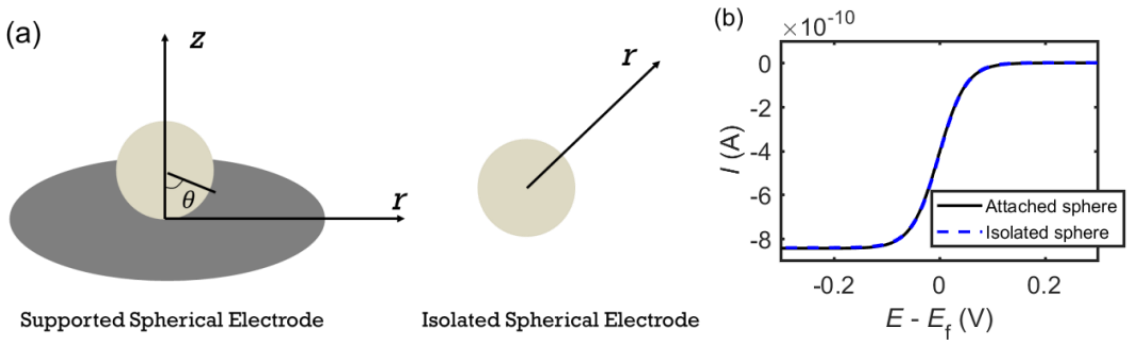


Figure B1. (a) Illustration of the geometries of the two spherical electrodes. (b) Cyclic voltammogram of the one-electron-transfer reaction. Black solid line: a spherical particle supported on a supporting electrode; blue dashed line: an isolated spherical electrode.

Appendix B4: Simulation and Experiment under Various MV^{2+} doping Levels.

Figure B2 shows the comparison between the simulations including (Figure B2a and 2b) and excluding (Figure B2c and 2d) the electrochemical oxygen reduction reaction. In the experiments of fully-doped MV^{2+} and half-doped MV^{2+}, the model including the electrochemical oxygen reduction reaction fits the experiment results much better, showing that it is available to distinguish the two competing catalytic reactions, the MV^{+} catalysed ORR and the electrochemical ORR, on a micro-/nano-size electrode.

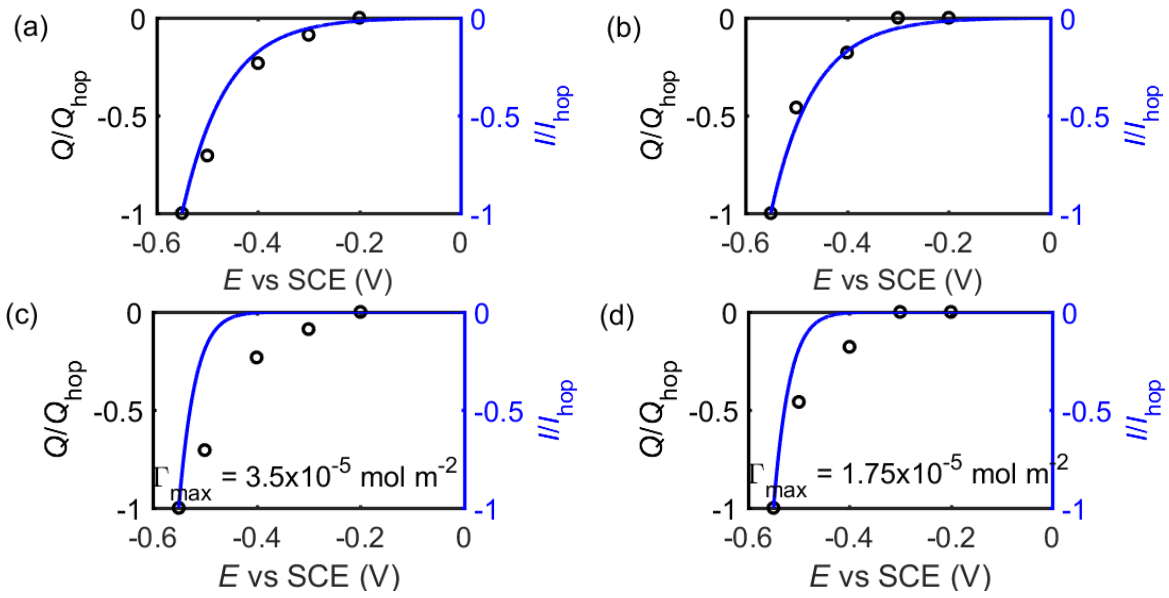


Figure B2. Potential dependence of the nano-impact charge and the simulated current-potential response. (a) fully-doped Nafion particles, where the MV^{2+} doping concentration in Nafion particles is 4.1 mM (the effective surface coverage of MV^{2+} Γ_{max} = 2.6×10^{-6} mol m^{-2}); (b) half-doped Nafion particles, where the MV^{2+} doping concentration in Nafion particles is 2.55 mM (the effective surface coverage of MV^{2+} Γ_{max} = 1.3×10^{-6} mol m^{-2}). (c) and (d) are the simulation excluding the electrochemical oxygen reduction reaction. Other simulation parameters are the same as used in Figure 15. The measurement is implemented in air saturated solution where c_{O2}^{*} = 0.26 mM. r_{el} = 0.43 μm.

Bibliography

(1) Yang, H.; Li, X.; Batchelor-McAuley, C.; Sokolov, S. V.; Compton, R. G. *Physical Chemistry Chemical Physics* **2018**, *20*, 682-689.
(2) Takamatsu, T.; Eisenberg, A. *Journal of Applied Polymer Science* **1979**, *24*, 2221-2235.
(3) Mauritz, K. A.; Moore, R. B. *Chemical Reviews* **2004**, *104*, 4535-4586.
(4) Bard, A. J.; Faulkner, L. R. *Electrochemical Methods: Fundamentals and Applications*; Wiley, 2000.
(5) Streeter, I.; Compton, R. G. *Journal of Physical Chemistry C* **2007**, *111*, 18049-18054.

Appendix C

Appendix C1: Radius of the Diffusion Domain

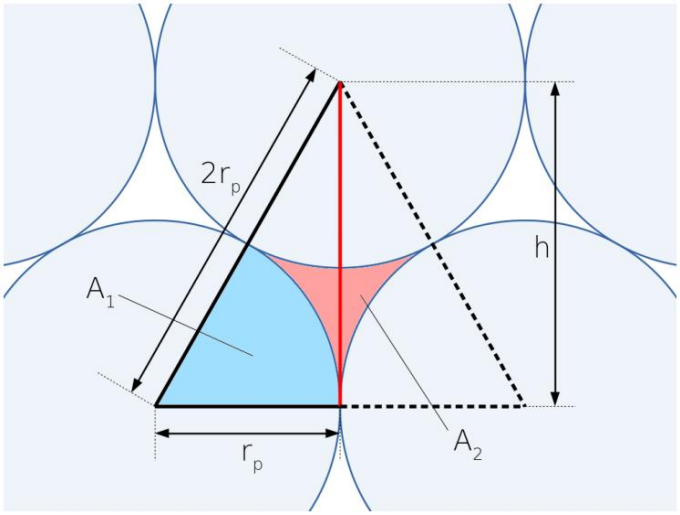


Figure C1: Illustration of the geometry considered in the approximation of the radius of the diffusion domain.

To find an approximate value for the radius of the diffusion domain, the two-dimensional projection of the first layer of spheres along an axis perpendicular to the electrode surface is considered, see Figure C1, and the packing density η of the spheres in this projection is determined. To this end, an equilateral triangle is considered, noting that the entire geometry can be constructed of such triangles and the packing density of spheres inside the boundaries of the triangle must hence equal the packing density in the entire structure. The length h can be calculated to:

$$h = \sqrt{\left(2r_p\right)^2 - \left(r_p\right)^2} = \sqrt{3}r_p \tag{C1}$$

Using this value, the total area A_{tot} of the triangle is:

$$A_{tot} = r_p h = \sqrt{3}\left(r_p\right)^2 \tag{C2}$$

As evident from the figure, the area A_{tot} can be expressed through the total area occupied by spheres $3A_1$ and the unoccupied area A_2:

$$A_{tot} = 3A_1 + A_2 \tag{C3}$$

where it is noted that A_1 equals the area occupied by a sixth of a sphere:

$$A_1 = \frac{1}{6}\pi\left(r_p\right)^2 \tag{C4}$$

Using the above results, the packing density η can calculated to:

$$\eta = \frac{3A_1}{A_{tot}} = \frac{\frac{1}{2}\pi\left(r_p\right)^2}{\sqrt{3}\left(r_p\right)^2} = \frac{\pi\sqrt{3}}{6} = 0.9069 \tag{C5}$$

The so-obtained packing density can now be implemented in the diffusion domain which sets the particle into the centre of a cylindrical space featuring the radius r_{max}. The electrode area occupied by a single particle in the diffusion domain is hence:

$$A_p = \pi\left(r_p\right)^2 \tag{C6}$$

while the total electrode area within the diffusion domain is:

$$A_{dd} = \pi\left(r_{max}\right)^2 \tag{C7}$$

The packing density within the diffusion domain can now be calculated and set to the value above:

$$\eta = \frac{A_p}{A_{dd}} = \frac{\pi\sqrt{3}}{6} \tag{C8}$$

which yields a value for the radius of the diffusion domain:

$$r_{max} = 1.0501 r_p \tag{C9}$$

Appendix D

Appendix D1: Estimation of the Nafion Film Thickness

0.1 μL of MV-Nafion stock mixture was drop-cast on the GC electrode and the film dry thickness can be determined as followed:

Mass of 0.1 μL Nafion is:

$$m = V \cdot \rho \cdot wt\% = 0.1\mu L \times 0.921 g / cm^3 \times 5\% = 4.61 \times 10^{-6} g$$

where ρ is the density of Nafion perfluorinated resin solution, whose value obtained from the supplier Sigma-Aldrich.

The density of dry Nafion is relevant to its storage and drying conditions and in this case the dry density of Nafion, $\rho_{DryNafion}$, is 1.965 g cm^{-3}.[1]

Therefore the dry volume of Nafion is:

$$V = \frac{m}{\rho_{DryNafion}} = 2.48 \times 10^{-12} m^3$$

The diameter of GC electrode is 3 mm, hence the area is:

$$A = \pi D^2 / 4 = 7.07 \times 10^{-6} m^2$$

The dry thickness for 0.1 μL of MV-Nafion thin film on the GC electrode is:

$$h = \frac{V}{A} = \frac{2.48 \times 10^{-12} m^3}{7.07 \times 10^{-6} m^2} = 0.35 \mu m$$

Similarly, the dry thickness for 0.5 μL and 1.5 μL of MV-Nafion thin film on the GC can be determined as 1.75 μm and 5.26 μm respectively.

Appendix D2: Estimation of the Number of MV-Nafion Particle Layers Drop-casted on Glassy Carbon Electrodes

For single MV-Nafion particle, the average radius is 0.43 ± 0.26 μm and the density of Nafion in water, $\rho_{DryNafion}$, is 1.858 g cm^{-3}.[1]

Hence the mass for single particles is:

$$m_{Nafion} = \frac{4}{3}\pi r^3 \rho_{Nafion} = 6.36\times10^{-13} g$$

Total mass of Nafion used to synthesize Nafion particles is:

$$m_{total} = V \cdot \rho \cdot wt\% = 50\mu L \times 0.921 g/cm^3 \times 12.5\% = 5.76\times10^{-3} g$$

The number of Nafion particle synthesized is:

$$N = \frac{m_{total}}{m_{Nafion}} = \frac{5.76\times10^{-3} g}{6.36\times10^{-13} g} = 9.05\times10^{9}$$

Final Nafion particle suspension volume is 0.5 mL.

Then the concentration of Nafion particle suspension is:

$$C = \frac{N}{V} = \frac{9.05\times10^{9}}{0.5mL} = 1.81\times10^{10}\ particles/mL$$

Hence the number of Nafion particle drop-casted on the GC electrode is:

$$N_{GC} = C \cdot V_{GC} = 1.81\times10^{10}\ particles/mL \times 10\mu L = 1.81\times10^{8}\ particles$$

Number of layers Nafion particles is:

$$N_{layers} = \frac{A_{particles}}{A_{GC}} = \frac{\pi\times(0.43\mu m)^2 \times 1.81\times10^{8}}{7.07\times10^{-6} m^2} = 15\ layers$$

Appendix D3: Simulation of the Cyclic Voltammetry of MV^{2+}/MV^{+} via the Single Nafion Particle Model

To explore the ion transport property of MV^{2+}/MV^{+} in Nafion particles, the cyclic voltammetry of immobilized Nafion particles with different drop-casting amounts under variable scan rates are measured. As the redox species are confined in Nafion particles, the single particle model is applied when simulating multiple layers of immobilized Nafion particles. The experiment data is analysed via the single Nafion particle model, by which the approximate ion transport time τ_{it}, the diffusion difference between the reactant and the product D_{MV+}/D_{MV2+} , and the contacting area where the immobilized particle attached on the electrode are determined.

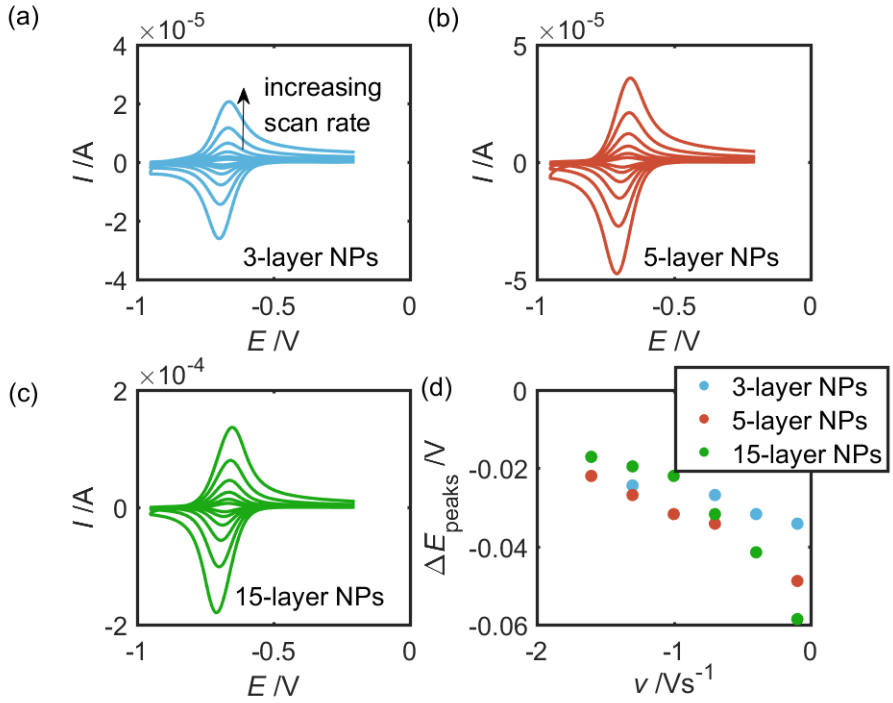


Figure D1. (a) Cyclic voltammograms of 3-layer Nafion particles modified electrode under various scan rates of 0.025, 0.05, 0.1, 0.2, 0.4, 0.8 V s^{-1}; (b) Cyclic voltammograms of 5-layer Nafion particles; (c) Cyclic voltammograms of 15-layer Nafion particles; (d) Scan rate dependence of the peak-to-peak separation of the 3-layer, 5-layer and 15-layer Nafion particles. Experiment conditions are mentioned in the main text.

The cyclic voltammetry of 3, 5 and 15 layers of MV^{2+} doped Nafion particles under variable scan rates is presented in Figure D1 a, b and c. The scan rate implemented in the experiment for each electrode is 0.025, 0.05, 0.1, 0.2, 0.4, 0.8 V s^{-1}. The scan rate dependence of the forward and backward peak currents has been shown in Figure 10.9 in the main text and the peak-to-peak separation ΔE_{peaks}, the difference between the forward and backward peak potentials, is shown in Figure D1d. Comparing to the current-time response measured from the single particle experiment, the immobilized particles provide three fitting features, the forward peak current, the backward peak current and the peak-to-peak separation, which can be used as the fitting objectives.

In the single particle simulation model, as explained in the main text, not only the ion transport time τ_{it} and the diffusion coefficient difference between MV^{+} and MV^{2+} D_{MV+}/D_{MV2+} but also the contacting angle of the particle ϕ_{cnt} are unknown. To explore the scan rate dependence of the cyclic voltammogram in the Nafion particles, Figure D2 shows the simulation results of various scan rates and three different contacting angles. The simulation results are presented in the dimensionless format, where J is the flux, θ is the overpotential, δ is the scan rate and N_{MV2+} is the mass of MV^{2+} in one Nafion particle. The dimensionless MV^{2+} mass in one particle is $4/3\pi$ before the electrochemical reaction. Figure D2 a and b are the simulation results in which the contacting area between the particle and the electrode is relatively small. In Figure D2a, the waveshape of the cyclic voltammogram with a small contacting area varies when the scan rate increases and only at low scan rate, the simulated waveshape is similar to that observed in the experiment. Figure D2b explains the waveshape variation as a function of the scan rate. It is found that only when the reactant can be fully assumed, for instance the case of δ = 0.01, the experiment-like waveshape can be observed in the simulation. Similar phenomena can be found in simulations with larger contacting areas as shown in Figure D2 c-f.

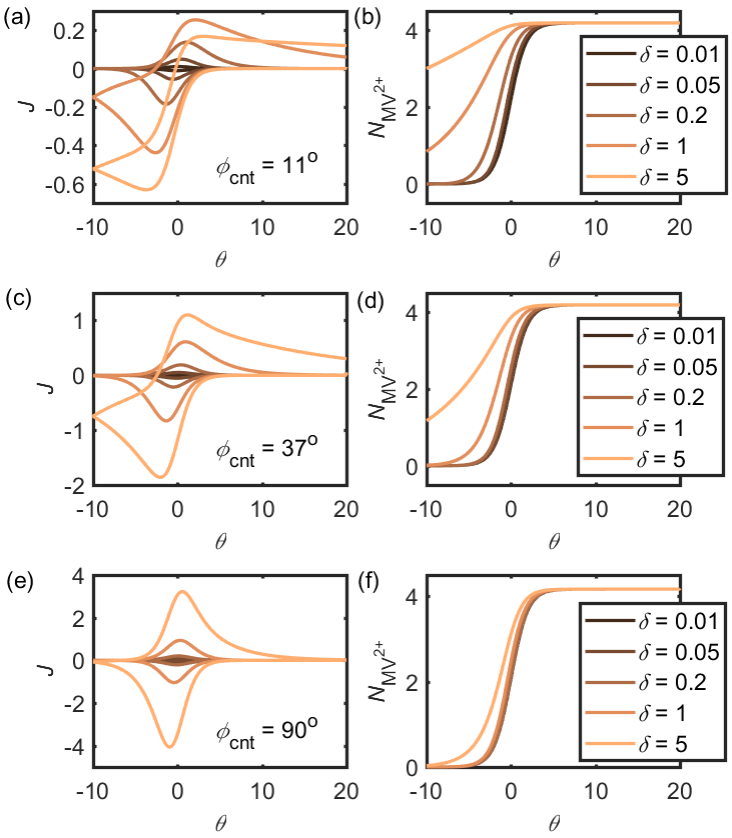


Figure D2. (a) Dimensionless cyclic voltammogram simulated for one particle of 11° contacting angle under a series of scan rates. (b) Dimensionless mass variation of the reactant during the reaction. (c) and (d) are the cyclic voltammogram and the mass variation for one particle of 37° contacting angle; (e) and (f) are the cyclic voltammogram and the mass variation for one particle of 90° contacting angle. In the simulation D_{MV+}/D_{MV2+} is set to be 0.5 and other simulation conditions are the same as in the main text.

To determine the unknown parameters τ_{it}, D_{MV+}/D_{MV2+} and ϕ_{cnt}, the forward peak current, the backward peak current and the peak-to-peak separation are compared. The transformation between the dimensionless and dimensional variables has been explained in the main text. Figure D3 illustrates the scan rate dependence of the simulated peak currents and peak-to-peak separation in the dimensional format. Three contacting areas with the same τ_{it} (0.025 s) and D_{MV+}/D_{MV2+} (0.5) are compared. It is found that only at low scan rate the peak current increases linearly as a function of the scan rate; and the scan rate dependence of the peak-to-peak separation varies with the contacting area. Figure D4 illustrates the scan rate dependence with constant contacting angle ϕ_{cnt} (37°) and

D_{MV+}/D_{MV2+} (0.5). Three ion transport times are applied in Figure D4. Varying τ_{it} alters the peak current increasing region while the scan rate dependence of the peak-to-peak separation is irrelevant to the value of τ_{it}. In the data fitting procedure, not only the scale of the fitting objectives but also the dependence on certain variables needs to be taken into consideration. As shown in Figure D1 and Figure 10.9 in the main text, the experimental peak currents increases with the scan rate and the peak-to-peak separation varies among the three Nafion particle modified electrodes. Therefore, combining the simulation result with the experiment data, it can be determined that τ_{it} is approximately 0.025 s for MV^{2+} in Nafion particles, D_{MV+}/D_{MV2+} is ca. 0.5 and the contacting angles for the 3-layer, 5-layer and 15-layer Nafion particles to be ca. 45°, 30° and 18°.

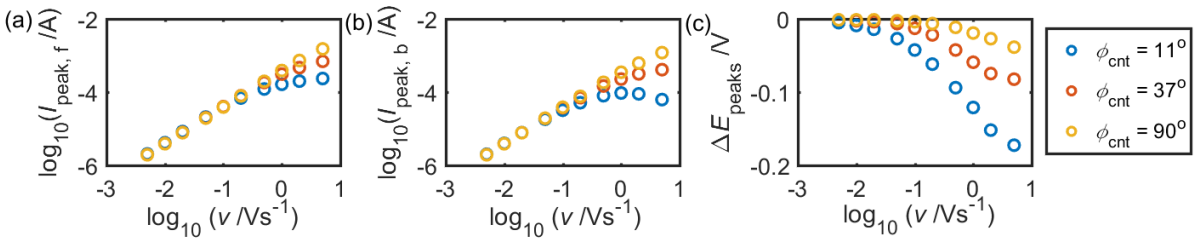


Figure D3. Scan rate dependence of (a) simulated forward peak currents, (b) simulated backward peak currents, (c) simulated peak-to-peak separations. Three different contacting angles are presented, 11°, 37° and 90°. In the simulation, τ_{it} is set as 0.025 s and D_{MV+}/D_{MV2+} = 0.5. The reaction charge Q applied is measured from the 15-layer Nafion particle experiment and Q = 4.0×10^{-5} C.

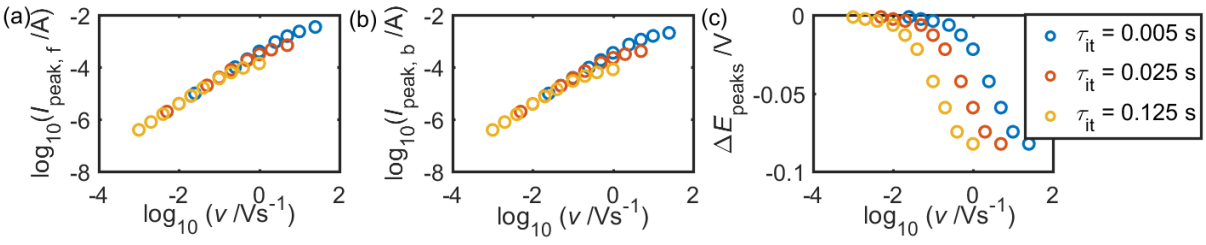


Figure D4. Scan rate dependence of (a) simulated forward peak currents, (b) simulated backward peak currents, (c) simulated peak-to-peak separations. Three different ion transport time are presented, 0.005, 0.025 and 0.125 s. In the simulation, ϕ_{cnt} is set as 37° and D_{MV+}/D_{MV2+} = 0.5. The reaction charge Q applied is measured from the 15-layer Nafion particle experiment and Q = 4.0×10^{-5} C.

Bibliography

(1) Takamatsu, T.; Eisenberg, A. *Journal of Applied Polymer Science* **1979**, *24*, 2221-2235.

Appendix E

Appendix E1: Stability of MV^{2+}/MV^{+} Nafion Film Electrodes

The potential of the optimized MV^{2+}/MV^{+} Nafion film reference electrode and its stability were also assessed electrochemically. The midpoint potential, E_{mid}, of the mediator was −0.165 V *vs.* MV^{2+}/MV^{+} Nafion film. The E_{mid} of reduction of $[Ru(NH_3)_6]^{3+}$ *vs.* SCE is −0.176 V, as shown in Figure 11.15. Therefore, the potential of fabricated MV^{2+}/MV^{+} Nafion film reference electrode in aqueous solution was determined as +0.011 V *vs.* SCE or +0.252 V *vs.* HNE. Figure E1 depicts a good stability of MV^{2+}/MV^{+} Nafion film reference electrode at optimized conditions (doping ratio of 1:30, film thickness of 35 μm and uniform film surface). The variation of E_{mid} with experimental time was within an average deviation of 4 mV over 12 h and less than 9 mV after 24 h in solution. The MV^{2+}/MV^{+} Nafion films also shows high stability over a series of measurements with only 1 mV drift after 600 successive cycles and 4 mV drift after 1000 successive cycles.

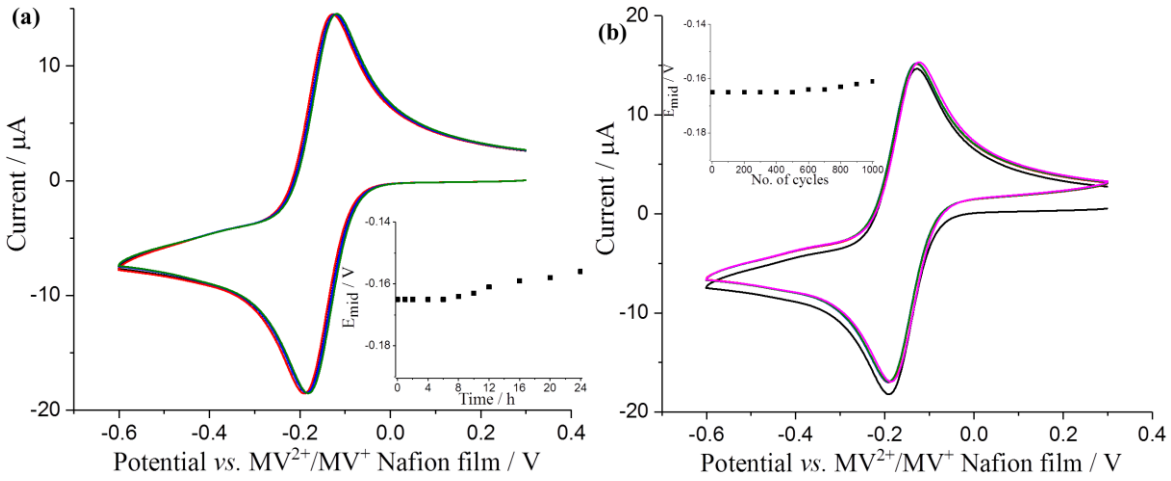


Figure E1. (a) Voltammograms of a glassy carbon working electrode with a MV^{2+}/MV^{+} Nafion film reference electrode in 0.1 M KCl aqueous solution containing 1 mM $[Ru(NH_3)_6]Cl_3$ at a scan rate of 0.1 V s^{-1} recorded after the electrodes immersing in solution (fresh, black line; 2 h, red line; 12 h, blue; 24 h, green line). Inset shows the midpoint potential, E_{mid}, over the time. (b) Voltammograms recorded over 1000 successive scans (1st scan, black line; 100th scan, red line; 200th scan, blue; 600th scan, green line; 1000th scan, magenta line). Inset shows the midpoint potential, E_{mid}, over the number of scans.

Appendix E2: Stability of $Ru(bpy)_3^{2+}/Ru(bpy)_3^{3+}$ Nafion Films

The potential of the optimized $Ru(bpy)_3^{2+}/Ru(bpy)_3^{3+}$ Nafion film reference electrode and its stability were also assessed electrochemically. The midpoint potential, E_{mid}, of the mediator was −0.561 V *vs.* $Ru(bpy)_3^{2+}/Ru(bpy)_3^{3+}$ Nafion film. The E_{mid} of reduction of $[Ru(NH_3)_6]^{3+}$ *vs.* SCE is −0.176 V. Therefore, the potential of fabricated $Ru(bpy)_3^{2+}/Ru(bpy)_3^{3+}$ Nafion film reference electrode in aqueous solution was determined as −0.385 V *vs.* SCE or −0.144 V *vs.* HNE. Figure E2 depicts a good stability of the $Ru(bpy)_3^{2+}/Ru(bpy)_3^{3+}$ Nafion film reference electrode at optimized conditions (doping ratio of 1:30, film thickness of 35 μm and uniform film surface). The variation of E_{mid} with experimental time was within an average deviation of 3 mV over 12 h and less than 8 mV after 24 h in solution. The $Ru(bpy)_3^{2+}/Ru(bpy)_3^{3+}$ Nafion films also shows high stability over a series of measurements with only 1 mV drift after 600 successive cycles and 4 mV drift after 1000 successive cycles.

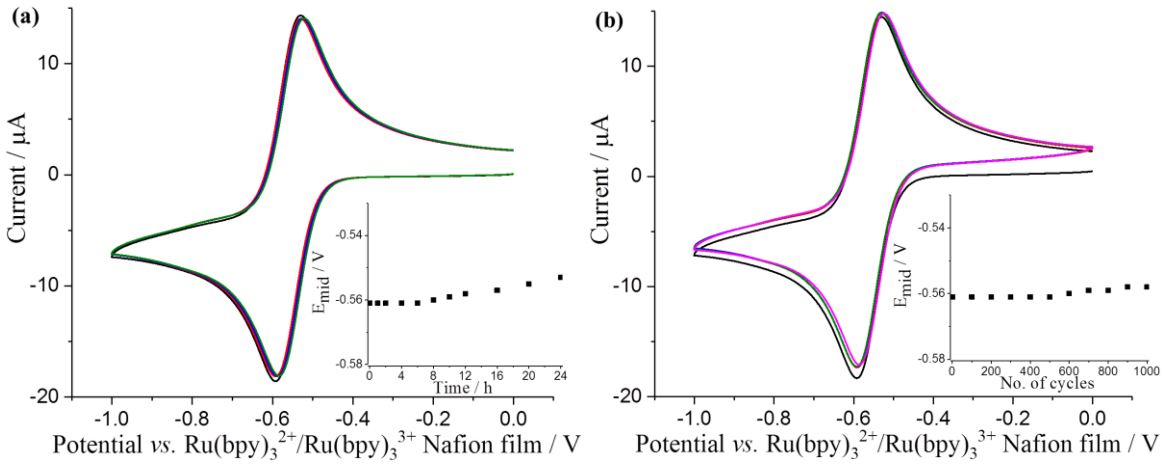


Figure E2. (a) Voltammograms of a glassy carbon working electrode with a $Ru(bpy)_3^{2+}/Ru(bpy)_3^{3+}$ Nafion film reference electrode in 0.1 M KCl aqueous solution containing 1 mM $[Ru(NH_3)_6]Cl_3$ at a scan rate of 0.1 V s^{-1} recorded after the electrodes immersing in solution (fresh, black line; 2 h, red line; 12 h, blue; 24 h, green line). Inset shows the midpoint potential, E_{mid}, over the time. (b) Voltammograms recorded over 1000 successive scans (1st scan, black line; 100th scan, red line; 200th scan, blue; 600th scan, green line; 1000th scan, magenta line). Inset shows the midpoint potential, E_{mid}, over the number of scans.

Appendix E3: Stability of PVFc/PVFc$^+$ Nafion Film Electrodes

The potential of optimized PVFc/PVFc$^+$ Nafion film reference electrode and its stability were also assessed electrochemically. The midpoint potential, E_{mid}, of the mediator was −0.233 V *vs.* PVFc/PVFc$^+$ Nafion film. The E_{mid} of reduction of $[Ru(NH_3)_6]^{3+}$ *vs.* SCE is −0.176 V. Therefore, the potential of fabricated PVFc/PVFc$^+$ Nafion film reference electrode in aqueous solution was determined as −0.057 V *vs.* SCE or +0.184 V *vs.* HNE. Figure E3 depicts a good stability of PVFc/PVFc$^+$ Nafion film reference electrode at optimized conditions (doping ratio of 1:30, film thickness of 35 μm and uniform film surface). The variation of E_{mid} with experimental time was within an average deviation of 2 mV over 12 h and less than 5 mV after 24 h in solution. The PVFc/PVFc$^+$ Nafion films also shows high stability over a series of measurements with no drift after 600 successive cycles and only 3 mV drift after 1000 successive cycles.

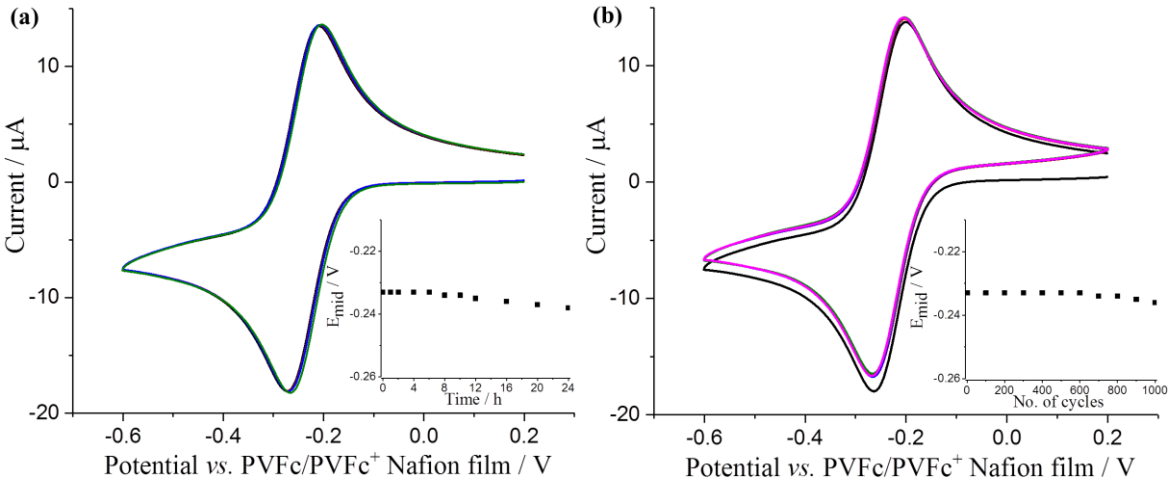


Figure E3. (a) Voltammograms of a glassy carbon working electrode with a PVFc/PVFc$^+$ Nafion film reference electrode in 0.1 M KCl aqueous solution containing 1 mM $[Ru(NH_3)_6]Cl_3$ at a scan rate of 0.1 V s^{-1} recorded after the electrodes immersing in solution (fresh, black line; 2 h, red line; 12 h, blue; 24 h, green line). Inset shows the midpoint potential, E_{mid}, over the time. (b) Voltammograms recorded over 1000 successive scans (1st scan, black line; 100th scan, red line; 200th scan, blue; 600th scan, green line; 1000th scan, magenta line). Inset shows the midpoint potential, E_{mid}, over the number of scans.

Appendix E4: Estimation of the Relative Amount of Dopant Redox Species in Nafion Film Reference Electrodes

The relative amount of Fc and Fc^+ in Nafion films under optimized conditions (the doping ratio of Fc^+:SO_3^- = 1:30 and thickness of 35 μm) can be estimated as followed:

Mass of 10 μL Nafion film (thickness of 35 μm) is

$$m = V \cdot \rho \cdot wt\% = 10\mu L \times 0.921 g/cm^3 \times 5\% = 4.61 \times 10^{-4} g$$

where ρ is the density of Nafion perfluorinated resin solution, whose value obtained from the supplier Sigma-Aldrich.

Equivalent weight (EW) of Nafion is defined as the number of grams of dry Nafion per mole of sulfonic acid groups when the material is in the acid form.[1] Nafion used in this work is 1100 EW.

The amount of SO_3^- can be then estimated as

$$n_{SO_3^-} = \frac{4.61 \times 10^{-4} g}{1100 g/mol} = 4.19 \times 10^{-7} mol$$

The doping ratio of Fc^+:SO_3^- is 1:30 hence the total amount of Fc^+ in the film is

$$n_{Fc^+} = \frac{4.19 \times 10^{-7} mol}{30} = 1.40 \times 10^{-8} mol$$

The Fc was electro-generated via partial reduction of Fc^+ as shown in Figure 11.1 and the charge of this partial reduction can be estimated, with the aid of the software Origin, from Figure 11.1b to be 2.46 × 10^{-6} C.

Hence the number and mole of Fc generated within the film is

$$N_{Fc} = \frac{2.46 \times 10^{-6} C}{1.60 \times 10^{-19} C} = 1.53 \times 10^{13}; n_{Fc} = 2.54 \times 10^{-11} mol$$

The relative amount of Fc and Fc^+ in Nafion films is

$$\frac{n_{Fc}}{n_{Fc^+}} = \frac{2.54\times10^{-11} mol}{1.40\times10^{-8} mol - 2.54\times10^{-11} mol} = \frac{1}{548}$$

Similarly, the relative amount of dopant redox species in Nafion film of other three reference electrodes under optimized conditions are estimated to be:

For the MV^{2+}/MV^+ Nafion film reference electrodes, $MV^+:MV^{2+}$ = 1:133

For the $Ru(bpy)_3^{2+}/Ru(bpy)_3^{3+}$ Nafion film electrodes, $Ru(bpy)_3^{3+}:Ru(bpy)_3^{2+}$ = 1:174

For the $PVFc/PVFc^+$ Nafion film reference electrodes, $PVFc^+$:PVFc = 1:903

Bibliography

(1) Mauritz, K. A.; Moore, R. B. *Chemical Reviews* **2004**, *104*, 4535-4586.